Bifurcations, Multiple solutions and Strange Attractors in Thermal Convection

PhD Thesis

Hermes Ferialdi

James Weir Fluids Laboratory
Department of Mechanical and Aerospace Engineering
University of Strathclyde, Glasgow

March 15, 2020

This thesis is the result of the author's original research. It has been composed by the author and has not been previously submitted for examination which has led to the award of a degree.

The copyright of this thesis belongs to the author under the terms of the United Kingdom Copyright Acts as qualified by University of Strathclyde Regulation 3.50. Due acknowledgement must always be made of the use of any material contained in, or derived from, this thesis.

Hermes Ferialdi

University of Strathclyde, March 15, 2020

Related research

he results described in Part II of this thesis have also been used for the preparation of research articles submitted to International Scientific Journals or chapters appearing in scientific books. Some specific results have also been presented in the framework of Conferences.

Journal papers

1. Lappa M., Ferialdi H.,"On the General Properties of Steady Gravitational Thermal Flows of Liquid Metals in Variable Cross-section Containers", Review of Applied Physics (RAP), Volume 5, 2017.

2. Lappa M., Ferialdi H.,"On the oscillatory hydrodynamic instability of gravitational thermal flows of liquid metals in variable cross-section containers", Physics Fluids 29, 064106 (2017).

3. Lappa M., Ferialdi H.,"Gravitational thermal flows of liquid metals in 3D variable cross-section containers:Transition from low-dimensional to high-dimensional chaos",Chaos 28, 093114 (2018).

4. Lappa M., Ferialdi H.,"Multiple solutions, oscillons, and strange attractors in thermoviscoelastic Marangoni convection",Physics of Fluids 30, 104104 (2018).

5. Ferialdi H., Lappa M., "An Experimental and Numerical Investigation into the Sensitivity of Rayleigh-Bénard Convection to Heat Loss Through the Side-walls" (paper in preparation).

6. Ferialdi H., Lappa M., Haughey C.," On the Role of Thermal Boundary Conditions in Typical Problems of Buoyancy Convection: A Combined Experimental-Numerical Analysis" (paper in preparation).

Book chapters

1. Lappa M., Ferialdi H.,"Oscillatory and Turbulent Flows of Liquid Metals in Differentially Heated Systems with Horizontal and Non-horizontal Walls.",In book: Recent Studies in Materials Science (Chapter 3) , Nova Science Publishers Inc., 2019.

Conference presentations

1. Ferialdi H., Lappa M., "Oscillatory motion of liquid metals in non?isothermal geometries with converging or diverging walls",30th Scottish Fluid Mechanics Meeting, 2017.

Abstract

In the present work the complex subject of thermal convection is tackled both numerically and experimentally. In the past, this subject has attracted the interest of many researchers due to its importance in many technological processes and natural phenomena. The present thesis has been devoted to explore some important aspects still requiring attention due to the inherent (physical) complexity and the difficulties embedded in the underlying (mathematical) models. In particular, its main objective has been an investigation into the specific routes taken by thermal convection to evolve from initial (steady and laminar) states towards (low-dimensional or high-dimensional) chaos. Towards this end, the problem has been approached in the framework of numerical (direct numerical solution of the governing non-linear equations) and experimental activities; these have been used in synergy with existing theories on the behaviour of non-linear systems (e.g. the bifurcation theory) and tools for the analysis of chaotic systems (algorithms for the evaluation of the fractal structure of attractors). Moreover, much effort has been devoted to identify the existence in the space of parameters of different branches of laminar flows that coexist and can be effectively selected by a fluid-dynamic process depending on its initial state, i.e. the so-called multiple solutions. In order to identify 'universality classes' in such dynamics, different types of convection (driven by thermal buoyancy and/or by surface-tension gradients) and different fluids (namely, liquid metals, gases, ordinary liquids and even non-Newtonian liquids) have been considered. As another possible degree of freedom potentially affecting the considered problems, the role of thermal boundary conditions has also been explored (assuming adiabatic and conducting boundaries, or walls with finite thickness, which can effectively exchange heat with the external environment). The thesis has been structured in order to elaborate a relevant physical and mathematical context in the first part and present extensively all the obtained results in the second part.

To my parents, hoping that my father would be proud of me

Acknowledgements

This PhD experience has been an important chapter of my life, allowing me to learn many new exciting topics and grow as a person. So here, I wish to thank all the people who helped me throughout this journey. First, I would like to thank my supervisor, Dr Marcello Lappa, for his support and guidance through every stage of my PhD. His suggestions and expertise indeed have been of invaluable importance. Moreover, I wish to thank my second supervisor, Dr Mónica S.N. Oliveira, for her support in the experimental part of this thesis. My gratefulness also goes to all my collogues and peers, with whom I had several beneficial and instructive discussions. Moreover, I would like to thank Paolo for having printed the hardbound copy of this thesis.

To conclude, an exceptional thank goes to my parents, who have always supported my and without whom, not only this PhD but also every goal of my life would never be possible.

Contents

Part I

Physical and mathematical framework

Chapter 1

Introduction

The main protagonist of this thesis is thermal convection and, as we will see throughout this work, we approach the subject under a fundamental and theoretical point of view. The shape of the domains considered indeed is kept simple, as our focus is on the emerging patterns, which are extremely sensitive to the variations of the parameters describing the system. There is a vast amount of literature dealing with thermal flows in simple systems and, as we will see in Chapter 4, probably the simplest and at the same time one of the most studied configurations is that of an infinite layer subjected to a vertical or horizontal temperature gradient. Despite the simplicity of the domain and the boundary conditions considered, we will see in Chapter 3 the richness in terms of patterns and temporal behaviours to which even such a basic system could undergo. In Part II, we consider more complicated shapes (Chapter 7), boundary conditions (Chapter 9) and also, as done in Chapter 8, more complex fluids. The present work aims to understand how the already variegated scenario becomes reacher by introducing some further degree of freedom into to system. The new complexities brought by the increased number of degrees of freedom can involve the geometry of the domain such as the cavity with convergent or divergent walls considered in Chapter 7 or the thermal boundary conditions, which can be assumed more realistic as done in Chapter 9. Another path that has been followed in Chapter 8 is to considerer still the infinite layer (mimicked by periodic boundary conditions) but filled with a more complex fluid with a viscoelastic behaviour. Part II of this thesis is entirely devoted to describing such systems and the emerging phenomena such as multiplicity of solutions, crises, chaotic behaviours... which are an important feature of the thermal convection.

On the other hand to gain a correct understanding of the results presented in this work

(Part II) we should first contextualise the notions and the concepts appearing in Part II in the correct physical and mathematical framework, which is the aim of Part I.
One reason why thermal convection attracted the interest of researchers in the past (and present) decades is that it offers a good testbed to study many dynamical phenomena, such as bifurcations, chaos, rising of turbulence.
Nevertheless, it has many implications, both in technical problems and natural phenomena. As the most of the present thesis is devoted to describe and analyse the theoretical aspects related to thermal convection, in the remaining part of this chapter we intend to provide some practical examples in which thermal convection plays an important role.

1.1 Some examples of thermal convection in technological processes

The buoyancy and surface-tension driven flows with their emerging patterns can strongly affect the heat and mass transfer in many technological applications such as heat exchangers, power plants, nuclear reactors, the formation of semiconductor crystals used to build processors and microchips. An important field where the emerging convective patterns have central importance is the material science (see, e.g. Amberg and Shiomi [1], Prud'homme and El Ganaoui [2], Hirata [3]). An important process in the field mentioned above, which we would like to describe more in detail, is the so-called crystal growth from the melt (see Lappa [4] and references therein). According to such technique, the semiconductor crystals are formed out from the melt. For this reason, the pattern emerging in the liquid phase could strongly affect the quality of the crystals. A first issue which could jeopardise the correct solidification of the crystal is the shape of the interface between the melt and the solid phase, which could undergo to a series of morphological instabilities (see, e.g. Delves[5], Schulze and Davis [6], Davis and Schulze [7]). Another detrimental effect which may arise in the semiconductor melts due to the convective phenomena are some differences of the dopant concentration in the different part of the crystal. These defects could be of the same scale as the crystal, called in this case macro-segregations, or involve a small scale (millimetres or micrometres), being micro-segregations. The oscillatory behaviour in the molten phase moreover could lead in extreme cases to the growth and remelting of the crystal at the

interface. This oscillatory behaviour of the growth rate of the solidified region leads to inhomogeneities in the dopant concentrations, which take the form of striations. Both the buoyancy effects, driven by gravity and the surface tension ones (Marangoni effect) could lead to the above phenomenon along with other undesirable consequences such as dislocations, strains fields, voids and grain boundaries. For this reason, a correct prediction of the patterns and related instabilities emerging in the fluid flows are of the primary importance in obtaining good quality crystals.

As the main classical techniques employed to obtain a crystal from a melt can be reproduced by using simple geometries such as parallelepipedic cavities, cylinders, annular cavities, it is worth to study the convection in such geometries. In the following paragraphs moreover, a short description of the methods mentioned above is given.

Bridgman method This technique implies two possible configurations: an open horizontal container sketched in Figure 1.1a), known as an open boat (HB) or a vertical ampoule (VB), represented in figure 1.1b. According to the VB, a directional solidification is imposed by moving the ampoule (made of, for example, quartz glass or graphite) through a furnace (or vice-versa: moving the furnace), equivalently the temperature can be slowly lowered with both the ampoule and the furnace can be kept fixed. Differently from its vertical companion, the HB has a horizontal orientation with a free surface exposed to an inert gas.

Being the latter configuration sensitive to heat dissipation through its sides, the HB is more prone to the Hadley convection (buoyancy convection with lateral heating, see Chapter 3) as VB. Moreover, due to the presence of the free surface, the HB could undergo thermo-capillary effects (Marangoni convection).

Floating-zone technique According to this method (FZ), the molten material is located between an upper feeding rod and a lower seed. The configuration of the FZ is sketched in Figure 1.2, where it is possible to notice a heating ring, which aims to keep the temperature higher than the melting point. Moreover, the FZ is put in relative motion w.r.t to the heating device to allow a correct solidification of the melt on the seed.

A clear advantage of this technique is the absence of contacts with the container (except for the upper part). However on the Earth, due to the gravity, the size of the crystals

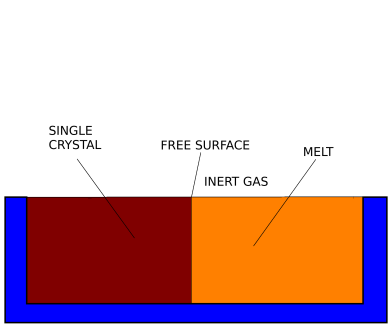

(a) Open boat configuration.

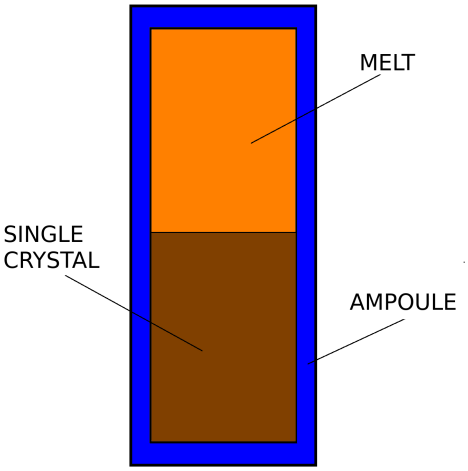

(b) Vertical Bridgman configuration.

Figure 1.1: Configuration assumed according to the Bridgman method.

obtained have to be kept very small otherwise the molten zone could collapse. On the other hand, it is possible to obtain larger samples in a microgravity environment.

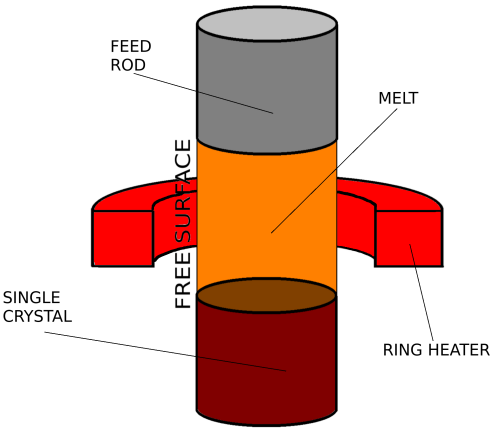

Figure 1.2: Floating zone configuration.

Czochralski technique This method is represented in Figure 1.3, where it is possible to see the melt contained in a crucible which can be heated arbitrarily from the side or the bottom. Once the melt is at the right temperature, a seed is introduced into it, and a rotating motion is impressed to it. When the melt starts to solidify on the seed, it is slowly removed as the crystal is forming. Similarly to the HB and FZ, due to the presence of the free surface, the melt may undergo motions originated by thermo-capillary effects (Marangoni effect) along with those caused by the gravitational forces.

Moreover, as the seed rotates, also Coriolis forces may arise, which combined with the buoyancy can be responsible for additional effects.

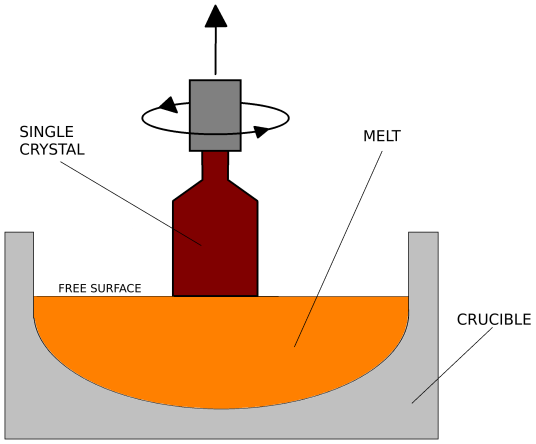

Figure 1.3: Representation of the Czochralski method

1.2 Thermal convection in natural phenomena

In the previous section, some examples of the thermal convection in technological and industrial processes were presented to highlight its influence in the construction of objects of everyday use. Along with such technological applications, thermal convection is the main actor of many natural phenomena. In this section, we give some example of natural convective phenomena on the Earth and also in our solar system.

Convection in the Earth mantle The fluid motion inside the liquid portion of the Earth is an example of the Rayleigh-Bénard convection (system heated from below and cooled from above), in which the decay of radioactive elements provides the heat. Indeed, as depicted in Figure 1.4 the Earth consists of four different layers: an inner solid and an outer liquid cores, made prevalently of iron and smaller amounts of nickel. The core is the most dense part ($10 - 13$ $\frac{g}{cm^3}$) and occupies the 16 % of the total volume of the Earth. The mantle, comprising the 83 % of the Earth volume, is the largest layer. It is more or less 3000 km thick, and the convective motions occur in it. In this region indeed the rocks, being subjected to high temperatures, behave like a highly viscous fluid. It consists for the largest part of peridotite, an igneous rock containing iron and magnesium, and it is less dense of the core ($3.3 - 5.7$ $\frac{g}{cm^3}$).

The most evident consequence of such convective motions is the plate tectonics (Plate

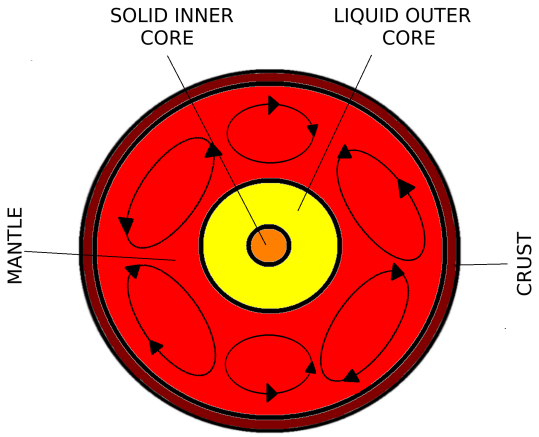

Figure 1.4: The earth layered structure

Tectonics Theory). According to which the outermost part of the crust, the lithosphere (with a depth comprised between 0 and 70 km) floats on the upper part of the mantle, the asthenosphere (see, e.g. Dietz [8], Morgan [9] [10]). The latter comprises the region between 100 km and 200 km below the Earth surface and behaves more plastically than the lower mantle (e.g. it is the region from where the magma comes).

While the mantle is responsible for the motion occurring on the crust, the convection happening in the outer core is responsible for the Earth magnetic field. The most accredited explanation of its presences relies on the motion of ionised liquid metal in the other core, acting like a dynamo. The strength of the magnetic field is not uniform on the Earth surface, ranging from less than 30 μT in an in the area comprising South America and South Africa, to more than 60 μT around the magnetic poles (located in northern Canada, part of Siberia and southern Australia).

The mechanism at the basis of mantle convection and that occurring in the outer core are similar, the resulting dynamics, however, is completely different as in the first case the Prandtl number is large while in the second it tends to 0 (we will see in the next chapter how this fact influences the dynamics).

The example of Galilean satellites The Galilean satellites are a clear example of how the convection is present also outside the Earth. An exciting example is Jupiter's moon Io, in which the friction originated by the tides supply the heat necessary to trigger the convection.

The mechanism just described above is believed to be responsible for the presence of

the oceans under the icy crust of the other Jupiter's satellites: Europa, Ganymede and Callisto.

Atmospheric circulation The inclination of the sun rays, hitting the Earth at the Equator and the poles, is responsible for different heating of these two zones. Indeed, being the rays almost orthogonal to the Earth surface at the Equator, this region is heated much more respect to poles, where the sun rays are almost horizontal, and heat lost to space overcomes that gained from the sunlight.
This consideration is at the basis of Hadley [11] work in 1735, who first proposed a model for the atmospheric circulation. According to his model, the differential heating described above produces four main convective cells, as depicted in Figure 1.5a. These four cells make the fluid raise at the Equator, which is the hotter side and sink at the colder poles. This model, however, disregards the shallow depth of the atmosphere, which prevents such elongated rolls from being formed. A more realistic model indeed is that represented in Figure 1.5b, according to which the main circulation is split into three rolls in each hemisphere.

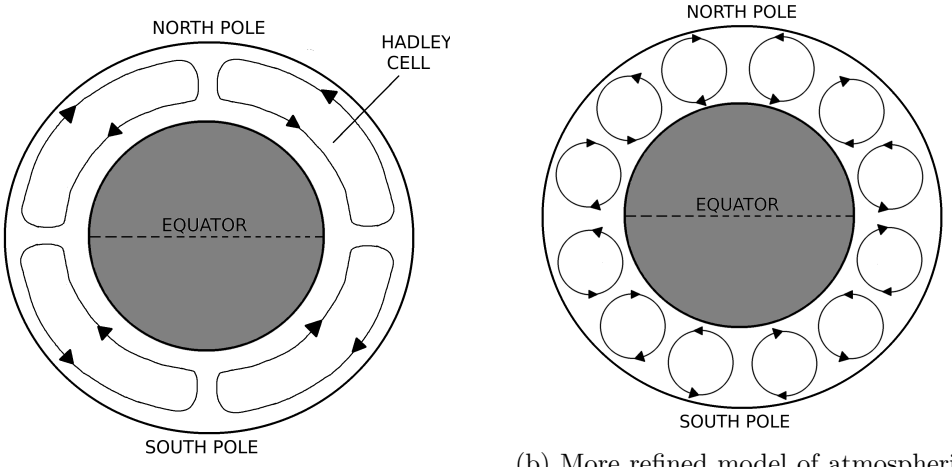

(a) Hadley circulation

(b) More refined model of atmospheric circulation.

Figure 1.5: Different models of atmospheric circulation.

Mesoscale atmospheric motions The models described in the previous paragraph describe large (planetary) scale motions. Along with those planetary convective phenomena, there are also mesoscale motions of the Rayleigh-Bénard type [1]. The clouds,

[1] The concepts of the Hadley and Rayleigh-Bénard configurations are accurately described in Chapter 3. For the present Chapter, however, it is enough to say that in the Hadley flows the temperature gradient is perpendicular to the gravity configuration, while in the Rayleigh-Bénard the two vectors

which can be regarded as tracers of the vertical motion, are a good detector of such mesoscale convection. Depending on the intensity of the vertical stream, the related convection is identified as deep or shallow. The first, as the name suggests, extends through the entire troposphere and is characterised by strong vertical motions. Examples of its manifestation are atmospheric phenomena like hurricanes. The latter involves only the lowest kilometres of the atmosphere and its characterised by weaker vertical streams. Although the first has a significant impact on human life, also the latter has been the object of several studies, due to its influence on the climate system.

(temperature gradient and gravity) are parallel and has the same verse.

Chapter 2

Physical models

2.1 The equations

This section aims to present the partial derivatives equations (PDE) governing the convection in the framework of the continuum. The phenomenon is ruled by the continuity and Navier-stokes equations plus an energy equation, which is needed to close the problem. In the following, we will start by describing the continuity equation, and then we will continue with the energy and Navier-Stokes equations.

2.1.1 Continuity

The continuity equation rules the total mass which flows inside and outside any open system. It states that the total mass variation over a certain amount of time equals the difference between the outflows and the inflows. Mathematically it takes the following form:

$$\frac{\partial \rho}{\partial t} + \nabla \cdot (\rho \underline{U}) = 0 \tag{2.1}$$

The equation 2.1 represent the continuity equation, which may have a variable density. As in the following, we will deal mainly with liquids in a condition under which the **incompressibility** hypothesis holds; we are allowed to simplify the 2.1 further, by imposing a constant density:

$$\nabla \cdot \underline{U} = 0 \tag{2.2}$$

The equation 2.2 can be regarded as the continuity equation applicable to any incompressible fluid, and it simply implies that the divergence of the velocity must to be 0 in any point of the domain. In other words, if the fluid is supposed to be incompressible,

its velocity field must be solenoidal, and hence no mass sources or sinks are allowed.

2.1.2 Energy equation

The other important transport equation, which rules the energy flow of a system is the energy equation:

$$\frac{\partial \rho c_v T}{\partial t} + \nabla \cdot (\rho \underline{U} c_p T) = \nabla \cdot (\lambda \nabla T) \tag{2.3}$$

The equation 2.3 is the form related to any fluid, which could be compressible and in general with variable properties. As outlined before in the most of the present text, we will deal with **incompressible** fluid **with constant thermophysical properties** (in the cases when we drop such hypothesis we explicitly mention it). With such an assumption, the equation 2.3 becomes:

$$\frac{\partial T}{\partial t} + \underline{U} \cdot \nabla T = \alpha \nabla^2 T \tag{2.4}$$

In the 2.4 α is the thermal diffusivity, defined as $\alpha = \frac{\lambda}{\rho c_p}$.

2.1.3 Momentum conservation: the Navier-Stokes equations

The derivation of this set of equations follows a similar procedure of the previous cases (continuity and energy equation). However,due to the vectorial nature of the momentum the calculations are slightly more involved. As the aim of the present Chapter is to give a quick review about the underlining physics the derivation of momentum equations is skipped, and only the final form is reported:

$$\frac{\partial \rho \underline{U}}{\partial t} + \nabla \cdot (\rho \underline{U}^T \underline{U}) = -\nabla p + \nabla \cdot \underline{\underline{\tau}} + \rho \underline{g} \tag{2.5}$$

As already done in the case of the energy equation, it is possible to rewrite the 2.5 for an incompressible fluid:

$$\rho \frac{\partial \underline{U}}{\partial t} + \rho \underline{U} \cdot (\nabla \underline{U}) = -\nabla p + \nabla \cdot \underline{\underline{\tau}} + \rho \underline{g} \tag{2.6}$$

The 2.5 and 2.6 are the Navier equations and as the final step to obtaining the final momentum equations the stress tensor $\underline{\underline{\tau}}$ needs to be further expanded. According to

the Newtonian fluid model, the **Stokes law** holds:

$$\tau = \mu(\nabla \underline{U} + (\nabla \underline{U})^T) \tag{2.7}$$

With the 2.7 it is possible to modify the 2.5:

$$\frac{\partial \rho \underline{U}}{\partial t} + \nabla \cdot (\rho \underline{U}^T \underline{U}) = -\nabla p + \nabla \cdot (\mu(\nabla \underline{U} + (\nabla \underline{U})^T)) + \rho \underline{g} \tag{2.8}$$

For an incompressible fluid with constant viscosity, knowing that $\nabla \cdot \nabla \underline{U}^T = 0$, the 2.8 becomes:

$$\rho \frac{\partial \underline{U}}{\partial t} + \rho \underline{U}(\nabla \underline{U}) = -\nabla p + \mu \nabla^2 \underline{U} + \rho \underline{g} \tag{2.9}$$

The 2.8 and 2.9 are the Navier-Stokes equation an together with the 2.3(or 2.4 if the fluid is incompressible) and continuity (2.1 or 2.2) are the equations which rule the motion of the fluids.

2.2 The Boussinesq approximation

As the main topic of the present manuscript is the thermal convection, and the buoyancy is one of the most important forces causing it (other forces are due to the Marangoni effect which will be explained in the next sections), this section is devoted to explaining how to deal with it especially in the case when the fluid is supposed to be incompressible. Qualitatively buoyancy can be understood knowing the fact that the hotter fluid is less dense than, the colder one, which tends to sink, giving rise to the convective motions. So the density difference is the main actor, which triggers the convection but, if the fluid is supposed to be incompressible, intrinsically means that the density must be constant both in space and in time. The question which arises here is: is it possible to retain the equations in their incompressible form and at the same time taking into account the buoyancy forces? Luckily the answer is yes, and this task can be accomplished through the so-called Boussinesq approximation, according to which the density is kept constant in all terms except in the last term in the RHS of 2.9 ($\rho \underline{g}$). In this last term the density is supposed to vary linearly with the temperature:

$$\rho \cong \rho_0(1 - \beta(T - T_0)) \tag{2.10}$$

Where ρ_0 is the density at the reference temperature T_0.

Now taking into account the equation 2.10 and the pressure without the hydrostatic component ($p' = p + \rho_0 g H$). The momentum equations take the following form:

$$\rho \frac{\partial \underline{U}}{\partial t} + \rho \underline{U}(\nabla \underline{U}) = -\nabla p' + \mu \nabla^2 \underline{U} - \underline{g} * [\rho_0(\beta(T - T_0))] \tag{2.11}$$

In all the following section it is implied that the pressure we will use is that of , so we can drop the superscript ' but knowing that pressure we refer comes without the hydrostatic term.

As a concluding remark, it is worth making a brief digression about the validity of such an approximation. As stated by Lappa (2009) [4] and Gray and Giorgini (1976) [12] the Boussinesq approximations applicable when both $\beta \nabla T$ and $\frac{\Delta T}{\overline{T}}$ are smaller than 0.1.This condition is commonly achieved in liquids, as are those treated in this chapter. So, for this reason, most of the simulations in the following have been carried out under such hypothesis.

2.3 Marangoni convection

This kind of convection occurs when two layers of immiscible fluids are in contact through a free surface, which has a temperature gradient different from zero on it. Thus the thermodynamics and the dynamics of the Marangoni convection are closely related to the layer separating the two fluids. In the following the interface is modelled as a rigid geometric boundary, fixed in time, with zero mass and the thermodynamic properties of such layer are also neglected. However, there are conditions in which the interface cannot be treated as just described, and more sophisticated models are needed. This topic has been treated exhaustively by Napolitano (1979) [13], who identified in the degree of interaction among the volume phases and the layer the need for more complex models. Indeed in such cases, the surface can not be treated as a simple boundary any more, but a closed set of equations for the surface must be derived.

In the following, as previously stated, we limit our analysis to the simplest case, according to which the interface is a rigid boundary and the Marangoni effect can be reduced to a boundary condition in the momentum equations on it. According to this framework, the Marangoni condition is a relation which links the stresses $\underline{\underline{\tau}}$ and the temperature gradient on the free surface (now regarded as a boundary). Being this

phenomenon an effect of the interface, the surface tension or more precisely its variation plays a central role in the quantification of the stresses caused by the Marangoni effect. Indeed the phenomenon can be qualitatively understood arguing that the surface tension is higher where the temperature has lower values than the surroundings, and hence the colder regions on the surface tend to attract fluid from the hotter ones. To conserve the mass when the fluid is moved away from the hot spot, it attracts other fluid from the bottom, which if it is hotter (in the Marangoni - Bénard configuration effectively it is), makes all the process to be self-sustaining. So from the short explanation just given the reader could understand that to correctly quantify this phenomenon the distribution of the surface tension σ, which in general could be a complex function of the temperature. As done in the previous section for the Boussinesq approximation, even in this case we can expand σ with the Taylor series and consider it up to the first derivative:

$$\sigma \cong \sigma_0(1 - \sigma_T(T - T_0)) \tag{2.12}$$

With the definitions given above and assuming that the dynamic viscosity of the gas is negligible respect to that of the layer (that is true if a liquid is in contact with a gas), on the free surface the forces due to the temperature differences must be balanced by the stresses, leading to the following condition:

$$\underline{\underline{\tau}}_b \underline{n}^T = -\sigma_T(\underline{\underline{I}} - \underline{n}^T \underline{n})(\nabla T)^T \tag{2.13}$$

In the 2.13 $\underline{\underline{\mathrm{I}}}$ is the identity *matrix*, $\underline{\underline{\tau}}_b$ are the stresses on the boundary and $\underline{n}^T \underline{n}$, following the row by column product is also a matrix:

$$\underline{n}^T \underline{n} = \begin{bmatrix} n_x \\ n_y \\ n_z \end{bmatrix} [n_x \;\; n_y \; n_z] = \begin{bmatrix} n_x n_x & n_x n_y & n_x n_z \\ n_y n_x & n_y n_y & n_y n_z \\ n_z n_x & n_z n_y & n_z n_z \end{bmatrix} \tag{2.14}$$

If the fluid is supposed Newtonian the condition can be written in the following form:

$$\mu \frac{\underline{\underline{U}}_s}{\partial \underline{n}} = -\sigma_T(\nabla T)_s \tag{2.15}$$

$$\underline{\underline{U}}_n = 0 \tag{2.16}$$

Where the s subscript indicates the components tangential to the free surface while n subscript is related to the normal components.

2.4 Non-dimensional numbers and equations

In this section, we will review the relevant non-dimensional numbers which are related to the convective motions and used throughout the text. They have been grouped w.r.t the kind of convection they are related: buoyancy convection and Marangoni convection. The last section deals with the Navier-Stokes equations in the non-dimensional form.

2.4.1 Byuoyancy non-dimensional numbers

The first number which is presented is not related to any convective motion but depends only on the nature of the fluid considered, and it is the **Prandtl number**, defined as:

$$Pr = \frac{\nu}{\alpha} \tag{2.17}$$

Where ν and α are the kinematic viscosity and the thermal diffusivity respectively. Physically it represents the ratio between the dynamic boundary layer and the thermal one. It can span to values much smaller than 1 ($\mathrm{O}(10^{-2})$) in case of liquid metals and semi-conductor melts to values greater than 1000 for viscous oils.
The next non-dimensional is the **Grashof number**:

$$Gr = \frac{g\beta\Delta T L^3}{\nu^2} \tag{2.18}$$

In 2.18 ΔT is the temperature difference, which is imposed on the system and L a reference length. It is proportional to the ratio among the buoyancy-driven forces ($\rho g \beta \Delta T$) and the viscous one ($\frac{\rho\nu^2}{L^2}$). With the numbers just defined, it is possible to introduce another non-dimensional parameter, the **Rayleigh number** defined as:

$$Ra = \frac{g\beta\Delta T L^3}{\nu\alpha} \tag{2.19}$$

$$Ra = Gr * Pr \tag{2.20}$$

This parameter can be understood as the ratio between the buoyancy velocity ($V_g = \frac{g\beta\Delta T L^2}{\nu}$) and the thermal diffusive velocity.

2.4.2 Non-dimensional numbers related to Marangoni flow

The first number presented in this section is the **Reynolds number**, which here has a slight different definition respect to the classical "inertial" one ($\frac{|\underline{U}|L}{\nu}$), indeed it is the ratio between tangential stress $\frac{\sigma_T \Delta T}{L}$ and the viscous one $\frac{\rho\nu^2}{L^2}$:

$$Re = \frac{\sigma_T \Delta T L}{\rho \nu^2} \tag{2.21}$$

Starting from this number it is possible to define the **Marangoni number**

$$Ma = Ra * Pr = \frac{\sigma_T \Delta T L}{\mu \alpha} \tag{2.22}$$

As the Rayleigh number Ma can be interpreted as the ratio between the Marangoni velocities ($V_{Ma} = \frac{\sigma_T \Delta T}{\mu}$) and the diffusive ones.
Now we will introduce the **Biot number** which is related to the conducting boundaries (hence also to the free surface) and it measures the relative importance of the heat exchanged through the border with convection respect to the conductive one:

$$Bi = \frac{hL}{\lambda} \tag{2.23}$$

Where h is the convective coefficient and λ the thermal conductivity.

2.4.3 Non-dimensional set of equations

The equations 2.2(continuity), 2.4 (energy) and 2.11 (Navier-Stokes) can be easily put in their non-dimensional form. Indeed the latter is preferred in most cases because it allows separating the problem from a specific geometry or a specific fluid, making it more general. Scaling the velocities with $\frac{\alpha}{d}$, the distances with L and introducing the non-dimensional temperatures as $T_{ad} = \frac{T - T_{cold}}{\Delta T}$, where $\Delta T = T_{hot} - T_{cold}$, it is possible to derive the following set of non-dimensional equations:

$$\nabla \cdot \underline{U} = 0 \tag{2.24}$$

$$\frac{\partial \underline{U}}{\partial t} + \underline{U}(\nabla \underline{U}) = -\nabla p + Pr \nabla^2 \underline{U} + PrRaT\underline{i}_g \tag{2.25}$$

$$\frac{\partial T}{\partial t} + \underline{U} \cdot \nabla T = \nabla^2 T \tag{2.26}$$

In 2.25 $\underline{i}_g$ is the unit vector pointing in the direction of the gravity and all the quantities in 2.24-2.26 are non-dimensional in this case. Moreover the time has been scaled with $\frac{d^2}{\alpha}$ and the pressure with $\rho\alpha$.

Before concluding this chapter, it is worth to spend some words about the hybrid convection when both surface tension and buoyancy effects are present. This kind of convection is indeed the most common form on the Earth, where the gravity can not be switched off and in many cases, it overshadows the companion Marangoni convection. To quantify the relative strength of the two kinds of convection, it comes useful to define the following parameter:

$$\frac{Ra}{Ma} = \frac{g\rho\beta}{\sigma_T} L^2 \tag{2.27}$$

Keeping this parameter low ensures that the Marangoni effects prevail on the Buoyancy forces. Looking to 2.27 this task can be practically accomplished on the Earth by reducing the characteristic length.

Chapter 3

Non-Newtonian fluids

This chapter aims to describe the main physical models used in the framework of the non-Newtonian fluid mechanics, with special attention to viscoelastic fluids. This chapter is a useful step to understand Chapter 8 in Part II related to thermal convection in viscoelastic fluids. For this family of fluids, the stress tensor transport equation is derived and different viscoelastic models originating from it (Oldroyd-B, FENE-CR...) are discussed.

In Chapter 2 we have derived the equations of motions in the framework of a Newtonian fluid model, according to which the viscosity of the fluid is constant and more precisely independent from the shear rate. Under such hypothesis we found out that the Stokes law ($\tau = \mu(\nabla \underline{U} + (\nabla \underline{U})^T)$) describes the constitutive law of such fluids with good precision. Luckily the most important fluids in industrial applications, namely air and water, behave as Newtonian at least in a wide range of conditions, however for the most of them, such as polymers, colloidal suspensions, and similar complex fluids the Newtonian model becomes inadequate. The Newtonian approximation gives good results when fluids made of small molecules like water or liquid argon are considered (Morozov and Spagnolie (2015) [14]). For such fluids indeed the separation among the characteristic times and lengths of the flow are much larger than the relaxation time of the stresses and molecular dimension.

The first assumption which falls when the Newtonian model is no longer able to describe the dynamics of the flow is the independence of the viscosity from the shear rate, indeed being $\eta(\dot{\gamma})$ the viscosity written as function of the shear rate $\dot{\gamma}$, it can have an increasing or decreasing trend as shear rate is varied. In the first case, we obtain a shear thickening fluid while in the second the so-called shear-thinning fluids are

obtained. Examples of the first are solutions of cornstarch and water, pastes..., while examples of the latter are solutions of polymers. There could be fluids which exhibit a combination of the two behaviours or also fluids which displays other non-Newtonian effects such as Bingham or viscoplastic fluids, which behaves as solids below the yield stress threshold and as fluids above it.

In the reminder of the following chapter, we expressly address our discussion to the description of the main physical models employed in the framework of non-Newtonian fluids, with particular emphasis to the viscoelastic ones. As already stated, the models presented in this chapter will come very useful to have a better understanding of Chapter 8. However, before embarking into the discussion of the physics of viscoelastic fluids, it is worth introducing two non-dimensional parameters: the first is the so-called **Deborah number**, defined as:

$$De = \frac{\lambda}{t_{fl}} \tag{3.1}$$

This number could be regarded as the ratio between the elastic forces and the viscous ones [15] and λ is the characteristic time of the fluid, related to the elastic effects while t_{fl} is the time scale of the flow. Very similar to the Deborah number is the **Weissenberg number**, which is employed when the flow has more the one characteristic time, and it is defined as:

$$We = \lambda \dot{\gamma}_{fl} \tag{3.2}$$

Where $\dot{\gamma}_{fl}$ is the characteristic shear rate of the flow. At this point, it is worth remarking that the Deborah number depends both on the kind of fluid through λ and on the kind of flow and in the limit that $De \to 0$ the Newtonian fluid behaviour is recovered while at the opposite limit ($De \to \infty$) the fluid (or better the material) behaves as a Hookean solid. Usually, it could be identified as a critical Deborah number (in many cases around unity [15]) above which it is no longer possible to neglect the elastic effects. So it is not properly correct to state that fluid is or is not Newtonian, but it can behave or not according to Newton constitutive law depending on its molecular structure (through λ) and the characteristic time of the flow. In other words, the same fluid could be perfectly described with the Newtonian model in some circumstances but not in others.

3.1 Relevant viscoelastic models

This section is limited to the presentation of the viscoelastic models relevant to a good understanding of Chapter 8. The reader is referred to specific textbooks such as [14] and [15] to have a better understanding of the different models employed in the framework of the non-Newtonian fluid mechanics, such as the Generalised Newtonian fluid models and the linear viscoelasticity. Here we limit ourselves to present the main non-linear viscoelastic models, starting with the easiest one, called the Maxwell model.

The Maxwell model If one wishes to take into account the memory effects (the dependence of the stresses from the past deformations). The simplest model is the so-called Maxwell model. Depending on which convective derivative (we will define them shortly) is used (upper or lower) we will obtain the Upper Convected Maxwell (UCM) or the Lower Convected Maxwell (LCM) models:

$$\underline{\underline{\tau}} + \lambda \overset{\triangledown}{\underline{\underline{\tau}}} = \eta_p \dot{\underline{\underline{\gamma}}} \qquad \text{UCM} \tag{3.3}$$

$$\underline{\underline{\tau}} + \lambda \overset{\triangle}{\underline{\underline{\tau}}} = \eta_p \dot{\underline{\underline{\gamma}}} \qquad \text{LCM} \tag{3.4}$$

In the equations 3.3 and 3.4 the $\overset{\triangle}{\underline{\underline{\tau}}}$ and $\overset{\triangledown}{\underline{\underline{\tau}}}$ are the lower and upper-convected derivatives respectively, defined as:

$$\overset{\triangle}{\underline{\underline{\tau}}} = \frac{D\underline{\underline{\tau}}}{Dt} + \nabla \underline{U} \cdot \underline{\underline{\tau}} + \underline{\underline{\tau}} \cdot \nabla \underline{U}^T \tag{3.5}$$

where $\dfrac{D}{Dt} = \frac{\partial}{\partial t} + U \cdot \nabla$ is the material or total derivative.While the **upper-convected derivative** takes the following form:

$$\overset{\triangledown}{\underline{\underline{\tau}}} = \frac{D\underline{\underline{\tau}}}{Dt} - \nabla \underline{U}^T \cdot \underline{\underline{\tau}} - \underline{\underline{\tau}} \cdot \nabla \underline{U} \tag{3.6}$$

The equations 3.5 and 3.6 are objective derivatives and along with other consideration can be used to construct constitutive laws when the deformations in the fluid are supposed to be finite (and hence the linear viscoelasticity theory could not be applied). The term objective in this context means that the equations must conform to the admissibility criteria set by Oldroyd [16].

The Oldroyd model This model is similar to the previous one, but the retardation time is also taken into account. Moreover, in a wide range of problems involving viscoelastic flows, it is useful to take into consideration a dilute solution where polymer molecules are dispersed in a Newtonian fluid matrix. According to this framework, the total stress can be written as a Newtonian contribution along with a viscoelastic one:

$$\underline{\underline{\tau}} = \mu \underline{\underline{\dot{\gamma}}} + \underline{\underline{\tau}}_p \tag{3.7}$$

where μ is the Newtonian viscosity and $\underline{\underline{\tau}}_p$ is the contribution to the stresses given by the polymer. With these considerations, it is possible to derive two different Oldroyd fluids, using the upper or the lower convected derivative: in the first case, we obtain the Oldroyd-A model while in the second the Oldroyd-B:

$$\underline{\underline{\tau}} + \lambda \overset{\triangle}{\underline{\underline{\tau}}} = \eta \left(\underline{\underline{\dot{\gamma}}} + \lambda_2 \overset{\triangle}{\underline{\underline{\gamma}}} \right) \qquad \text{Oldroyd-A} \tag{3.8}$$

$$\underline{\underline{\tau}} + \lambda \overset{\triangledown}{\underline{\underline{\tau}}} = \eta \left(\underline{\underline{\dot{\gamma}}} + \lambda_2 \overset{\triangledown}{\underline{\underline{\gamma}}} \right) \qquad \text{Oldroyd-B} \tag{3.9}$$

In the equations above $\eta = \mu + \eta_p$ is the total viscosity, taken as the sum of the Newtonian and polymer contributions. λ_2 is the retardation time, which is not independent and can be written as a function of λ and the viscosities:

$$\lambda_2 = \lambda \frac{\mu}{\eta} \tag{3.10}$$

Phan-Thien-Tanner (PTT) model Another model which takes into account the non-linearities in the stresses is the *Phan-Thien-Tanner (PTT)* model which is given by:

$$f\left(\underline{\underline{\tau}}_p\right) \underline{\underline{\tau}}_p + \lambda \overset{\triangledown}{\underline{\underline{\tau}}}_p = \eta_p \underline{\underline{\dot{\gamma}}} \tag{3.11}$$

The non-linear function $f\left(\underline{\underline{\tau}}_p\right)$ could be linear or exponential:

$$f\left(\underline{\underline{\tau}}_p\right) = \begin{cases} exp\left(\frac{\lambda \epsilon}{\eta_p} Tr(\underline{\underline{\tau}}_p)\right) \\ 1 + \frac{\lambda \epsilon}{\eta_p} Tr\left(\underline{\underline{\tau}}_p\right) \end{cases} \tag{3.12}$$

In the equations above $\underline{\underline{\tau}}_p$ are the polymer stresses (not the total ones) and the dimensionless parameter ϵ indicates how fast the polymeric viscosity and relaxation time decreases with $\underline{\underline{\tau}}_p$.

FENE models Another non-physical drawback which arises in the Oldroyd models is the unboundedness of the stresses. Indeed being the molecules free to elongate themselves up to infinity the stresses could rise indefinitely. In order to avoid this non-physical behaviour, the so-called Finite Extensibility Non-linear Elastic models (FENE) has been developed. There are two main versions of such models: FENE-CR and FENE-P. Chilcott and Rallison proposed the first (1988) [17] while the second comes from a closure of the kinetic theory model developed by Peterlin (1966) [18]:

$$\underline{\underline{\tau}}_p + \lambda \left(\frac{\overset{\triangledown}{\underline{\underline{\tau}}}_p}{f\left(\underline{\underline{\tau}}_p\right)} \right) = \eta_p \dot{\underline{\underline{\gamma}}} \qquad \text{FENE-CR} \tag{3.13}$$

$$\underline{\underline{\tau}}_p + \lambda \left(\frac{\overset{\triangledown}{\underline{\underline{\tau}}}_p}{f\left(\underline{\underline{\tau}}_p\right)} \right) = \frac{\eta_p}{f\left(\underline{\underline{\tau}}_p\right)} \dot{\underline{\underline{\gamma}}} - \eta_p \frac{D}{Dt} \left(\frac{1}{f\left(\underline{\underline{\tau}}_p\right)} \right) \underline{\underline{I}} \qquad \text{FENE-P} \tag{3.14}$$

The function f is given by:

$$f\left(\underline{\underline{\tau}}_p\right) = 1 + \frac{\lambda}{\eta_p L^2} Tr\left(\underline{\underline{\tau}}_p\right) \tag{3.15}$$

Where L is a dimensionless parameter indicating the maximum elongation of the polymer chains.

Chapter 4

Thermal Convection: A focused review of known instability mechanisms

4.1 Thermo-gravitational convection

As discussed in Chapter 1, the buoyancy convection plays an important role in many natural and industrial processes. The two main configurations that a system immersed in a gravitational field and subjected to a temperature gradient could undergo are the Rayleigh-Bénard convection and the Hadley flow or a combination of both. The first occurs when the temperature gradient and the gravity have the same verse and direction while in the second, the two vectors are orthogonal. Despite the same nature and the similar configuration, except for the angle between gravity and temperature gradient, the two problems present a very different behaviour and this is the reason why they are usually treated separately.

The Rayleigh-Bénard convection takes its name from the two scientists, who first gave a characterisation to the phenomenon. Although this kind of convection is named with both names, it is worth remarking that the phenomenon was tackled theoretically by Lord Rayleigh (1916) and studied experimentally by Henri Bénard (1900,1901). The theoretical analysis of the first supposed that the only driving force was due to the temperature and the lateral walls have been assumed adiabatic. This fact led to considering different problem respect to that seen experimentally by Bénard in which there was the effect of the surface tension as well. These disagreements between theory and

experiments were successfully addressed by Pearson(1958), who first proposed a linear stability analysis taking into account the surface tension effects.

Due to its theoretical and practical importance since the first studies have been carried out, the Rayleigh-Bénard convection assumed the role of the protagonist of many studies during the last century. Probably the fascinating feature of such convection, which attracted many scientists to consider it prevalently under a theoretical point of view was the wide range of bifurcations and route to chaos scenarios (Gollub and Benson,1980 [19]), which occur in a system passing from a steady state to a fully turbulent pattern. Many efforts have been spent to classify and characterise all the possible scenarios occurring after the first steady bifurcation. What emerged from the studies was a very fascinating and complex landscape of different modes, which can be effectively resumed in the so-called Busse Ballon, which has been named in this way thanks to the landmark studies of Busse and co-workers (Busse, 1978 [20], Clever and Busse, 1974 [21])

The companion of the Rayleigh Bénard convection is the Hadley flow, named by the pioneering study of Hadley(1735) [11], who theorised o model of the Earth circulation. So this kind of convection has many important applications in several industrial and technological problems ranging from the materials manufacturing to the cooling of nuclear reactors. As an example of the first class of applications can be mentioned the manufacture of semiconductor crystals from the melt(Carruthers,1977 [22], Thevenard et al. 1991 [23]). Indeed as Hurle (1972) [24] demonstrated the oscillatory motion, triggered in the liquid phase could lead to some defect called striations in the solid phase and hence jeopardise the quality of the final product. Due to its implications both in the natural and industrial environment and its different dynamics respect to the Rayleigh-Bénard convection, e Hadley flow can be regarded as an autonomous field, despite the similarities with the systems heated from below in the form of the equations which rules the phenomenon.

4.1.1 The Rayleigh-Bénard problem

This kind of convection, thanks to its practical relevance and theoretical, complexity, has attracted many scientist and researchers, who have proposed several models to study it. Even if in the real world the geometries could assume complex shapes and the boundary conditions could not be trivial functions of several parameters, a

configuration which received much attention during the past century is the infinite two-dimensional layer. The reasons why such a simple and idealised configuration had a widespread is to understand under a theoretical point of view the complexity and intricate bifurcations hierarchy which the system undergoes. It is worth saying that an infinite layer geometry is impossible to obtain in the real world. However, it is possible to practically achieve such kind of configurations when the depth of the layer is much smaller than the horizontal dimensions. So, for the motivations just outlined, a review of the findings related to the infinite horizontal layer is given in the following sections, the geometry of which is shown in Figure 4.1.

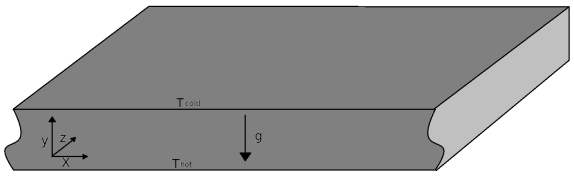

Figure 4.1: Infinite layer in Rayleigh-Bénard configuration

In the following sections to understand the dynamics in such configuration we will briefly review the results appearing in the literature, which rely on the approach of linear stability analysis, the principles of which are outlined in Appendix D. It is known that in such kind of convection at "sufficiently" small Rayleigh numbers the quiescent state is a solution of the equations 2.24 - 2.26. The first goal of the next sections hence is to understand at which Ra such state becomes unstable and the first bifurcation occurs and which are the characteristics of such instability (namely the wavenumber). In the following, the results are reported for a stress-free and no-slip horizontal boundaries.

First steady pitchfork bifurcation

For small Rayleigh numbers, the quiescent state is a solution to the problem. However, if this control parameter has increased, this state is taken over by an instability having the form of convective rolls. In the case of stress-free boundaries a solution has been derived by Rayleigh (1916) [25] who found an analytical solution of the critical Rayleigh

number (Ra_{cr} in terms of the wavenumber (q):

$$Ra_{cr} = \frac{(q^2 + (n\pi)^2)^3}{q^2} \tag{4.1}$$

The solution in the case of no-slip walls is more involved than the previous one, and it will no be presented here. An accurate procedure can be found in Pellew and Southwell (1940) [26], who found that $Ra_{cr} = 1707$. The outcomes discussed above are graphically reported in Figure 4.2.

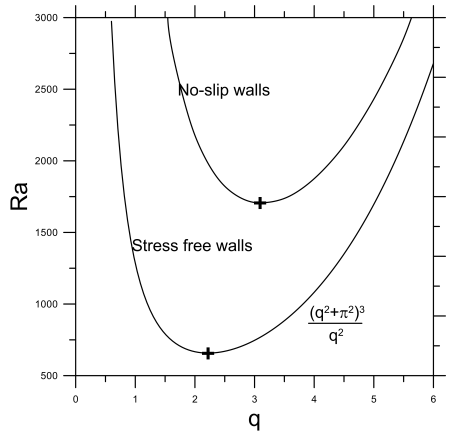

Figure 4.2: Neutral stability curves for the stress free and no-slip walls boundary conditions. The Rayleigh number is defined used the depth of the cavity: $Ra = \frac{g\beta\frac{\partial T}{\partial y}d^4}{\nu\alpha}$, where $\frac{\partial T}{\partial y}$ is the imposed vertical temperature gradient and d is the depth.

Pellew and Southwell [26] showed that for this linearised problem the eigenvalues are real, meaning that this first instability is always stationary.

Secondary instabilities: the Busse balloon

In the previous section, we have assumed a two-dimensional layer, and hence the only disturbances possible have the form of parallel rolls with their axis oriented along the z-direction. However, if the third dimension is considered there are different patterns possible depending on how many pairs of wave number vectors are considered (1 pair: rolls, two pairs: squares, three pairs: hexagons). First Malkus and Veronis (1958) [27] in case of a stress-free BC and than Schüter, Lortz and Busse [27] (also for no-slip walls) showed that only the two-dimensional rolls are stable, while the 3D patterns (squares and hexagons, shown in Figure 4.3) are unstable. However at Rayleigh numbers high enough the other two modes are possible as well (Lappa (2009) [4], Clever and Busse (1996)[28], Busse and Clever (1998) [29]): the hexagons have been proved to be stable

at Pr $>$ 1.2 and Ra $>$ 3000 in some region of (Ra, q) space [28]. On the other hand, if the Rayleigh number exceeds by 3 -4 times the critical value the asymmetric square could become stable [29] with a sinking central core.

After the two-dimensional rolls have occurred, several secondary modes are possible. An extensive characterization and classification is due to Busse and co-workers (see Clever and Busse (1974) [21], Busse (978) [20], Busse and Clever (1979) [30]).They started from the two-dimensional rolls solution (using a Galerkin expansion) and through a technique called Toroidal-Poloidal Decomposition (see Lappa (2009) [4] for an exhaustive review) they solved the system in slightly supercritical conditions. This fact led them to find a multiplicity of secondary modes that the rolls could undergo: the fact that the two-dimensional rolls are stable depend on the wavenumber q, on the Prandtl number (Pr) and the Rayleigh number (Ra). A whole picture of this region of stability can be summarised in the so-called Busse balloon (Busse (1978) [20])), represented in Figure 4.3. Inside the region of the balloon, the 2D-rolls are stable, while outside other patterns occur. As shown in Figure 4.3, there an entire zoo of secondary modes which the system could undergo: the one that the system will choose strongly depends on the Prandtl, wave and Rayleigh numbers. A detailed description of every secondary mode is outside the scope of present review. However, it is worth saying that some of these secondary modes are universal and do not depend on the RB configuration, but the symmetries of the rolls: some examples are the Eckahaus instability (invariance through translation) and zig-zag instability (invariance through rotation) or they could depend on the fact that the convection is weak near the threshold of the marginal stability curve (cross-roll instability). Other mechanisms are specific of the Rayleigh-Bénard convection such as the bimodal instability.

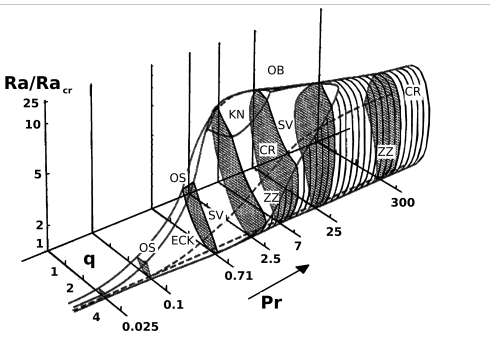

Figure 4.3: Busse balloon, after Busse 1978 [20]. The letters written outside the balloon indicate the secondary instability: ECK $\longrightarrow$ Eckhaus instability, SV$\longrightarrow$ skewed varicose instab.,CR$\longrightarrow$cross roll instab.,OS$\longrightarrow$ oscillatory instability with travelling waves, ZZ$\longrightarrow$ zig-zag instab., KN$\longrightarrow$knot insatb., OB$\longrightarrow$ oscillatory blob instab.

Effects of the lateral walls

The idealised condition of an infinite layer can be achieved with good approximation in the laboratory when the cavity length is much larger than its depth. However, if the enclosure has its length and depth of the same order of magnitude or the first much larger than the latter (tall cavities) the walls are supposed to have a strong effect on the emerging pattern. The first linear stability calculation is due to Davis (1967) [31] who predicted that the axis of the rolls is parallel to the shortest dimension of the box. Cross et al. (1980) [32] found that the presence lateral walls severely restricts the number of wave vectors allowed in the domain even if the aspect ratio is large and the wavelength becomes larger as the Rayleigh number is increased. According to them, the wavenumber restriction depends on the Prandtl number and the thermal properties of the side walls.

4.1.2 Hadley flow

As proceeded for the RB problem also here, we will consider the infinite layer due to its simplicity and the existence of exact solutions. In this case, however, the quiescent state is no longer a solution of the equations 2.24-2.26 so which kind of solution shall we use as a basic state to apply the linear stability principles? Luckily analytical solutions exist in case of buoyancy and thermo-capillary convection when the system is considered with an infinite extension along the direction of the imposed temperature gradient(see Lappa (2009) [4] for more details). The system, moreover, has the configuration displayed by Figure 4.4. The disturbances which affect the basic state of the Hadley flow

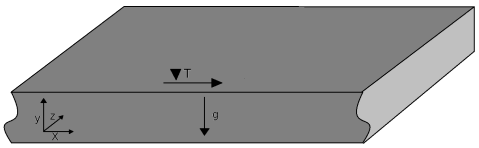

Figure 4.4: Hadley flow configuration

strongly depend on the Prandtl number: at low Pr (< 1) the possible instabilities are the 2D hydrodynamic modes, the oscillatory longitudinal rolls (OLR) and the steady longitudinal rolls (SLR). At large values of the Prandtl number ($Pr > 1$), the so-called Rayleigh modes replace the disturbances described above. Due to this dichotomy of the emerging pattern, the cases of low and high Prandtl numbers will be treated in separate sections in the following.

Low Prandtl (< 1) modes

The first instability we are going to discuss is the 2D hydrodynamic or transverse mode. As shown in Figure 4.6, it is clear that this disturbance has a two-dimensional nature, having the roll axis perpendicular to the direction of the imposed temperature gradient. It is the most sensitive (in sense that it has the lowest threshold) at low Prandtl numbers (until O(-2)), being replaced by three-dimensional modes (OLR, SLR) at higher values of Pr. Hart (1972, 1983) [33] [34] characterised both the transverse (Figure 4.8 a) and longitudinal (Figure 4.6 b) disturbance, while Gill (1974) [35] focused prevalently on the latter. Both the authors explained that the nature of the first 2D family of disturbances is hydrodynamic in nature: the instability is driven by mean shear stress (close to the inflexion point of the velocity profile). Differently from their two-dimensional companion, the longitudinal rolls arise due to the dynamic coupling among the mean shear stress and buoyancy forces. This pattern, as depicted in Figure 4.6 b, has the axis of the rolls aligned with a temperature gradient. Moreover, this disturbance could combine with the basic flow producing helical trajectories and depending on the Prandtl number it can assume an oscillatory (OLR, Oscillatory Longitudinal Rolls) or steady (SLR, Steady Longitudinal Rolls) behaviour.

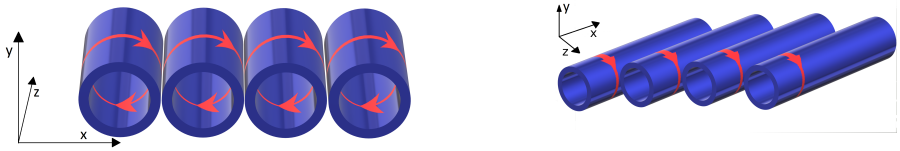

(a) 2D hydrodynamic (or transverse) mode

(b) Longitudinal rolls

Figure 4.5: Basic state for the Hadley flow

As outlined before the 2D modes are the primary mechanism of instability at the lowest values of Pr, being substituted at lager values of such parameter by the OLR. Increasing the Pr further the OLR become steady SLR. According to Kuo and Korpela (1988) [36] the hydrodynamic modes are dominant at $Pr \leq 0.033$, the OLR are the primary mechanism at $0.033 < Pr < 0.2$ while the SLR become the most sensitive one at $Pr \geq 0.2$. This threshold is plotted in Figures 4.7a and b, where the critical Grashof number and the wave number at the onset are reported.

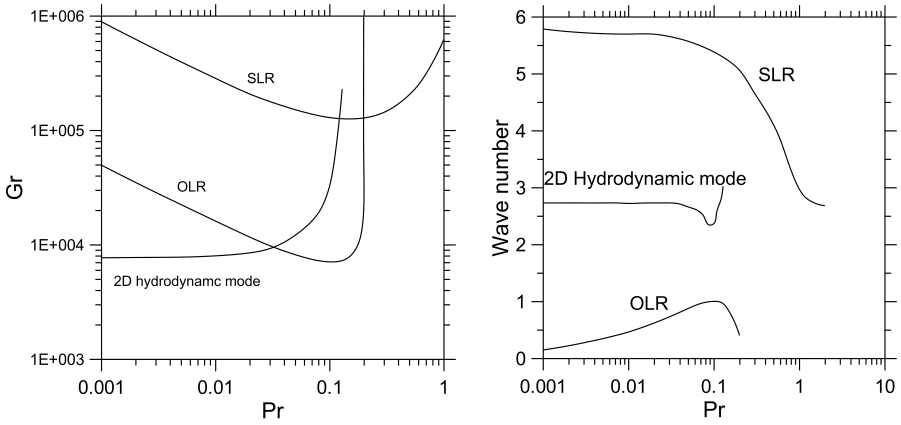

(a) Critical Grashof number as function of Prandtl

(b) Critical wave number as function of Prandtl.

Figure 4.6: Critical Grashof and wave number after Kuo and Korpela [23]. rashof number defined as:$Gr = \frac{g\beta\frac{\partial T}{\partial x}d^4}{\nu^2}$, where $\frac{\partial T}{\partial x}$ is the imposed horizontal temperature gradient and d is the depth.

Figure 4.7a shows an interesting aspect regarding the OLR, which shows an upward trend very close to Pr=0.2. Above this value, indeed, the most sensitive disturbance is the steady rolls (SLR). The analysis of Kuo and Korpela [36] was limited to adiabatic solid walls while the effect of the different boundary conditions was studied by Laure and Roux (1989) [37], who considered two configurations: the layer with two rigid boundaries (R-R) and one with an upper free surface (R-F). Moreover, for each of the two cases, the perfectly adiabatic and the conductive boundaries have been taken into

consideration. They found that the different boundary conditions strongly affect the thresholds of the 2D hydrodynamic and OLR mode: in the R-R case with adiabatic walls indeed they found the intersection among 2D and OLR modes at Pr=0.034, which is in good agreement with Kuo and Korpela [36]. This intersection generally shifts to higher values of the Prandtl number for both R-R and R-F cases when the conducting walls are considered. In the first case, according to [37], the intersection moves from Pr=0.034, when the walls are supposed adiabatic, to Pr=0.114 in the layer with conducting walls. In the latter configuration (R-F) the trend is qualitatively the same: the intersection travels from Pr=0.0045 (adiabatic) to Pr=0.077 (conductive). Moreover, when the R-F layout with adiabatic walls is considered, two spatiotemporal behaviours of the OLR modes are allowed depending on the Prandtl number: travelling wave($0.0045 \leq Pr \leq 0.38$) and standing wave ($0.38 \leq Pr \leq 0.41$).

Before concluding this review about the main instabilities at low Prandtl numbers, it is worth remarking a fact which appears in both [36] and [37]. Looking at Figure 4.7a, the reader may notice that the branch of the 2D hydrodynamic mode is almost horizontal at the lowest values of Pr, assuming a value which is not dependent by Pr. This behaviour at the lowest Prandtl number does not change if other boundary conditions are considered (those taken in consideration by [37]). Indeed, this fact is a further confirmation of the hydrodynamic nature of the 2D modes: they are triggered regardless to the thermal coupling, and they are still possible even when the energy and momentum are completely decoupled (Pr=0).

High Prandtl (> 1) modes

In the previous subsection, the situation at $Pr < O(1)$ has been discussed, and two main mechanisms have been found: the 2D transverse modes and 3D longitudinal rolls (steady or oscillating). All these disturbances, however, are no longer possible at the higher values of Prandtl and a different kind of instabilities become the most sensitive mechanism when the Pr is increased: the so-called Rayleigh modes (see Gershuni et al. (1992) [38]). These disturbances derive their name due to the presence of an unstable stratification near the upper and lower walls. This stratification could eventually lead to instabilities of the Rayleigh-Bénard type, which could take the form of steady longitudinal rolls (axis along the temperature gradient direction, 3D Rayleigh modes) or, when the Rayleigh number is slightly larger, oscillatory transverse rolls (axis perpen-

dicular to temperature gradient, 2D Rayleigh modes). This second mode has a pattern consisting of travelling rolls localised near the upper and lower walls. These moving cells originate two waves: one located in the upper part moving towards the colder side (to left referring to Figure 4.4) and the other constituted by the lower rolls drifting to the right. A picture is shown in figure 4.7, where the various instabilities are plotted as a function of the Prandtl number.

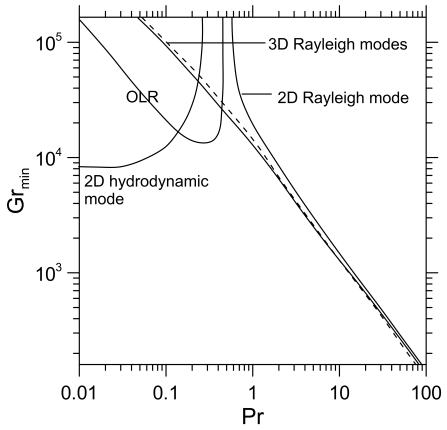

Figure 4.7: Critical Grashof number as function of Pr, after Gershuni et al. [38].The solid curve related to 3D Rayleigh modes represents the even ones, while the dashed line indicates the odd modes. Grashof number defined as:$Gr = \frac{g\beta\frac{\partial T}{\partial x}d^4}{\nu^2}$, where $\frac{\partial T}{\partial x}$ is the imposed horizontal temperature gradient and d is the depth.

As discussed above at values of Pr $> O(1)$ only the Rayleigh modes remain as possible instability mechanism. Moreover, the 3D Rayleigh modes, which are steady, can assume an odd or even pattern, which is shown in Figure 4.8.

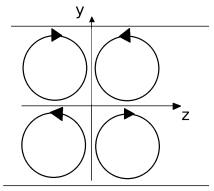

(a) Even 3D Rayleigh mode

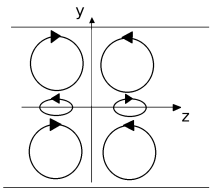

(b) 3D Rayleigh mode

Figure 4.8

As a concluding remark of this section, it should be pointed out that, being the neutral curves of the various modes very close to each other at some Pr, a competition among 2D and OLR modes should be expected, when the Rayleigh number (or equivalently Grashof number) is further increased.

4.2 Convection driven by thermo-capillary effects

The previous section aims to describe the convection arising when the fluid is subjected to a gravitational field, and no other forces have been taken into account. However, there are other effects, which in principle could trigger the convection: one of them is the variation of the surface tension due to an imposed temperature gradient. Indeed it is a known fact that the surface tension is a decreasing function of the temperature. Hence the colder regions of the free surface tend to attract fluid from the hotter ones, eventually triggering the convection. Similarly to the thermo-gravitational case, there are two different main configurations: the temperature gradient perpendicular to the free surface or parallel to it. The first case is regarded as the Marangoni-Bénard convection, while the second refers to the so-called thermo-capillary convection. Although driving mechanism is the same in the two configurations, the resulting dynamics comes to be very different, making necessary a separate treatment of the two cases.

The Marangoni-Bénard convection brings the name of two scientists: Carlo Giuseppe Matteo Marangoni and Henry-Bénard. The reason why the last names both this kind of convection and its thermo-gravitational counterpart has been briefly outlined in the previous section: indeed it is due to him the seminal experiments (1900,1901) which led to the observation of the characteristic honeycomb (hexagonal) pattern. At first Rayleigh (1916) [25] gave a theoretical explanation in terms of a pure buoyancy flow (see the previous section for the linear stability analysis outcomes) without taking into consideration the thermo-capillary effects. It was only during the '50s that the responsibility of the thermo-capillary effects came out. In 1956 Block [39] demonstrated the role of surface tension in the formation of the hexagonal structures experimentally, by observing such structures at $Ra < Ra_{cr}$. However, it was only in 1958 that Pearson [40] gave a mathematical explanation with a linear stability analysis, which takes into account the surface tension.

The configuration with the temperature gradient parallel to the free-surface, like the Hadley flow, has important technological implications in the field of crystal growth from the melt. Indeed a very undesired feature in such industry is the so-called striations, which are a regular banded concentration of the dopant and they are believed to be caused by the oscillatory motion of the fluid (Lappa [4]). This fact is the reason why this configuration has been studied in strong relation with the most used techniques in the field of crystal growth from melt: mainly the Czochralsky (see, e.g. Nakamura

et al. (1999)[41]), the floating-zone and the open-boat (e.g. Schwabe and Scharmann (1979) [42]).

4.2.1 Marangoni-Bénard convection

As proceeded in case of thermo-gravitational flows, also in the following the case of an infinite layer is reviewed. The reasons behind this choice are the same as those highlighted in the previous section: the simplification of the problem, allowing a mathematical treatment but being still able to capture the main features of the physics behind the convection. The basic mechanism, which triggers the instability, can be described using the idea of the hot spots on the free surface. Indeed, being the temperature on the free surface free to vary, according to the heat transfer through it, the presence of a hot spot triggers the fluid motion from it to colder regions (where the surface tension is higher). In doing so the departing fluid, due to continuity, recalls hotter fluid from below, making the hot spot even hotter. This mechanism is self-sustaining and could eventually lead to global convection.

The first landmark study, which dealt with such a configuration, as already mentioned earlier, was the linear stability analysis of Pearson (1958) [40].The procedure he followed was similar to that employed in the studies of the Rayleigh-Bénard convection, recalling the fact that, similarly to it, the rest state is a solution of the MB convection as well. However, Pearson considered a pure MB convection, neglecting gravity and imposing the Marangoni boundary condition, as described in Chapter 2, on the free surface. Moreover, he considered different Biot numbers, with Bi=0 being the case of an adiabatic free surface. In Figure 4.9 the results obtained by Pearson are plotted parametrised at different Biot numbers: the critical Marangoni number is $Ma_{cr} = 79.607$ with a wave number k=1.99.

With the linear stability analysis, it is possible to asses the critical Marangoni and wavenumbers of the disturbances, but it fails to provide the shape of the convective cells, which is it determined by the non-linear effects. Hence other techniques, such as weakly non-linear analysis are needed for this purpose. In the following subsections, the various possible shapes of the convective cells are briefly discussed.

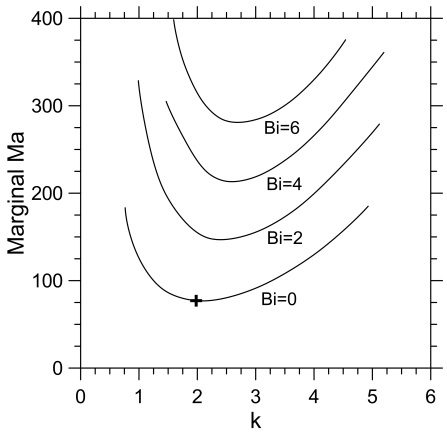

Figure 4.9: Marginal stability curves at different Biot numbers. k is the wave number.After Pearson [40]. Marangoni number defined as: $Ma = \frac{\sigma_T \frac{\partial T}{\partial y} d^2}{\mu\alpha}$, where $\frac{\partial T}{\partial y}$ is the imposed vertical temperature gradient and d is the depth.

High Prandtl number (≥ 1)

For this kind of fluids, the hexagons are the preferred shape at Marangoni number close to the critical one. Increasing the control parameter further leads to a change in the topology of the cells, which becomes square-shaped (Bestehorn(1996) [43]). In particular, Eckert et al. (1998) [44] demonstrated that the Nusselt number increases when the system undergoes to a hexagon- square transition, making the latter configuration more efficient to transport heat. Moreover, they found that the threshold of such transition increases with the Prandtl number, raising from $\frac{Ma-Ma_{cr}}{Ma_{cr}} \approx 3$ at Pr between 30 and 40 to values higher than 5 at $Pr \approx 100$.

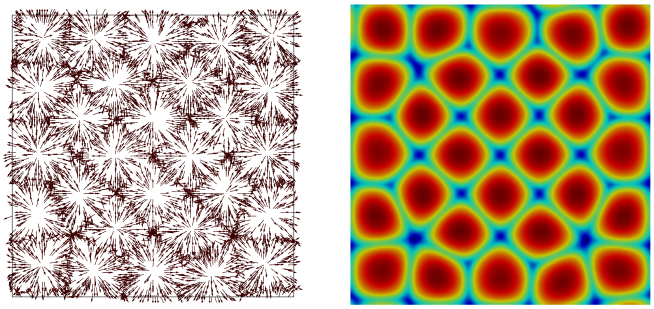

(a) Vector plot (b) Temperature contour

Figure 4.10: Free surface for a layer: Ma=300, Pr=10

The square pattern is retained when the Pr is decreased to Pr=O(1) (instead of hexagons). Near the threshold, at these values of Pr, coexistence with the roll patterns could occur, however, if the Marangoni number is increased those patterns are replaced

by the oscillating triangular cells, shown in Figure 4.11.

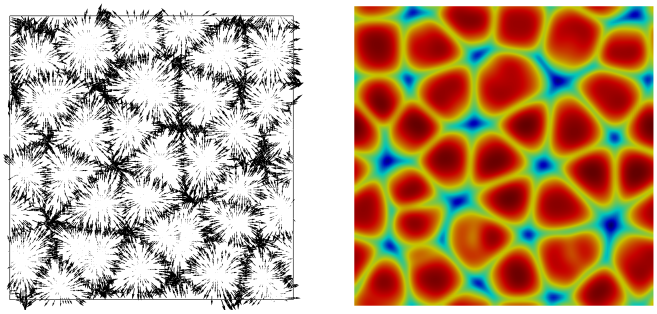

(a) Vector plot (b) Temperature contour

Figure 4.11: Free surface for a layer: Ma=300, Pr=1

Low Prandtl (< 1)

In case of liquid metals and semi-conductor melts (the two families of fluids have the $Pr \ll 1$) probably the most remarkable difference with their "transparent companions" is the appearance of inverted hexagons as the first instability mechanism, which is characterised by the fluid descending in the centre of the cell. Due to the lack of experiments involving liquid metals, most of the studies have been carried out in the framework of direct numerical simulations. The first who predicted the onset of the inverted hexagons were Thess and Bestehorn (1995) [45], assessing a critical Prandtl number (Pr_c) under which the hexagon are inverted. They found that Pr_c lies between 0.22 and 0.3, increasing slightly with Biot number. After the Marangoni number increases twice its critical value, the convective cells undergo a time dependence, which quickly leads to spatio-temporal chaos. However between $Ma_{cr} < Ma < 2Ma_{cr}$ several patterns are possible, giving rise to a very complex and fascinating bifurcation hierarchy, which is shown in Figure 4.12, where the various emerging patterns are reported as function of the Marangoni number at Bi=0 (it is worth recalling that at Bi=0 the first bifurcation occurs at Ma=79.607).

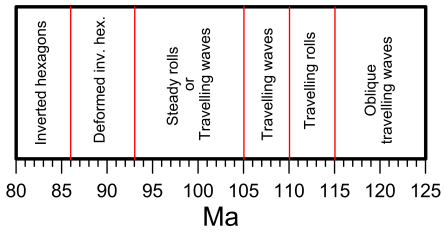

Figure 4.12: Various pattern as function of the Marangoni number at $Pr \approx 0$ Bi=0. After Lappa (2009) [4].

4.2.2 Thermo-capillary convection

Differently from Marangoni-Bénard configuration, this kind of convection has the imposed temperature gradient parallel to the free surface. As occurred in case of pure thermo-gravitational among RB and Hadley flows, even in this case the rest state is no longer a solution of thermo-capillary flows, making the emerging patterns very different from the MB convection. As proceeded in the previous sections, a more detailed description is given to the case of the infinite layer.

Linear stability analysis

The first linear stability analysis for the thermo-capillary flows is due to Smith and Davis (1983) [46], who in their landmark study considered an infinite layer, subjected to the Marangoni stresses on its rigid free surface and with the adiabatic boundaries. They found two families of instabilities: the *stationary multicellular rolls* (SMC) and the *oblique hydrothermal waves* (HTW). The emerging instability strongly depends on the Prandtl number and the different kind of the basic flow considered: the return flow or the linear profile, shown in Figure 4.13. While the latter, as the name suggests, has a linear trend, the first is a parabolic function of the cavity height.

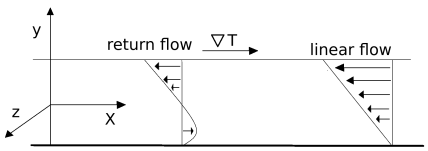

Figure 4.13: Return flow and linear velocity profile

Before going further, it is worth emphasising an aspect which occurs at $Pr \to 0$ and differentiates this kind of flows with their thermo-gravitational counterpart (Hadley flow): both the velocity profiles considered by Smith and Davis lack of inflexions points($\frac{\partial^2 u}{\partial y^2} = 0$). According to Squire theorem [1] this flows at sufficiently low Pr do not admit two-dimensional disturbances, which could propagate along x-direction in this case.

The following results are grouped according to the two velocity profiles considered by Smith and Davis: the linear and return one.

[1] In a shear flow a necessary condition for instability to be triggered in the presence of an inflexion point in the velocity profile

Linear velocity profile

The overall picture of the various instabilities is shown in Figure 4.14, where the critical Marangoni number is plotted as a function of Prandtl. At $Pr < 0.6$ the preferred pattern are the hydrothermal waves (HTW), which could come purely longitudinal or oblique, forming an angle with the base flow direction $\Phi \neq 0$, being $\Phi = tan^{-1}\left(\frac{q_z}{q_x}\right)$(with q_z and q_x being the wavenumbers in z and x-direction respectively). At Pr values close to one ($0.6 < Pr < 1.6$) the most sensitive mechanism becomes the two-dimensional HTW, while at larger Pr the primary instability mechanism is the stationary longitudinal rolls ($\Phi = 90°$).

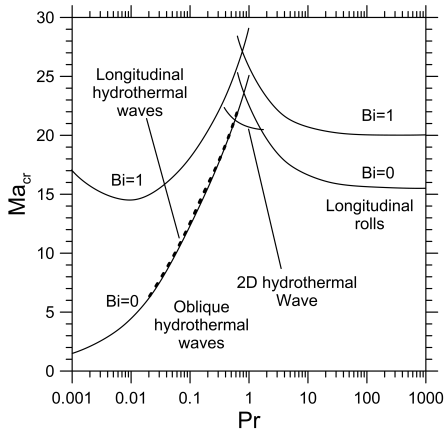

Figure 4.14: Critical Marangoni number as a function of Prandtl number for the hydrothermal wave. Base state with linear velocity profile. After Smith and Davis [46].The Marangoni number has been defined as: $Ma = \frac{\sigma_T \frac{\partial T}{\partial x} d^2}{\mu\alpha}$, where $\frac{\partial T}{\partial x}$ is the horizontal imposed temperature gradient while d is the depth.

Before going further to the discussion of the return flow case, it is worth spending some words about the raising mechanism of the longitudinal rolls. The explanation is similar to that pursued in case of MB convection, in this case. However, the initial disturbance is a hot line parallel to the temperature gradient. Similarly to the hot spot, the line, being hotter attracts warmer fluid from below, which on the other hand has a horizontal velocity smaller respect to the upper fluid particles, leading in this manner to a reduction of the convective heating, produced by the base state velocity. If the imposed temperature gradient is large enough, this mechanism will overcome the heat loss through the free surface triggering the convection.

Return flow

As done in the previous case, the main mechanisms of instability are plotted in Figure 4.15a at two different Biot numbers (namely 0 and 1). The main difference with the previous section is the absence of the stationary longitudinal rolls, leaving as the only primary instability the HTWs. Indeed, according to the explanation given above, the stationary roll tend to be suppressed by the colder fluid coming from below With this base flow Smith and Davis [46] found that the HTW comes to be always oblique and the angle Φ formed with the base state velocity is a decreasing function of the Prandtl number: going from values close to 90°(orthogonal to base flow) at Pr=O(0.001) to few degrees (almost 2D) at $Pr > 100$. It is worth noticing that Φ is always smaller the 90°, allowing the HTWs to have a component which points in the upstream direction (opposite to the base velocity). Such behaviour of the propagation angle as a function of the Prandtl number is plotted in Figure 4.15b.

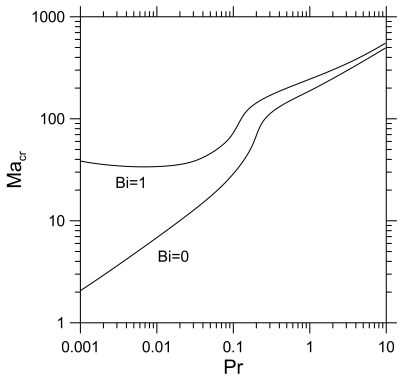

(a) Critical Marangoni number as function of Prandtl number. Base state with return flow.After Smith and Davis [46].

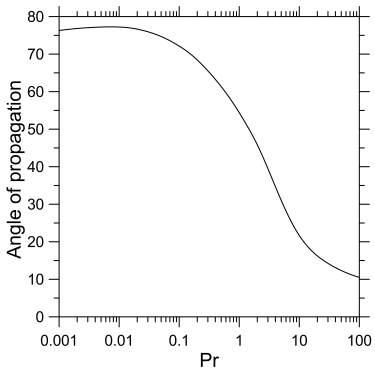

(b) Angle of propagation of the HTWs as function of the Prandtl number. Base state with return flow.After Smith and Davis [46].

Figure 4.15: The Marangoni number has been defined as: $Ma = \frac{\sigma_T \frac{\partial T}{\partial x} d^2}{\mu \alpha}$, where $\frac{\partial T}{\partial x}$ is the horizontal imposed temperature gradient while d is the depth.

Figure 4.15b remarks the great difference among the $Pr \to 0$, in which case the HTWs travels almost orthogonally to the base flow and $Pr \to \infty$, where the HTWs are nearly two-dimensional. Smith (1986) [47] gave a detailed explanation about the driving instability mechanisms in case of low and high Prandtl numbers. In case of $Pr \to 0$, a good understanding can be obtained considering a hot spot in the form of a line which extends along the x-direction. This hot spot tends to attract the fluid beneath it, being such a fluid (coming from the lower regions) slower it produces a

net upstream inertial force. Thanks to such force and related flow, which brings the downstream colder fluid, a cooling effect is triggered on the hot spot. While the spot is cooled down the upflow intensity is reduced, on the other hand until when there is a presence of an upflow there is also an upstream inertial force and hence an increase of the upstream velocity perturbation which cools down the hot spot. At a certain point, this cooling effect produces on overshoot in the spot temperature, transforming it in a cold spot. Such a transformation has, as a result, the inversion of the vertical flow, which now points downwards. With this change also the inertial force is reversed, pointing now in the downstream direction with the consequent reduction of the upstream flow intensity and the cooling effect. When the heating from the surrounding areas takes over the cooling mechanism, just explained, the temperature of the spot starts to raise and at the same time, when the temperature reaches its minimum, a reversal in the upstream flow occurs. This downstream flow now has the opposite effect of heating the spot, and when the temperature difference among the spot and the surroundings becomes zero the down-flow reaches its minimum while the downstream flow is maximum, causing an overshoot in the spot's temperature (now hotter than the adjacent areas again) and the process is repeated. If the imposed temperature gradient is large enough it could make the entire process self-sustaining, eventually triggering time-dependent convection.

The mechanism reported above completely changes when fluids with high Pr are considered. In such a case, indeed the flow is dominated by the viscous effects and a hot line on the free surface is still able to trigger an up-flow. However, the stream-wise velocity is no longer present, due to the inertial effects are now negligible. Now the only effect is the cooling one, due to the vertical flow, which tends to eliminate the initial disturbance. On the other hand, when the Pr is large, the temperature advection due to the sinking fluid originated by continuity in upstream and downstream positions brings the warmer fluid to the colder layer located underneath. This effect has, as a result, the birth of the internal hot spots which, due to the reversed base flow in the lower part of the layer, are created only upstream respect to the original disturbance. This internal spot heats the interface, producing another one on the interface, which is shifted upstream respect to the original disturbance. This process could become recursive, giving rise to a pattern which travels in the upstream direction.

The main macroscopic difference between the two mechanisms described above is that

in the first case, the disturbances travel in an almost span-wise direction while in the second case, the HTWs are nearly two-dimensional. The other consideration about the nature of the instability has to be pointed out: differently from the Hadley flow, which presents an inflexion point in the base state velocity profile, here the velocity lacks it. The presence of such inflexion indeed allows the pure two dimensional disturbances of hydrodynamic nature, which are not triggered by the dynamic coupling among the velocity and temperature. On the other hand, a mandatory requirement of the HTWs is the coupling of the velocity and temperature, which means they are a completely different mechanism to those considered in section 4.1.2 (Hadley flow).
The last point it is worth remarking is the fact that, similarly to the MB convection, the linear stability is not able to predict if the span-wise component (along the z-direction, referring to 4.13), which is chosen according to non-linear interactions.

2D enclosures with finite extent

Before concluding this chapter, the two-dimensional cavities are briefly discussed in this section. The flow which develops at very low Marangoni numbers is a steady unicellular flow with a large central roll with axis perpendicular to the temperature gradient. However for the closed cavities, if the Marangoni is increased, the central rolls shift towards the cold side if the Pr is low or towards the hotter side if the Pr is large (see Mercier and Normand (2002)[48]). This phenomenon is graphically shown in Figure 4.16.

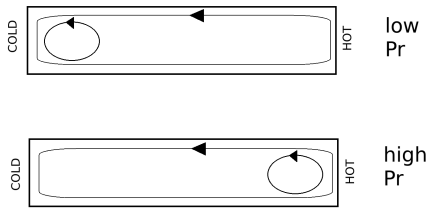

Figure 4.16: Roll shifting in two-dimensional enclosures.

In case of two-dimensional cavities (or short length in the z-direction, $A_z = \frac{L_z}{d} \to 0$ the spanwise travelling waves are no longer allowed, more precisely all the wavelengths greater than the L_z are not admitted as a solution. So in case of $Pr \to 0$, being the angle of propagation close to 90 °, for Marangoni number sufficiently large the oscillatory solutions (HTWs) are ruled out, and only stationary rolls are possible. On the other hand, at large Pr, the HTWs, according to Smith and Davis [46], have a strong

upstream component, which allows them to be a reliable solution in two-dimensional simulations as well.

4.3 Overstability in viscoelastic fluids

Concerning the systems heated from below, we found that for fluids with a Newtonian behaviour the first instability, breaking the quiescent state, is always stationary. However, this fact is not always true when complex fluids, especially those showing viscoelastic behaviour, are considered. For this category of fluids, indeed, the first bifurcation could lead to a time-dependent pattern (Hopf bifurcation). This behaviour seems to be linked to the elastic properties not only in thermal convection problems but also in other flows such as the Taylor-Couette one, as pointed out by Khayat [49]. This change of the bifurcation nature, from stationary to a time-dependent occurs above a critical threshold of the Deborah number, which depends on the specific flow and on Prandtl number. Specifically, to the Rayleigh-Bénard problem this phenomenon has been treated by Khayat (see [50],[51]), who considered a layer filled with an Oldroyd-B fluid, finding that together with the overstability phenomenon in viscoelastic fluids a drop in the critical value of the control parameter (namely the Rayleigh number) also occurs. In particular, the threshold at which the fluid becomes overstable is triggered only at values of Deborah number such that $De > De_c$, where De_c is a critical value. The onset of overstability moreover depends also on the retardation time and Prandtl number: the first being responsible to a rise of the threshold when is increased, while the latter produces the overstability at lower values of the critical parameters when it becomes bigger.

Very similar behaviour occurs in the companion problem, the Marangoni-Bénard flow, as well. This configuration indeed has been studied by Parmentier et al. [52], who conducted a linear and weakly non-linear stability analysis on a layer, modelled according to different viscoelastic models, namely the upper convected, the lower convected and co-rotational Jeffreys models. Moreover, they took into account hybrid convection, comprising both the buoyancy and the Marangoni effects. The relative strength of these two effects is taken into account by two parameters: the critical rate of heating $\lambda = \frac{Ra}{Ra_0} + \frac{Ma}{Ma_0}$ and the gravity parameter $\alpha = \frac{\frac{Ra}{Ra_0}}{\lambda}$(being $0 \leq \alpha \leq 1$), where Ra_0 and Ma_0 are the critical values of such parameters for the Newtonian case. Similarly to [50] and [51], they found that the threshold at which the bifurcation changes nature:

from stationary to oscillatory is sensitive not only to the Deborah number but also to the retardation time. More specifically this threshold tends to raise when the retardation time grows, and this happens in the entire range of α (from 0 in case of pure Marangoni-Bénard convection to 1 in case of gravitational flows).

In this brief overview of overstability, we have identified some features that seem to be related to the viscoelasticity more than the specific flow configuration. The same behaviour has been reported not only in a different kind of convection but in the Taylor-Couette flow.

Chapter 5

Methods for the solution of the governing partial differential equations

In Chapter 2 we have presented the equations, which govern the fluid flows (and the thermal convection), namely the continuity, the energy and the Navier-Stokes equations (the equations 2.2, 2.4 and 2.9 respectively). Moreover, in the same chapter, we have further enriched that set of equations with the Boussinesq approximation (2.11) and Marangoni boundary condition, taking into account the buoyancy and surface-tension effects, respectively. In Chapter 3, we have further enriched the model of the Newtonian fluid presented in Chapter 2, discussing several constitutive laws, which lead us to introduce different non-Newtonian fluids: in particular the viscoelastic models. With the models presented in chapter 3, it is possible to describe physical phenomena such as the shear-thinning or (thickening) and the so-called memory effect.

The equations cited above constitute the physical background of the entire Part II of the present work, in the most of cases however it is impossible to find an exact analytical solution of the equations presented in the previous chapters, due to their non-linear nature. On the other hand, it is still possible to gain some knowledge through approximated solutions. There are several methods, which allow assessing an approximate solution: the Finite Difference Method (FDM), Finite Element Method (FEM), spectral methods, Finite Volume Methods (FVM)..., to cite some of them. All these methods are a part of the so-called Computational Fluid Dynamics (CFD) which is a branch of fluid mechanics. CFD is a relatively new subject (it grew around the '60

of the previous century), and it uses the numerical analysis, implemented through the computers to perform the calculations of the fluid flows. So CFD is strongly relying on computers, and for this reason, its popularity grew in parallel with computers and supercomputers power. Nowadays it is a widely used approach in fluid mechanics and thermal convection as well.

Along the lines outlined above for the most of the analyses of Part II we rely on the CFD and in particular we make use of the open-source software OpenFoam, which is based on the Finite Volume Method. An accurate description indeed would need an entire dedicated volume, which falls out of the scope of this thesis. Here we only would like to outline the basic principles behind the solutions of the incompressible fluid flow problems and give the reader the basic knowledge and the terminology used throughout Part II. For more detailed information about the FVM and CFD, we address the reader to more specific literature such as Moukalled et al. [53], Ciofalo et al. [54] and references therein.

5.1 Solution of incompressible fluid flow problems

The problems we deal with in Part II involve the solution of a system of transport equations, which in principle are coupled. So, for this reason, we shall discuss the issues which may arise when solving a system of equations such that introduced in Chapter 2.

The first aspect, which it is worth highlighting here is that there are two strategies of solving the system of equations ruling the thermal convection: the first is to solve them separately, according to a **segregated approach**. This method implies that every equation composing the system is solved using the latest values of the variables available. Another strategy employed to solve the system such that presented in Chapter 2, is to rely on a **coupled approach**, in which the variables belonging on a given sub-domain are assessed iteratively (i.e. solving a system). The simulations performed in Part II are carried out through a segregated approach, due to its cheaper computational effort and memory usage. The latter approach indeed could be preferred in problems where the coupling between the variables is robust, and the convergence may not be attained using a segregated approach.

Another argument which deserves some attention is the position of the variables on the grid. The variables are defined in the centres of the cells for a generic transport equa-

tion. However, it is worth noting a particular aspect of the system formed by equations 2.2 (continuity) and 2.9 (momentum) (for thermal convection there is also the energy equation 2.4, coupled with momentum through Boussinesq approximation expressed by 2.11): in the momentum equations only the gradient of the pressure appears, and in the continuity, it is not present at all. If both the pressure and the velocity were defined at the same point (in this case on the centre of the cell)s, it would lead to decoupling problems between the pressure and velocity fields, as only the pressure gradient is present in the momentum equations. This fact happens because in the discretisation of the pressure gradient it turns out that the value of such variable on a point P depends only on that assumed on the neighbouring cells and not directly on P. This fact leads to having a mesh two time coarser than that effectively used for the pressure. This fact does not allow to capture rapid variations of this quantity (e.g. checkerboard fields). In order to overcome this problem, it is possible to define the pressure on the cell centres while the velocity on the cell faces. This process of staggering these two variables is equivalent to using different grids for the pressure and velocity. Unfortunately, this approach is difficult to handle on unstructured meshes so in many cases it is preferable a **collocated approach**, in which the pressure - velocity coupling is handled through special interpolation techniques, e.g. Rhie and Chow [55]. In OpenFoam indeed the latter class of techniques is used.

A further point which should be addressed about the resolution of the system introduced in Chapter 2 (in case of incompressible flows) is the pressure calculation. Indeed it is not possible to derive the pressure directly from the incompressible version of continuity, as it does not appear there. For this reason, different strategies have been followed in the past years to overcome this issue. E.g. when the flow is supposed to be two-dimensional, it is possible to readdress the problem in terms of stream-function and vorticity. In OpenFoam, however, this approach is not employed as it is based on another category of algorithms: the so-called **projection methods**. Several algorithms are belonging to this family, and they have in common the fact that a Poisson equation for the pressure is derived in two steps: the first, the so-called **predictor step** in which the momentum equations are solved using an old value of the pressure (of the previous time step or iteration). As a result, we obtain a velocity field which does not satisfy the continuity (i.e. it is not divergence-free). So at this point, the **corrector step** needs to be applied: imposing the continuity a Poisson equation for the pressure

(or equivalently for the pressure correction) is derived. Once the pressure is correctly assessed the velocity is corrected in such a way that its divergence is zero.

To dig deeper into the theoretical framework of such methods, we should remark the fact that they are based on the fundamental property of viscous fluids of possessing some vorticity when they are subjected to a driving force. This is mathematically achieved by setting $\nabla \times \underline{U} \neq 0$, being $\nabla \times \underline{U}$ the curl of the velocity field. Moreover, this quantity does not depend directly on pressure gradient [1]. So these algorithms consist of three stages: in the first one, a velocity field $\underline{U}^*$ is assessed, disregarding the pressure gradient in the momentum equations. As stated above the curl of the velocity does not depend on the pressure gradient, so $\underline{U}^*$ possess the right amount of vorticity but it is not solenoidal yet ($\nabla \cdot \underline{U} \neq 0$) . During the second step the $\underline{U}^*$ is corrected, using the pressure gradient:

$$\underline{U} = \underline{U}^* - \epsilon \nabla p$$

Where ϵ is a (dimensional) constant. The last step is accomplished by forcing the divergence of the velocity to be zero ($\nabla \cdot \underline{U} = 0$), which is the same as imposing the continuity. Hence a Poisson equation for the pressure is derived:

$$\nabla \cdot \underline{U}^* = \epsilon \nabla^2 p$$

After the pressure has been correctly assessed the velocity can be calculated from momentum equations by using the correct value of the pressure gradient. Moreover the inverse theorem of calculus [2] assures us that the velocity field, obtained through such operations, is unique.

As anticipated there are several algorithms which are based on the approach described above, and we present two of them: the SIMPLE algorithm (Semi-Implicit Method for Pressure Linked Equation), elaborated by Patankar and Spalding [56] [57] and the PISO (Pressure Implicit Split Operator) by Issa [58]. The first usually finds its application in steady-state problems whereas the second in the transient ones. In the following paragraph, we briefly describe the two methods, which are those used in the OpenFoam solvers. For most of the simulations, we have relied on the PISO (algorithm) as the

[1] This can be seen taking the Navier-Stokes and eliminating the pressure gradient with opportune cross differentiations and subtractions.

[2] The inverse theorem of calculus states that a vector field $\underline{V}$ is uniquely determined , having the following properties in a domain D :$\nabla \cdot \underline{V} = a$ in D,$\nabla \times \underline{V} = \underline{b}$ in D and $\underline{V} \cdot \underline{n} = f_n$ on ∂D with $\int_D a dV = \int_{\partial D} f_n dS$.

present work deal with transient phenomena. However, in some circumstances, we tried a combination with the PISO a SIMPLE as well (known as PIMPLE in OpenFoam).

SIMPLE method The simple method with a collocated variables approach can be summarised with the following sequence of operations:

1. start with the old solution p^n, $\underline{U}^n$, $\dot{m}$ at time t as the first guess;
2. solve the momentum equations (implicitly) to derive a velocity filed $\underline{U}^*$, which does not satisfy the continuity (predictor step);
3. update the mass flow rate $\dot{m}$ at the face cells by using the Rhie and Chow interpolation, deriving in this manner $\dot{m}^*$;
4. with the flow rates just calculated, build a Poisson equation for the pressure corrections p';
5. once the pressure correction field p' has been obtained, update the pressure, the mass flow rate and the velocities (corrector step). The variables are now denoted with p^{**}, $\underline{U}^{**}$, $\dot{m}^{**}$ respectively;
6. use the solution assessed at point (5) as an initial guess and return to point (2) until convergence is achieved;
7. go to the next time step $t + \Delta t$ and use the converged solution just found as the initial guess;
8. repeat the procedure for the step $n + 1$.

PISO algorithm The PISO algorithm is an extension of SIMPLE. Indeed the point (1)-(5) of the previous paragraph are the same, however, in this case, a further corrector step is added: once the quantities in the point (5) are assessed, the momentum equations are again solved to obtain $\underline{U}^{***}$. Differently from the point (2) this time, the momentum equations are solved explicitly (the matrix of coefficients stays the same). So between points (5) and (6) of the previous algorithm, the following operation have to be added:

5a Solve explicitly momentum equations to calculate $\underline{U}^{***}$;

5b Compute the new flow rates $\dot{m}^{***}$ using Rhie and Chow interpolation;

5c derive the Poisson equation for pressure corrections p";

5d correct p^{**}, $\underline{U}^{***}$, $\dot{m}^{***}$ to obtain p^{***}, $\underline{U}^{****}$, $\dot{m}^{****}$;

5e repeat (5a)-(5d) for a prescribed number of times. When the number of iterations (of (5a)-(5d)) is reached go to point (6).

Here we have just limited ourselves to present the two basics algorithms. However, there is a plethora of modified version of such methods. Just to stay in the perimeter of the SIMPLE like methods there are: SIMPLEC [59], SIMPLER [57], SIMPLEX [60], SIMPLEM [61], SIMPLEST [62]...

Chapter 6

Tools for the analysis of chaotic systems

In this chapter, we introduce some important notions, such as dynamical systems and bifurcations, being these concepts important to interpret some results obtained in Part II. We have indirectly already introduced the concept of bifurcation in Chapter 4 when we dealt with thermal convection. In that chapter, indeed, we recalled the principles of linear stability analysis given in Appendix D, to linearise the momentum and energy equations. This process is beneficial to find some threshold values of the control parameters (in those cases the parameters were the Rayleigh or Marangoni numbers) characteristic of the "system" beyond which the flow changes qualitatively. This chapter is devoted to giving a better and more comprehensive insight into the concepts of "control parameters "and "system "used above. We will introduce the notion of bifurcation in the framework of dynamical systems as it acquires a much more mathematical and general meaning as that given in Chapter 4. We will see how certain overtaking value of a parameter in a differential equation representing a system brings to a sudden change in its behaviour. Moreover, the bifurcations are not all the same, and we will distinguish among them: in Chapter 4 talking about the Rayleigh-Bénard convection we have seen that after a critical Ra the system evolves from a configuration which is at rest to a steady one and no time-dependent motions are involved. On the other hand, when we dealt with thermo-capillary problems, we talked about hydrothermal waves which are a typical example of an unsteady phenomenon. The bifurcation leading to the patterns mentioned indeed is different and in this chapter, we will first define them and then introduce the mathematical tools to distinguish among them.

As of last but probably the most interesting and fascinating topic, the chaos will be presented. Indeed we will see how also systems ruled by deterministic laws, when integrated numerically, could undergo completely unpredictable behaviour. More precisely, we should talk about deterministic chaos because the system remains fully deterministic, but even infinitesimal perturbations could lead to a large difference of the trajectories in the phase space. Another task of this chapter is indeed to give an appropriate definition of the phase space and show how the trajectories of chaotic systems lay on topologically complex sets: the so-called "strange attractors". These spaces are characterised by the peculiar property of having a non-integer dimensionality: hence to understand better this aspect the notion of Hausdorff and correlation dimensions along with the Lyapunov exponents will be given.
As already said, all the concepts treated in this chapter find a direct application in the field of thermal convection.

6.1 Bifurcations

In the introduction, we said intuitively that a bifurcation is a sudden change in the system behaviour while a parameter in the equations is varied and the value at which this occurs is said to be the **critical value**. Moreover, we argued that they are not all the same, and this section and Appendix F aim to distinguish among them. However, before embarking in the classification of the possible bifurcations, it is useful to define what is an **attractor**.

Attractor An attractor is a set in the phase space which despite the initial conditions taken by a dynamical system, after a certain number of orbits, the trajectories fall over it. So a definition of attractor could be given as a region of the phase space towards which all the trajectories starting from some other set contained in the phase space tend to evolve. The set of all initial conditions, having the trajectories falling on the attractor is called the **basin of attraction**. Topologically an attractor can be a bunch of different entities: a point, a curve, a T^n torus or more, in general, a stable manifold. However, it could also be some other more complicated object: a strange attractor, characterised by a fractal dimension. The dimensionality [1] of the attractor is strictly

[1]The definition of dimension used to topology is more general from that given by algebra, and here we are using the first one. A rigorous definition will be given next, and it will be shown that different notion of dimension exists

linked with the dynamics of the system, and we will resume the connection among the motion in the time domain and the topological shape of the attractor:

Attractor	Dimension	Motion
fixed point	0	steady state
limit cycle	1	periodic
T^n torus	n	quasi-periodic n incommensurate frequencies
strange attractors	any real number	chaos

Table 6.1

With the concepts defined above, it is easy to cast the bifurcation as a topological change of an existing attractor or, when there are more of them as an interaction among them. Indeed more complex non-linear systems could have more than one attractor, which in principle could be unstable and in such case, they are called **repellors**. These unstable counterparts have the property that the trajectories tend to flow away from them.

In the present section, we limit ourselves to make a little distinction about a stationary bifurcation and time-dependent (Hopf) one, leaving Appendix F a much more detailed classification. A stationary bifurcation, as the name suggests, leads to spatial changes in the dynamics, without affecting the temporal behaviour, which remains steady. According to the notions given in Appendix D about the linear stability analysis, this bifurcation is characterised by the emergence of real positive eigenvalues of the corresponding linearised problem. The Hopf bifurcation, on the other hand, involves the temporal behaviour as well, leading the system from a stationary state to a time-dependent one and it is characterised by eigenvalues of the associated Jacobian having, together with a positive real part also a non zero imaginary part. In the phase space, the Hopf bifurcation is reflected by a topological change of the associated attractor, which evolves from a fixed point to a limit cycle.

6.2 Chaos

In this section, we deal with the notion of chaotic dynamical systems. Before embarking in such a description, it is worth remarking that we will only scratch the surface of

such suggestive and complex topic. A complete description would require much more than a chapter, and this section aims to introduce some concepts and algorithms which will come very useful in the analysis of the results presented in Part II. Chaos indeed is a permeating feature of thermal convection, and it is challenging to give a correct interpretation of the results without having at least a raw knowledge of the main characteristics about the behaviour of chaotic dynamical systems.

The first studies about chaotic systems were due to Henri Poincaré with the problem of the three bodies. However, it was only in 1963 that Edward Lorenz [63] laid the groundwork for a complete theory. He considered a system of three ordinary differential equations mimicking a simplified model of the atmospheric convection, and he found a completely aperiodic and unpredictable behaviour of the system associated. However, chaos does not mean randomness! Although chaotic systems are characterised by the impossibility to make long term predictions, they have some properties which differentiate them from pure random behaviour. A clear difference indeed is the fact it takes its origin from differential equations which are completely deterministic. To resume chaos is a recipe which needs three ingredients:

- the deterministic nature of the underlining equations;
- aperiodicity in the long term behaviour;
- sensitivity to the initial conditions.

About the first point, it is worth saying that completely deterministic equations rule all the phenomena in the present thesis. Indeed thermal fluid flows are governed by the equations described in the previous chapters (Navier-Stokes and energy equation, viscoelastic constitutive law) which do not have any randomness.

The second aspect is characterised by an important property in the phase space: The trajectories do no longer settle down to a fixed point or periodic orbit. Instead, they are attracted by another subset of the phase space: a **strange attractor**, which has a fractal dimension. Before defining them more rigorously, an interlude about topological and box-counting dimension is needed.

The sensitivity of initial conditions (SIC) is mostly known with the suggestive appellative of the **butterfly effect**, which has the meaning that even an infinitesimal perturbation in the starting condition could lead to finite-difference after a certain amount of time. Even if this concept has spread into the popular culture through many films and

books, it can be phrased in a precise mathematical form using the notion of the phase space. Indeed the tool used to quantify it are the so-called **Lyapunov exponents**.: in the next paragraph, we will deal with them, explaining their meaning.

6.2.1 Sensitivity to Initial Conditions (SIC) and Lyapunov exponents

f the system is dissipative the volumes in the phase space tend to shrink, in sense that if we start with an initial condition ($\underline{v}_0$) in the n-dimensional phase space and consider an n-dimensional ball U of slightly perturbed conditions around it al the trajectories starting on U will cluster together after the system has evolved for a certain amount of time. However, if the system exhibits SIC, there are some directions along which the distance between the trajectories will grow. This fact is graphically shown in Figure 6.1.

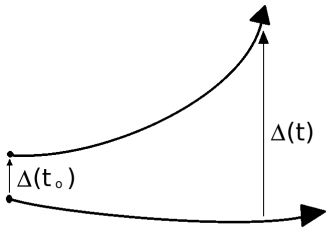

Figure 6.1: Exponentially diverging trajectories

This distance moreover grows at an exponential rate:

$$||\Delta(t)|| \approx ||\Delta(t_0)|| e^{\lambda(t-t_0)} \tag{6.1}$$

The exponent λ is called **Lyapunov exponent** and it gives the rate of divergence (or convergence if it is negative) of nearby trajectories. To be more precise we have to talk about the **Lyapunov spectrum** because there are n exponents λ_i, one for each dimension of the phase space. Being the system dissipative means that the sum of all the exponents in the spectrum has to be negative, on the other hand, one positive Lyapunov exponent is enough to state that the system undergoes to SIC. Assessing the Lyapunov spectrum numerically in case of complex systems is not a trivial task there are algorithms such as that proposed by Wolf et al. (1985) [64], which are based on the time delay reconstruction, ruled by Takens theorems [65] .

As final remark for this section, we notice that the Lyapunov spectrum is strictly related

to the dimension of the attractor in the phase space through the Kaplan-Yorke relation [66]:

$$D_\lambda = k + \sum_{j=1}^{k} \frac{\lambda_j}{\lambda_{k+1}} \tag{6.2}$$

In equation 6.2 the Lyapunov exponents have been ordered in a decreasing manner, from the largest to the smallest and k is the largest value of j such that $\sum_{j=1}^{k} \frac{\lambda_j}{\lambda_{k+1}} > 0$.

6.2.2 Strange attractors and fractals

In this section, we will consider the chaotic dynamical systems under another perspective. While in the previous paragraphs, we have underlined that an important ingredient of chaos is sensitivity to initial conditions in this section, we will look at the chaotic systems under a new perspective: the aperiodicity. This property indeed automatically rules out any possible closed one-dimensional cycle, so the question is, do the trajectories settle down to any sub-set in the phase space? Does this subset have a structure? Luckily the answer to both questions is yes, and this set is known to be strange attractor which has some properties in common with other topological objects: the **fractals**, which have some important features:

- they have a structure at arbitrarily small scales;
- they are characterised by self-similarity, i.e. that they contain smaller copies of itself;
- they have a non-integer dimension.

While the first two features are fascinating, and there are many examples of fractals exhibiting these properties such as the Cantor and Mandelbrot set, in the following, we will focus on the last property.

Topological and box-counting dimension

A classical and in some sense simple definition of the dimension of a given set is the minimum number of independent parameters or coordinates necessary to locate a point on it. The notion of **topological dimension** in some sense reflects this aspect assuming only integer values and for many simple sets, this definition is enough to describe the concept of dimension. However, this is not true for fractals. So we need to widen the

classical notion of dimension introducing the **box counting dimension**[2]. To define it lets take a sub-set embedded in a metric space (it could be R^n or any space (X,d) provided with a metric through which is possible to define a distance) and take the minimum number N of boxes of size r necessary to completely cover it. The number N will of course increase as the size r is decreased, being the minimum number somehow proportional to the measure of the set M and the size r through:

$$N(r) \propto \frac{M}{r^{D_0}} \tag{6.3}$$

Adjusting and taking the limit (if it exists) of the 6.3 the box-counting dimension D_0 is defined as:

$$D_0 = \lim_{r \to 0} \frac{logN(r)}{log\frac{1}{r}} \tag{6.4}$$

In particular, equation 6.4 is a special case of a more general set of definitions of the fractal dimension (see, e.g. Grassberger 1983 [16]). The box-counting dimension takes into consideration only geometry of a given set without considering its density, intended as an indicator of how often a trajectory passes through a given region of the set in a time interval. It can also be regarded as a fraction of time that a trajectory starting from the point p_0 on the attractor spends in a given region R while the time Δt interval considered tends to ∞, in other words:

$$\tau(R, p_0) = \lim_{\Delta t \longrightarrow \infty} \tau(R, p_0, \Delta t) \tag{6.5}$$

The 6.5 may be thought of as a weighting factor for the boxes considered in 6.4. In the definition of the box-counting dimension the boxes are not weighted, on the other hand, using different weight allows us to reach a more general definition of dimension: the **generalised or Renyi dimension** (Baltoni and Renyi (1956) [67]):

$$D_\alpha = \lim_{r \longrightarrow 0} \frac{1}{1-\alpha} \frac{log\left\{\sum_i [\tau(C_i)]^\alpha\right\}}{log\left(r^{-1}\right)} \tag{6.6}$$

It can be noticed that for a given value of α we obtain a different definition of dimension: for $\alpha = 0$ we have the box-counting dimension, while for $\alpha = 1$ and 2 we have the **information** and **correlation dimension** respectively. The first is strictly linked to

[2]For many fractals this dimension coincides with the Hausdorff dimension. However, they are not the same in general.

the entropy of a given dynamical system, and according to the Kaplan-Yorke conjecture, it is equal to the Lyapunov dimension:

$$D_1 = \lim_{r \leftarrow 0} \frac{\sum_i \tau(C_i) log\left[\tau(C_i)\right]}{log\left(r\right)} = D_\lambda \tag{6.7}$$

The latter can be estimated much more easily than the box-counting dimension, and hence in literature, it has become a measure widely used to detect chaos. In the next paragraph, indeed we will show the algorithm which allows an estimation of it. Before embarking in such description, however, it is worth emphasising that the dimension given by 6.6 is a non-decreasing function of α:

$$D_2 \leq D_1 \leq D_0 \tag{6.8}$$

Correlation dimension

Since the pioneering work of Lorenz many strange attractors have been characterized through the Lyapunov coefficients or the Hausdorff dimension: some examples are the Henon map, Lorenz and Rossler attractors. Most of these attractors are described by a set of ordinary equations, which are much simpler than the partial differential equations describing the non-isothermal flow of Newtonian and viscoelastic fluids. So for this reason assessing the quantities mentioned above for the complex systems is not an easy task, and several methods have been developed to estimate directly these quantities or others, which are linked to them. The quantity which has been used to describe the chaotic states in the following is the correlation dimension ν (Grassberger and Procaccia (1983) [68]), which is defined, through a correlation integral, as:

$$C(r) = \lim_{N \to \infty} \frac{1}{N^2} \sum_{i,j=1}^{N} H(r - |\vec{X}_i - \vec{X}_j|) \tag{6.9}$$

and

$$C(r) \propto r^\nu \tag{6.10}$$

Where:

- N is the number of points of the time series;
- H is the Heaviside function

- $\vec{X}$ are the points in the embedded space;
- r is a distance, chosen in the embedded space.

To assess the correlation dimension, the attractor, which lies in the phase space has to be "projected" in another space, called embedded space. The technique used to pursue this is called time delay reconstruction and relies on the Takens theorems [65].

Drawbacks of the method The Grassberger and Procaccia algorithm (GPA) is very suitable to be applied to the practical problems as it allows to give an estimation of the strangeness of the attractors only having a measurement of one quantity (such as temperature or one velocity component) in a single point of the domain.
Moreover, the algorithm is pretty simple to implement and do not require a deep knowledge of chaos theory. Unfortunately, the method has some limitations: mainly, it fails to give an estimation when chaos is high dimensional and the time series is noisy. According to Eric J.Kostelich and Harry L. Swinney (1989), [69] when the dimension of the attractor is too large the plateau region (that with linear scaling in the $log_2 r - log_2 C(r)$ graph) is absent making an estimation of ν very difficult. Another constraint is on the length of the time series, indeed as stated by Eckmann and Ruelle (1992) [70] the minimum length of the time series in terms of the number of measurements scales as:

$$2logN > \nu log(\frac{1}{\rho}) \tag{6.11}$$

Where N is the number of the points and $\rho = \frac{r}{D}$, with D being the diameter of the attractor.

6.2.3 Routes to chaos and transition to turbulence

Before concluding this chapter, we shall discuss how a system evolves towards chaos as the control parameters are varied. Indeed chaos and transition to turbulence could arise according to different scenarios, depending upon the equations governing a given dynamical system. Usually, before becoming chaotic, a system undergoes to bifurcation cascade, which brings it from a steady state to developed turbulence. The first to introduce the concept of scenario trough which the system evolves towards chaos was Landau (1944) [71], who stated that the turbulence is reached after an indefinite superposition of Hopf bifurcations, each adding an incommensurate frequency to the system.

This scenario, however, is in contrast with that proposed by Newhouse, Ruelle, Takens [72], who mathematically showed that before the appearance of chaos the system has to undergo to three Hopf bifurcations with incommensurate frequencies. The first bifurcation leads the system to a periodic behaviour, while the second one to a quasi-periodic state, represented in the phase space by a T^2 torus. According to [72], after the third Hopf bifurcation has occurred the T^3 becomes unstable to infinitesimal perturbations, leading directly to chaos. The Ruelle-Takens-Newhouse scenario described above has been observed in many dynamical systems included in the Rayleigh-Bénard convection, there are however some cases (and we will discuss some of them in Part II) where the chaos arises before the T^3 bifurcation has occurred. This latter route to chaos is known as Curry-Yorke scenario [73].

Along with the scenarios described above some maps (see, e.g. logistic map) and also the Rayleigh-Bénard convection (see, e.g. Fauve and Libchaber (1982) [74] for a description of Rayleigh-Bénard in liquid mercury) could undergo to the so-called period-doubling scenario. Feigenbaum initially described it (see, e.g. [75] [76]) and according to it chaos is reached through a subharmonic cascade in which each subsequent frequency is twice as the former.

A third scenario which has historically been developed in the framework of the theory of dynamical systems is the route to chaos through intermittency. Pomeau and Manneville first described this phenomenon (1980) [77] according to whom a nearly periodic system undergoes to chaotic bursts irregularly. A phenomenon which could exhibit an intermittent behaviour is the crisis, which is triggered when a sudden appearance or disappearance of a strange attractor occurs. Moreover, according to Grebogi et al. (1983) [78], it could be of three types: a boundary or an exterior crisis, when the attractor is abruptly destroyed, an interior one, when the size of an attractor undergoes to a sudden increase and collide with another unstable set. The last one is the attractor merging crisis, which occurs when two strange attractors merge when the control parameter passes a critical value.

Part II

Results

Novelties of the present research

Part I of the present manuscript has been devoted to the description of the physical and numerical models behind the results presented in Part II. Moreover, the first six chapters aim to focus on the relevant arguments and tools used throughout the second part of this thesis. Particularly in Chapter 4, a short review of thermal convection has been given. The main configuration treated in that chapter was the infinite layer subjected to a temperature gradient. Despite the simplicity of that configuration, a multitude of different flow patterns and instabilities has emerged. Such an aspect has been particularly encouraging to take that geometry as a starting point for the present work. Indeed, we have further expanded the notions presented in Chapter 4, by adding some other degree of freedom to the system.

The main topic of Chapter 7 is the gravitational thermal flows of low Prandtl fluids (i.e. liquid metals and semiconductor melts) in converging or diverging cavities. Although these configurations have received much attention in the past decades, the introduction of the tilted walls is the new aspect described here. Even with such a simple addition, i.e. the contraction or expansion of the cavities, a new dynamics has emerged. The key feature of the novelties is probably the travelling waves (in 2D enclosures), which have not been observed in that kind of flows so far.

On the other hand, the situation in 3D cases is very different. Indeed a remarkable competition among the hydrodynamic and OLR modes has been observed.

Chapter 8 investigates the classical Marangoni-Bénard convection in an infinite layer. Such a problem received widespread attention by researchers in the past. However, most of the efforts were related to Newtonian fluids, leaving a gap in the field of complex fluids (e.g. viscoelastic ones). Chapter 8, indeed, aims to investigate this problem, underlining the main differences with the Newtonian case. We will see how the introduction of the viscoelasticity completely changes the dynamics, allowing the existence of localised convective structures (i.e. oscillons). Although this kind of structures are

characteristic of other fields (e.g. granular media and colloidal suspensions), they have never been observed in Marangoni-Bénard convection.

Chapter 9 considers thermo-gravitational convection in an inclined cavity. As the classic Marangoni-Benard case, also this problem has been widely considered during the past decades. However, the impact of boundary conditions on the flow patterns has received much less attention. Indeed the walls of the domains usually are supposed to be perfectly adiabatic or conducting.

On the other hand, a correct modelling of the heat flow through the walls is needed to get a closer agreement with experimental studies. The effort of Chapter 9, indeed, is to understand how the introduction of more realistic boundary conditions (i.e. the modelling of the heat flow through lateral walls) helps to achieve a more realistic situation. The key aspects, which have emerged from Chapter 9, are the very different symmetries and Spatio-temporal behaviours assumed by the system when the more realistic BC are considered.

Chapter 7

Gravitational thermal flows of liquid metals in variable cross section containers

Non-isothermal flows of liquid metals induced by buoyancy are omnipresent in engineering and related technological applications (see e.g. Okano et al. [79]; Delgado-Buscalioni and Crespo del Arco [80]; Kaddeche et al. [81]; Li, Peng, Wu, Imaishi and Zeng [82]; Jaber and Saghir[83]; Lappa [4]). The related hierarchy of bifurcations and mechanisms of transition to chaos also constitute a significant and relevant part of the problem. As an example, they have a significant impact on the solidification of industrial castings and ingots. The quality and mechanical properties of such products are adversely affected by such flows as they can produce "defects" such as channels and freckles in the material structure(Ludwig et al.[84], Abhilash et al. [85]). In other circumstances, convection has just the opposite effect, i.e., it can be employed for melt homogenization and prevention of slab macroscopic irregularities (such as the entrapment of bubbles or other non-metallic inclusions). Often such casting processes rely on liquid metal compartments equipped with "baffles", which cause a significant departure of the effective geometry from the classical rectangular solidification chamber often assumed in related numerical studies. Flows of liquid metals and their oscillatory or chaotic states also affect the production of crystals of semiconductor or superconductor materials (in the context of "crystal-growth-from-the-melt" techniques, e.g., the horizontal Bridgman (HB), the Floating zone (FZ), or the Czochralski (CZ) technique). Leaving aside for a while the differences among such production techniques (differing

essentially in the shape of the container used to host the liquid and/or in the shape of the resulting crystallized material, see, e.g., Lappa [86]), all such methods share a common feature, that is, the presence of flow of gravitational (buoyancy) nature in the liquid undergoing solidification. Such flows can have detrimental effects on the perfection and purity of the ordered crystalline structures of the resulting solidified material (typically emerging at the micro or macro scale in the form of "striations" or "segregations", respectively;Dupret and Van der Bogaert [87]; Monberg [88]).Actual geometries in practice are often found to have shapes with top or bottom boundaries being more or less inclined with respect to the horizontal. Additional relevance for such flows can be found in the nuclear engineering area. As an example, liquid-metal cooled nuclear reactors (liquid metal fast reactor or LMFR) represent a class of advanced-type nuclear devices where water as the primary coolant has been replaced by a liquid metal. Because a metal has obviously a much higher thermal conductivity than water, it can be used to remove heat more efficiently. Moreover, a liquid metal can lower the chance of neutron leakage due to the presence of favourable neutron properties. This makes the use of these liquids as primary coolants very attractive in situations where containing the size of the plant is a factor of crucial importance (Zrodnikov et al. [89]; Gorse Pomonti and Russier [90]). Similar ideas are being applied to devise new advanced heat exchangers for high power electronic devices. To better tackle the high-density heat dissipation difficulty within the limited space usually associated with such systems, a new generation of mini-channel exchangers based on metals that are liquid at ambient temperature (or have a small melting point temperature) is being developed (Luo ad Liu[91]).

Apart from applications of a practical or prototypical nature, however, there is no doubt that most of the interest in such subjects is essentially academic. Indeed, the instabilities of thermo-gravitational flows in liquid metals and related hierarchy of bifurcations do exert an appeal to researchers and scientists because of their inherent complexity. There seems to be no obvious limit to the richness of such dynamics and the variety of related patterns. Such organized structures (and their spatio-temporal evolution) are often aesthetically pleasing and "philosophically" challenging (in terms of the implications they have on the theory of chaos), which makes them irresistible to theoretical physicists [4].

From a purely mathematical point of view, a rigorous formulation of this problem can

be cast in the form of the so-called initial-boundary value problem (IBVP) where the governing balance equations for mass, momentum, and energy have to be solved together with the related initial and boundary conditions. In turn, this requires implicitly the adoption of a given solution strategy, be it analytical, approximate (semi-exact), or "numerical".

Determining solutions of the equations governing such flows (Navier-Stokes + energy equations) in the analytic form is an extremely challenging task (Ostroumov [92]; Birikh [93] and Lappa [94]). These exact solutions are known to exist only in very special circumstances (most of which being purely "ideal"), such as domains infinitely extended along the direction of the imposed temperature gradient or flows attaining a purely "parallel state", which is a kind of motion for which only one of the two velocity components in the plane containing the temperature gradient is not zero (which makes the resulting IBVP problem essentially "linear").

The so-called class of Adomian's decomposition methods (see, e.g., the work of Adomian [95]; Cherruault and Adomian [96] and Babolian et al. [97]) can provide an approximate solution without the need for linearisation, perturbation, or discretisation. Such an approach has been applied with a significant rate of success to the case of liquid metals flowing in converging or diverging channels for a variety of conditions and physical effects (Makinde [98]; Mhone and Makinde [99]; and Asadullah et al. [100]). These studies, however, have been limited essentially to unidirectional (Couette-like) flows.

The specific case of the thermo-gravitational flow of liquid metals in differentially heated "converging or diverging" containers, encompassing both the direct (from the hot side to the cold side) and "return" currents (in the opposite direction), has been addressed most recently by Lappa and Ferialdi [101] on the basis of a hybrid approach relying on the numerical integration of the IBVP problem in conjunction with analytic solutions of the temperature field (used as initial conditions). The complex dependence showed by the system even at a very low Rayleigh numbers ($Ra \approx 100$) justifies a preliminary section describing the system behaviour at such values of the Rayleigh number before embarking into the description of the two-dimensional instabilities occurring at higher values of the parameter. After this two sections the fully three-dimensional case will be presented, showing the deep difference respect to its 2D companion.

7.1 The System, governing equations and numerical method

We consider a two-dimensional shallow cavity symmetric with respect to the horizontal direction with average depth d, laterally delimited by solid walls at different temperatures (one cooled and the other heated) having heights d_{hot} and d_{cold} . The overall system aspect ratio A is naturally defined as it length-to-average-depth ratio: $A = \frac{L}{d}$, where $d = \frac{d_{hot}+d_{cold}}{2}$. Another relevant characteristic geometrical parameter (refer to Figure 7.1) is the aforementioned expansion (compression) ratio $\eta = \frac{d_{hot}}{d_{cold}}$, which can be > 1 (diverging geometry) or < 1 (converging geometry), while for $\eta = 1$ one would recover the classical case with horizontal boundaries originally introduced by Hadley [11]. Moreover in the following the Rayleigh number has been defined as in Chapter 2. However in this case the average depth of the cavity ($d = \frac{d_{hot}+d_{cold}}{2}$) as reference length has been chosen.

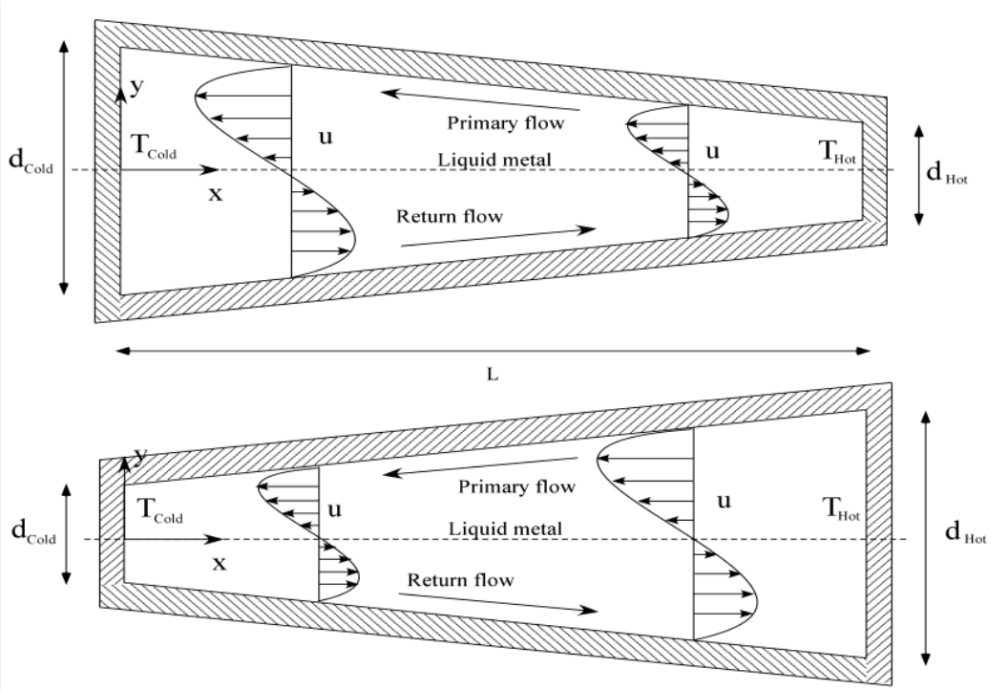

Figure 7.1: Geometry of the cavity: upper picture $\eta < 1$, lower picture $\eta > 1$

We assume the top and bottom walls to be adiabatic (no heat exchange). As schematically shown in Figure 7.1, the natural buoyancy flow emerging in such configurations for relatively small values of the control parameter consists of a single horizontally elongated convective roll (with fluid rising in proximity to the heated wall, moving along the upper wall from the right side to the left side, moving downward when it meets the left (cold) wall, and finally coming back to its original position along

the bottom wall).

The equations solved are the Navier-Stokes and energy, described in chapter 2, moreover the results are presented in non-dimensional form as discussed in the same chapter (section 2.4.3). The buoyancy force has been modelled according the Boussinesq approximation.

7.1.1 Analytic Solutions for Quiescent Conditions

Before starting to deal with the nature and structure of the emerging flow for finite values of the Rayleigh number, it is instructive to consider the behaviour of the temperature field in the limit as $Ra \to 0$, namely conditions of creeping flow or quiescent state. For such a case, indeed, though the assumption of horizontal parallel top and bottom boundaries is removed, an analytic solution can be still found. Our interest in such an expression stems from a two-fold purpose. First it can be used to show that the assumption of linear temperature increase along the horizontal (x axis) is no longer valid. This assumption is generally invoked for differentially heated rectangular enclosures with adiabatic top and bottom walls in quiescent (no flow) conditions or even in non-quiescent conditions for liquid metals provided one of the two following conditions (or both) is satisfied: $Pr \to 0$ or the flow is parallel, i.e. the considered system has an infinite extension along the horizontal direction.

Second, such an analytical expression can be used as a relevant initial condition to accelerate the convergence of the algorithm relating to the numerical solution of the momentum and mass conservation equations in the more general case for which both A, Pr and Ra have finite values and $\eta \neq 1$.

Most conveniently, we start from the balance of energy cast in its simplest form, that is, the conservation of energy flux along the horizontal direction:

$$d(x)\frac{dT}{dx} = c_1 \tag{7.1}$$

where $d(x)$ is the non-dimensional extension of the generic cross section, which in turn can be expressed as:

$$d(x) = d_{cold} + \left[\frac{d_{hot} - d_{cold}}{A}\right] = d_{cold}\left[1 + (\eta - 1)\,\frac{x}{A}\right] \tag{7.2}$$

Substituting eq. 7.2 into eq. 7.1 gives:

$$\frac{dT}{dx} = \frac{c_1}{d_{cold}\left[1 + (\eta - 1)\,\frac{x}{A}\right]} \tag{7.3}$$

which, once integrated, yields:

$$T(x) = \frac{c_1 A}{d_{cold}\,(\eta - 1)} \log\left[1 + (\eta - 1)\,\frac{x}{A}\right] + c_2 \tag{7.4}$$

The two constants c_1 and c_2 can be determined forcing eq. 7.4 to satisfy the boundary conditions at the two side walls, namely:

$$x = 0 \qquad T = 0 \rightarrow c_2 = 0 \tag{7.5}$$

$$x = A \qquad T = 1 \rightarrow c_1 = \frac{\log(\eta - 1)}{A \log(\eta)} \tag{7.6}$$

Accordingly, eq.7.4 can be cast in compact form as:

$$T(x) = \frac{\log\left[1 + (\eta - 1)\,\frac{x}{A}\right]}{\log(\eta)} \tag{7.7}$$

where obviously:

$$\lim_{\eta \to 1} \frac{\log\left[1 + (\eta - 1)\,\frac{x}{A}\right]}{\log(\eta)} = \frac{x}{A} \tag{7.8}$$

Equation 7.7 plotted in Figure 7.2 for different values of the parameter η clearly shows the departure of the temperature profile from the purely linear distribution theoretically established for $\eta = 1$. The resulting profile is concave or convex for $\eta < 1$or $\eta > 1$, respectively. As anticipated, such behaviours should be regarded as an evident difference with respect to past situations in which the flow was assumed to be purely parallel or "purely thermally diffusive" conditions were considered in finite-size rectangular enclosures (for very small values of the Prandtl number such as those which are typical of liquid metals ($Pr \ll 1$) and for relatively small values of the control parameter Ra).

7.1.2 Numerical method, boundary and initial conditions

Though a mathematical basis for the study of these problems is the theory of stability and the theory of bifurcation, as shown in different studies, also direct numerical discretisation and solution of the system model equations (the Navier-Stokes equations in

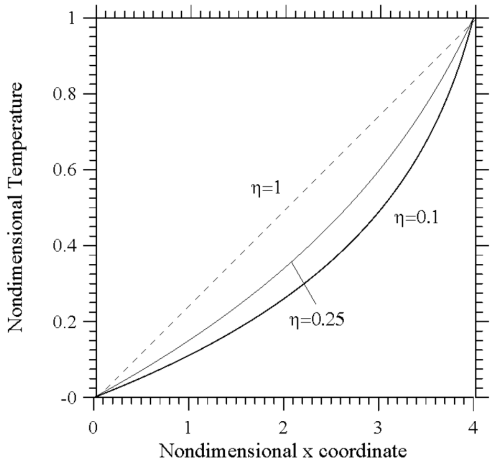

(a) $\eta < 1$

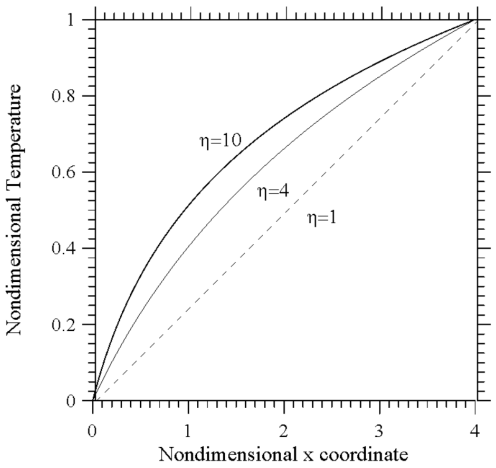

(b) $\eta > 1$

Figure 7.2: Analytical solution for the temperature distribution for A=4 and Ra=0.

their complete form together with the energy equation, also referred to as thermal convection equations) can provide significant information. Here the governing equations have been solved numerically assuming no-slip conditions on the walls, conditions of prescribed temperature at the left and right side-walls, and adiabatic top and bottom (non-horizontal) boundaries. Moreover, most conveniently (to speed up algorithm convergence), for each simulation the initial temperature field has been initialized using the analytic solution 7.7 derived in the previous section (diffusive conditions). In particular, we solved the balance equations and related boundary conditions in their complete non-linear and time-dependent form using the open source software OpenFoam which is based on Finite Volume Method (FVM). The solution strategy relies on the so called projections methods on collocated grids as discussed in Chapter 5.

7.1.3 2D vs 3D simulations

The present chapter is structured as follows: first, a complete parametric study for two-dimensional cavities is given, then the three-dimensional simulations are presented. A question which arises spontaneously at this point is: why 2D simulations? The answer resides in Chapter 4: indeed, at a very low Prandtl, such that considered in the present chapter, the 2D transverse rolls are the most dangerous instability. Moreover, being the 2D simulations much less computationally expensive, it is possible to carry out a complete parametric study. These are the two reasons why an entire section of the present chapter has been devoted to the two-dimensional cases.

On the other hand, it is known from the literature that the marginal stability curve of the OLR modes (Oscillating Longitudinal Rolls)is pretty close to that related to the 2D instabilities. Moreover, at slightly larger Prandtl, the OLR modes become the most dangerous instability mechanism. So the second part of this chapter is entirely dedicated to the presentation of three-dimensional outcomes.

7.2 Low Rayleigh numbers ($Ra = 100$)

This preliminary results are focused on a very low Rayleigh numbers in converging and diverging cavities. The results shown here serve as justification for a more detailed analysis, indeed in the following is shown how the velocity profiles have not a monotonic behaviour as η is varied. Moreover the presence of an inflection point in such profiles constitute a proof about the hydrodynamical nature of possible disturbance occurring at higher Rayleigh numbers.

For each aspect ratio a mesh refinement study has been conducted in advance in order to determine the minimum number of computational points required to get grid-independent solutions in the case of uniform grids ($N_x x N_y = 100x30$ and 200x30 for $A = 4$ and $A = 10$, respectively). The typical structure of buoyancy flow is shown in Fig. 7.4 for different values of the aspect ratio and of the parameter η. All cases correspond to subcritical conditions, namely circumstances for which the asymptotic state attained by thermo-gravitational flow is steady. The governing equations have been solved assuming no-slip conditions on the walls, conditions of prescribed temperature at the left and right side-walls and adiabatic top and bottom (inclined) boundaries.

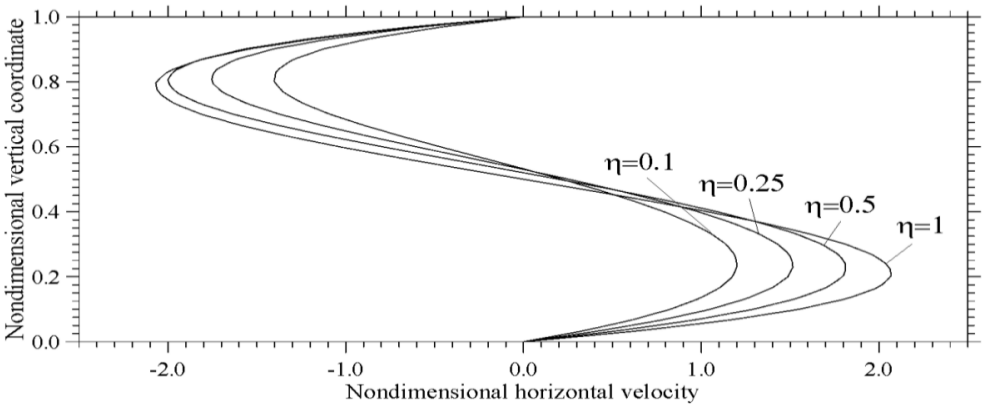

Figure 7.3: Horizontal velocity profile at $x = \frac{1}{2}$
,for $A = 4$ and $Ra = 100$ and different values of η

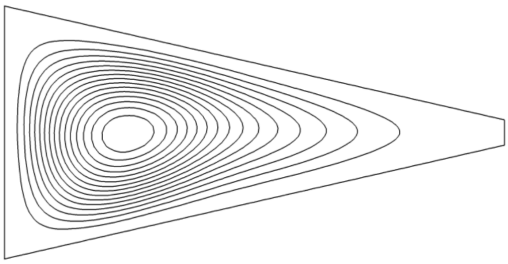

(a) $A = 4, \eta = 0.1$

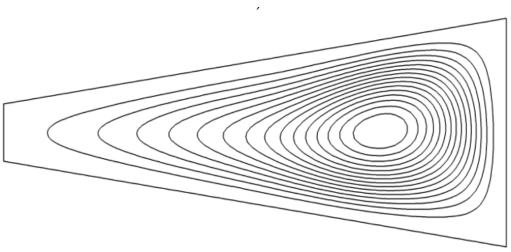

(b) $A = 4, \eta = 4$

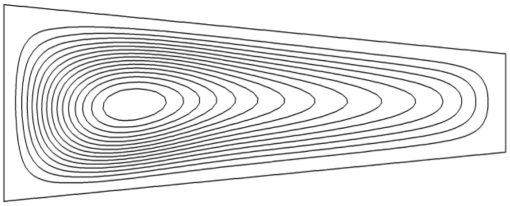

(c) $A = 4, \eta = 0.5$

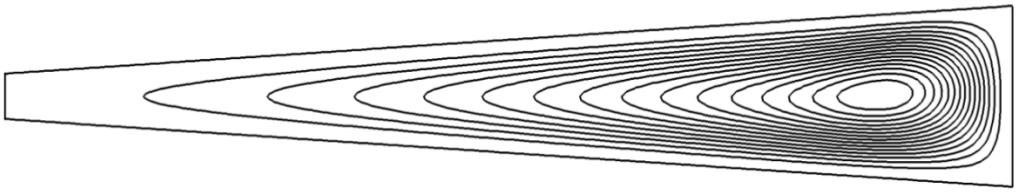

(d) $A = 10, \eta = 4$

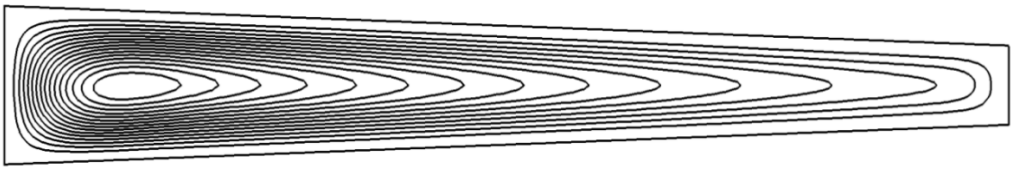

(e) $A = 10, \eta = 0.5$

Figure 7.4: Streamlines at Ra=100.

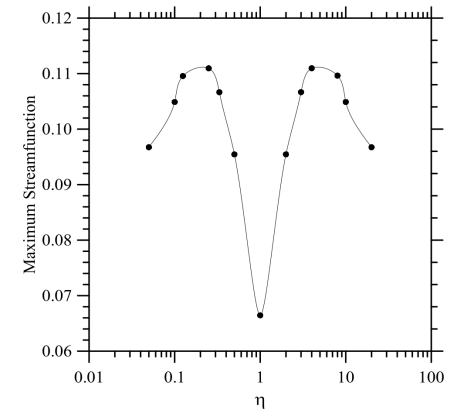

(a) Maximum streamfunction: $A = 4$.

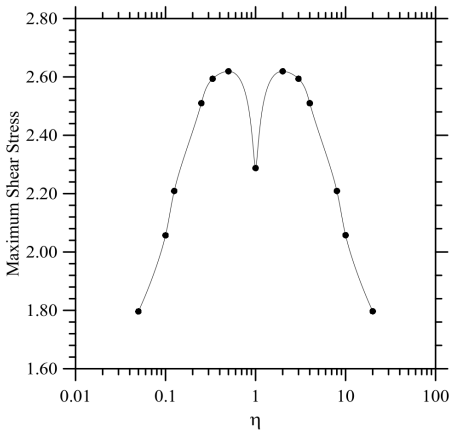

(b) Maximum shear stress: $A = 4$.

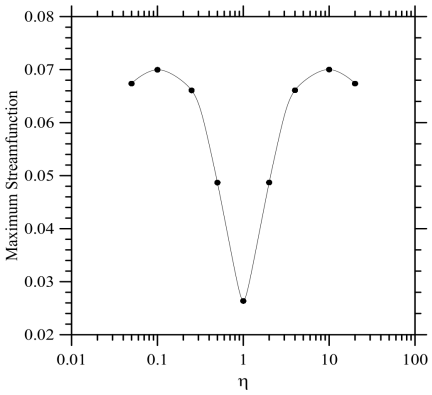

(c) Maximum stream function: $A = 10$.

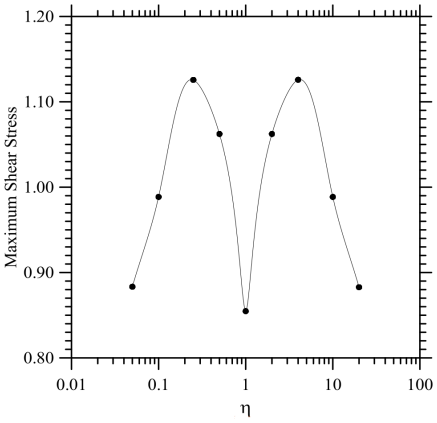

(d) Maximum shear stress: $A = 10$.

Figure 7.5: Maximum values of the stream function and shear stress as function of η for $Ra = 100$.

Figure 7.5 shed some additional light on the problem considered illustrating the non-trivial dependence of the flow strength (in terms of maximum value attained by the stream function) and the (maximum) shear stress ($\frac{\partial u}{\partial y}$ where u is the horizontal component of velocity and y the vertical coordinate) on the parameter η. As shown in such figure, both the stream function and the non-dimensional shear stress attain a minimum when the walls are perfectly horizontal, i.e. for $\eta = 1$. This case has been already extensively investigated in the literature (the reader being referred, e.g., to the excellent numerical study by Gelfgat et al., 1999 [102]). Any departure from this ideal condition, however, causes an increase in the shear stress and ψ. The related dependence is relatively complex (non-monotone) as witnessed by the existence of two relative maxima. These can be seen in th e shear stress curve for $\eta = 0.5$ and $\eta = 2$ for $A = 4$ and $\eta = 0.25$ and$\eta = 4$ for$A = 10$. Similarly, for the stream function the maxima are located at $\eta = 0.25$ and $\eta = 4$ for $A = 4$ and $\eta = 0.1$ and $\eta = 10$ for $A = 10$. Both

quantities display a symmetric distribution with respect to the situation of horizontal top and bottom walls (the plots in logarithmic scale are mirror symmetric with respect to $\eta = 1$).

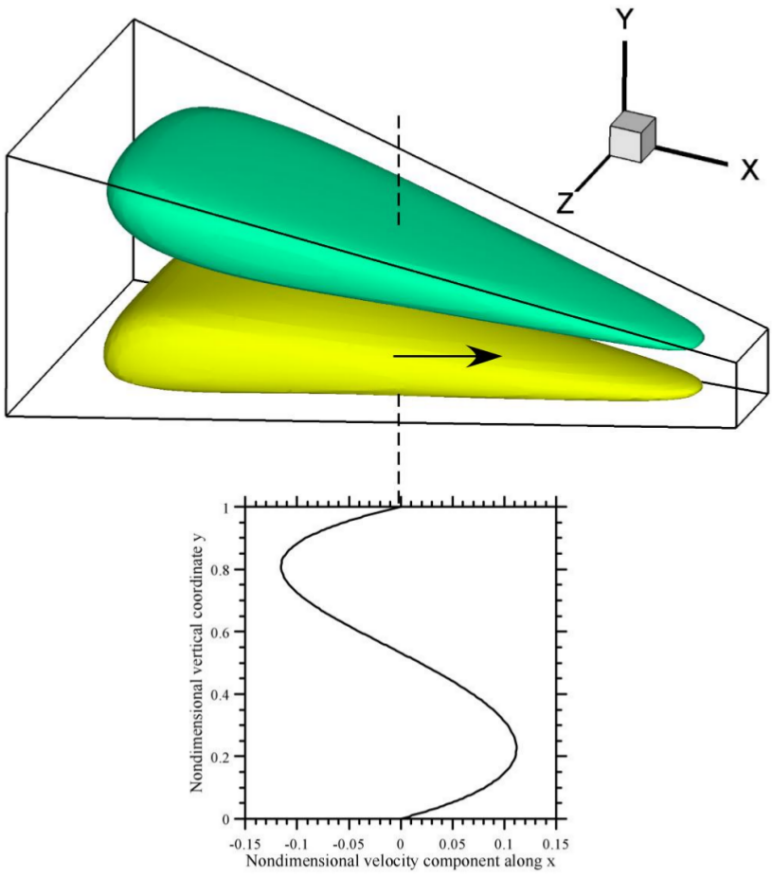

Figure 7.6: Iso-surfaces of the velocity field for:$A = 4$, $Ra = 100$ and $\eta = \frac{1}{16}$ (3D simulation for a container having the shape of a frustum of pyramid, $N_x x N_y x N_z = 100x30x30$) , maximum shear $\frac{\partial u}{\partial y} = 1.3$. Lower plot: u velocity profile at $x = \frac{A}{2}$ and $z = \frac{1}{2}$.

Figure 7.3 provides some information about the existence of "inflection points" in the velocity profile. Such points are known to play a crucial role in determining the "future" behaviour of the system when the intensity of the driving force is increased. For purely parallel flow, indeed, it is known that in the limit as $Pr \to 0$ the following (Rayleigh's) theorem holds: In a shear flow a necessary condition for instability is that there must be a point of inflection in the velocity profile $u = u(y)$, i.e. a point where $\frac{\partial^2 u}{\partial y^2}$. As illustrated by Tollmien (1936) [103], this theorem can be regarded as also a sufficient condition in many situations. For more comprehensive discussions the interested readers may consider Lin (1944) [104], Rosenbluth and Simon (1964)[105],

Drazin and Howard (1966)[106]. According to Figure 7.3, though in our case the flow is not parallel, inflection points in the profile of horizontal velocity u can be still identified. Similar conclusions can be applied to fully three-dimensional (3D) configurations having a frustum-of-pyramid shape (for which we performed a limited set of simulations using yet eq. 7.7 as initial condition, the parameter η appearing there, being this time the ratio between the areas of the two end walls). Such results, shown, e.g., in Figure 7.6 for the case $A = 4$ and $\eta = 1/16$, confirm that, though the maximum of the shear stress $\frac{\partial u}{\partial y}$ experiences a decrease with respect to the corresponding 2D case ($\frac{\partial u}{\partial y} \cong 1.3$ for the 3D case to be compared with $\frac{\partial U}{\partial y} \cong 1.84$ for the 2D case having the same value of η), the existence of inflection points in the distribution of horizontal velocity u is retained. Furthermore, inflection points can be also found in the profile of the other horizontal velocity component pertaining to the 3D simulations, namely the component w along the z axis (Fig.7.7).

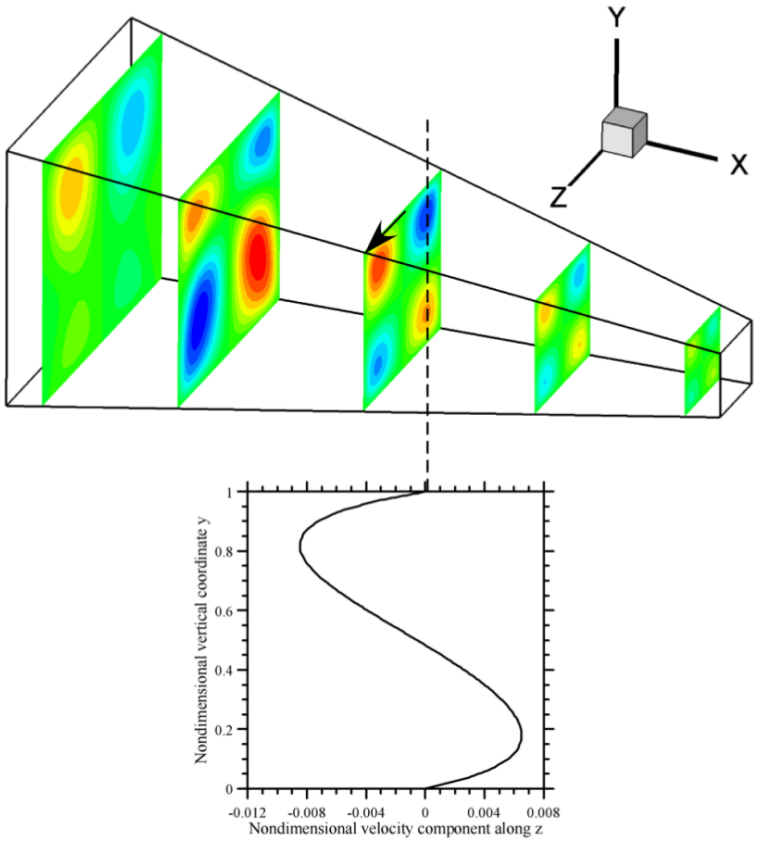

Figure 7.7: Slices of the w velocity component (along z) for $A = 4$, $Ra = 100$ and $\eta = \frac{1}{16}$ (3D simulation for a container having the shape of a frustum of pyramid, $N_x x N_y x N_z = 100x30x30$). Lower plot w velocity profile at $x = \frac{A}{2}$ and $z = \frac{1}{4}$.

Given the very small value of the Prandtl number considered ($Pr = 0.01$), the

simple observations above give rise to the important question to understand whether such 2D or 3D flows could become unstable against the onset of disturbances of hydrodynamic nature. Such instabilities, in the past studies essentially for parallel flows or flows in rectangular cavities with finite extent, are known to be driven by t he mean shear stress (this is the reason why they are often referred to as "shear instability" and the related disturbances as hydrodynamic ones). As a result, some vortices appear on the frontier of the two opposing (primary and return) horizontal currents characterizing the basic flow. Such disturbances are in general stationary (the general outcome of this instability is the replacement of the initial "unicellular" Hadley flow with a multicellular convective structure) and become oscillatory when a second threshold in terms of applied temperature gradient is exceeded (Gelfgat et al., 1999 [102]; Kaddeche et al., 2003 [81]).

7.2.1 Conclusions

The typical structure of the Hadley flow in containers having varying cross -sectional area in the case of liquid metals has been investigated on the basis of a hybrid approach based on the numerical solution of the Navier-Stokes equations in conjunction with analytic solutions of the temperature field (used as initial conditions). The analysis has provided theretofore unseen information about the role played by converging or diverging walls on the fundamental properties of the emerging flow in terms of strength, patterning behaviour and the existence of "inflection" points in the velocity profile. The existence of such points and the non-trivial dependence displayed by the intensity of the flow and the related shear stress on the geometry characteristic parameters call for an analysis specifically conceived to address the potential onset of disturbances of hydrodynamic nature at larger values of the control parameter Ra. Such disturbances are expected to break the typical initial uni-cellular flow via stationary or oscillatory bifurcations and produce significant asymmetries in the dependence of the maximum shear stress and stream function on the compression (or expansion) ratio.

7.3 Two-dimensional oscillatory instabilities

The interesting results of the previous section encourage to further deepen this subject considering the same geometries at higher values of the Rayleigh number. However,

before embarking in a full description os such instabilities it is worth discussing the minimum mesh size as the Rayleigh number is increased respect to the previous section.

7.3.1 Mesh independence and validation study

The mesh used to solve the problem has been generated using the "blockmesh" utility available in the standard OpenFoam platform. A grid tailoring preliminary analysis for structured grids has been performed towards the end of evaluating (quantitatively) the benefits produced by progressive grid refinement. On the basis of such a study, in particular, we decided to use different meshes according to the aspect ratio (the outcomes of such a preliminary investigation being summarized in Table 7.1.

As shown in the first part of Table I, for $A = 4$ the minimum mesh required to guarantee independence of the velocity field (and its oscillation frequency) from the used spatial resolution has been found to be 200 points and 50 points along the horizontal and vertical directions, respectively (by doubling the mesh resolution, the change experienced by the disturbance angular frequency is less than 2%).

These results confirm the expectation that, as in the case of liquid metals and moderate values of the Rayleigh number no thermal boundary layers are formed in proximity to the heated and cooled walls, a uniform mesh (fixed space step along the horizontal direction) can adequately capture the dynamic of interest.

For $A = 10$, however, the grid refinement assessment has clearly evidenced the need for a denser mesh. Accordingly, we increased the mesh resolution to 400 x 50. As shown in Table 7.1, for this value of the aspect ratio and with such a grid, the percentage variations experienced by the angular frequency of the emerging oscillatory disturbances (when the mesh density is doubled) are of the order of 3% even if the worst conditions are considered ($\eta = 0.1$ and the highest value of Ra examined in the present study).

The numerical method described in chapter 6 was validated through comparison with available results in the literature (Gelfgat et al. [102]) (see Table 7.2).

As a fundamental part of the general process summarized above, we also deemed it necessary to evaluate separately the role played by the "nature" of the specific numerical "scheme" used to treat the convective terms. Indeed, we could verify that in the delicate process leading a time-marching numerical process to capture a fluid-dynamic instability, the "accuracy" of the scheme (being first order, second order, or third order accurate) should not be regarded as an "absolute" parameter or the sole factor

determining the success of the used approach. This is an aspect specifically relevant to the case of hydrodynamic disturbances for which it is generally known that "multiple solutions" can exist for a fixed set of parameters (namely, the same geometry and the same value of the Rayleigh number, Gelfgat et al. [102]). Accordingly, in our research we had to sift through existing studies with different foci in order to get indications and elaborate inferences about what factors may increase the probability of success in such a quest.

It is a general consensus that the ability of the algorithm to capture one state or other states depends essentially on the specific initial conditions used for the simulation (Gelfgat, 2017, private communication). This means that different initial conditions should ideally lead to different states (if such alternate states effectively "coexist" in some regions of the space of parameters, Crespo del Arco et al. [107], Pulicani et al. [108] and Okada and Ozoe [109]). As an example in the work of Gelfgat et al. [102] this philosophy was found to be highly effective in allowing their numerical approach to capture different coexisting solutions. In the present study, we could verify that the emerging hydrodynamic modes can even be sensitive to the specific numerical scheme used to discretise the convective terms in the balance equations. In other words, apart from varying the initial conditions, the use of different schemes can also be instrumental in re-directing the CFD (Computational Fluid Dynamics) process towards a different state or solution. We will provide some additional information along these lines in the next section where we will discuss in detail the main outcomes of the present work. Here we limit ourselves just to mentioning that this is the reason why Table 7.1 about the grid independence analysis contains duplicated data about different cases simulated with three different types of numerical schemes (just to demonstrate our "judicious" use of different computational schemes). As we shall further discuss in the next section, we conducted most of the simulations using both central difference (of the Lax-Wendroff family) schemes and upwind-family schemes (Quadratic Upstream Interpolation for Convective Kinematics, i.e. QUICK, Van Leer, and related variants, the reader being referred to the work of Moukalled et al. [110] for the related implementation in OpenFoam). Table 7.1 clearly proves the intended outcome of such an assessment, i.e., the ability of the algorithm to converge towards a mesh-independent solution (as the mesh density is increased) is retained when central differences are replaced with the QUICK or the Van Leer scheme. It also shows that the percentage difference between

the results obtained with different schemes lies below 1% even if the worst conditions are considered in terms of Rayleigh number (namely, the highest value of Ra, i.e., 9000). Though in majority of the cases we found that different schemes give exactly the same results, we could detect differences in the emerging oscillatory behaviour in a few circumstances. Together with a variation of the initial conditions, such an approach allowed us to "detect" effectively the existence of multiple states, which is known to be a general feature of this kind of flow.

				$A = 4$		
η	Ra	Parameter	Mesh 200x50	Mesh 400x100	Variation %	Scheme
0.1	5000	ω	1.944	1.906	1.99	Central difference 2nd order
				$A = 10$		
η	Ra	Parameter	Mesh 400x50	Mesh 800x100	Variation %	Scheme
0.1	9000	ω	0.2666	0.2761	3.04%	Central difference 2nd order
				$A = 4$		
η	Ra	Parameter	Mesh 200x50	Mesh 400x100	Variation %	Scheme
0.5	9000	ψ_{max}	2.717	2.766	1.77	Central difference (2nd order)
0.5	9000	ψ_{max}	2.772	2.793	0.75	QUICK (3rd order)
0.5	9000	ψ_{max}	2.657	2.741	3.06	Van Leer (2nd order)

Table 7.1: Grid refinement study: maximum value of the stream function or angular frequency ω of measured velocity oscillations as function of mesh resolution for different values of the aspect ratio A, compression ratio η and Rayleigh number at $Pr = 0.01$.

Ra	Angular frequency	Value	Code
22170	ω	17.002	Gelfgat et al. (1999) [102]
23000	ω	16.983	Present

Table 7.2: Code validation study: comparison with the results by Gelfgat et al. [102] for $A = 4$ and $Pr = 0.015$ (present result obtained using a mesh 200x50).

7.3.2 Results

We concentrate on three specific values of the aspect ratio A, namely, $A = 4$ (already extensively considered in past studies on the subject due to its relevance to typical industrial techniques for crystal growth), $A = 10$ and $A = 20$ to study the system response in the limit as $A \to \infty$ (the case of the core flow ideally not disturbed by end walls). Though a discrete set of values for the aspect ratio is selected, the corresponding compression (or expansion) ratio is allowed to span a relatively large interval (namely, $0.1 \leq \eta \leq 10$). The system control parameter, i.e., the Rayleigh number is varied in the range $O(10^3) \leq Ra \leq O(10^4)$ with progressive (finite) steps of 500 in order to assess the evolution of the system from simple steady or weakly oscillatory states up

to more complex (multi-frequency and multi-disturbance) situations. By probing the system response for fixed increments in the value of the Rayleigh number, a "grid" of cases is built (and simulated) with the express intention to define a "map" of possible spatio-temporal states in the space of parameters.

The zoo of 2D modes

No definition is perfect, and it is hard to distillate a definition from an observation, but the following categorization captures the essential aspects of the phenomena revealed by the present numerical simulations:

1. unicellular steady states (US);
2. multi-roll steady states (MS);
3. quasi-stationary states with weakly oscillating rolls (QS);
4. "classical" oscillatory rolls (with slender "appendages" undergoing a kind of rhythmic displacement) (P);
5. states with periodically touch- ing or "kissing" rolls (K);
6. regimes with periodically coalescing rolls (C);
7. purely travelling waves (TWs);
8. mixed states (PLT) with travelling waves "locally" modulated by roll pulsations or splitting behaviours.

Given the complexity of the subject, it is instructive (and "convenient" at the same time) to start from a "canonical case", namely, the cavity with perfectly horizontal bottom and top walls. Indeed, this may be regarded as the most natural way to create a link between the present study and valuable earlier efforts in the literature (where the analysis of the nature and structure of hydrodynamic disturbances was limited to the case of purely rectangular cavities).
As already outlined in the previous section, a notable known feature of these modes is their intrinsic ability to switch from one pattern to another for even minute changes in the value of the Rayleigh number or initial conditions. These aspects were originally revealed, e.g., in the landmark studies by Crespo del Arco et al.[15], Pulicani et al.

[108], Okada and Ozoe [109] and Gelfgat et al. [102], where hydrodynamic modes were found to display a variety of potential behaviours, including the emergence of multi-roll states, transitions from steady to time-periodic solutions, coalescence of multiple states, and backward transitions from multi-roll to unicellular regimes. The most interesting of such features was, perhaps, the "multiplicity" of possible solutions, that is, the existence of distinct branches of the flow for specific values of the aspect ratio (unlike the bifurcation to the transverse-roll flow in the infinite fluid layer, the roll-type structure of the convective flow in finite cavities can undergo a continuous variation of the flow pattern). In general, Gelfgat et al. [102] found the dependence of the flow on the aspect ratio and the Rayleigh number to be very complex.

Cavity $A = 4$

Without loss of generality, a first example of such dynamics for the present conditions (we consider $Pr = 0.01$) can be seen in Figure **??**, where the pattern emerging from purely diffusive (quiescent) conditions in an enclosure with $A = 4$ and $\eta = 1$ is shown for two different values of the Rayleigh number.

According to our simulations starting from thermally diffusive conditions, for a relatively low Rayleigh number, i.e.,$Ra = 10^3$, the flow is simply given by a "twisted" recirculation embracing three co-rotating (anticlockwise in the figures) rolls; when the Rayleigh number is increased, however, a double-vortex configuration also becomes a possible solution of the problem; these flows are both steady and centrally symmetric (namely, the pattern does not change with respect to rotation through 180 °C about the centre of the cavity).

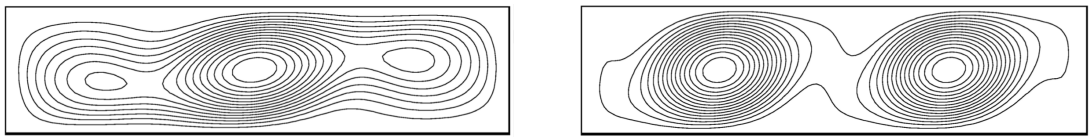

(a) $A = 4$, $\eta = 1$, $Ra = 1000$ (b) $A = 4$, $\eta = 1$, $Ra = 2000$

Figure 7.8: Multiple states in steady convection: cold and hot sides on the left and on the right respectively.

The patterning behaviour as a function of the Rayleigh number can be also tracked by using the synthetic information that we have summarized in Figure 7.8. By taking a look at these maps (solutions have been reported there as a function of Ra and arranged accordingly as "columns", whereas "rows" correspond to variations in the

value of η), the reader will immediately realize that at $\eta = 1$ a further increase in the Rayleigh number makes the aforementioned two-roll solution essentially oscillatory (as witnessed by the related finite values of the disturbance angular frequency).

As also reported in earlier numerical studies on this subject for the specific case of rectangular cavities, these oscillatory disturbances appear as morphological variations affecting periodically the shape of the peripheral streamlines of each roll (as shortly mentioned before, the oscillatory distortions may be thought of as resembling the rhythmic displacement displayed by the cilia or flagella of bacteria or other microorganisms, (P)-mode). A clear example of such a behaviour is shown in Figure 7.10 for Ra = 9000. Additional useful information on such a case can be gathered from Figure 7.11. When the threshold for the onset of time-dependence is exceeded ($Ra > 5000$) and the angular frequency of the disturbance increases as a function of the Rayleigh number, the related growth law scales approximately as $(Ra - 5.4 * 10^3)^{\frac{1}{2}}$ (see the P(2) curve in Figure 7.11).

According to the simulations, however, a departure of the expansion (or compression) ratio from the unit value can produce dramatic changes in the dynamics, which deserve a separate and exhaustive discussion.

In order to describe such results, conveniently, we start from two representative values of η for which the system behaviour is relatively simple, namely, the geometry with $\eta = 0.5$ and the "mirror" configuration with $\eta = 2$. As a first distinguishing mark with respect to the case $\eta = 1$, by taking a look at Figure 7.9, the reader will immediately realize that for such cases the flow structure is not centre-symmetric. Indeed, this kind of symmetry is no longer a property of the physical domain and, as a natural consequence, it cannot be inherited by the related pattern. The most striking finding emerging from the analysis of these simulations,however, is the strong stabilization experienced by convection in the considered range of Rayleigh numbers (the P(2) branch visible in Figure 7.9 for $\eta = 1$ is taken over by a branch of steady states for $\eta = 0.5$).

Though no onset of oscillations occurs for the range of Rayleigh numbers visible in Figure 7.9, some interesting phenomena when the driving force is increased can still be observed: the initial flow with two rolls (m = 2) visible for $Ra = 1000$ (similar to that seen in Figure 7.8b) is taken over by a three-roll structure when the Rayleigh number is increased to $Ra = 2000$. This new state seems to be rather stable, as we could not detect any change in the number of rolls (or transition to oscillatory state) for Ra up to

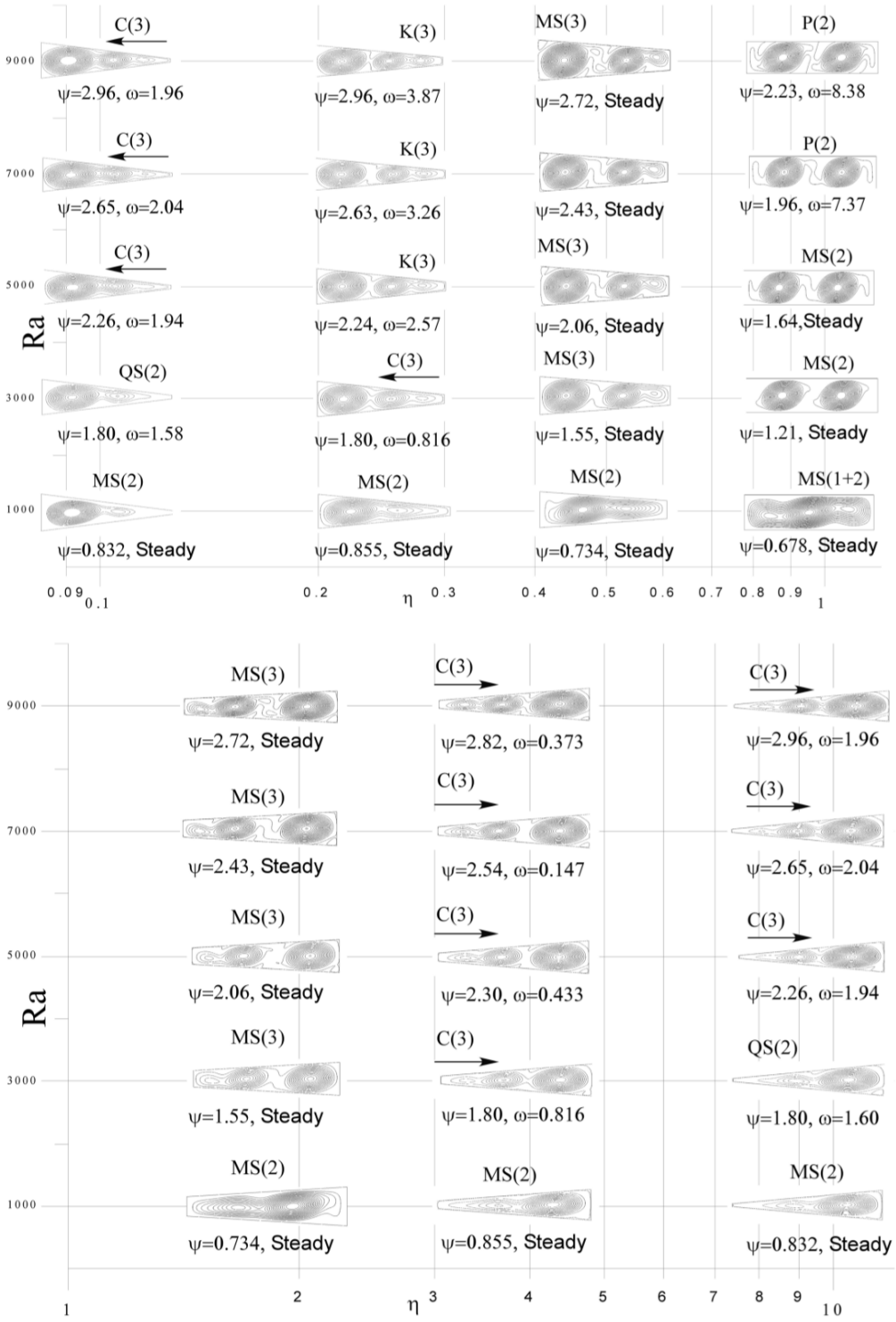

Figure 7.9: Map of the various states found for $A = 4$ at different values of the compression ratio η and Rayleigh number.ψ is the maximum value of the stream function while ω is the frequency when the flow is oscillatory.

16000()[we had to increase Ra a to 16500 in order to find the P(2) oscillatory flow, with an angular frequency 8.82). Most notably, the behaviour observed for $\eta = 0.5$ is the "mirror image" of that for $\eta = 2$. In fact, as shown in Figure 7.9, the related patterns are "identical" in terms of number of rolls and related morphological properties: as an

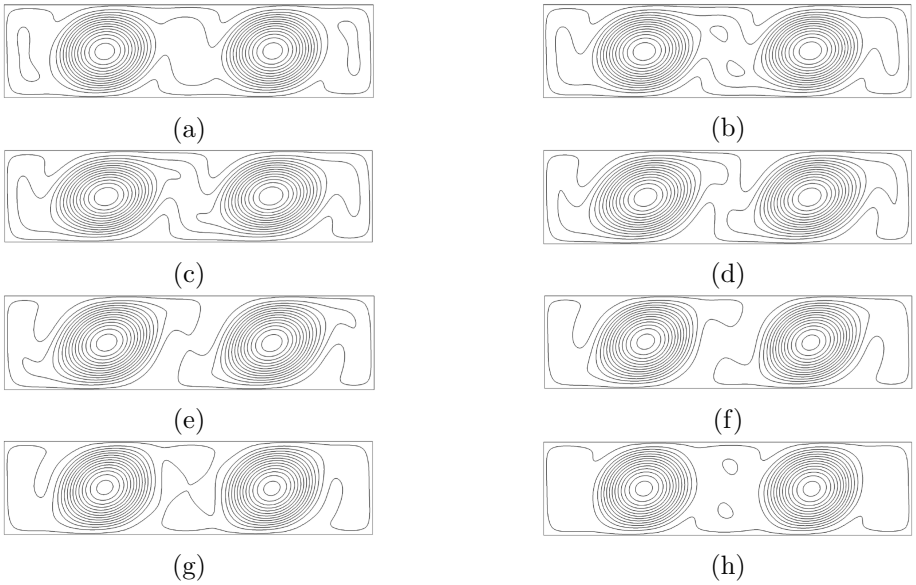

Figure 7.10: Eight snapshots evenly distributed along the period. $A = 4$, $Ra = 9000$,$\eta = 1$

example, all the flow configurations for $\eta = 0.5$ could formally be turned into those obtained for the same value of the Rayleigh number for $\eta = 2$ by simply applying a rotation of 180 °.By replacing the hot side with the cold side, indeed such a rotation turns the initial problem with $\eta < 1$ and gravity directed downwards (where the fluid raises in proximity to the side wall of a smaller size, namely, the hot wall located on the right of the figure) into a completely equivalent problem for $\eta > 1$ in which gravity is directed upwards and the fluid raises in proximity to the cold side (the cold side being located on the right side after the 180 °rotation).Hereafter, we will refer to this property of the velocity field for η , 1 as the "180 ° rotation invariance principle after η reversal" ,which from a purely mathematical point of view would be equivalent to the following transformation (the tilde being used to indicate the transformed quantities):

$$\begin{bmatrix} \tilde{u} \\ \tilde{v} \end{bmatrix}_{\eta} = \underline{\underline{R}}(180°) \begin{bmatrix} u \\ v \end{bmatrix}_{\frac{1}{\eta}} \tag{7.9}$$

with the rotation matrix defined as:

$$\underline{\underline{R}}(\theta) = \begin{bmatrix} cos\theta & sin\theta \\ -sin\theta & cos\theta \end{bmatrix} \tag{7.10}$$

Notably, however, the same transformation would not work for the temperature field,

i.e.,

$$T\left(\tilde{x},\tilde{y}\right)_{\eta} \neq T\left(x,y\right)_{\frac{1}{\eta}} \tag{7.11}$$

(we will explore other theoretical extensions which attach to the above arguments later in this work). We observed that the response of the system is similar to that just described for $\eta = 0.5$ and $\eta = 2$ in a given neighbourhood of these values of η (the system experiencing strong stabilization for $0.4 \leq \eta < 0.75$ and $1.33 < \eta \leq 2.5$). As shown in Figure 7.9, however, for $\eta = 0.75$ ($\eta = 1.33$) oscillations of the P type are again possible for $Ra \geq 7000$. This behaviour also occurs at $\eta = 0.65$ ($\eta \approx 1.5$) provided the Rayleigh number is increased to $Ra \geq 9000$.

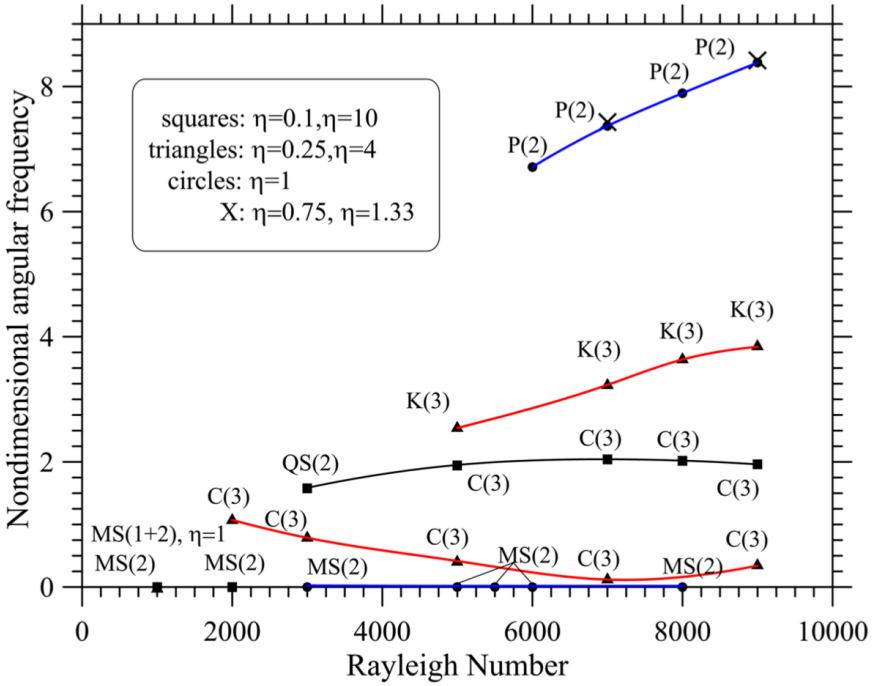

Figure 7.11: Angular frequency as function of Rayleigh number for $A = 4$ and different values of the compression ratio η

Nevertheless, further departure of η from these conditions (i.e., η smaller than 0.4 or larger than 2.5) makes the flow again sensitive to the onset and amplification of oscillatory disturbances for moderate values of the Rayleigh number. This can be seen again in Figure 7.9: for both $\eta < 0.4$ and $\eta > 2.5$, we identified transition to time-dependence for relatively small values of Ra (the corresponding angular frequency values can be found directly in this figure; hereafter, we will limit ourselves just to discussing the results for $\eta < 1$, those for $\eta > 1$ being related to the former by the above mentioned invariance principle).

As an example, in a limited neighbourhood of $\eta = 0.25(0.2 \leq \eta \leq 0.3)$, initially steady flows with $m = 2$ for $Ra = 1000$ are quickly taken over by oscillatory states for $Ra \geq 2000$. The related frequencies are generally smaller than those pertaining to states of the P type (see again Figure 7.11). An interpretation of these cases, however, is not as straightforward as one would imagine. Indeed, in this range of η, initially we found the variation of angular frequency with Ra (shown in Figure 7.11, e.g., for $\eta = 0.25$) to follow a non-trivial path potentially hiding different mechanisms.

Keeping fixed the initial conditions (corresponding to a quiescent and thermally diffusive state as explained in the previous section) and the numerical scheme used for the treatment of the convective terms (central differences) as we did for the solutions shown in Figure 7.8, we noticed for $0.2 \leq \eta \leq 0.3$ sudden changes in the typical spatio-temporal behaviour displayed by the emerging solutions at different values of the Rayleigh number, which might be the typical "signature" of multiple states coexisting in the considered sub-region of the space of parameters.

The "non-progressive" nature of these modes of convection in the space of parameters (the solution jumping from one regime to another in an apparently illogical way when changing the Rayleigh number or η) led us to address the question of understanding whether such apparent "discontinuities" in the system response might be a consequence of the well-known property of the Hadley flow in liquid metals to support multiple states of convection. In this range of values of η $(0.2 \leq \eta \leq 0.3)$ and for $Ra \geq 3000$, in particular, we identified two different kinds of solutions alternating in the space of parameters, namely, states pertaining to the (K) or (C) regime.

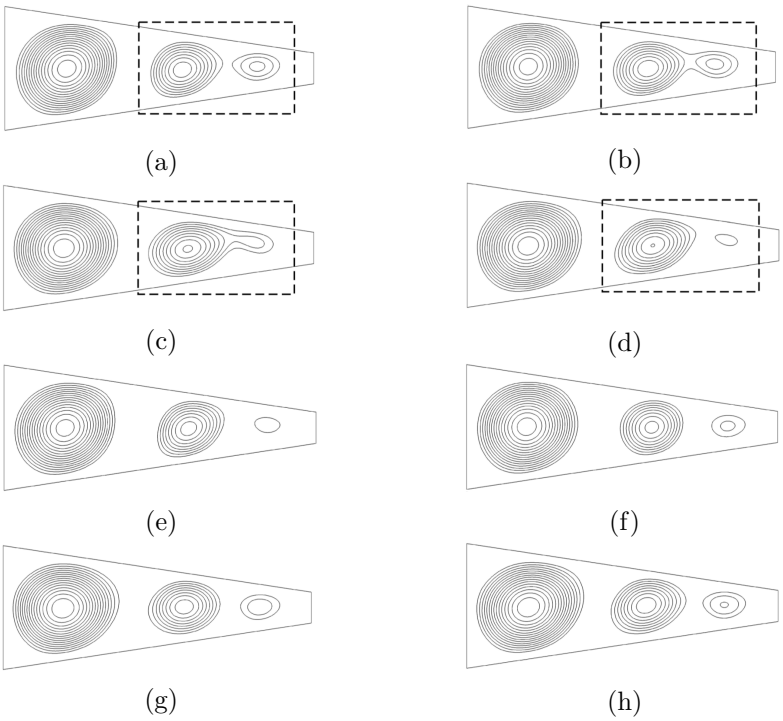

Figure 7.12: Eight snapshots evenly distributed along the period. $A = 4$, $Ra = 9000$, $\eta = 0.25$.

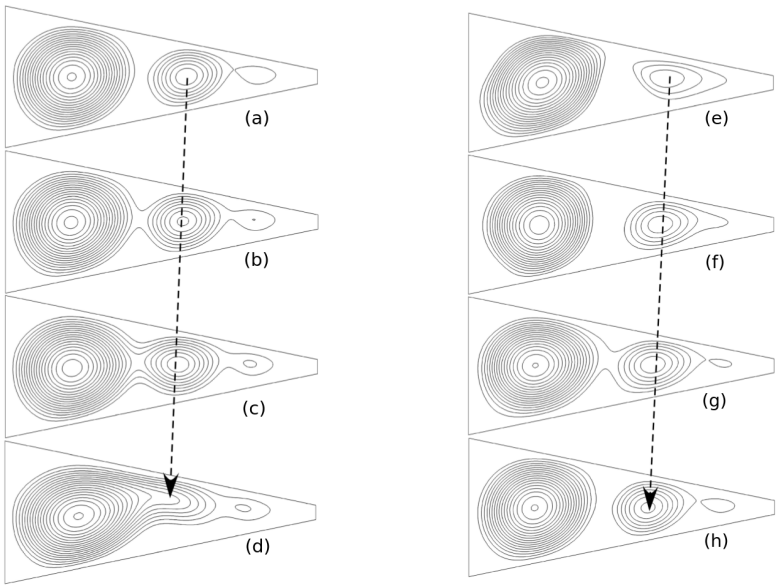

Figure 7.13: Eight snapshots evenly distributed along the period. $A = 4$, $Ra = 9000$, $\eta = 0.1$.

Examples of such states are shown in Figures 7.12 and 7.13. Though for both cases, the related flow is characterized by the presence of three rolls, the typical features displayed by the emerging oscillatory flow, however, are rather different. In the following,

in particular, first we describe the (K) states (which have been occasionally observed also in past studies dealing with classical rectangular cavities) and then concentrate on the (C) regime, which seems to be specific to geometries with $\eta \neq 1$. In the first case, two of the tree rolls which are present at the same time in the cavity (the roll in the centre and the roll located in proximity to the right wall) undergo a weakly oscillatory process in which one roll touches periodically its neighbour ("kissing" rolls behaviour, which explains why we used a "K" letter to label it). As shown, e.g., by the simulations for $\eta = 0.25$ and $Ra = 9000$, when the two rolls meet, a single circulation (encapsulating the two initially distinct rolls) is temporarily established in the right part of the cavity (while a single roll remains steadily located in proximity to the left(cold) wall). When solutions pertaining to the (C) regime emerge, however, the spatio-temporal behaviour is completely different. According to the simulations, indeed, the above dynamics with the two (central and right) distinct periodically touching rolls are replaced by a much more evident coalescence phenomenon. This process takes place essentially in the left part of the cavity as a result of the displacement of the roll initially located in the centre of the cavity towards the left.

When the central and left rolls merge completely, a new roll nucleates on the right side thereby making the entire process an endless phenomenon (remarkably, this also gives the observer the feeling of a disturbance continuously spreading from the right side to the left side, i.e., in a direction opposite to the temperature gradient). We could observe exactly the same mechanisms for $\eta \geq 3.3$. However, in this range of η, we found that the disturbance propagates from the left side to the right side, i.e., in the same direction as that of the applied temperature difference (we will come back to this apparently innocuous observation later).

We observed that this alternate mode of convection (with a disturbance spreading from regions of reduced cross-sectional area towards regions where the area is larger) becomes the preferred mode of oscillatory instability in the end regions of the considered interval of η (namely, when η is very small or very large, see, e.g., Figure 7.13 for $\eta = 0.1$). As a clear distinguishing mark of this waveform with respect to the (K) regime, its frequency also displays a relatively weak dependence on the Rayleigh number (the reader being referred again to Figure 7.11).

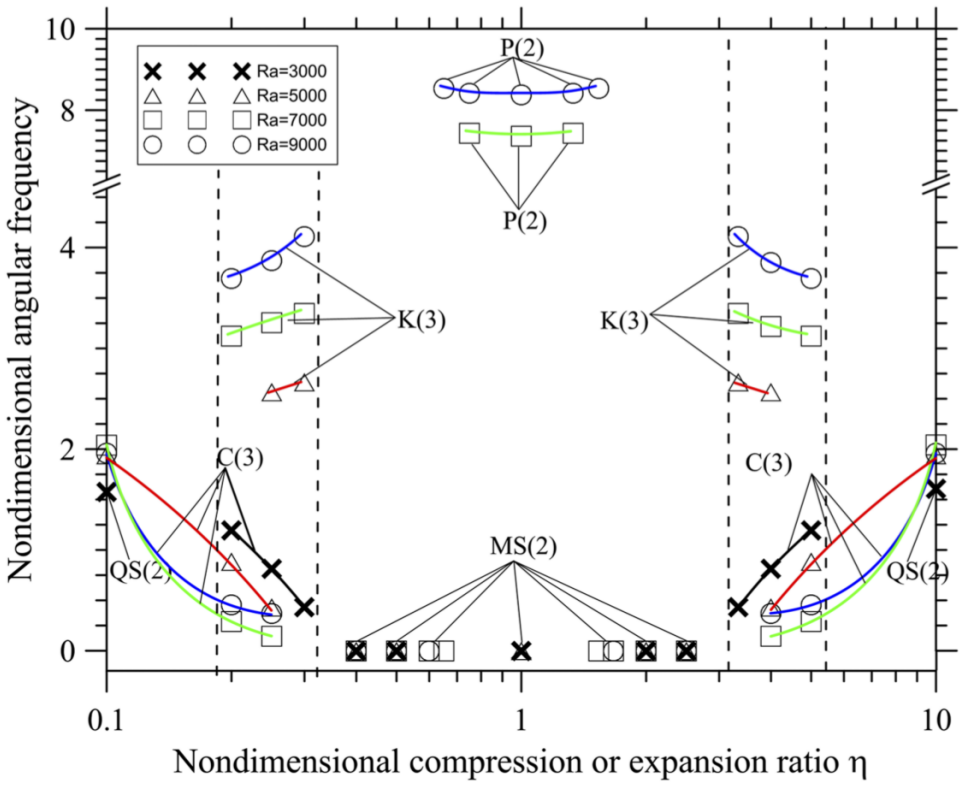

Figure 7.14: Angular frequency as function of expansion or compression ratio η for $A = 4$ and different values of the Rayleigh number.

As mentioned before, we identified both modes of convection ((K) and (C)) in the range $0.2 \leq \eta \leq 0.3$ (delimited by the vertical dashed lines in Figure 7.14) with no apparent progression or connection between the two states (this leading to an apparently scattered set of frequency points in this interval).

Though this counterintuitive behaviour initially resisted our attempts to clarify the underlying dynamics (due to its disorganized appearance in the space of parameters), the strategy discussed previously was instrumental in leading us to the conclusion that these two modes of convection are both possible solutions to the problem. In order to do so, we performed several numerical simulations for fixed couples (η, Ra) by changing the initial conditions (i.e., starting from a uniform temperature distribution or using the solution obtained at a given value of the Rayleigh number as the initial condition for other values of Ra) and/or applying the other "principle" defined in the previous section, namely, the use of a different category of schemes for the convective term in the energy and momentum equations. As an example, by replacing the central difference scheme with a scheme of the upwind family (the Van Leer), we successfully observed the (K) states found for $\eta = 0.25$ to transform into spatially spreading (C) modes.

This peculiar approach was instrumental in turning our initial conjecture about the existence of multiple states of convection into reality. Among other things, it also allowed us to "reconstruct" the clearly recognizable continuous different branches reported in Figure 7.11 for $\eta = 0.25$.

Some additional illuminating insights into the above scenario can be obtained by taking a look at the ensemble picture provided by Figure 7.14 where the angular frequency has been reported as a function of parameter η for different (fixed) values of the Rayleigh number.

This figure clearly shows the existence of multiple solutions with their different frequency and convective modes in selected sub-intervals of η (delimited by vertical dashed lines in this figure); outside these intervals, the just discussed strategy based on the use of different initial conditions and spatial integration schemes did not produce any notable change in the emerging solutions.

Leaving aside for a while the existence of multiple states and their influence on the considered problem, other remarkable or notable features of this plot can be summarized as follows: it makes particularly evident the difference in the dynamics occurring in a given neighbourhood of $\eta = 1$ and those occurring in the two external regions ($\eta \leq 0.3$ and $\eta \geq 1.33$). In such regions, time-dependence sets in for much smaller values of the Rayleigh number; moreover, for a fixed value of Ra, the frequencies are relatively smaller than those obtained in the inner region. Superimposed on such observations is the fact that while for η in the central region the dynamics are rather similar to those already known for rectangular cavities, in the two "external" right and left intervals some heretofore unseen mechanisms become possible (i.e., the (C) mode with the spatially spreading disturbance).

The regions supporting different spatio-temporal behaviours are separated by conditions of a stable flow (for $0.3 < \eta < 0.65$, $1.5 < \eta < 3.33$, and $Ra < 7000$), which further supports the idea that a substantial change occurs in the fundamental mechanisms driving an oscillatory flow when such bounds are crossed. While in the internal region modes of the P type seem to be the preferential mechanism of the oscillatory flow, the external regions are dominated by (C) modes (though (K) solutions are possible as well in some intervals). As shown in Figure 7.14, the region of existence of (P) modes increases with Ra. Vice-versa the size of the η intervals in which (C) disturbances are possible seems to expand when Ra becomes smaller (we will come back to

this interesting finding in the next paragraph, discussing the simulations with $A = 10$).

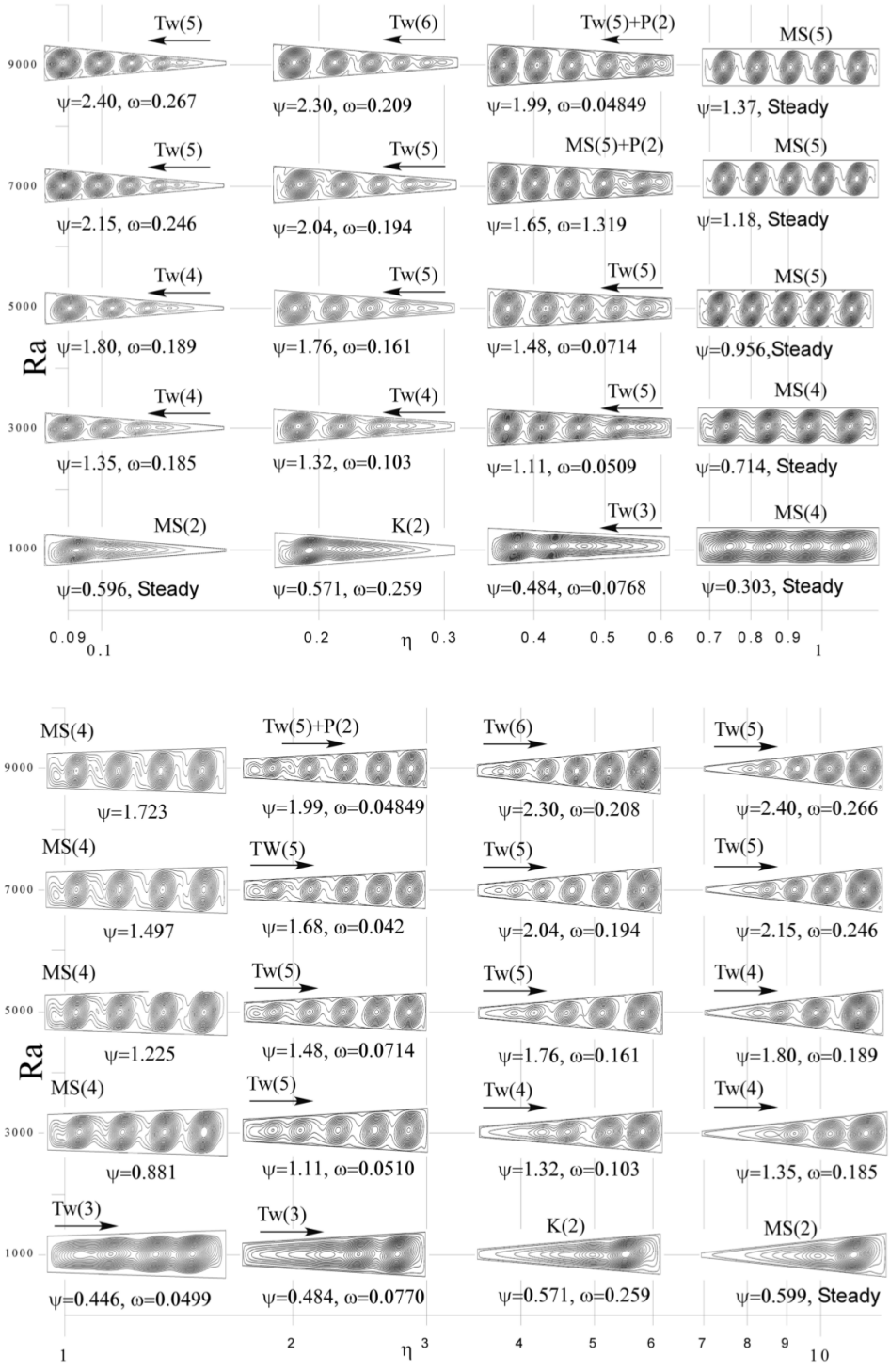

Figure 7.15: Map of the various states found for $A = 10$ at different values of the compression ratio η and Rayleigh number.ψ is the maximum value of the stream function while ω is the frequency when the flow is oscillatory.

As a concluding remark for this section, we limit ourselves to mentioning that at the highest values of the Rayleigh number considered (namely, $Ra \geq 7000$), we could find in some cases ($\eta = 0.2$ and $\eta = 5$) modes of the (K) and (C) types to coexist in the same numerical solutions (mixed states), as witnessed by the presence of two distinct frequencies clearly recognizable in the frequency spectrum for such cases.

Cavity $A = 10$

This section is devoted to examining another important aspect embedded in the considered problem, namely, its dependence on the aspect ratio.
By concentrating on a relatively high value of the aspect ratio (that is $A = 10$), we could obtain some additional interesting insights into the properties of the emerging convective modes, especially for the case of spatially travelling disturbances. Indeed, we found that such a perturbation becomes the dominant (or preferential) mode of oscillatory convection through the entire range of Rayleigh numbers and values of $\eta \neq 1$ considered, with some interesting "variants" or mixed states emerging for specific couples (η, Ra). Along these lines, in the present section we change completely the approach with respect to the previous paragraph related to the case $A = 4$ and expressly initiate the description of the observed dynamics from the ends of the interval of η rather than from its center.
The related evolution as a function of Ra can be gathered from Figures 7.15 and 7.16 (these figures give information on the patterning behaviour and frequency dependence on Ra, respectively).

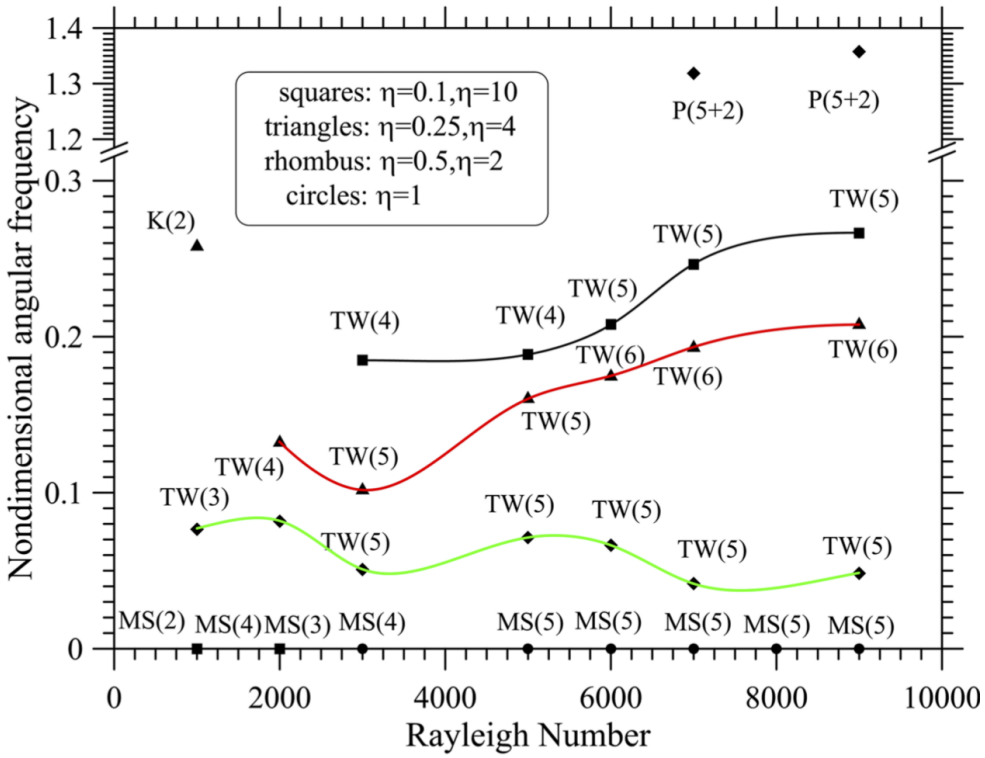

Figure 7.16: Angular frequency as function of the Rayleigh number for $A = 10$ and different values of the compression ratio η.

It is worth stating the related description from the simple observation that, for both $\eta = 0.1$ and $\eta = 10$, the initially steady solution obtained for $Ra = 1000$ and 2000 is quickly taken over by an oscillatory mode of convection for higher values of Ra. A remarkable feature of this emerging mode is that the disturbance always clearly travels in the direction in which the cross section of the domain increases, namely, from the hot wall to the cold wall for converging walls and in the opposite direction in the case of diverging walls. In practice, the oscillatory disturbance manifests itself as a well-defined series of cells moving from the side with smaller vertical extensions towards the other side (Figure 7.17).

Interestingly, however, an almost motionless roll remains steadily located in proximity to the target wall, regardless of whether $\eta < 1$ or $\eta > 1$ (in practice, such a stationary roll is maintained in that location by the relatively strong buoyancy forces being active in the portion of the domain with larger vertical extensions).

When one of the moving cells meets this roll, a coalescence mechanism is triggered (leading to the incorporation of the incoming smaller cell into the larger roll). When the coalescence process is finally over, a new roll nucleates in proximity to the other

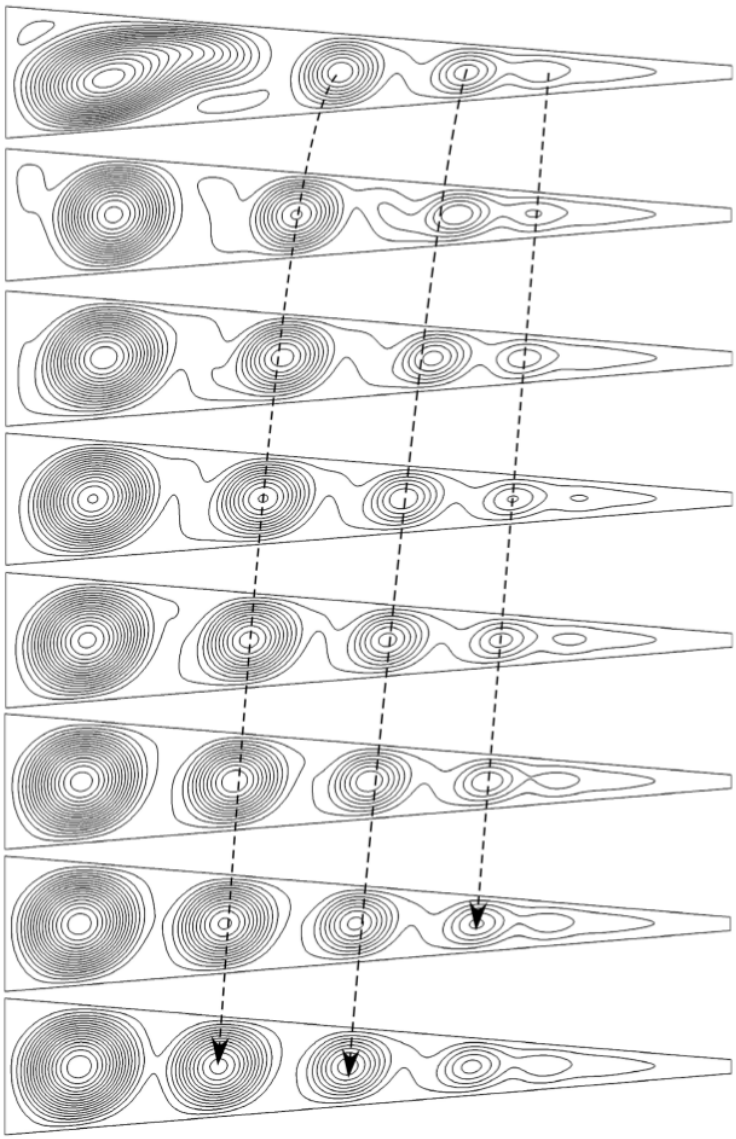

Figure 7.17: Oscillatory convection for $A = 10$, $\eta = 0.1$ and Ra=9000. Eight snapshots evenly distributed along the period of oscillation

side wall, thereby preserving the average number m of convective cells present in the cavity at any instant (and making the overall process cyclic).

We clearly detected such dynamics at all the considered values of $Ra \geq 3000$ for both $\eta = 0.1$ and 10, which could (with no doubt) be regarded as the clear manifestation of "waves" (TWs) travelling in the system, such a conclusion also being supported by the velocity signals provided by N "numerical probes" evenly distributed along the horizontal direction. The typical signature of a disturbance travelling continuously along a given direction, indeed, is represented by a continuous phase shift visible in the signals measured at different locations, which are equally spaced along the direction of propagation (Figure 7.18a).

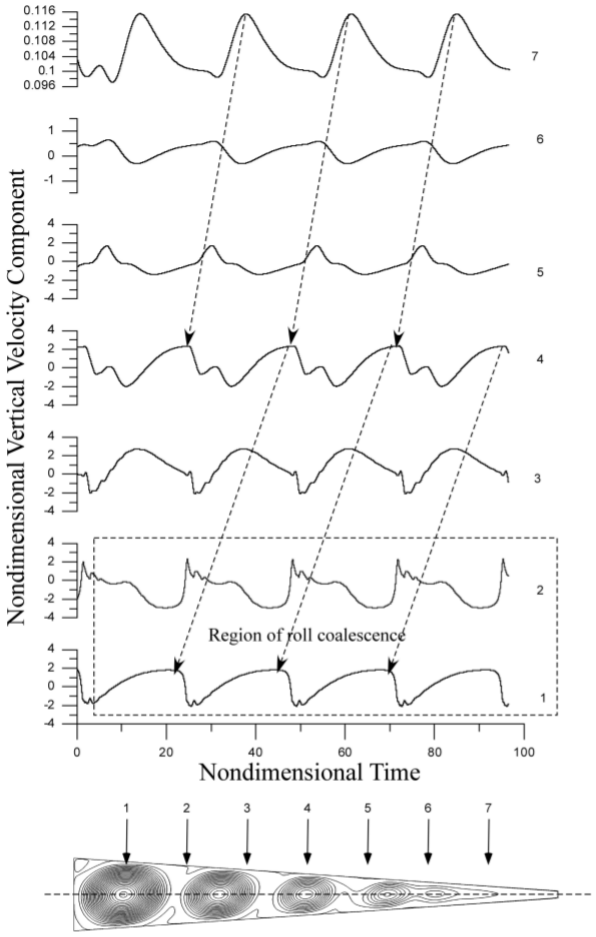

(a) Velocity (vertical component) signals collected by seven probes evenly spaced along horizontal direction (and at mid-height) of the cavity. $A = 10$, $\eta = 0.1$, and $Ra = 9000$.

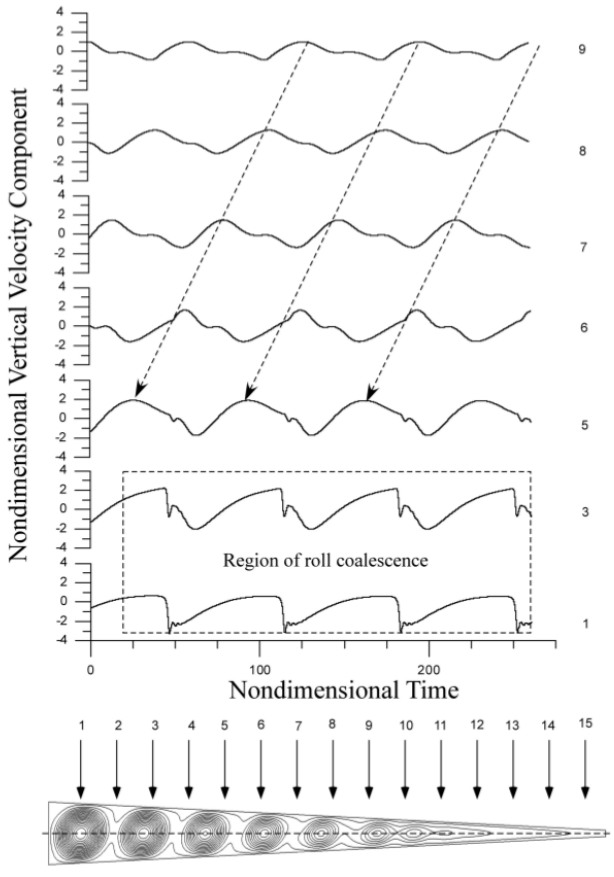

(b) Velocity (vertical component) signals collected by fifteen probes evenly spaced along horizontal direction (and at mid-height) of the cavity. $A = 20$, $\eta = 0.1$, and $Ra = 9000$

Figure 7.18: Traveling waves

An exception to the above scenario is obviously represented by the aforementioned

roll coalescence process occurring in proximity to the side wall with larger vertical extension (the cold wall for $\eta = 0.1$ and the hot wall for $\eta = 10$). Along these lines, Figure 7.18a reveals that the velocity of propagation of the wave is not constant along the x axis. The train of moving rolls targeting the side wall can be clearly seen to accelerate in the course of their migration (see also Figure 7.17). For $\eta < 1$, in the left side of the cavity (say $x < 0$), the velocity of the rolls increases until the first roll of the chain "meets" the vortex residing in proximity to the side-wall. At that stage, the two rolls merge and a new roll nucleates in proximity to the other side-wall (the right side for $\eta < 1$).

A general picture of the overall scenario can, therefore, be provided as follows: for $\eta < 1$ the group of cells spatially spreading periodically towards the side with larger vertical extensions (the left side) is bounded from the right (where such rolls are being continuously created) by the hot wall and from the left (where their propagation velocity rises) by a region where coalescence (C) periodically occurs between an incoming roll and another roll being steadily located there (such a localized roll coalescence phenomenon is responsible for the additional high-frequency pulsation mechanism evident in the velocity signal at station "2" in Figure 7.18a).

The clearly travelling nature of the disturbance is relatively surprising if one takes into account that transverse waves have never been observed or predicted for the case of laterally heated liquid metals. This behaviour becomes even more evident when the $A = 20$ case is considered (Figure 7.18b).

The intrinsic properties of the TW (its direction of propagation parallel to the horizontal direction with travelling rolls having axes perpendicular to the basic flow) support the conclusion that such a phenomenon is still of a hydrodynamic kind, as the so-called "helical waves" of a hydrothermal nature (which are also known to potentially affect gravitationally unstable liquid metals) generally travel in the span-wise direction, i.e., perpendicularly to the basic flow (the interested reader being referred to the work of Hart [33] [111], Gill [35] Laure and Roux [112] and Kuo and Korpela [36] for additional information on this mode of convection).

Some interesting analogies could be perhaps identified with a completely different phenomenon, typically occurring in high-Pr fluids subjected to thermally induced surface-tension gradients (namely, the so-called hydrothermal waves of the Marangoni flow, Smith and Davis [46] Shevtsova et al. [113] and Lappa ([114] [115] [116]). Such waves,

which also typically manifest as a chain of travelling cells, however, do not display the local roll coalescence phenomena seen here. Moreover, their direction of propagation is univocally determined by the direction of the imposed temperature gradient (hydrothermal waves in the Marangoni flow are known to propagate always in the same direction as that of the imposed temperature gradient, i.e., from the cold side to the hot side, whereas in the present case, they can propagate in either direction depending on the value of η).

For $A = 10$, we found that the scenario for $\eta = 0.25$ and $\eta = 4$ is very similar to that for $\eta = 0.1$ and $\eta = 10$, respectively, with the prevailing mode being essentially a wave travelling in the direction of increasing cross-sectional area (though the variation in η can exert some influence on the properties of the emerging solution, the fundamental mechanism does not change). More specifically, we observed that the increase in η from 0.1 to 0.25 produces in some circumstances a higher number of coexisting rolls (m) participating in the wave mechanism (a variation from $m = 4$ to $m = 5$ for $Ra = 5000$ and from $m = 5$ to $m = 6$ for $Ra = 9000$). For $Ra = 3000$ and 7000, though a larger value of η does not change m, it can lead to a mitigation of the velocity of propagation of the rolls (as witnessed by the shrinkage visible in the related angular frequency). These trends can be also seen by taking a look at Figure 7.16.

In the interest of conciseness, we do not discuss explicitly the results for $\eta > 1$ as the aforementioned invariance principle relating to exchanging η with its reverse value ($\frac{1}{\eta}$) is still applicable. At this stage, however, we should clearly mention that though such a principle is valid for the velocity field, it does not hold for the temperature field (see again Equation 7.11). This is witnessed by the change of the direction of travelling waves with respect to the imposed temperature gradient when converging walls are replaced with diverging ones. In other words, for a fixed η, the problem is not symmetric with respect to a change of the direction of the horizontally imposed temperature gradient (namely, the replacement of the hot and cold side walls). Another way to think about the thermal anisotropy intrinsically associated with this system is to consider that by keeping the direction of the horizontal temperature gradient fixed, the problem would not be symmetric by replacing η with its reverse, i.e., $\frac{1}{\eta}$. This anisotropy is typical of the Hadley flow, which being a shear flow (directed from the hot side to the cold side in proximity to the top wall and in the reversed sense near the bottom) breaks the isotropy of the considered system with respect to the x coordinate.

Continuing with our review of the numerical results, it is also worth examining in detail the case $\eta = 0.5$ ($\eta = 2$) for which we could notice some departure from the purely travelling disturbance seen for smaller (larger) values of η.

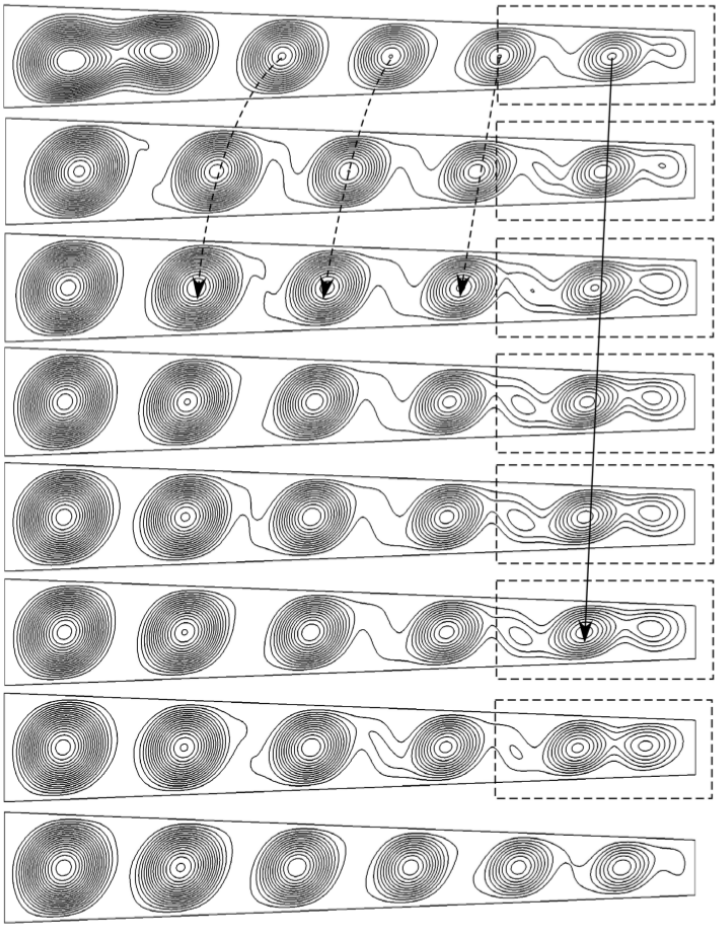

Figure 7.19: Eight snapshots evenly distributed along the period of oscillation for$A = 10$, $\eta = 0.5$ and$Ra = 9000$.

For relatively small values of the Rayleigh number ($Ra = 3000$ and 5000), some limited differences can be noticed in the maximum of the stream function and in the angular frequency of the travelling wave for $\eta = 0.5$ ($\eta = 2$) and $\eta = 0.25$ ($\eta = 4$) (these quantities decrease as a function of η at fixed Ra for $\eta < 1$ and vice versa for $\eta > 1$). Nevertheless, for relatively higher values of Ra ($Ra \geq 7000$), the most notable feature distinguishing the patterns at $\eta = 0.25$ and $\eta = 0.5$ ($\eta = 4$ and $\eta = 2$) is the emergence of a modulation locally affecting the flow in the right (left) part of the cavity.
Surprisingly, starting from initially diffusive thermal conditions and using central differences, we found that this (P) mode becomes the dominant mechanism causing oscil-

lations for $\eta = 0.5$ ($\eta = 2$) at $Ra = 7000$ with the ensuing suppression of the travelling disturbance.

In terms of patterning behaviour, such a local effect manifests itself essentially via the formation of a three-roll structure periodically visible in the right part of the cavity (Figure 7.19). This structure seems to be produced by the "splitting" of the original roll located near the right wall (this is why we have labelled this state as m = "5 + 2"). As the reader will easily realize, most notably, this local sub-pattern closely resembles the "twisted" recirculation embracing three co-rotating vortices that we have already discussed for the purely rectangular cavity with $A = 4$ and $Ra = 10^3$ (Figure 7.8a). Because we found that the TW mechanism re-enters the dynamics for $Ra = 9000$, this led us again to the conclusion that for $\eta = 0.5$ ($\eta = 2$) multiple states of convection are possible (two in this case, namely, the TW and the P states) with one state being preferred to another according to the initial conditions and/or numerical scheme being used for the integration of the balance equations.

In order to verify once again the validity of the above statement, we repeated the simulation for $\eta = 0.5$ and $Ra = 7000$ by replacing central differences with the Van Leer scheme and obtained a purely travelling wave as for $Ra = 5000$ and 9000. Most interestingly, as for the case $\eta = 0.2$ and $A = 4$ discussed at the end of the previous paragraph related to the discussion of cavity with $A = 4$, for $A = 10$ and $\eta = 0.5$, we observed that both mechanisms are operative at $Ra = 9000$ (Figure 7.19), as witnessed by the two-frequency spectrum associated with this regime (it could be regarded as an example of what we have named (PLT) mode, namely, a travelling wave "locally" modulated by roll pulsations or splitting behaviours). In particular, we found that the typical time scale of the (P) mode is smaller than the characteristic period of the TW (the characteristic frequency of the P disturbance is $\omega = 1.319$, whereas that of the wave is approximately 0.05).

If η is finally increased (decreased) to 1, the above waveforms and related modulation effects are taken over by a completely different oscillation scenario where no clear direction of propagation of the disturbances can be identified. For such a specific case (rectangular enclosure), multiple states are known to exist in the form of configurations with different numbers of rolls. We have already discussed the typical properties of this regime in the case of $A = 4$ and for this reason the related description is not duplicated here. We just limit ourselves to emphasizing once again the role played by the specific

geometrical condition $\eta = 1$ in separating regimes with leftward propagating waves from situations with rightward disturbance propagation.

As a concluding remark for this section, towards the end to provide some additional insights into the influence of η on the threshold for the onset of time-dependence, we finally discuss the specific dynamics seen for $Ra = 1000$.

By moving along the horizontal direction for $Ra = 1000$ in Figure 7.15, indeed, the reader will immediately realize that an increase in η starting from $\eta = 0.1$ (where the flow is steady with $m = 2$) leads to flow destabilization with the onset of oscillatory disturbances of the (K) type (still with $m = 2$) for $\eta = 0.25$ and a TW with $m = 3$ for $\eta = 0.5$. A further increase in η can revert the flow to steady conditions as witnessed by the solution obtained for $\eta = 1$ (stationary flow with $m = 4$).

The general destabilizing role played by $\eta \neq 1$ is also evident in Figure 7.16 where the frequency has been reported as a function of η for fixed values of Ra. It can clearly be seen there that, while for $\eta = 1$ the flow is steady for any value of $Ra \leq 9000$ (according to our simulations, for such a specific condition, the Rayleigh number must be increased to 14500 in order to obtain an oscillatory flow), for $\eta = 0.75$ time-periodic convection is already possible for $Ra = 1000$.

Taken together, Figures 7.15 and 7.16 also suggest that though TW branches are dominant in the "external regions" the effective η intervals in which (TW) disturbances are possible at different values of the Rayleigh number shrink when Ra rises. This observation confirms the trends already discerned for $A = 4$, i.e., the preferential mechanism of oscillations is gradually transferred from low-frequency waves to high-frequency disturbances of the (P) type when Ra is increased.

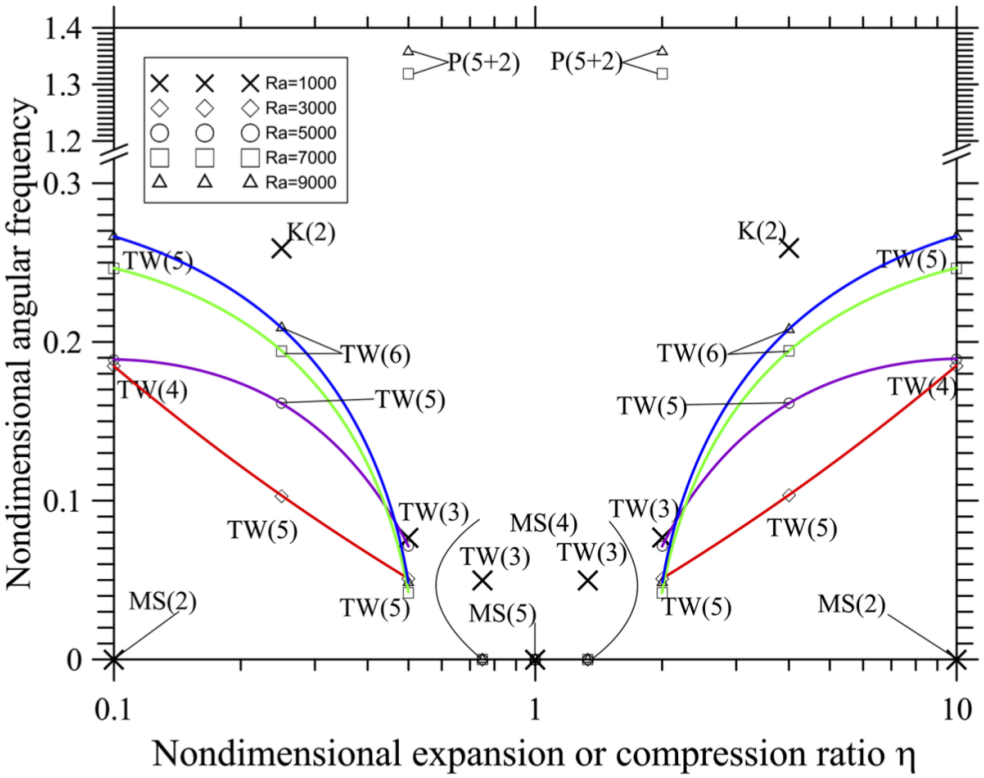

Figure 7.20: Angular frequency as function of expansion or compression ratio η for $A = 10$ and different values of the Rayleigh number. The MS(5) flow becomes oscillatory for $Ra > 14000$ with $\omega \approx 6.48$ at Ra=14500, not shown in this plot.

7.3.3 Conclusions

Having completed a detailed description of the dynamics as a function of the aspect ratio, compression (or expansion) ratio η, and Rayleigh number, we now turn to elaborating some general conclusions by filtering out specific details and concentrating on general trends.

To some extent such a discussion is aimed to simplify the problem by abstracting from specific cases the essential features. In doing so, in particular, we will heavily rely on the general maps shown in Figures 7.9 and 7.15, by which a thorough analysis of the problem can be made more intuitive and manageable (as explained before, such maps are essentially diagrams with η as the abscissa and Ra as the ordinate where the results provided by the numerical simulations have been collected in an ordered fashion).

In the following, in particular, we start from an analysis of the wave number, namely, the number of rolls simultaneously present in the enclosure.

From a purely theoretical standpoint, it is known that, in general, the spacing of the

cells pertaining to the 2D hydro-dynamic mode can be assumed to depend on a number of factors. First is the fact that an integral number of cells must be accommodated into a cavity of finite extension and the inter- roll distance must satisfy this constraint. The second factor is the magnitude of the departure (in terms of Ra) from the onset of instability. Third is the obvious role played by converging or diverging boundaries in constraining the flow in the end regions and how this effect changes with the Rayleigh number.

The influence of the aspect ratio can be immediately clarified by a cross-comparison of the results for $A = 4$ and $A = 10$ from which it becomes evident than an increase in A significantly expands the set of wave numbers allowed in the system (this ranging from 1 to $5+2$ for $A = 10$ and from 1 to 3 only for $A = 4$ over the considered interval of Ra). Such a dependence, however, is not as straightforward as one would imagine because it is mediated by the influence of the expansion (or compression) ratio η, especially for $A = 10$.

For such a value of A, we found that an increase (a decrease) in η from the condition $\eta \approx 1$ determines a shrinkage in the number of rolls, whereas an increase in the Rayleigh number is generally responsible for higher values of the wavenumber m, the angular frequency, and an increase in the complexity of the frequency spectrum (with the possible coexistence in some circumstances of disturbances operating at different time and spatial scales).

The most interesting information provided by these maps, however, is the evidence they give in terms of transition from one regime to another. Indeed, it is possible to clearly discern three distinct regions of a spatio-temporal behaviour. The central one is the region of "standard" hydrodynamic modes emergence, which is the area of the space of parameters (η and Ra) where the Hadley flow is affected by the typical "pulsating" disturbances (P) already revealed in past studies for the case of perfectly rectangular cavities. The two external regions, however, are the loci of heretofore unseen dynamics. The typical pulsating disturbance can be taken over in such intervals by a completely new mechanism by which the disturbance is seen to spread continuously along the horizontal direction giving rise to "travelling waves".

While for $A = 4$ such phenomena can be barely seen because of the coexistence with (K)-modes at intermediate values of η, or they are hardly recognizable because of the simultaneous occurrence of roll coalescence processes (which overshadow or mask the

continuous propagation of the disturbance), for $A = 10$ they become the preferred mode of oscillatory instability over a wide range of η. Moreover such a value of the aspect ratio is sufficiently large to allow the observer to filter out other localized phenomena (such as the roll coalescence process taking place in proximity to the walls).

Another conclusion stemming from all these observations is that for relatively large aspect ratios, two main categories of disturbances affecting the considered dynamics can be identified in terms of frequency, namely, a small-frequency large-scale disturbance (manifesting itself in space as a TW) and a high-frequency small-scale disturbance (corresponding essentially to localized pulsating phenomena or kissing rolls). The preceding discussion, however, should not be misread as implying that these modes follow a precise trajectory in the space of parameters. Though, for relatively small values of Ra, the two disturbances manifest separately, they are not mutually exclusive, nor are they truly progressive. As revealed by the present approach based on extensive parametric simulations (assuming different initial conditions and/or integration schemes for fixed cases), these modes correspond to the existence of "multiple" states of convection. In some cases (essentially in the high-Ra part of the space of parameters), modes pertaining to different branches can coexist leading to states in which a low-frequency (travelling) disturbance is modulated locally by a high-frequency (pulsating) perturbation.

7.4 Three-dimensional containers with variable cross section

This section extends the previous ones related to the two-dimensional enclosures. In the following indeed the third dimension along z has been added and the flow instabilities are allowed to spread in such direction.

In this section we will explain carefully that the situation in three-dimensional cavities is no longer that depicted in the previous part of this chapter. The Tws and (P) modes indeed are taken over either by chaotic and spatially disordered 3D-instabilities or by waves travelling in the spanwise direction (along z).

Despite the relevance of these flows to a variety of problems, the literature on such a subject, however, seems to be still relatively limited. Most of existing studies, indeed, have been limited to two-dimensional configurations for which the dominant disturbances

causing transition to time-dependent convection are expected to be purely hydrodynamic in nature.

Nevertheless, lines of evidence exist indicating that the emerging flow might have a remarkable 3D nature in many circumstances. Along these lines, as an example, Hart [33] [111] was the first to determine the sensitivity of this kind of convection (under the assumption of infinite layer i.e., "parallel flow") to both transverse (2D) and longitudinal (3D) disturbances. Later, Gill [35] concentrated specifically on the latter disturbances. These initial studies revealed that while the transversal instability is driven by the mean shear stress (this is the reason why it is often referred to as "shear instability" and the related disturbances as hydrodynamic one), the longitudinal instability involves dynamical coupling between the mean shear stress and the buoyancy force (a dynamical balance that makes thermal effects directly relevant to the instability mechanism, from which the denomination of "hydrothermal disturbances").

In terms of patterning behaviour, the outcomes of these instabilities are different as well. In the first case, 2D circulations appear close to the inflection point of the basic velocity profile. These perturbation rolls are therefore perpendicular to the basic flow. The latter mode of convection is featured by a pair of gravitational waves travelling in the span- wise direction. This means that the axis of the perturbation rolls is parallel to the basic flow. In practice, these longitudinal rolls combine with the basic parallel flow to produce helical trajectories of the fluid particles (from which the denomination of "Helical wave" or OLR mode, where OLR stands for "oscillatory longitudinal rolls"). Other (later) studies have been instrumental in clarifying that the ranges of existence of the different modes of oscillatory instability determined for the infinite horizontal layer might not be directly applicable to real situations.

As an example, assuming ideally a fluid with zero Prandtl number fluid, Afrid and Zebib [117] found that the extension of a classical rectangular geometry (with horizontal top and bottom walls) along the direction perpendicular to the basic flow can have an important effect on transition to oscillatory convection (it was shown that reducing this extension from two to one could cause a significant increase in the value of the critical Rayleigh number). A similar trend was also observed in experiments (see, e.g., Refs. [118] and [119] for $Pr = 0.026$). Remarkably, Pratte and Hart [119] found longitudinal waves to be the preferred mode of oscillatory convection in proximity to the critical threshold.

In general, some indication has been provided that the location of the points in the (Ra, Pr) space where the branches pertaining to the different instability mechanisms (transverse or longitudinal) intersect might change with respect to the idealized layer with infinite extent according to the effective spatial configuration of the fluid container (see Lappa [120]). Along these lines, indeed, there have been specific experimental works considering the possible interplay of these two fundamental modes of convection. For instance, four "new" modes of oscillation were reported in the study by Braunsfurth and Mullin [121] for Pr spanning the interval $0.016 \leq Pr \leq 0.022$. Similarly, by investigating numerically the onset of oscillations as a function of the cavity aspect ratio and Pr in the range $0 \leq Pr \leq 0.027$, Wakitani [122] observed an increase in the value of the critical Rayleigh number for larger Pr and/or by reducing of the span-wise aspect ratio. These variations were not regular, which may be regarded as evidence of the competition of different oscillatory modes at onset.

Due to such disorganized manifestations, these convective regimes have so far resisted a deeper analysis. The problem is even more complex than as discussed above if one considers that, following the original model introduced by Hadley [11] most of past efforts have been devoted to geometrical domains with relatively simple shapes (cubic or parallelepipedic enclosures with straight horizontal and vertical walls and temperature gradient perpendicular to gravity).

For relevant work where this constraint has been removed, the reader may consider the numerical studies by Delgado-Buscalioni and co-workers. As an example, Delgado-Buscalioni [123] [124] illustrated that, when the system is inclined, new types of instabilities can be enabled; examples along these lines being represented by the Stationary Longitudinal long-wavelength instability (SLL) and the Oscillatory Transversal long-wavelength instability (OTL). While the first may be regarded as a close relative of a classical Rayleigh-Bénard mode, the second is essentially a kind of standing wave with a rather long wavelength appearing only if the cavity is inclined and heated from below. Owing to these studies, it is also known that the inclination can even alter the properties of the typical modes of convection of the Hadley flow, namely, the aforementioned hydrodynamic and hydrothermal disturbances. For instance, the stationary transverse rolls (the 2D hydrodynamic instability), that for horizontal configurations are generally observed for fluids with $Pr \ll 1$ and are suppressed for $Pr > 0.1$ can become unstable even in gases ($Pr \approx 1$) [123]. Moreover, the OLR instability is damped at a

certain cut-off value of Pr, which increases with the inclination angle with respect to the horizontal direction (θ) (e.g., for $\theta = 0°$ and $10°$ OLR perturbations are damped for $Pr \geq 0.21$ and $Pr \geq 0.26$, respectively) [124].

Despite these remarkable results, only in the last couple of years, however, has the importance of the different inclination of the walls been realised. As an example, most recently, the ability of oppositely inclined walls (delimiting the fluid from above and from below) to further expand the set of convective modes potentially excitable when the Rayleigh number is increased has been shown by Lappa and Ferialdi [125] under the constraint of 2D flow. These systems may be regarded as an additional variant, for which though the top and bottom walls are not horizontal, no net inclination is present as these two boundaries are one the mirror image of the other. Thereby, a new line of inquiry in the study of these subjects has been opened up for cases in which, though the system is not tilted, the widespread assumption of "parallel flow" is no longer applicable. The present work continues this investigation by probing the role of the third dimension (z). Given the lack of information for 3D configurations, in particular, we concentrate on cavities with converging or diverging walls in the xy (basic flow) plane and different span-wise aspect ratios (assuming either periodic boundary conditions or solid walls as limiting condition along the z axis).

7.4.1 The system and boundary conditions

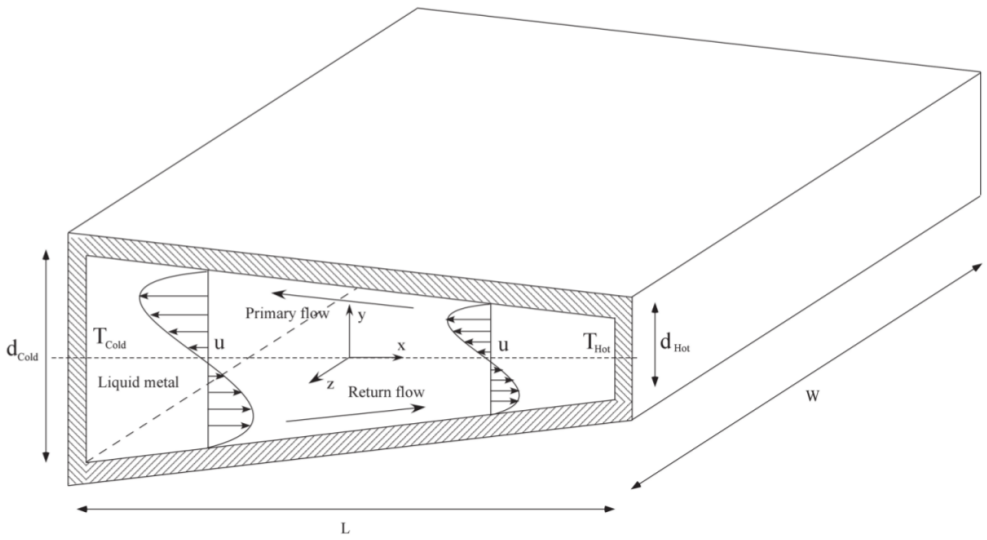

Figure 7.21: Geometry of the three dimensional enclosure considered

The system considered in this section is the 3D version of that considered in the previous one: namely the cavity with converging or diverging walls, which has undergone to an extrusion along the z direction, represented in Figure 7.21.

Along with the geometrical parameters already introduced previously in this chapter, namely the aspect ratio related to the x direction A, from now on denoted as A_x and the expansion, compression ratio η this modified geometry needs also the aspect ration relative to z direction A_z.

For all cases, we assume the top and bottom walls to be adiabatic (no heat exchange) and the two different BC have been considered on the end-walls along the z direction: adiabatic rigid walls or periodic boundary conditions.

In past linear stability analyses on the subject (for the case of horizontal parallel flows), hydrodynamic and hydrothermal disturbances were observed as the preferred (most critical) perturbations for $Pr = O(10^{-2})$ and $Pr = O(10^{-1})$, respectively. Furthermore, for systems featuring a net inclination with tilts similar to those considered in the present work (though with opposite sign for the top and bottom boundaries), such modes were found to interact (codimension-two point) for Pr located in a certain neighbourhood of $Pr = 0.03$ (see Ref. [123]). Accordingly, in the present analysis, we consider $Pr = 0.01$ and $Pr = 0.05$. Moreover, as in Ref. [125], we assume $A_x = 10$.

7.4.2 Mesh independence study

As the code is the same of that use in the previous section the validation outcomes are those represented in Table 7.2. On the other hand the modified geometry respect to that considered in the previous section requires to investigate further the minimum mesh size needed.

Table 7.3 illustrates the outcomes of the grid refinement process. Stripped to its basics, the convergence scheme that we have used for the mesh refinement process envisions an analysis of the variations displayed by a representative quantity as the grid density is progressively increased. As representative (relevant) case, we have focused on $A_x = 10$, $\eta = 0.1$, $Pr = 0.01$ and $Ra = 4000$ ($Gr = 4 * 10^5$) . Five different meshes have been tested using the non-dimensional angular frequency of the emerging oscillatory flow as the convergence criterion.

As shown in Table 7.3, the relative percentage error becomes smaller than 2% as the mesh density exceeds that corresponding to$N_x \times N_y = 175 \times 25$. Accordingly, a mesh

200×30 has been used to discretise the flow in the xy plane for all the cases treated in the present work. Following a common practice in the literature, for the 3D simulations, we have scaled the number of points along the third (z) direction in a proportional way (i.e., 200 points along z when the extension in that direction is equal to the system size along x, leading to a total of 1.2×10^6 nodes).

Obviously, an algorithm capable of targeting the broadest range of applications would also require assessment of the mesh resolution against typical criteria relating to the simulation of turbulent flows. For the sake of clarity, we delay the treatment of this specific point to the next section, where we address it in conjunction with a description of chaotic convection and the typical related flow "scales" (in practice, the validity of the present approach has been further assessed by comparing the spatial grid spacing, in terms of Δx, Δy and Δz, with the so-called Kolmogorov length, which is the smallest, i.e., most demanding in terms of required numerical resolution, scale developed by the flow when turbulent conditions are established).

Mesh	ω	$\Delta\%$
150x20	0.214	...
175x25	0.209	2.39
200x30	0.205	1.95
225x40	0.202	1.49
250x50	0.200	1

Table 7.3: Outcomes of the grid refinement study: $Pr = 0.01$, $A_x = 10$ and $Ra = 4000$

7.4.3 Results

A synthetic description of the salient outcomes of our numerical studies is reported in the remainder of this section (articulated in focused subsections) together with a critical discussion of some accompanying necessary concepts (provided to support reader's understanding).

Rather than an extensive parametric investigation (not possible given the high computational time required by fully 3D transient simulations), what follows provides a critical analysis of potentially key aspects in the process leading to pattern formation and the emergence of chaos in these systems. In particular, as anticipated, we concentrate on two different values of the Prandtl number: 0.01 and 0.05, both being representative of semiconductor or metal melts (e.g., silicon and aluminium, respectively). Moreover,

we fix $\eta = 0.1$ and vary the Rayleigh number in the range $400 \leq Ra \leq 4000$.

While the role of hydrodynamic and hydrothermal flow instabilities as one cause of the onset of oscillatory phenomena in these systems is not questioned here, the details of how, when, and where such instabilities or other initiating causes can lead to spatially pervasive oscillatory phenomena and eventually chaotic states are the main subject of interest.

Most conveniently, first we address the case with the same value of the Prandtl number (i.e., $Pr = 0.01$) already considered by Ref. [125] (in order to appreciate the differences, i.e., the new dynamics enabled by the third dimension), then we discuss in detail the effects produced by an increase in the Prandtl number.

Hydrodynamic and hydrothermal disturbances

Following a deductive approach with systems of growing complexity being treated as the discussion progresses, we start from the trivial case in which the emerging flow is steady. As an example, for $Pr = 0.01$, $A_z = 10$, and periodic boundary conditions with respect to the z direction, not surprisingly, at $Ra = 400$, the flow pattern provided by the 3D simulations consists of a steady two-dimensional unicellular structure (not shown), which indicates that this relatively small value of the Rayleigh number is sufficient to excite neither hydrodynamic oscillatory disturbances nor OLR modes.

In agreement with Ref. [125], if the Rayleigh number is increased to 1000, a second circulation nucleates in the original unicellular structure (as shown in Figure 7.22). This flow is still steady.

When Ra is further increased, however, interesting departures from 2D behaviours occur.

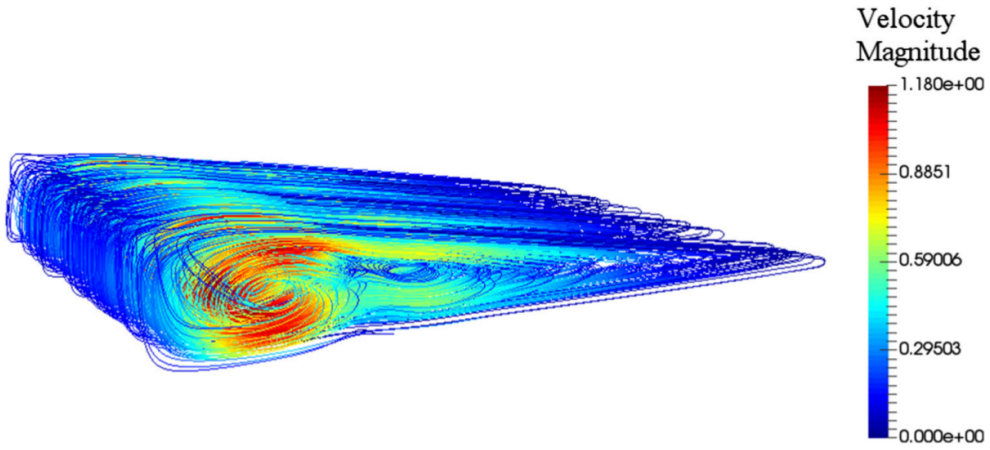

Figure 7.22: Streamlines of the steady base flow in different sections along the z direction for $Pr = 0.01$ and $Ra = 1000$.

As a first example along this path, in particular, we examine the field obtained by doubling the Rayleigh number, i.e., $Ra = 2000$.

According to the aforementioned 2D numerical study, for this case, the solution with two steady rolls should remain stationary until the Rayleigh number attains a value ≈ 3000 (for which the initial bi-cellular steady state is taken over by a travelling wave with four distinct rolls continuously spreading in the horizontal x direction, see Figure 7.16 in the previous section). Nevertheless, it can be seen that, by enabling the flow to expand along the third dimension, it displays a remarkable tendency to become oscillatory even if values of the Rayleigh number as small as 2000 are considered. The related structure, shown in Figure 7.23, among other things, clearly unveils the essentially three-dimensional nature of the emerging oscillatory disturbances.

Indeed, some peaks of velocity (red arrows) distributed along the span-wise direction (the z axis) can be recognised in this figure in proximity to the left side of the cavity (the thickest one), which undoubtedly prove the existence of a disturbance extending along this direction. The essentially 3D nature of the flow is also made evident by the presence of vortices in the entire xz plane.

Following up on the previous point, notably, these vortices do not undergo a progressive displacement (in time) along the positive or negative z direction (as one would expect for a travelling wave); rather they take part in an endless wandering process (moving back and forth about a position fixed in space), which resembles the behaviour of a standing wave.

Given the very small value of Pr relating to these phenomena ($Pr = 0.01$) and the relatively low value of the Rayleigh number for which the oscillatory disturbances manifest themselves (a value smaller than that required to excite hydrodynamic disturbances in the equivalent 2D case), these simple observations implicitly define a conundrum, that is, understanding whether these disturbances are of a hydrodynamic or hydrothermal (OLR) nature In such a quest, we exclude the presence of SLL modes like those reported in the study by Delgado-Buscalioni [123] as though the walls of our cavity are inclined, the system is perfectly symmetric with respect to the horizontal direction (in other words, non net inclination is present as the opposite tilts of the top and bottom walls balance each other).

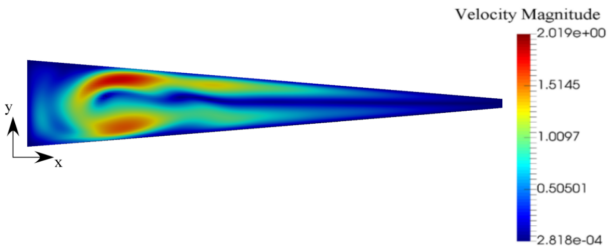

(a) Velocity magnitude in the xy plane

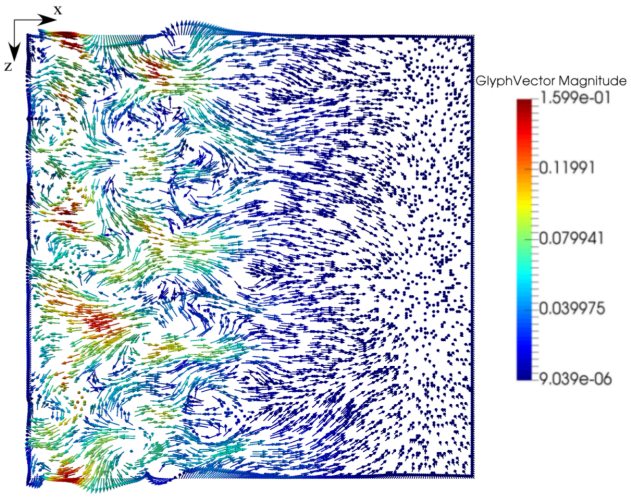

(b) Velocity vector plot in the xz mid plane

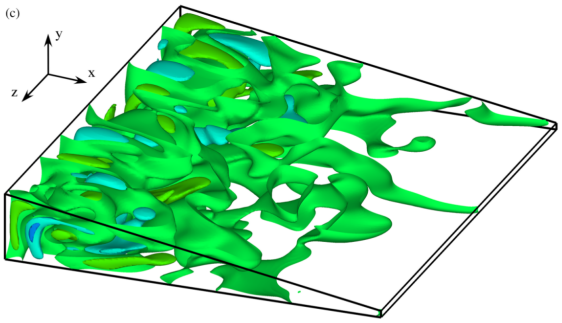

(c) Iso-surfaces of the w component (along z) of the velocity

Figure 7.23: Structure of the oscillatory 3D flow for $A_x = A_z = 10$, $Ra = 2000$ and preiodic boundary conditions on the end-walls along z

It is worth recalling that Delgado-Buscalioni [123] found stationary longitudinal

rolls only in the presence of Rayleigh-Bénard modes excited in conjunction with inclinations able to produce a destabilising vertical component of the temperature gradient. In the present case, this is not possible as the heated and cooled sides of the cavity remain always perfectly vertical, therefore, no heating from below effect can be introduced due to wall inclination. Moreover, the vertical projection of the temperature stratification (eventually produced by the Hadley flow for relatively high values of Ra) is always opposite to gravity (leading to a heating-from-above effect).

Similarly, the occurrence of "Rayleigh" modes like those predicted in the linear stability by Gershuni et al. [38] for non-tilted layers with top and bottom conducting boundaries can also be filtered out. That kind of mode (yet emerging in the form of steady rolls with their axes aligned with the shear flow), indeed, follows from the presence of zones of potentially unstable stratification near the upper and lower horizontal boundaries induced by the basic flow, which are suppressed if the top and bottom walls are adiabatic (as in the present case). Even with such initial simplifications, resolving the question formulated above about the nature of the present disturbances, however, is not straightforward as one would imagine as it requires separating different contributions, which are generally interwoven. Perhaps, the most obvious attempt to discern the underlying intricacies would be to start from the widespread existing consensus in the literature that for such systems some relevant considerations might be derived on the basis of simple "theorems" (which provide necessary and/or sufficient conditions for the onset of certain disturbances).

The presence of "inflection points" in the velocity profile for such a kind of systems with converging or diverging walls was already shown previously, discussing about the low Rayleigh number patterns (Section 7.2), (see also [101]). For purely "parallel flow" such points are known to play an important role if they are considered together with the so-called Rayleigh's theorem stating that: *"In an inviscid shear flow a necessary condition for instability is that there must be a point of inflection in the velocity profile* $u = u(y)$*, i.e. a point where* $\frac{d^2u}{dy^2} = 0$*"*. As illustrated by some author (see Refs. [103], [104], [105], [106]), this condition also acts as a sufficient condition in many circumstances. Furthermore, the related disturbances are expected to be hydrodynamic in nature and purely two-dimensional [126].

To some extent, all these theorems apparently simplify the problem by abstracting some essential and distinctive features. Such arguments have often been used by sev-

eral authors to support the conclusion that for small values of the Prandtl number, the oscillatory disturbances found in two-dimensional numerical simulations of buoyancy flow in differentially heated rectangular cavities should be considered of a hydrodynamic origin (Refs. [102]and [112], [36], [127], [107], [108], [128] and references therein).

Squire's theorem, however, is not applicable in the present case as the flow is not parallel (due to the opposing inclination of the top and bottom walls). Superimposed on this bottleneck, there are some drawbacks of conceptual nature. Since the Prandtl number is not exactly zero, technically speaking, the momentum and energy equations cannot be uncoupled, which also invalidates the outcomes of the Rayleigh theorem.

These initial reflections are instructive as they illustrate how any attempt to discern the origin of the perturbations shown in Figure 7.23 on the basis of simple criteria or theoretical arguments should not be considered as a viable option.

Though some relevant information could be gathered by using the typical protocols of the linear stability analysis and related energy transport considerations, here we take a different approach potentially applicable also to situations in which the flow has rather a chaotic nature. More precisely, we show that direct numerical solution of the model equations in non-linear form has still the potential to offer valuable insights provided it is critically used together with some physical reasoning about the different "natures" of the hydrodynamic and hydrothermal fundamental modes of instability.

Put simply, in order to shed some light on this issue, we apply the following strategy: additional simulations are performed uncoupling the energy and momentum equations (i.e., by assuming a fixed initial thermally diffusive distribution of temperature inside the entire physical domain and solving the balance equations for mass and momentum only).

The physical reasoning underlying this modus operandi is quite obvious. If the instability was thermal in nature (OLR mode), the oscillations would cease under such conditions because the temperature effects have been switched off; vice versa, they should survive if they were related to a hydrodynamic mode (owing to its purely shear-driven origin).

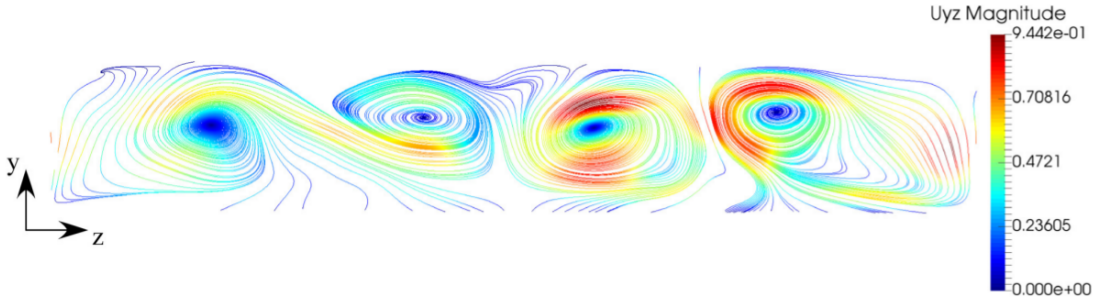

Figure 7.24: Projection of te velocity field in the yz plane at $x = \frac{1}{8}A_x$, $Pr = 0.01$, $A_z = 10$, periodic boundary conditions, $Ra = 2000$, temperature equation uncoupled.

The outcomes of such simulations are shown in Figure 7.24 where a snapshot of the strong longitudinal oscillatory structures formed near the cold thickest cavity side has been reported (in order to make these longitudinal rolls clearly visible, we have plotted the projection of the velocity in a yz plane located near the cold wall, i.e., $\frac{1}{8}$ of the cavity length). As any processes that depend on the amplification of the aforementioned helicoidal disturbances are excluded in this case, these findings are of remarkable conceptual significance as they indicate that the main source of the oscillatory dynamics shown in Figure 7.23 must, therefore, be ascribed primarily to a mechanism of hydrodynamic nature.

On the basis of these arguments the following partial conclusions can therefore be drawn for this specific case: Allowing the flow to extend along the third direction can cause a modification in the emerging dynamics with respect to those seen under the constraint of two-dimensionality. The flow becomes oscillatory for a slightly smaller value of the Rayleigh number and displays 3D features due to the presence of vortices in the xz plane (in addition to those generally seen in the xy plane). Despite these remarkable differences, however, evidence points toward the conclusion that the fundamental nature of the most critical disturbance does not change (the spatio-temporal appearance is more complex, but the fundamental mechanisms driving the instability are essentially the same in 2D and 3D).

At this stage, however, we have to warn the reader that these observations should be considered "partial" or "local" to the specific region of the space of parameters considered; i.e., no attempt should be made to generalise them (as we will illustrate in the following, in fact, they cannot be applied to the companion case with larger value of the Prandtl number). Indeed, for $Pr = 0.05$ and the same conditions considered in Figure

7.23 (periodic boundary conditions, $A_z = 10$ and $Ra = 2000$), the intricate behaviour seen for $Pr = 0.01$ is replaced by a much more periodic and regular pattern.

As evident in Figure 7.25, another distinguishing mark of this emerging mode is its spatial configuration, the oscillatory behaviour being confined to the part of the cavity with the larger vertical extension, with a quasi-steady state attained in the narrower region.

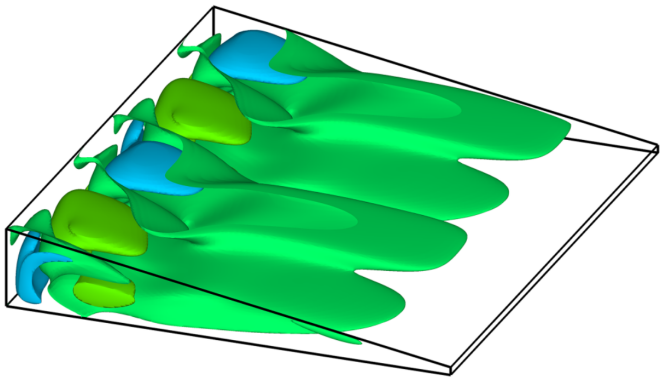

Figure 7.25: Isosurface of the w component (along z). $Pr = 0.05$, A_z, $Ra = 2000$, periodic boundary conditions. OLR mode.

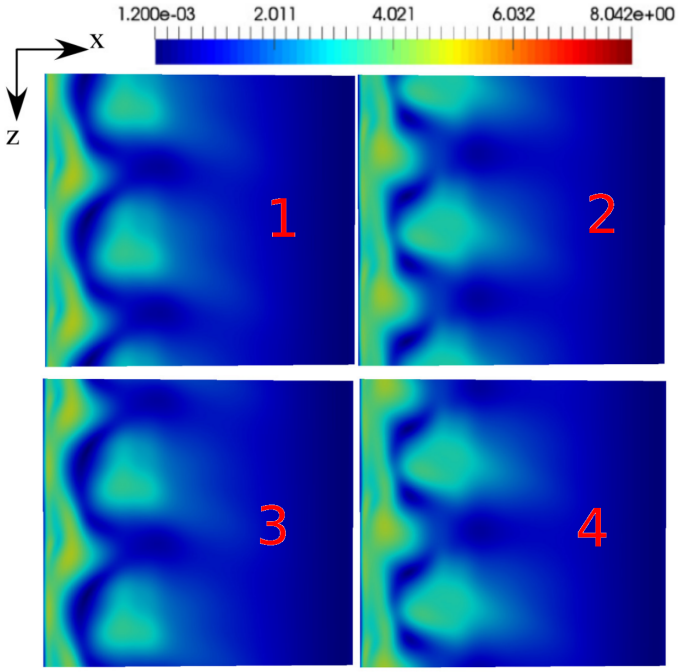

Figure 7.26: Four snapshot evenly distributed along the period of the non-dimensional velocity magnitude in the xz plane. $Pr = 0.05$, $A_z = 10$, $Ra = 2000$, periodic boundary conditions. OLR with non-dimensional angular frequency of 2.81.

Moreover, the sequence of snapshots evenly spaced in time as shown in Figure 7.26 clearly demonstrates the travelling nature of the disturbance in that area (as witnessed by the propagation of two peaks along the z direction, manifested in the velocity field as two "spots" located in proximity to the left wall). Figure 7.27 finally reveals the essentially sinusoidal morphology of the perturbation (a classical "wave" spreading continuously along the z direction).Following the same approach undertaken for $Pr = 0.01$, toward the end to clarify the nature of this disturbance, we have repeated such simulation switching off the solution of the temperature equation (yet to filter out any disturbance of thermal buoyancy nature). The outcomes of this study are summarised in Figure 7.28, where we have reported the spectrum of frequencies for the different situations examined so far, namely, $Pr = 0.01$ with coupling between the energy equation and the Navier-Stokes equations enabled and disabled (Figures 7.28a and 7.28b, respectively) and the analogous spectra for the case with $Pr = 0.05$ (Figured 7.28c and 7.28d, respectively, the reader being referred to the next section for additional discussions).

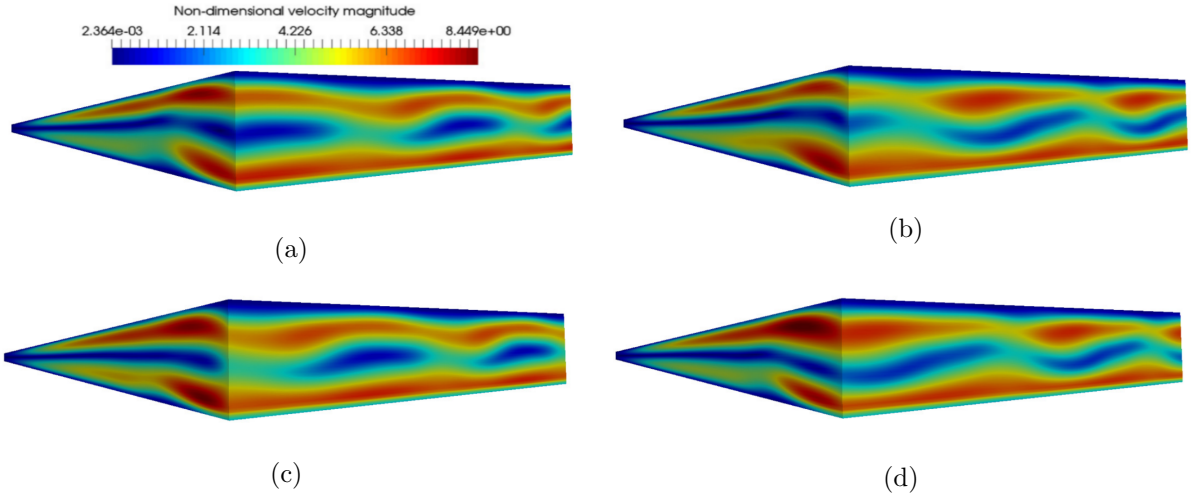

Figure 7.27: Four snapshot evenly distributed along the period of the non-dimensional velocity magnitude for the same parameters of Figure 7.26

Frequency spectra and multiple solutions

By simple visual inspection of the frequency spectrum, it is evident that it is rather chaotic for $Pr = 0.01$ [Figure 7.28a corresponds to the disordered pattern shown in Figure 7.23], whereas only one frequency and its multiples appear in Fig. 7.28c (corresponding to Figure 7.25).

Additional insights follow naturally from the corresponding plots obtained by uncoupling the momentum and energy equations.

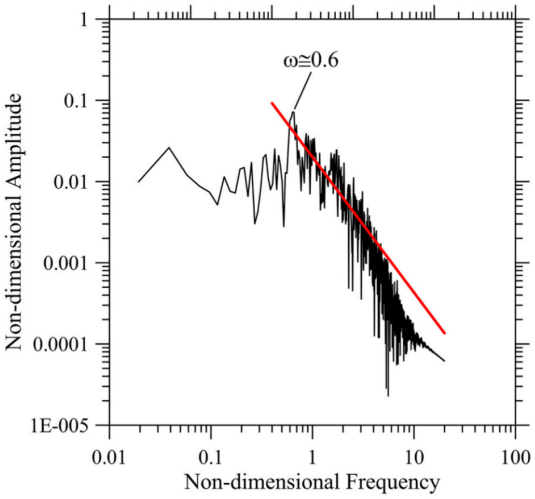

(a) $Pr = 0.01$, temperature equation coupled.

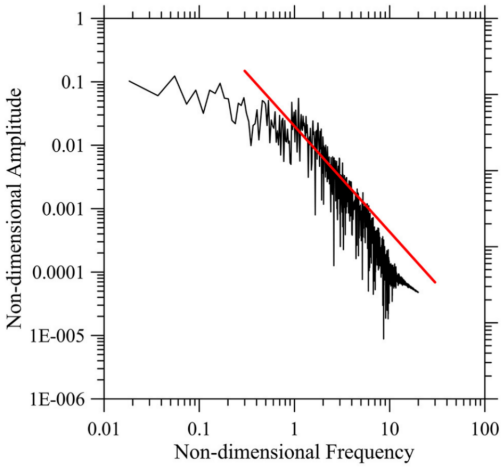

(b) $Pr = 0.01$, temperature equation uncoupled.

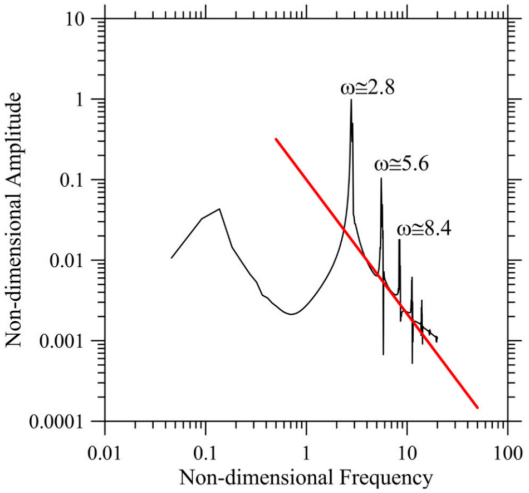

(c) $Pr = 0.05$, temperature equation coupled.

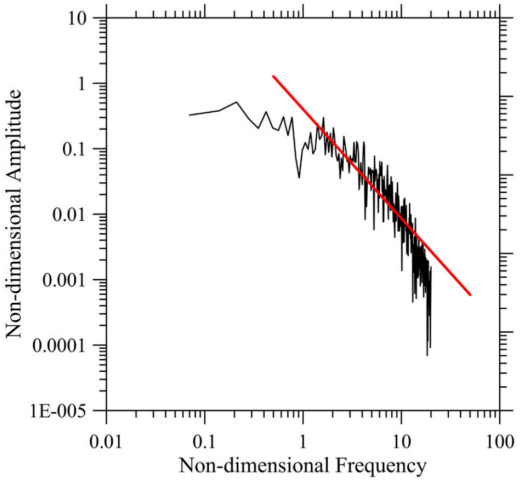

(d) $Pr = 0.05$, temperature equation uncoupled.

Figure 7.28: Frequency spectra for $Ra = 2000$, $A_z = 10$ and periodic boundary conditions.

The notable change displayed by the frequency spectrum for $Pr = 0.05$ when temperature and momentum are decoupled (Figure 7.28d) with respect to the nominal situation as shown in Figure 7.28c is particularly significant as it definitely sheds some light on the origin and nature of the observed perturbations for this case. The transition from periodic flow (with disturbance travelling continuously along the z direction) to chaotic flow similar to that shown in Fig. 7.23, indeed, indicates that the frequency mode ($\omega \approx 2.8$) seen for $Pr = 0.05$ is an OLR and that it is taken over by a hydrody-

namic disturbance (similar to that occurring for $Pr = 0.01$) when dynamical coupling between the mean shear stress and the buoyancy force (at the root of the OLR mechanism) is no longer allowed. None of the peaks visible in Figure 7.28c survives in Figure 7.28d.

Also the comparison between Figures 7.28a and 7.28b is instrumental in producing some additional useful information about these phenomena. Though the spectrum retains a similar multi-frequency (broad-band) structure when the temperature equation is uncoupled, the main peak visible in Figure 7.28a in the small-frequency region of the spectrum (around $\omega = 0.6$) disappears in Figure 7.28b. This should be regarded as a clear hint for the OLR nature of the perturbations being associated with that specific peak. Another way to think about this observation is that it indirectly confirms that hydrodynamic disturbances and the OLR modes can be present at the same time in some circumstances. This is not so surprising if one considers that the neutral curves predicted by the linear stability analyses for these two fundamental modes of convection in infinite layers are relatively close. As an example, in the case of horizontal layers, Hart [111] found the hydrodynamic disturbances to be the most dangerous for $Pr < 0.015$, this role being taken over by the OLR mode in the range $0.015 < Pr < 0.27$. Kuo and Korpela [36] confirmed and slightly revised these results showing that for Prandtl number less than 0.033, the shear disturbances are the dominant instability mechanism, whereas the instability is triggered in the form of oscillating longitudinal rolls in the range $0.033 < Pr < 0.2$ (the critical curves for these two different categories of disturbances were also found to be relatively close one to another in terms of values of the Rayleigh number). Delgado-Buscalioni [123] confirmed the existence of a codimension-two point located approximately at $Pr \approx 0.03$ for purely horizontal cavities, showing that it moves toward smaller values of Pr if the considered configuration undergoes a net tilt.

Though the coexistence of different instability modes might have been anticipated on the basis of the information provided by linear stability analyses, the most unexpected aspect revealed by the present simulations is the rather turbulent nature of the flow emerging for small values of the Rayleigh number when the dominant disturbances are hydrodynamic in nature (Figures 7.28a, 7.28b, and 7.28d). In equivalent 2D simulations (Ref. [125]) the flow was found to be laminar. As an example, for $Ra = 9000$ (see Figure 7.16 in the previous section), a bimodal state with two incommensurate frequen-

cies was obtained. As shown here (Figures 7.28a and 7.28b), the 3D flow is featured by a much more complex multimodal temporal behaviour even if the Rayleigh number is as small as 2000. Even more interestingly, this flow displays the ability to develop a range of scales where the energy power spectrum satisfies the well-known scaling law predicted by Kolmogorov ([129], [130], [131],[132]) (represented by the inclined red line in Figures 7.28a and 7.28b).

In order to emphasize this specific aspect, we have used the same approach illustrated by De et al.[133] i.e., we have reported the frequency and related amplitude using logarithmic scales for the axes and comparing the resulting diagram with a power law $P(\omega) = (\frac{\omega}{\omega_c})^{-s}$ (where ω_c is a fitting parameter). Such a comparison has provided evidence that the frequency spectrum of velocities aligns perfectly with an $\omega^{-\frac{5}{3}}$ law in a wide band of frequencies, as implicit in the so-called turbulence similarity hypothesis. The related range of scales corresponds to the energy cascade process originally theorised by Kolmogorov. This author argued that in the chaotic scale-reduction mechanism typical of turbulence, the directional biases of the large length scales are lost as energy is transferred to increasingly smaller scales. In particular, according to the aforementioned similarity hypothesis, a region of wave numbers or frequencies exists where, at any considered scale pertaining to this interval, the flux of the cascading quantity depends only on the dynamic variables on that scale (which leads to the related concept of statistically isotropic and universal turbulence, not to be confused with the large scale flow, which may still be highly anisotropic as shown, e.g., in Figure 7.23).

Such an interval is limited from one side by the length-scale L at which energy is injected into the fluid to produce fluid motion and from the other side by the scale where the kinetic energy of the flow at that scale is converted into internal energy due to frictional effects (we will come back to this concept later).

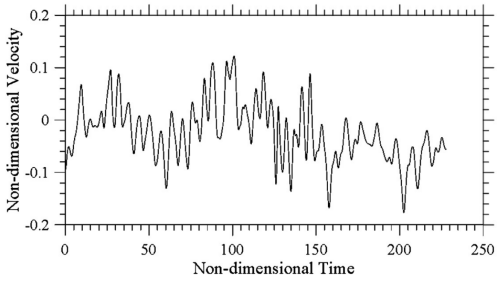

(a) Time plot

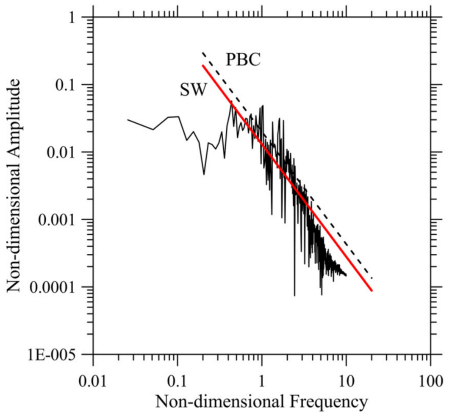

(b) Spectrum

Figure 7.29: Numerical simulation for $Pr = 0.01$, $A_z = 10$, $Ra = 2000$ and with solid walls. Velocity signals at point ($x = \frac{3}{8}A_x$, $y = 0$, $z = \frac{A_z}{2}$.

Interestingly, this behaviour is retained if the periodic boundary conditions at $z = 0$ and $z = A_z = 10$ are replaced by adiabatic solid walls (see Figure 7.29), which indicates the hydrodynamic disturbances, responsible for the cascade of energy from large scales toward smaller ones, have all non-dimensional wavelength in the range between zero and A_z .

To put our results in a broader context, we have allowed the Rayleigh number to grow further. Results for $Pr = 0.01$ and $Ra = 4000$ can be seen in Figs. 7.30a and 7.31a . The major outcome is that, while for this value of the Rayleigh number, the emerging state under the constraint of two-dimensionality would correspond to a simple periodic (single-frequency) wave travelling in the stream-wise direction [123] the 3D results yet demonstrate the existence of an extended set of scales through which the energy is transferred from larger to smaller eddies (slightly shifted to the right of the plot with respect to the corresponding interval seen in Figure 7.28a).Making Ra higher, as expected, also produces an increase in the energy content of the flow (as witnessed by the upward shift of the straight line representing the aforementioned $\frac{5}{3}$ law).

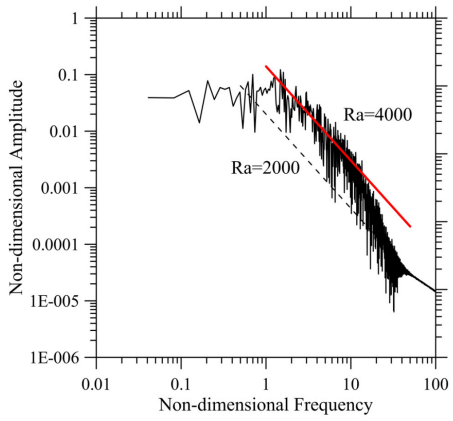

(a) $Pr = 0.01$, regime with dominant hydrodynamic mode.

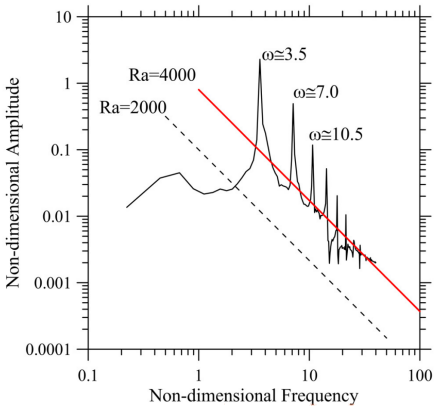

(b) $Pr = 0.05$,OLR mode: though for this case the scaling seems to be compatible with Kolmogorov law, this regime cannot be considered a turbulent one as the spectrum displays just a fundamental frequency and its high order multiples.

Figure 7.30: Frequency spectra: $Ra = 4000$, $A_z = 10$, periodic boundary conditions.

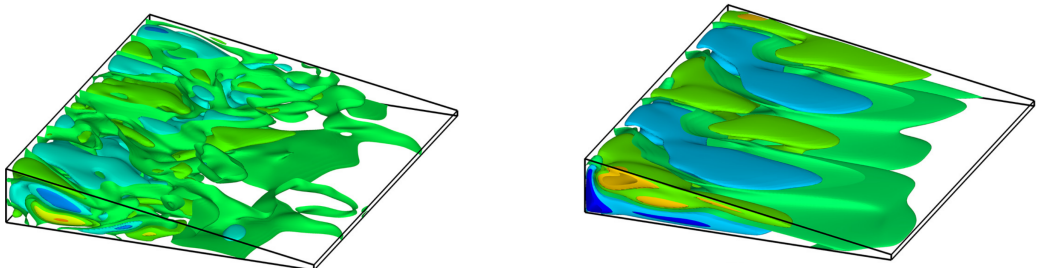

(a) $Pr = 0.01$

(b) $Pr = 0.05$

Figure 7.31: Iso-surfaces of the w velocity component (along z) for the same conditition considered in 7.30a and 7.30b

Apart from the differences between 2D and 3D results, the present findings are relatively surprising if one also considers that in other "similar" problems (buoyancy convection in heated systems for fluids with Prandtl number $Pr \geq O(1)$ and values of $Gr = O(10^5)$ or $O(10^6)$), in general, the two just mentioned scales limiting the cascade from below and from above differ by several (3 or more) orders of magnitude [133], [134].

In the present case, they just span a couple of orders of magnitude. This witnesses the fundamentally different nature of the process leading to the onset of turbulence with respect to other situations in which neither hydrodynamic disturbances nor OLRs are possible (the main source of instability for $Pr \geq O(1)$ being transferred to other mechanisms, see, e.g., Refs. [4] and [134]). For liquid metals, on the one hand, the inertial

regime can be entered by the system for relatively small values of the Rayleigh number (if 3D hydrodynamic disturbances represent the dominant mechanism of instability), on the other hand, the extension of the inertial range is relatively limited (covering a reduced set of scales as shown in Figures 7.28a, 7.28b, 7.28d, and 7.29).

Continuing with the description of the results for $Pr = 0.05$, Figures 7.30b and 7.31b provide evidence that on increasing Ra to 4000, the flow essentially retains its ordered OLR-based spatio-temporal behaviour. Though the overall spectrum shifts to right and upwards when the Rayleigh number is increased (in agreement with the expected increase in the energy content of the flow and frequency of the fundamental mode of oscillation), the peaks are still sparse and correspond to multiples of the fundamental frequency (the reader is referred to Figs 7.28c and 7.30b for$Ra = 2000$ and 4000, respectively). In general, Figures 7.31a and 7.31b may be regarded as a natural continuation of Figures 7.23 and 7.25, respectively.

Under a slightly different perspective, these simple observations might be used to conclude that while the flow is allowed to enter the so-called inertial regime at low Ra when hydrodynamic disturbances are spontaneously selected (most critical disturbances), or artificially induced (preventing the system from "selecting" OLR modes), the attainment of this regime is delayed to larger values of the Rayleigh number when the OLR perturbations are preferred.

Following this very interesting argument and taking into account that $Gr = \frac{Ra}{Pr}$ represents directly the ratio of buoyant to molecular viscous transport, we deemed it necessary to compare the response of the two different fluids for the same value of the Grashof number (as Gr measures the relative importance of the driving force with respect to the opposing viscous effects, it can be regarded as an analogous of the Reynolds number generally used in the literature as a universal "control" parameter in studies about the onset of turbulence).

In line with the expected outcomes, Fig. 7.32 shows that for $Gr = 2 * 10^5$, for both values of Pr conditions are established for which the inertial regime can develop (cf., e.g., Figures 7.28a and 7.32a).

The left region (low-frequency interval) of the spectrum presents a peak (at $\omega \approx 5$), which seems to be the natural evolution of the fundamental mode with frequency $\omega = 3.5$ highlighted in Figure 7.30b, whereas the right part (high-frequency interval) closely resembles that found for the case of dominant hydrodynamic disturbances.

Taken together, Figures 7.32a and 7.32b further witness that the two categories of disturbances can (1) coexist (the reader is also referred to the iso-surfaces in Figure 7.32b displaying an appearance intermediate with respect to the structure of disturbances visible in Figures 7.31b and 7.23) and (2) enhance the turbulent nature of the emerging flow by making the spectra more involved.

Following up on the observation above, we conclude the present section by highlighting the interesting affinity between the present findings and some earlier results presented by Delgado-Buscalioni et al. [135].

These authors performed 3D numerical calculations of natural convection for $Pr =$

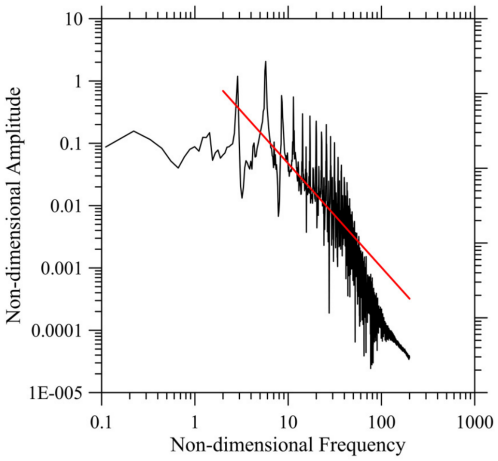

(a) Spectrum.

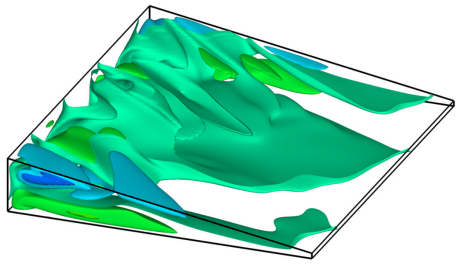

(b) Iso-surfaces of w velocity component (along z).

Figure 7.32: Oscillatory convection (mixed regime with OLR an hydrodynamic modes). $Pr = 0.05$, $A_z = 10$, periodic boundary conditions, $Ra = 20000$ ($Gr = 4 * 10^5$)

0.025 in an enclosure with $A_x = 4$ and$A_z = 6$ inclined at 10 °with respect to the horizontal direction (such a case being considered due to the expected coexistence of transversal and longitudinal instabilities given the location of the aforementioned codimension-two point at $Pr \approx 0.03$). For the sake of comparison between 3D and 2D results, they also examined the corresponding 2D enclosure (allowing purely two-dimensional oscillatory hydrodynamic modes only to develop).

Under the constraint of two-dimensionality, a first bifurcation to oscillatory flow was identified, followed by increasing the Rayleigh number by a period-doubling bifurcation. When the constraint of 2D flow was removed, the initial two-dimensional stationary convection was found to undergo a Hopf bifurcation at values of Ra lower than the corresponding ones for the 2D case, with the flow breaking due to the onset of an oscillatory convection with three longitudinal rolls. A secondary frequency for the 3D

flow, observed at $Gr \approx 5 * 10^5$, was found to be basically related to the formation of a bicellular transversal pattern giving rise to a mixed regime with hydrodynamic and OLR modes resembling the dynamics described in the present section (namely, the visible enhancement of turbulence where more instabilities can easily interact).

Kolmogorv scales and multiple solutions

Additional insights into the dynamics presented in previous sections follow naturally from direct comparison with estimates available in the literature about the time scale limiting the inertial range from below, i.e., the so-called Kolmogorov time scale (η_t). Following Paolucci [136] and Farhangnia et al. [137] in a transversely heated cavity, the Kolmogorov time and length scales can be evaluated, respectively, as:

$$\eta_t = 8\pi(PrRa^3)^{-\frac{1}{4}} \tag{7.12}$$

$$\eta_s = \pi \left(\frac{16Pr}{Ra}\right)^{\frac{3}{8}} \tag{7.13}$$

which, for the present conditions, yield the values reported in Table 7.4.
By comparing Table 7.4 with the spectra shown in Figures 7.28a and 7.30a for $Pr = 0.01$, the reader will realise that the shift to the right of the inertial regime produced by an increase in the value of the Rayleigh number is in agreement with the corresponding decrease in the Kolmogorov time scale predicted by equation 7.12 (by indicating with ω_{max} the recognisable maximum value taken by the angular frequency of the disturbance at the end of the inertial regime in these two figures, it can easily be verified that the following correlation holds: $\omega_{max} \approx \frac{2\pi}{\eta_t}$). Such a relationship, however, is no longer valid for the cases with $Pr = 0.05$ and $Ra = 2000$ or 4000 and the only key to understanding such results lies in considering that the related flow has not entered yet the inertial regime ($\frac{2\pi}{\eta_t} \gg \omega_{max}$).

Pr	Gr	Ra	η_t	η_s
0.01	$2 * 10^5$	2000	0.266	0.091
0.01	$4 * 10^5$	4000	0.158	0.070
0.05	$4 * 10^4$	2000	0.178	0.167
0.05	$8 * 10^4$	4000	0.106	0.129
0.05	$2 * 10^5$	10000	0.053	0.091
0.05	$4 * 10^5$	20000	0.032	0.07

Table 7.4: Kolmogorv length and time scales as function of the Prandtl, Grashof and Rayleigh numbers

Nevertheless, the agreement between ω_{max} and the corresponding Kolmogorov frequency for $Pr = 0.05$ holds for $Ra = 10000$ ($Gr = 2 * 10^5$), which confirms the expectation (as already discussed to a certain extent in the preceding text) that the Grashof number should be considered as a more relevant parameter in comparative studies of the process leading liquid metals in differentially heated cavities to develop turbulence (for $Gr = 2 * 10^5$ and both values of Pr, the frequency spectra display the typical features of this regime, Figures 7.28a and 7.32a).
Nature, however, does not always follow apparently logical rules or "straightforward" (obvious) evolution paths, especially when highly non-linear systems are considered. Most unexpectedly (see Figure 7.33a), the agreement with the predicted Kolmogorov frequency ceases, and the typical features of the inertial regime are no longer there as the Grashof number grows further. For $Gr = 4 * 10^5$, indeed, the frequencies visible in the spectrum take again the same scattered appearance already reported for smaller values of Gr. Along these lines, the reader may compare directly Figure 7.33a with the corresponding spectrum shown in Figure 7.30b for $Gr = 8 * 10^4$; apart from the expected increase in the main frequency (maximum visible peak) and ensuing displacement of the other harmonics to the right, these spectra are very similar; comparison of the iso-surfaces in Figures 7.32b and 7.33b also leads to the conclusion that on increasing Gr, the flow takes a more spatially regular structure resembling that of classical OLR disturbances.

These apparently counterintuitive results (showing a kind of "intermittency" with turbulence entering and leaving the dynamics as the Grashof number becomes progressively higher) should be regarded once again as the evidence for the existence of "multiple solutions" potentially affecting the system, i.e., multiple states which can replace each other in given sub-regions of the space of parameters depending on the

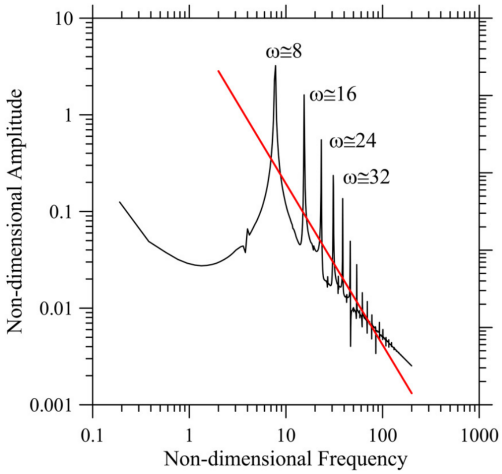

(a) Frequency spectrum.

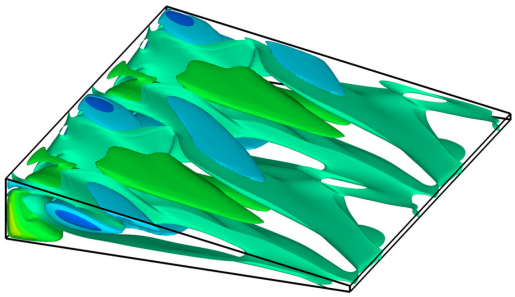

(b) Isosurfaceos of w velocity component (along z).

Figure 7.33: OLR mode at$Pr = 0.05$, $A_z = 10$, $Ra = 20000$ $(Gr = 4 * 10^5)$

considered initial conditions. Even though the relevance of this "aspect" to the case of transversely heated liquid metals has specifically been shown for the case of purely hydrodynamic disturbances under the constraint of two-dimensional flow (see, e.g., Refs. [102] and [125] for the cases with horizontal and converging or diverging walls, respectively), it cannot be excluded that similar dynamics might still be at play when three-dimensional cavities are considered. Among other things, this preconception is further supported from a theoretical point of view by the aforementioned "proximity" of the neutral curves of hydrodynamic and hydrothermal disturbances revealed by existing linear stability analyses on the subject (see, e.g., Refs.[111], [123], and [36]).
As it is known that in a problem developing coexisting branches of solutions, the trajectories of the system in the so-called space of phases can converge selectively to either of the attractors depending on the considered initial conditions (by definition, the basin of attraction of an attractor is the set of initial points whose trajectories fall on the given attractor), in order to address this specific question, we have used an approach similar to that implemented by the aforementioned Gelfgat et al. [102] and Lappa and Ferialdi [125] .Namely, we have explored the system response caused by a variation of the basin of attraction; more precisely, we have repeated the numerical simulation corresponding to the case$Pr = 0.05$ and $Gr = 4 * 10^5$, using the solution obtained for $Gr = 2 * 10^5$ and shown in Figure 7.32b as initial state.

The results, summarised in Figure 7.34, definitely confirm that the multiplicity of solutions is indeed a feature of the considered problem as the velocity field produced

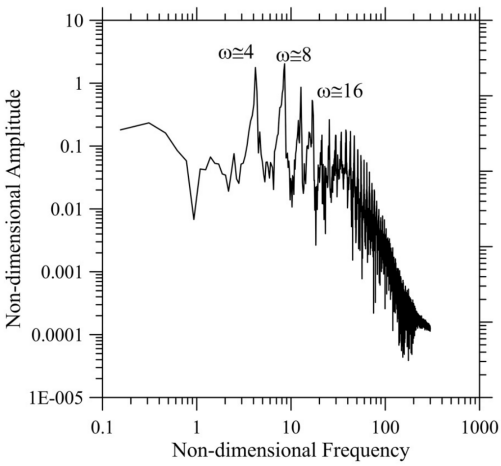

(a) Frequency spectrum.

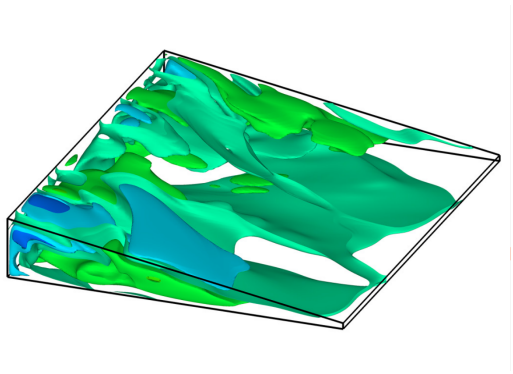

(b) Isosurfaceos of w velocity component (along z).

Figure 7.34: Mixed regime (OLR and hydrodynamic mode) at$Pr = 0.05$, $A_z = 10$, $Ra = 20000$ ($Gr = 4 * 10^5$)

in this way retains the same "turbulent" features seen in Figure 7.32 . The discrete frequency spectrum reported in Figure 7.33a is taken over by a distribution where the amplitude of oscillations varies continuously with ω over an extended interval (to fix ideas, we can think of the state shown in Figure 7.34 as a "continuation" of that reported in Figure 7.32 , existing in parallel with that in Figure 7.33).

This interesting result also sheds some additional light on our earlier finding (the main outcomes being shown in Figures 7.28c and 7.28d) about the possibility to replace a state dominated by the OLR mode with a new solution in which hydrodynamic disturbances become pervasive by uncoupling the momentum and energy balance equations. Besides the canonical method based on a variation of the basin of attraction, the inhibition of temperature disturbances by equations uncoupling should indeed be seen as another possible way to drive the system along a given path of evolution in the case of coexisting "attractors" .Obviously, while with the approach based on a variation of the initial conditions, it is not possible to predict in which "direction" the system will evolve, by disabling the energy equation the system is forced to select and amplify hydrodynamic disturbances, these being the only allowed ones when the temperature does not play an active role in the instability mechanism.

Notably, the agreement with the data reported in Table 7.4 is back when the end of the spectrum in Figure 7.34a is considered.

Apart from the interesting information provided in terms of relationship between the minimum time scale involved in the phenomena and related connection with Pr and

Ra, as anticipated at the end of the section related to the mesh validation, the estimates reported in Table 7.4 can also retrospectively be used to demonstrate further the relevance of the present mesh and its ability to capture the complex dynamics described before. As stated, e.g., by Shishkina [138] in a perfect simulation the mesh size should not be larger than the Kolmogorov length. For the present case, by indicating with Δx, Δy and Δz the space integration steps along the three fundamental directions of the Cartesian coordinate system (refer to the information reported in the section of the mesh validation), the reader will easily realise that the above criterion is largely met with $\frac{\eta_s}{\Delta x}$, $\frac{\eta_s}{\Delta y}$ and $\frac{\eta_s}{\Delta z}$, all being ≥ 1 for all the values of Gr reported in this table.

Taken together, Figures 7.35 and 7.36 finally show that the presence of limiting walls perpendicular to z can have an appreciable impact on the properties of the inertial regime by causing, on the one hand, a decrease in the number of modes (due to the suppression of all disturbances with wavelength larger than $A_z = 10$) and, on the other hand, an ensuing mitigation of the energy content.

As a concluding remark, we would like to point out the following: All the information reported in this section are valuable on their own due to the insights they give into the high-dimensional chaotic state of these flows in terms of involved time and length scales (and their scaling with the problem characteristic numbers). Unfortunately, however, they cannot be used to provide clues or hints about the "process" leading the flow to enter this regime. In other words, targeting an improved understanding of the mechanisms by which a number of coexisting modes can be developed when the main problem parameter (the Rayleigh number or the Grashof number in our case) is progressively increased is not possible in this framework.

The reader is referred to the next section for further elaboration of these aspects, the introduction of adequate concepts and related applications/implications.

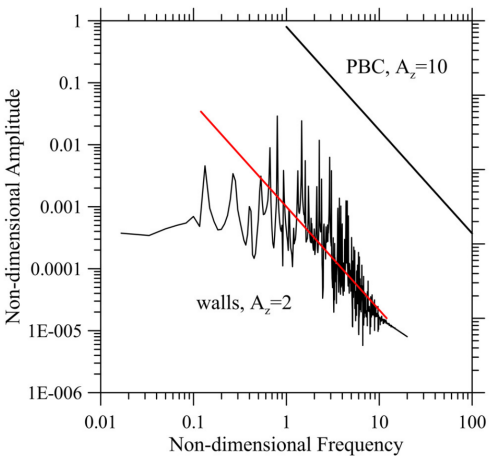

(a) Frequency spectrum for $A_z = 2$

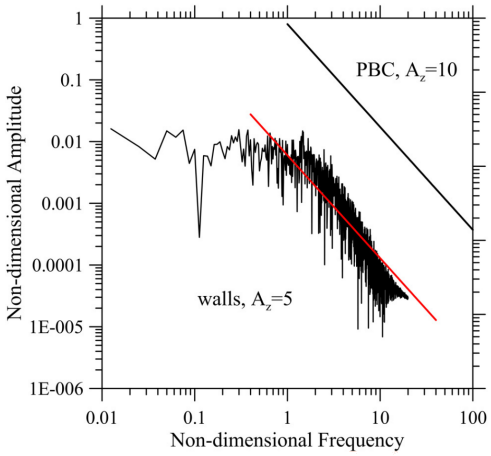

(b) Frequency spectrum for $A_z = 5$

Figure 7.35: Frequency spectra with solid walls delimiting the system along the z direction.$Pr = 0.01$, $Ra = 4000$, $Gr = 4 * 10^5$.

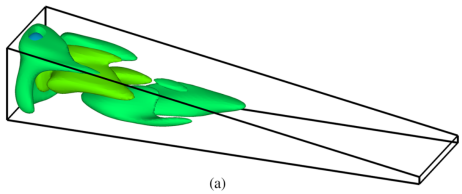

(a) Isosurfaces for $A_z = 2$

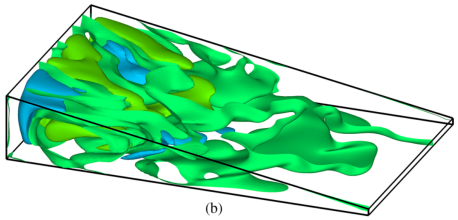

(b) Isosurfaces $A_z = 5$

Figure 7.36: Isosurfaces of the w velocity component (along z) for the same conditions of figures 7.35a and 7.35b

Correlation dimension and transition from low-dimensional to high-dimensional chaos

In the present paragraph we rely on the notions given in Chapter 6a especially those discussed in the section 6.3.2. Indeed once we have distinguished among the nature of two main categories of instabilities, namely the OLR and the hydrodynamic modes, a further aspect which needs to be discussed is the system evolution towards chaos. We will not further discuss the main concepts needed, addressing the interested reader to Chapter 6a. Especially we will make use of the correlation dimension defined in equation 6.9 and to assess it we will rely on the algorithm of Grassberger and Procaccia [68], described in detail in Chapter 6a. The aim of assessing this quantity is to understand how the system evolves towards chaos and try to infer some information about the onset of chaos.

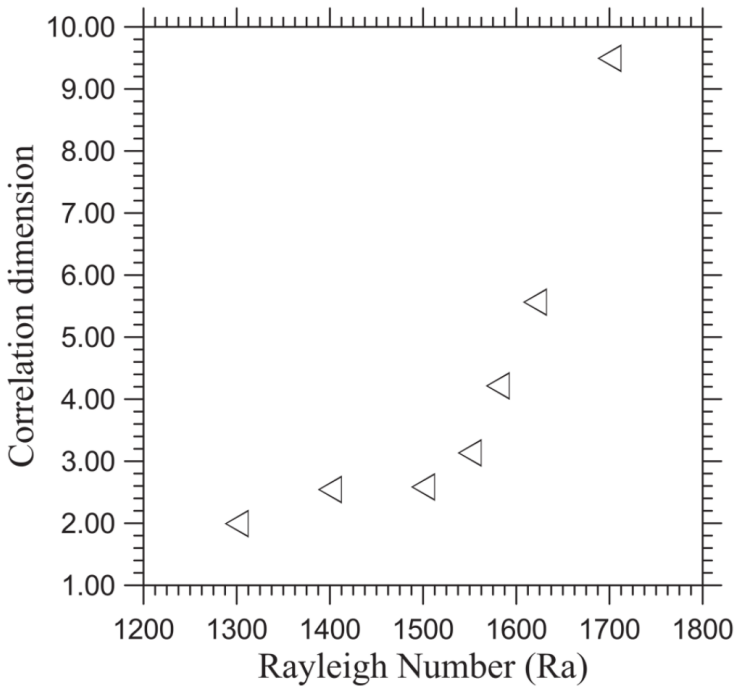

Figure 7.37: Correlation dimension as function of the Rayleigh number $Pr = 0.01$, $A_z = 10$, periodic boundary conditions.

The values taken by D_2 for typical conditions considered in the present work are summarised in Figure 7.37. By embodying the concept of progressively increasing structure on finer and finer length scales and the related concept of sensitivity to the initial conditions, the growing non-integer values displayed by D_2 clearly reveal the emergence of features typical of chaos.

Interestingly, as soon as Ra exceeds 1550, D_2 becomes larger than 3 ($D_2 \approx 3.14$ for $Ra = 1550$, $D_2 \approx 4.22$ for $Ra = 1580$) and then suddenly grows for higher values of Ra. Such a gain in chaotic features can clearly be interpreted as the quick development of fully developed turbulence (as witnessed by the number of coexisting modes visible in the final state shown in Figure 7.28a for $Ra = 2000$; the reader is also referred to the sequence of signals reported in Figure 7.38 for increasing values of Ra).

For the sake of precision, at this stage, we should expressly mention that we could not track precisely the evolution of the system in terms of correlation dimension for Ra exceeding 1600 as the algorithm by Grassberger and Procaccia [68],[139] (and other similar approaches, see Refs. [140] and [69]) works only for low-dimensional chaos (correlation dimension close to 4; notably, similar concepts also apply to the Liapunov exponents and related quantities, see, e.g., Ref. [70]). In line with the considerations reported in all these studies, our attempts to measure D_2 for the above cases provided

non-converging values. We decided to include them in the plot solely for the sake of completeness (to provide the reader with a clear clue about the quick progression toward chaos displayed by the system as a value of the Rayleigh number as low as 1600 is exceeded).

Another remarkable conclusion stemming from a careful inspection of Figure 7.37

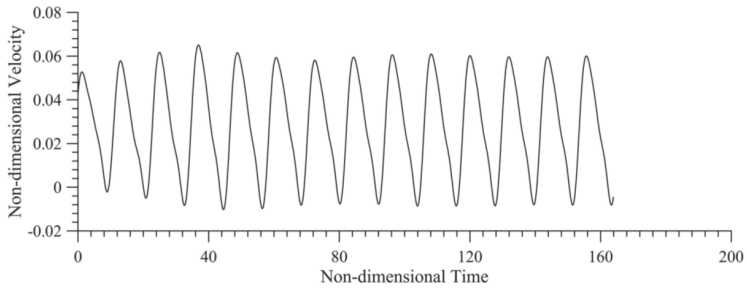

(a) $Ra = 1400$

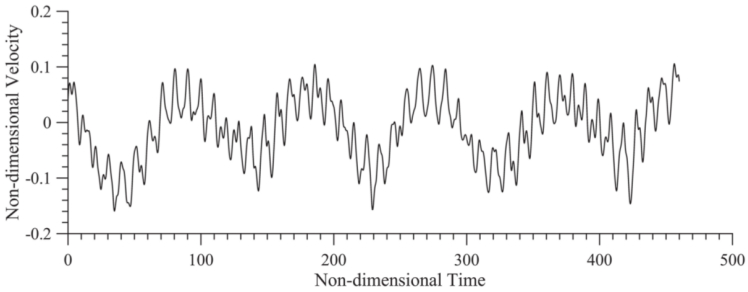

(b) $Ra = 1550$

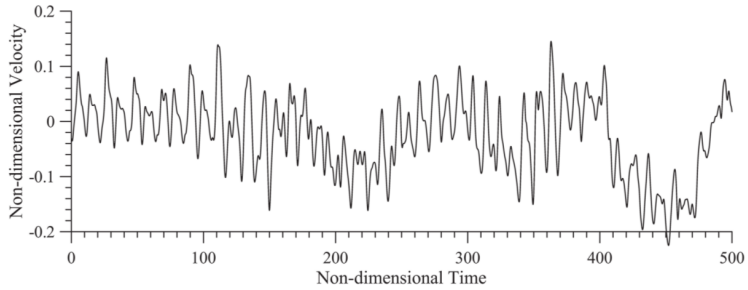

(c) $Ra = 1700$

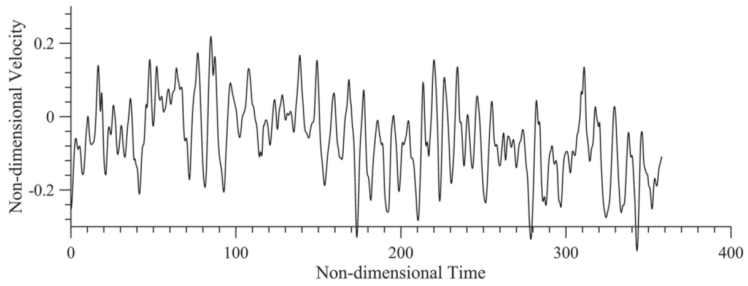

(d) $Ra = 2000$

Figure 7.38: Velocity signals at $x = \frac{3}{8}A_x$, $y = 0$, $z = \frac{A_z}{2}$.$Pr = 0.01$, $A_z = 10$, periodic boundary conditions and different values of the Rayleigh number.

is that for the present problem, fractalisation can be produced starting from a condition where the spectrum displays two incommensurate frequencies only ($D_2 \approx 2$ for $Ra = 1300$ and $D_2 \approx 2.59$ for $Ra = 1500$).

For the simple case of only two incommensurate frequencies, the phase trajectory may be imagined as a set of points pertaining to a toroidal surface T^2 in the three-dimensional phase space. According to the classical Ruelle-and-Takens scenario, a third independent frequency should always appear before transition to chaos is permitted, i.e., the attractor should become a hyper-torus T^3. This is indeed what is formalised by the so-called Newhouse-Ruelle-Takens theorem [72] which asserts that a torusT^3 , under the actions of some perturbations, degenerates to a "strange attractor", and therefore, the existence of three frequencies (i.e., three degrees of freedom) should generally be regarded as a necessary and sufficient condition for the onset of a chaotic regime. The indirect outcome of our observations in the present case is that, by allowing transition to chaos directly from a torus T^2 , the present findings are another example of results supporting the alternate route toward chaos proposed by Curry and Yorke [72]. These authors theorised direct transition to chaos via gradual deformation of an initially closed curve in the phase space due to a continuous stretching and folding process (the reader is referred to the work by Paul et al. [141] and reference therein about other related examples in the literature, e.g., the Curry-Yorke scenario in Rayleigh-Bénard convection).

7.4.4 Conclusions

Continuing an earlier work where the analysis of the problem related to the Hadley flow circulation in containers with non-horizontal top and bottom walls and no net inclination was limited to purely two-dimensional flow (chosen as an archetypal situation where the well-known Squire and Rayleigh criteria are no longer valid), in the present analysis, we have explored the 3D effects that emerge when the constraint of two-dimensionality is removed.

In the literature, often a dichotomy has been drawn between the two fundamental categories of fluid-dynamic disturbances thought to be enabled in such circumstances, namely, two-dimensional hydrodynamic and 3D hydrothermal (helicoidal) modes. We have shown that these two models (transverse and longitudinal rolls) are opposite idealised extremes, both being severe approximations to a more complete representation

of reality. In particular, we have found that these disturbances are not mutually exclusive, nor are they progressive and that the development of turbulence via a hierarchy of instabilities can involve a rich variety of concurrent paths or lines of evolution. The subject has been addressed via numerical solution of the overarching set of equations, including the mass, momentum, and (internal) energy balance laws. These equations have been solved numerically in their complete, non-linear, time-dependent, and fully coupled form.

A variegated strategy of attack has been implemented to address such a complex subject, including (but not limited to) an analysis of the ability of these systems to develop multiple branches of solution and related progression from low-dimensional to high-dimensional chaos.

As the main driver for the selection of different "attractors" in systems with multiple solutions is generally represented by a variation of the basin of attraction, simulations have been performed assuming canonical initial conditions corresponding to a thermally diffusive quiescent state or using already developed flow at a given value of the Rayleigh number as initial state to explore the effects produced by an increase in such parameter.

As such strategy, however, cannot produce clues about the connections between the initial state and the nature of the emerging disturbance, in parallel, further understanding of these instabilities has been gained by uncoupling the momentum and energy equations (a fruitful alternative for obtaining insights that are hidden to experimental analysis and which allows new paths of enquiry to be proposed). Both these approaches provided independent lines of evidence pointing toward the same conclusion, namely, that for this problem, multiple states exist which can replace each other in given subregions of the space of parameters.

In particular, for the smallest considered values of the Prandtl number ($Pr = 0.01$), the emerging disturbances have been found to cause sudden transition to relatively chaotic states for values of the Rayleigh number even smaller than those required to excite regular (time-periodic) waves travelling in the stream-wise direction in the 2D case. These perturbations clearly display a 3D nature as witnessed by the presence of recognisable velocity peaks along the third direction and spatially extended vortices in the xz plane. Equation uncoupling (in the framework of the approach described above) has been instrumental in discerning that temperature variations and related buoyancy

effect play no role in the mechanisms leading to the amplification of such (hydrodynamics) perturbations and ensuing sudden transition to chaos.

On the other hand, fully coupled simulations have demonstrated that the spatially pervasive presence of hydrodynamic modes does not prevent the system from developing in parallel OLR flow, as witnessed by the presence of specific recognisable peaks in the frequency spectrum (these peaks are no longer visible inasmuch the OLR is no longer allowed to exist without temperature and momentum coupling).

Though these OLR modes tend to be more frequent as the Prandtl number is increased and their emergence seems to rule out the development of hydrodynamic disturbances (at least for relatively small values of the Rayleigh number), however, hydrodynamic modes overwhelmingly re-enter the dynamics as soon as the momentum and energy balance equations are uncoupled or the Grashof number is sufficiently increased.

The spectra relating to these systems are relatively complex, displaying an extended range of "active" frequencies. Interestingly, for all these cases (being naturally produced for $Pr = 0.01$ or artificially induced by equation uncoupling for $Pr = 0.05$), relatively wide intervals of frequency can be identified in which the spectrum of velocities aligns perfectly with an $f^{\frac{5}{3}}$ law, as implicit in the Kolmogorov similarity hypothesis. This indicates that when the constraint of two-dimensionality is removed, hydrodynamic disturbances can cause turbulence to become isotropic much in advance (in terms of applied value of the Rayleigh or Grashof number) with respect to equivalent 2D cases. For $Pr = 0.05$, though solutions with more regular frequency spectra (being limited to the fundamental frequency and its higher harmonics) are generally preferred, these flows can coexist (for the same value of the Grashof number) with the turbulent ones discussed above in the form of "multiple solutions".

Regardless of the considered Prandtl number, in general, higher values of the Grashof number have been found to produce a twofold effect, i.e., an increase in the average energy content of the flow and an expansion of the "extension" (in terms of involved scales) of the inertial range.

Additional insights into the onset of this kind of turbulence have been obtained through evaluation of the so-called correlation dimension for conditions in which the chaos can still be considered low-dimensional (relatively small values of Ra or Gr). Through this quantity (generally used to characterise the "fractal nature" of "attractors" in the space of phases), we could track precisely the progression of the system from an initial

quasi-periodic state toward fully developed turbulence due to the progressive excitation of new degrees of freedom. By virtue of this approach, in particular, we could discern that the transition from low-dimensional to high-dimensional chaos takes a specific path, which falls under the general heading of Curry-Yorke scenario (that is, direct transition to chaos being allowed via gradual corrugation of a T^2 torus).

Chapter 8

Marangoni-Bénard convection in a viscoelastic fluid

As discussed by Bergè et al. [142] the evolution of a dynamical system can be described by means of a phase trajectory, which is a curve traced in the phase space having as many dimensions as the number of degrees of freedom of the system. A framework for understanding such dynamics is represented by the so-called chaos theory, a modern development standing at the intersection of physics and mathematics. In the last 30 years, certain universal routes, which dissipative systems take in transitioning from regular to irregular states, have been identified, including (but not limited to) the Ruelle-Takens scenario, the Feigenbaum scenario, and the Manneville-Pomeau scenario (see Chapter 6a for a more detailed description about this topic).

The field continues to burgeon and bring surprises to this day (not all of the potential paths of evolution and related intricacies have been discovered or observed yet). Leaving aside for a while the related differences, such scenarios share a feature, that is, they predict the evolution toward chaos due to the excitation of new degrees of freedom in the considered system [142].

A typical workhorse to test these theories is represented by thermal convection: The study of pattern formation in thermal convection is an extremely vast field encompassing different "variants" such as thermo-gravitational (Ref.[143]), thermo-capillary (Refs. [144], [145], [146], [147], [148], [149]), and thermo-vibrational flows (Ref. [150]). As an example, for the case of gravitational Rayleigh-Bénard (RB) flow, a fairly comprehensive picture has been elaborated in the last three or four decades. These studies include the pattern formation in layers of infinite extent (formulated in Busse's exten-

sive theory), the discovery of spiral-defect chaos (Ref. [151]), transition to turbulence (Refs. [152] and [153]), the dynamics of systems transversely heated, the joint influence of vertical and horizontal temperature differences (inclined layer convection; see, e.g., Ref. [134]), natural flows in nanofluids (Ref. [154]), and so on (see, e.g., Refs. [4] and [155] for a recent review). For the specific case of liquid metals and systems being heated from the side (temperature gradient perpendicular to gravity), interestingly, a running line of inquiry has entirely been devoted to the ability of these systems to produce multiple solutions (see, e.g., Refs. [107], [108],[102], [125]), i.e., to explore the existence in the space of parameters of different branches of laminar flows that coexist and can be effectively selected by a fluid-dynamic process depending on its initial state. Interestingly, this property is akin to that of fully turbulent flow for which SIC (sensitivity to initial conditions) is a well-established feature.

Paralleling such an increase in our understanding of dissipative systems such as those represented by the natural fluid-dynamic processes mentioned above, has been the recent identification of some special states, which can be "excited" in granular matter or colloidal suspensions when they are subjected to "vibrations" or other types of harmonic forcing (Refs. [156], [157], [158], [159]). These excitations, typically manifesting as localised time-periodic convective structures in an otherwise uniform or patternless background, have been named "oscillons". Unlike states that display confinement only in the direction perpendicular to the pattern's wave vector (e.g., wormlike solutions such as those reported by Refs. [160], [161] [162]), oscillons are highly localised in all spatial directions. Rather than producing chaos, these features have typically a propensity to assemble into "molecular" and "crystalline" structures forming very regular and ordered patterns (Refs. [157] and [163]).

In the present work, we identify similar features in a completely different problem in which, for the first time, oscillons, which we loosely define as the spontaneous localization or confinement of oscillatory phenomena to a limited subregion of an otherwise stationary pattern in a translationally invariant system, are seen even if no mechanical forcing is present. More precisely, we consider simple surface-tension driven convection in a layer of a viscoelastic fluid uniformly heated from below (i.e., Marangoni-Bénard convection, MB, also known as the Pearson instability after Ref. [40]), which we expressly select as a minimal model to inquire about the role of oscillons in determining the states of a dissipative system when new degrees of freedom are progressively ex-

cited.

There is a vast literature dedicated to this type of flow and related hierarchy of bifurcations when the control parameter is increased for the case of Newtonian fluids. The interested reader may consider, for instance, Schwabe [164] for recent experiments and Colinet et al. [165] for an extensive review of existing studies for Newtonian fluids.

For high-Pr fluids, it is known that when the disturbances responsible for the onset of convection saturate their amplitude, the flow self-organizes to form steady aesthetic hexagonal cells. Other steady patterns, however, become possible if the Marangoni number is increased. They differ from the classical honeycomb structure essentially due to a change in the prevailing topology, which shifts from a hexagon-based symmetry to a new organization based on the coexistence of squares (Ref. [43]). Interestingly, the transition sequence arises via localised changes by which threefold vertices of the initial hexagonal cells become fourfold. The tendency to develop square cells can also be reinforced by a decrease in the value of the Prandtl number (while keeping fixed the Marangoni number). Indeed, at Pr = O(1), the primary mode of MB convection is given by square cells instead of hexagons. These cells coexist with rolls near the threshold of the primary instability. On increasing Ma, in turn, such structures tend to be replaced by unsteady triangular cells. If the Prandtl number is further reduced (liquid metals, $Pr < 0.23$), as predicted by Thess and Bestehorn [45] (the reader being also referred to Ref. [166]), steady hexagons are recovered as the preferred mode of convection. Nevertheless, the flow perpendicular to the free surface changes direction with respect to the typical structure seen for $Pr > 1$, which makes such hexagons the mirror image of those generally seen for high Prandtl number liquids, thereby explaining why they are generally called "inverted hexagons"(see Chapter 4a for more information about this topic).

Some attempts aimed to clarify the dynamics in the case of viscoelastic fluids are relatively rare and sparse (relevant and valuable examples along these lines being represented by the few studies cited in the following). By careful readings of these works, the reader will easily realise that some general consensus exists that when fluid elasticity enters the dynamics, as the well-known principle of exchange of stability is no longer valid, both stationary and oscillatory solutions become possible at the onset of convection. In particular, steady states are taken over by oscillatory solutions when a given threshold in terms of the relaxation time is exceeded (Refs. [167], [168], [169],

[170], [171]). In general, the critical Marangoni number required for these oscillatory flows to emerge is smaller than the corresponding value for Newtonian fluids. This condition is generally referred to as "overstability" see, e.g., Ramkissoon et al. [172]and Hernández Hernández and Dávalos-Orozco [173].

Notably, with a few exceptions, where some attempts were made to explore the system response for slightly supercritical conditions (see, e.g., Refs. [174] and [52] who proposed some numerical experiments which elegantly illustrate weakly nonlinear dynamics), existing studies have essentially been limited to the determination of the conditions for the onset of the primary (steady or oscillatory) flow in the framework of the typical protocols of the linear stability analysis

. In the present work, we expressly target the investigation and ensuing understanding of the system dynamics for conditions in which solution of the complete overarching fluid-dynamic equations in their non-linear and time-dependent form is required. Indeed, we consider circumstances with the Marangoni number attaining magnitudes corresponding to several times the critical value for the Newtonian case.

Beyond the mere motivation to bridge the abovementioned gap, we are specifically interested in pushing forward the MB system as a new archetypal problem to improve our fundamental understanding of some of the processes discussed before (about the general and specific dynamics of dissipative systems). More precisely, our two-fold purpose is to show that:

- MB convection in viscoelastic fluids can produce oscillons just as vibrated granular matter or colloidal suspensions;
- apart from supporting the formation of ordered patterns [157] oscillons and their interactions can even promote transition to chaos (via the alternate route represented by the Curry-Yorke scenario, a still debated possible substitute of the Ruelle-Takens scenario; see, e.g., Refs. [49] and [175]).

Most interestingly, as we will show later, for the present conditions such a mechanism is mediated by the coexistence of "multiple solutions" and the emergence of strange attractors as the relaxation time of the considered viscoelastic fluid is increased.

8.1 Mathematical model, system and boundary conditions

In order to approach the problem described in the present chapter the set of equations presented in Chapter 2, namely the continuity 2.2, energy 2.4 and momentum 2.9 (or they non-dimensional counterparts: 2.24, 2.26 and 2.25) need to be enriched by a further transport equation describing the stresses $\underline{\underline{\tau}}$. Such equation can be built up considering a different constitutive law. The newton law discussed in Chapter 2 indeed has to be replaced by one of the models discussed in Chapter 3a Section 5. In particular in the following the Oldroyd-B model has been used.

The system considered in the present analysis is a layer of viscoleastic fluid shown in Figure 8.1 and an extension L_x and L_z both in x and in z direction and a depth d.

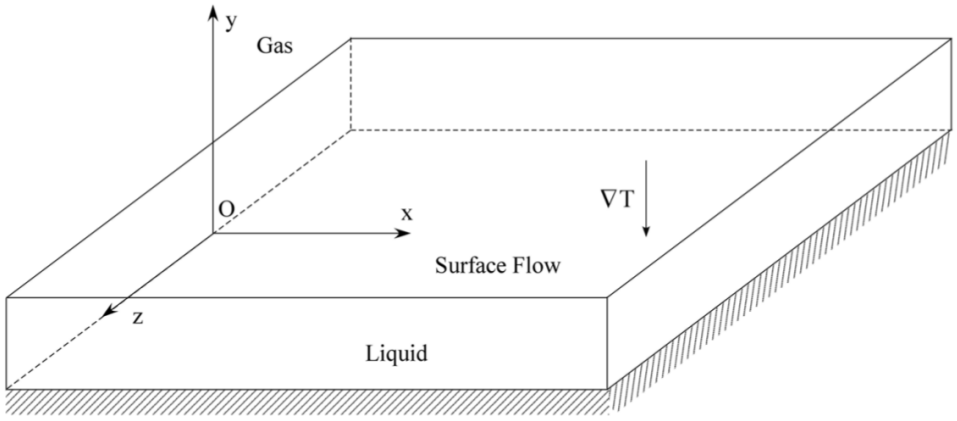

Figure 8.1: System considered in the present chapter

With the two quantities introduced above it is possible to define the aspect ratios along x and z, being $A_x = \frac{L_x}{d}$ and $A_z = \frac{L_z}{d}$ respectively. In particular in the result shown in the following L_x has been kept equal to L_z and hence $A_x = A_z = A$.

In addition to classical Prandtl and Marangoni numbers a variety of other parameters can be introduced. Some of them, such as Deborah number have been defined in Chapter 3a, however here they take a more specific form. The Deborah number indeed in this chapter is defined as follows:

$$De = \Theta = \frac{\alpha\lambda}{d^2} \tag{8.1}$$

The quantity defined in 8.1 is also known as "elasticity number", see e.g. Parmentier et

al. [52], Li and Khayat [175] other important parameters which we will need throughout this chapter are the so-called viscosity ratios ζ and β_0:

$$\zeta = \frac{\eta_p}{\mu} \tag{8.2}$$

$$\beta_0 = \frac{\mu}{\mu + \eta_p} \tag{8.3}$$

$$\tag{8.4}$$

where μ and η_p are the Newtonian and polymer viscosities respectively. Moreover through the 8.3it is possible to define the generalised Prandtl number:

$$Pr_g = \frac{Pr}{\beta_0} \tag{8.5}$$

The equations introduced above applied to the system of Figure 8.1 have to be supplied by a relevant set of boundary conditions, namely:

- periodic boundary condition on the patches perpendicular to the free surface;
- Rigid wall with fixed temperature on the bottom;
- on the rigid free surface the Marangoni boundary condition (see chapter 2 equations 2.15 and 2.16) has been imposed. Moreover in order to model the temperature on such boundary a heat flux has been imposed through a fixed Biot on it.

The latter point need s some further explanation. First the Marangoni boundary condition has to be slightly modified in order to take into account the viscoleastic effects, hence the modified version in non-dimensional terms reads:

$$\left[\left(\nabla \underline{V} + (\nabla V)^T\right) + \underline{\underline{\tau}}_p\right] \cdot \underline{n} = -Ma\left(\underline{\underline{I}} - \underline{nn}\right) \cdot \nabla T \tag{8.6}$$

where $\underline{V} + (\nabla V)^T$ is the Newtonian contribution while $\underline{\underline{\tau}}_p$ is the viscoelastic one. Secondly the heat flow on the free surface is given by:

$$\nabla T \cdot n = -BiT \tag{8.7}$$

The last point which need some explanation before leaving this section is the numerical solution of the equation mentioned above. As done in all the calculations throughout

this thesis in order to solve the equations the Finite Volume Method (FVM) has been employed. It is not the aim of the present section to give a full description about the numerical method, discretisation schemes and the solution algorithms used in the following, addressing the interested reader to Chapter 5a, where the FVM and related arguments are treated in detail. Here we just remind that all the simulations has been carried out using the open source software OpenFoam, which is based on the FVM and relies on the so-called category of projection methods in order to obtain an equation for the pressure. More precisely the present results have been obtained with the PISO (Pressure Implicit with Splitting Operator see Chapter 5a) on a collocated grid (see e.g. Rhie and Chow [55]).

Moreover, the diffusive and convective terms in the parabolic (momentum and energy) equations have been treated with standard central differences and second-order accurate Lax-Wendroff spatial schemes, respectively.

Due to the lack of diffusive terms, which would make it parabolic in time or elliptic in space, unfortunately, the constitutive equation for the viscoelastic stresses is hyperbolic in nature. For this reason, in order to mitigate problems relating to the numerical stability of the algorithm, for this equation we have replaced the Lax-Wendroff schemes with upwind schemes. This approach proved successful over the entire range of considered values of the elasticity number.

Some special attention has been devoted to the momentum equation as well. Following Favero et al. [176] we have increased its numerical stability by introducing two diffusive terms having similar computational "weight" and meaning, one at the left-hand side and the other at the right-hand side of the equation. With these two mathematically equivalent contributions, one being numerically implemented in an implicit way, while the other is treated explicitly, the enriched equation reads (in non-dimensional terms):

$$\frac{\partial \underline{U}}{\partial t} + \nabla \cdot [\underline{U}\underline{U}] - Pr\,(1+\zeta)\,\nabla^2 \underline{U} = -\nabla p - Pr\zeta \nabla^2 \underline{U} + Pr \nabla \cdot \underline{\underline{\tau}}_p \tag{8.8}$$

Though the two terms are equivalent from a mathematical point of view, they are not from a numerical point of view, which provides the solution with an amount (quantitatively negligible) of residual diffusion sufficient to increase appreciably the "ellipticity" of the momentum equation and improve its numerical stability.

8.2 Validation and mesh refinement study

8.2.1 Validation

Toward the end of using such an algorithm to address the fundamental questions set in the Introduction, it is extremely important the validation study. In this regard, we have examined a relatively wide spectrum of conditions through comparison with well-established results and other available (relevant) solutions for both cases of isothermal and non-isothermal flows.

In particular, as a first-level activity to test the response of the current implementation of the Oldroyd-B model, we have focused on the classical problem relating to the non-inertial flow through a 4:1 planar contraction (set in the benchmark study by Ref. [177]). The outcomes of such comparisons are summarised in Table 8.1, from which it can easily be verified that the discrepancy between the present results and the very accurate data reported in that study lie below 2%.

De	X_r Ref [177]	X_r (Present)
0.5	1.452	1.479
1.0	1.279	1.301

Table 8.1: Comparison with the data reported in the benchmark study by Alves et al. [177]. Variation of the size of the vortex X_r formed in the corner of the contraction as function of the Deborah number for the Oldroyd-B fluid (present mesh 2×10^4)

As a second-level of such a validation hierarchy, after sifting through existing studies in the literature, we have considered the data available in the linear stability analysis by Parmentier et al. [52] for $Pr_g = 1$; this is the most relevant case we could identify with respect to the subjects addressed in the present work. The results of [52] are obtained with $Bi = 0$, meaning that the free surface is adiabatic. This is achievable in the framework of the linear stability analysis, however it is not possible to obtain the same outcomes through the numerical integration because, being the interface adiabatic, the system after a certain amount of time will become perfectly isothermal, preventing the convection to be triggered. To overcome this issue two test cases at Bi slightly larger tha 0 have been run and then the results have been interpolated at $Bi = 0$. Moreover two values of β_0 have been considered, namely 0.1 and 0.2, producing the following matrix of the test cases:

Another aspect which has to be taken into account is that the numerical simulations

Case	Test 1	Test 2	Test 3	Test 4
Pr	1	1	1	1
β_0	0.1	0.2	0.1	0.2
θ	0.2	0.2	0.2	0.2
Bi	0.1	0.1	0.2	0.2

Table 8.2: Test cases parameters

need to be run at Ma slightly larger than the critical one, leading to the critical values of such parameters slightly larger to those obtained by [52]. On the other hand how we will see in the following this difference is relatively small.

Before introducing the critical values it is worth noting that the critical thresholds, according to [52] tend to increase when the Bi is raised. Moreover it is useful to introduce the critical rate of heating defined as

$$H = \frac{Ma}{Ma_{cr}} \tag{8.9}$$

where Ma_{cr} is the Newtonian critical Marangoni number equal to 79.607. H and Ma for the for test case reported in Table 8.2 are shown in Table 8.3. Moreover in the same table there are also the critical wavenumber and non-dimensional angular frequency: The values at $Bi = 0$ are obtained through a linear interpolation of those shown in

Case	1 (Bi=0.1,$\beta_0 = 0.1$)	2 (Bi=0.1,$\beta_0 = 0.2$)	3 (Bi=0.2,$\beta_0 = 0.1$)	4 (Bi=0.2,$\epsilon = 0.2$)
Ma	65.505	81.031	68.010	82.478
λ	0.823	1.018	0.854	1.036
ω	7.1-7.3	4.76	7.3	4.83
k	3.740	3.324	3.808	3.324

Table 8.3: (Rate of heating, Marangoni numbers, angular frequencies, and wave numbers for the test cases described in Table 8.2

Table 8.3. The results of such operation are compared to the values of [52] in Table 8.4. From the Table 8.4 it is possible to see a good agreement with the results of [52], producing in case of $\beta_0 = 0.1$ a non-dimensional frequency of 7.3, which agrees to that predicted by [52] with an error less than 1.5 %. similarly for $\beta_0 = 0.2$,we found a percentage difference limited to 3%.

β_0	0.1		0.2	
	Present	Result of [52]	Present	Result of [52]
H	0.792	0.775	1	0.96
ω	7.3	7.4	4.69	5
k	3.672	3.7	3.324	3.4

Table 8.4: comparison with results obtained by [1] at Bi=0 and for $\beta_0 = 0.1$ and 0.2 wit a mesh of 200x40 points

8.2.2 Mesh refinement study

The influence of the number of grid points on the numerical solution can be gathered from Tables 8.5 and 8.6 for two representative cases corresponding to the onset of stationary and oscillatory convection, respectively. For such simulations, the value of the Marangoni number has been fixed to 300 as for all the other cases considered in the present work . Starting from initial thermally diffusive conditions, it can be seen that the numerical solution tends toward a well-defined state as the mesh density is increased.

It is evident that the percentage difference displayed by the maximum of the stream function $|\psi_{max}|$ and the angular (non-dimensional) frequency ω falls below 2% as soon as the mesh density exceeds that corresponding to the$200x40$ resolution. Accordingly we have used 40 points along the vertical direction (y) and 200 points along the horizontal direction (200 points along x and 200 points along z leading to a total of $1.6x10^6$ grid nodes in the case of three-dimensional simulations).

Mesh $N_x \times N_y$	$\|\psi\|_{max}$
160 x 32	2.240
180 x 36	2.243
200 x40	2.249
250 x50	2.249

Table 8.5: Influence of mesh refinement on the maximum value of the non-dimensional stream function. $Pr_g = 1$, $\beta_0 = \frac{1}{5}$, $Ma = 300$, $Bi = 0.1$, $\Theta = 5 * 10^{-3}$.

Mesh $N_x x N_y$	ω
160 x 32	0.772
180 x 36	0.798
200 x40	0.814
220 x44	0.827
250 x50	0.831

Table 8.6: Influence of mesh refinement on the maximum value of the non-dimensional stream function. $Pr_g = 1$, $\beta_0 = \frac{1}{5}$, $Ma = 300$, $Bi = 0.1$, $\Theta = 5 * 10^{-3}$.

8.2.3 2D vs 3D

Similarly to the previous chapter, in the present one, the discussion has been divided into two sections as well. Indeed, the first part of the present chapter is entirely devoted to the description of the two-dimensional simulation, while in the latter part, the 3D outcomes are presented. The three-dimensional simulations are needed to investigate an intrinsically 3D phenomenon as the Marangoni Benard convection. The convective structures appearing on the free-surface are, indeed, three-dimensional. On the other hand, the numerical effort needed to conduct an entire parametric study is excessive. For this reason, the introductory 2D parametric study aims to identify possible patterns and Spatio-temporal behaviours which do not depend on the two-dimensionality of the system.

8.3 Results

In order to investigate the sensitivity of the system with respect to a single control parameter, i.e., Θ, we have fixed $Pr_g = 1$, $\beta_0 = \frac{1}{5}$ ($\zeta = 4$), $Ma = 300$, $Bi = 0.1$, with Θ spanning the interval $0 \leq \Theta \leq 0.1$. The considered value of Ma corresponds to approximately four times Ma_{cr} for an unbounded layer of a Newtonian fluid. As implicitly defined by the first two conditions, the considered fluid would reduce to a standard Newtonian liquid with $Pr = 1$ in the limit as $\Theta \to 0$ (which is equivalent to setting $\eta = 0$ [175]). Fluids with $Pr_g \approx O(1)$ (although Pr is not exactly ≈ 1) are representative of a class of water-based polymer dilute solutions at relatively high temperatures, e.g., water at 70 °C with limited amount of a polymer such a PAM, PEG, PEO, PVP, xanthen gum, etc. Assuming $\lambda \approx 10^{-3}$ s (a typical realistic value for small polymer concentrations), this value would correspond to $\Theta = \frac{\alpha\lambda}{d^2}$ spanning the

range from $\approx 5*10^{-3}$ to 0.05 on varying the depth of the layer from 0.5 mm to 0.05 mm. Though in the initial part of this section, we limit ourselves to discussing two-dimensional (2D) findings as a first necessary step toward the interpretation of the even more intricate three-dimensional (3D) behaviours, we are obliged by the complexity of the results to articulate their presentation in different stages of discussion (for increasing values of Θ). In particular, first we address the cases in which the emerging dynamics are clearly recognizable in terms of well-defined attractors in the phase space and then move to more complex situations requiring concepts, methods, and tools typical of the chaotic systems analysis.

8.3.1 Two-dimensional simulations

As shown in Figure 8.2, as soon as Θ is increased starting from the condition of Newtonian fluid ($\Theta = 0$), the first striking feature displayed by the problem is the multiplicity of steady solutions in the interval $0 < \Theta \leq 0.08$.

Indeed, regions of multistability, where the system exhibits up to five disconnected

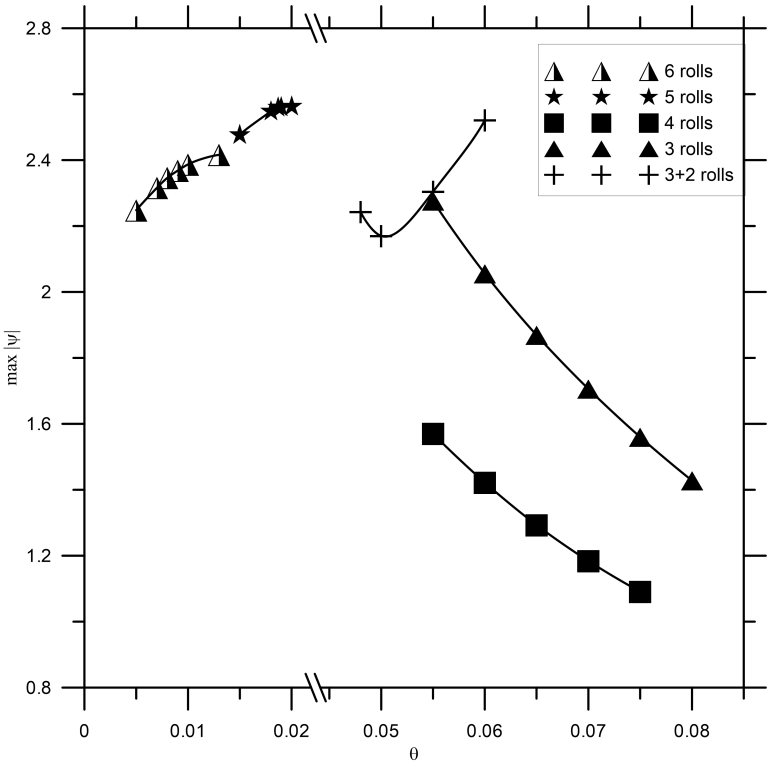

Figure 8.2: Multiple states of stationary convection in the range $0 < \Theta \leq 0.08$ (the integer number in round parentheses indicates the couples of counter-rotating rolls present in the system, splines have been used to connect the different points).

steady-state attractors, can be identified. Such attractors manifest over the considered

range of Θ as different branches of solutions (clearly distinguishable in Figure 8.2). Though they exist in the full phase space as invariant sets, what we observe in practice (as a result of the numerical simulations) is a projection of these sets onto the physical space, namely, multicellular states. These states differ in the extension of the rolls (proportional to the wavelength), the intensity of the emerging flow (ψ_{max}), and its dependence on Θ; indeed, for some branches, the maximum value attained by the stream function behaves as an increasing function of Θ, while for others the opposite behaviour can be seen.

It is known that in a problem developing coexisting branches of solutions, the trajectories of the system can converge selectively to either of the attractors depending on the considered initial conditions. Let us recall that, by definition, the basin of attraction of an attractor is the set of initial points whose trajectories fall on the given attractor. For these reasons, in order to identify the window in which the system is subjected to multiple coexisting attractors, we have used an approach similar to that implemented by Gelfgat et al. [102] and Lappa and Ferialdi [125] for the case thermo-gravitational flows in transversely heated liquid metals (see Chapter 6a for more details). We have explored the system response when the basin of attraction is varied. More precisely, in addition to the "standard" initial conditions corresponding to a quiescent state, a "forward and backward continuation" method has been used, i.e., the final state at each iteration of the control parameter Θ has been set as the initial condition for the next iteration (Ref. [178]).

In this way, the coexistence of the branches located on the right of 8.2 has been identified. As shown in this figure, solutions with either an even (4) or odd (3) number of couples of rolls are possible in the interval$0.055 \leq \Theta \leq 0.075$. Interestingly, these regimes also coexist in a more restricted range of Θ ($0.055 \leq \Theta \leq 0.06$) with (3 + 2) states, which perhaps deserve some additional description.

Indeed, apart from being the only branch for which the maximum of the stream function displays a non-monotone behaviour, these flows also exhibit a remarkable difference in terms of patterning behaviour. This difference (e.g., with respect to the branch with 3 couples of rolls extending from $\Theta = 0.055$ to $\Theta = 0.08$) is due essentially to the presence of two additional couples of counter-rotating rolls with relatively limited strength and spatial extension, which emerge as evenly spaced localised features separating rolls with larger size and intensity. In order to have a graphical idea of such bunch of

steady patterns they are reported Figure 8.3. As summarised in Figure 8.4, the just

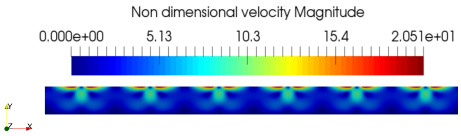

(a) Six rolls steady state, $\Theta = 0.005$

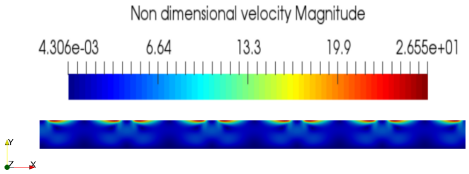

(b) Five rolls steady state, $\Theta = 0.015$

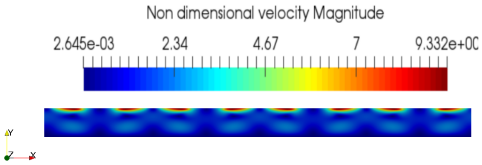

(c) Four rolls steady state, $\Theta = 0.07$

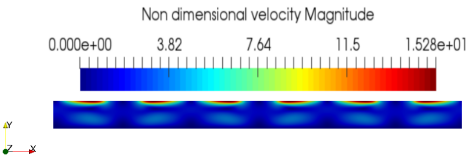

(d) Three rolls steady state, $\Theta = 0.065$

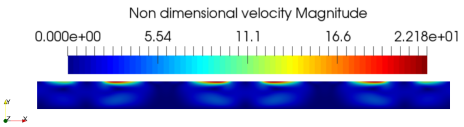

(e) 3+2 rolls steady state, $\Theta = 0.055$

Figure 8.3: Snapshots of the non-dimensional velocity magnitude for each of the steady states described above.

mentioned states of stationary convection with their specific properties even coexist in given sub-intervals of Θ with oscillatory solutions. There are several of them, however they can be grouped into three main families: the Purely Bouncing Rolls (PBR), rolls with localised flickering behaviour (FRCE) and hybrid states (HS). The first kind of instability (PBR) consists of constant amplitude rolls "bouncing" left and right, as depicted in Figure 8.5. As it can be noted form Figures 8.4 and 8.5 there are two main intervals where this instability take place, namely between $0.007 \leq \Theta \leq 0.01$ and $0.04 \leq \Theta \leq 0.048$. Similarly to the steady states an increase of Θ brings to a reduction of the number of counter-rotating pairs of rolls. Indeed in the first interval we have a PBR with five pair of rolls while in the interval with higher values of Θ the number reduces to three.

The second mechanism we have identified are the localised flickering rolls (FRCE), according to which one periodically expanding and contracting or breaking pair of counter-rotating rolls are immersed in an almost stationary background (see e.g Figure 8.6). As happened for the PBR the FRCE reduces its rolls increasing Θ.

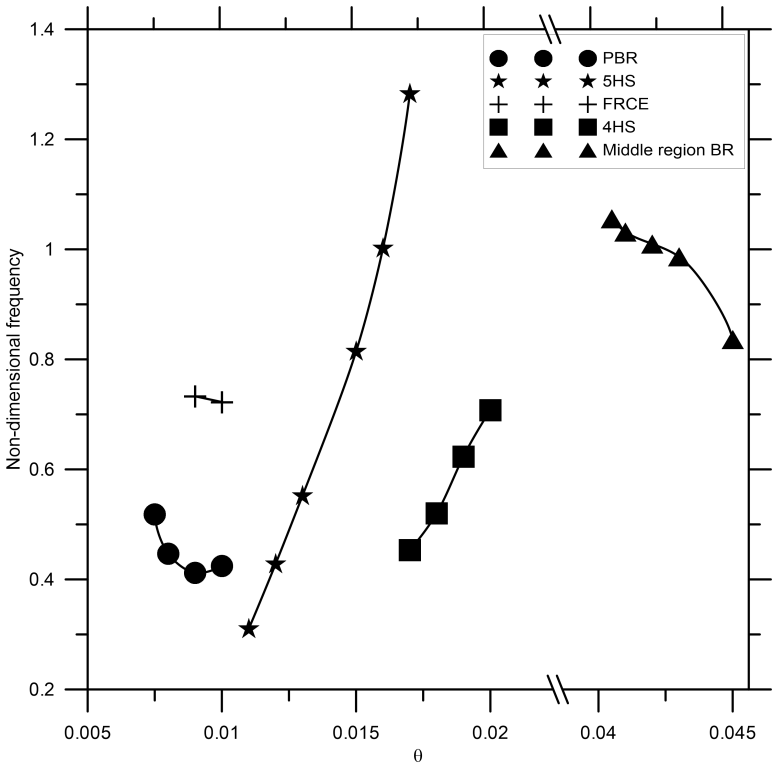

Figure 8.4: Multiple states of oscillatory convection in the range $0 < \Theta \leq 0.045$ (Legend: PBR: Purely Bouncing Rolls with fixed shape and size; FRCE: flickering couple of rolls weakly affecting the surrounding stationary state; HS: Hybrid State in which the rhythmic expansion and contraction of a couple of rolls is synchronous with the behaviour of the other rolls, which do not change amplitude but spread periodically along the positive x axis and then in the opposite direction; the integer number in round parentheses indicates the couples of counter-rotating rolls present in the system).

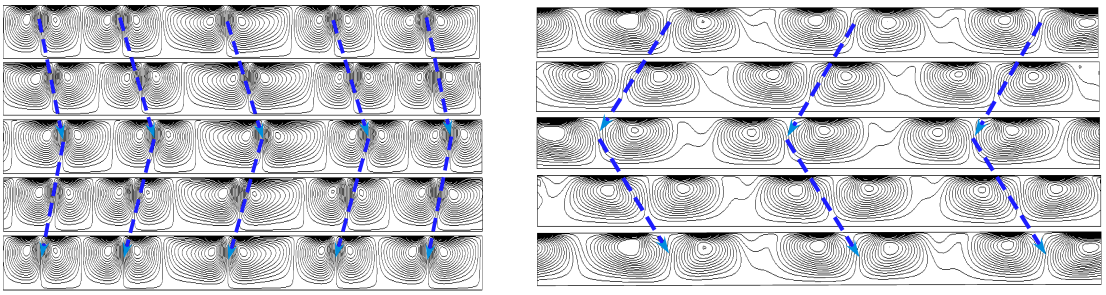

(a) 5 rolls PBR at $\Theta = 0.01$.

(b) 3 rolls bunching rolls at $\Theta = 0.045$.

Figure 8.5: Pure Bouncing Rolls Instability (PBR). 5 snapshots of theψ iso-lines evenly distributed along the period.

The third instability mechanism which could undergo the layer are the so-called Hybrid States (HS), which show the features of both the disturbances described above (PBR and FRCE).Indeed as shown in in Figure 8.7 there is a set of central pair of counter-rotating rolls which bounces rigidly left and right while a lateral roll contracts

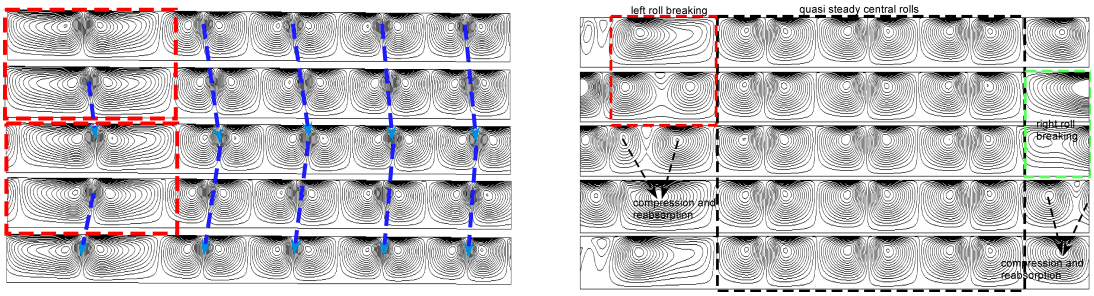

(a) 5 rolls FRCE at $\Theta = 0.012$

(b) 4 rolls FRCE at $\Theta = 0.0175$.

Figure 8.6: Localised Flickering Rolls (FRCE instability).5 snapshots of theψ isolines evenly distributed along the period.

and expands. Even in this case the number of pairs of counter-rotating rolls decreases from 5 to 4 as Θ is increased. This bunch of instabilities as depicted in Figure 8.4 is a

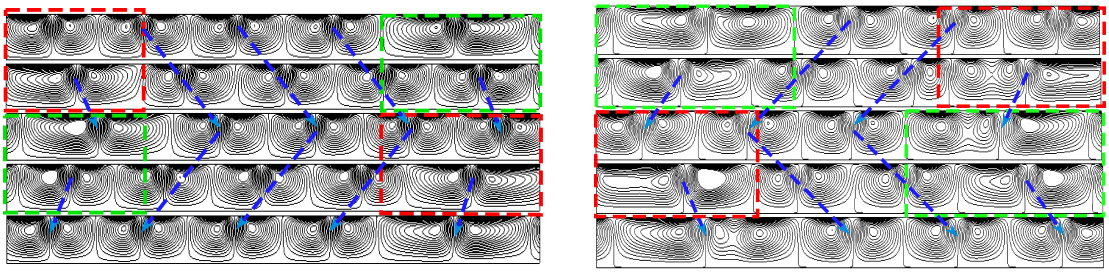

(a) 5 rolls HS at $\Theta = 0.012$

(b) 4 rolls HS at $\Theta = 0.019$.

Figure 8.7: Hybrid States (HS instability).5 snapshots of theψ iso-lines evenly distributed along the period.

complex function of Θ, being them interwoven and coexistent in certain regions of Θ. To have a better picture they have been reported in tabular form in Table 8.7.

Θ	Solution	Description
$0.007 \leq \Theta \leq 0.01$	PBR (5)	Purely Bouncing Rolls
$0.009 \leq \Theta \leq 0.01$	FRCE(5)	Flickering Rolls
$0.011 \leq \Theta \leq 0.017$	HS (5)	Hybrid State
$0.016 \leq \Theta \leq 0.021$	FRCE (4)	Flickering Rolls
$0.017 \leq \Theta \leq 0.0215$	HS (4)	Hybrid State
$0.04 \leq \Theta \leq 0.048$	PBR (3)	Purely Bouncing Rolls

Table 8.7: Different modes of oscillatory convection and their interval of existence.

Taken together, all these figures indicate that, in general, an increase in Θ causes an expansion in the horizontal extension of the rolls (this leading to a shrinkage of their number). The most interesting information emerging from a careful analysis of these modes of oscillatory convection (and the related "ranges of existence" summarised in

Table 8.7), however, is the realisation that, while stationary modes are no longer possible when Θ exceeds the threshold 0.08, coexistence of different solutions is still possible. Indeed overlap of oscillatory modes clearly occurs in the ranges $0.007 \leq \Theta \leq 0.01$, $0.016 \leq \Theta \leq 0.017$ and $0.017 \leq \Theta \leq 0.021$ for the regimes [PBR(5), FRCE(5)], [HS(5), FRCE(4)], and [HS(4) and FRCE(4)], respectively.

Before embarking in further consideration its worth looking at the instabilities described above under a different perspective, i.e. in the framework of the phase space. This tool is particularly useful to characterise the mechanisms introduced above and to explain the chaotic states found in certain intervals (we will come to that later). The phase portraits are shown in Figure 8.8 and it is worth noting as in the HS, represented in Figure 8.8c, both the PBR and FCR are recognizable. Returning on the chaotic inter-

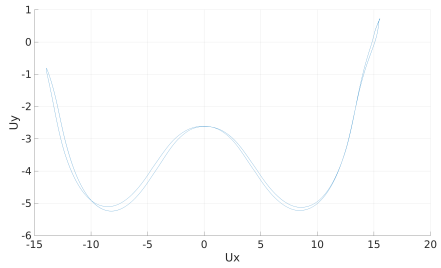

(a) PBR at $\Theta = 0.01$.

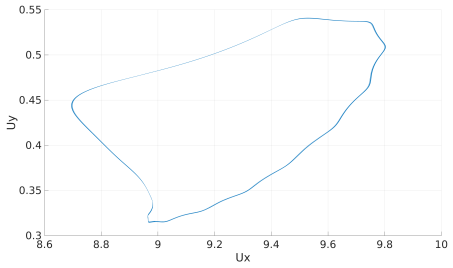

(b) FRCE at $\Theta = 0.009$

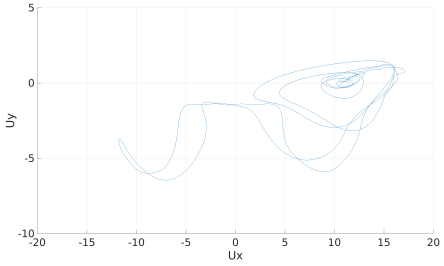

(c) HS (4) at $\Theta = 0.019$

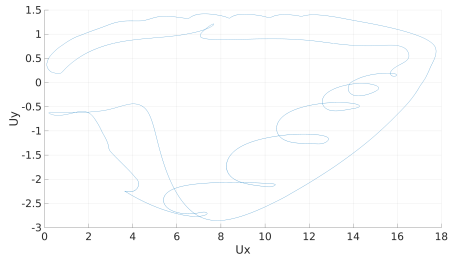

(d) PBR at $\Theta = 0.04$.

Figure 8.8: Phase portrait of different oscillatory instabilities.

val anticipated above on increasing the control parameter Θ past 0.02, a sub-region of "chaotic behaviour" is encountered just after the interval in which the FRCE(4) and HS(4) solutions coexist. Additional meaningful information about this special state can be gathered from Figure 8.9, in which we have reported a sequence of typical phase portraits for different (increasing) values of Θ.

These plots provide some evidence that for $\Theta \approx 0.02$, random switching of the system trajectory among two or more concurrent attracting sets can occur. Indeed, the reader will easily realise that the evolution path shown in Figure 8.9 looks like a trajectory

formed by the reiterated superposition of those shown in Figures 8.8b and 8.8c pertaining to FRCE(4) and HS(4) states, respectively.

These observations confirm that the presence of multiple attractors can act as an additional source of randomness in a chaotic system producing sudden and repeated jumps from a branch of solutions to another branch. Past $\Theta = 0.04$, however, the chaotic attractor reduces to a simple time-periodic flow following a chaos "crisis" similar to that observed in standard Rayleigh-Bénard convection, by Paul et al. [141]. As discussed, e.g., by Kitano et al. [55] this kind of bifurcation can be viewed as a sudden change in the size of the attractor. In line with these studies and the general arguments provided by Grebogi et al. [78] and Arnol'd et al. [179] we argue that such intermittent behavior is induced by the "collision" of the chaotic attractor with an unstable periodic orbit or its stable manifold. As the orbit approaches the unstable orbit its distance from the previous attractor increases, thereby driving the system toward a different scenario [represented by the PBR(3) branch in Figure 8.4]. Continuing with the description of

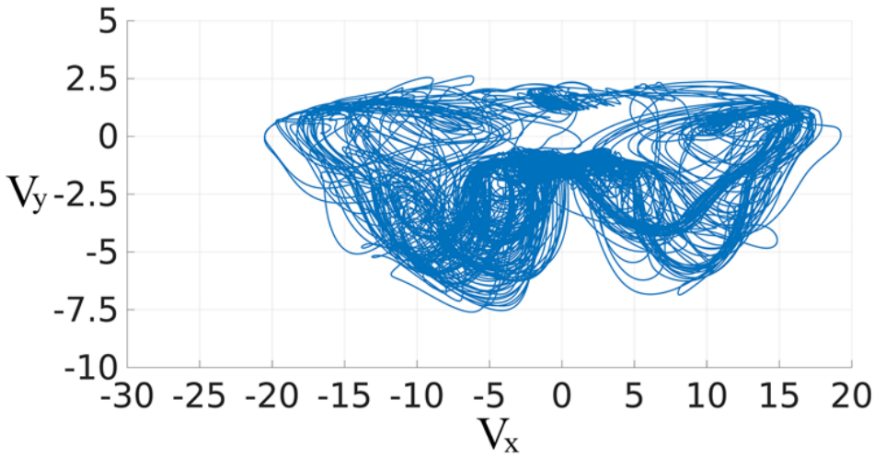

Figure 8.9: Chaotic state at $\Theta = 0.0218$

the new states revealed by the numerical simulations, it is worth pointing out that all these stationary and time-dependent solutions are taken over by a completely different scenario as Θ exceeds another threshold. This is shown, in Figure 8.10. For $\Theta \geq 0.08$, in particular, a new mechanism of oscillatory convection becomes dominant. It consists of the coexistence of different "units ". For simplicity, hereafter we will use the term "unit" to denote the couple formed by a roll and its counter-rotating companion such that fluid is transported toward the surface at the centre and toward the bottom at the periphery of the couple.

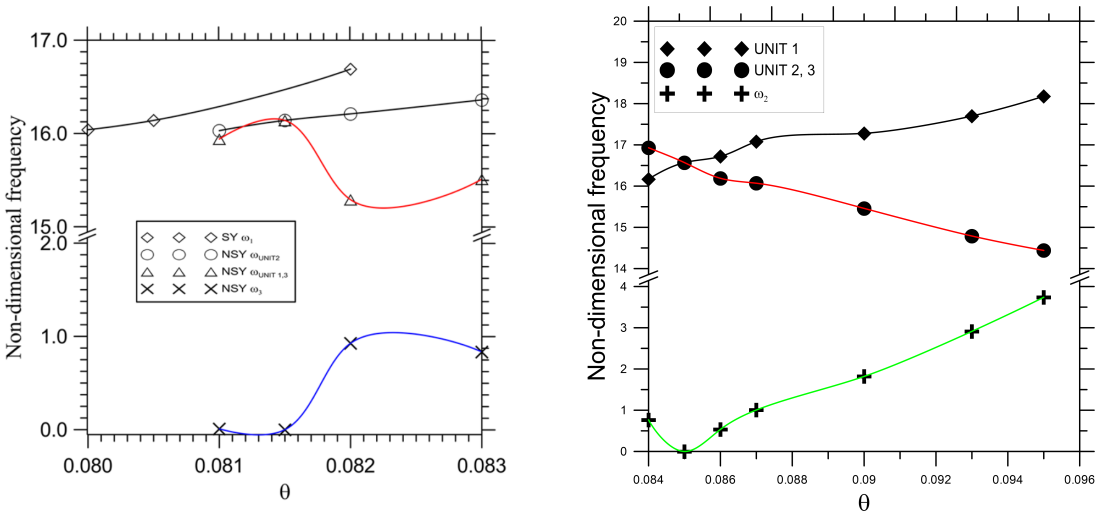

(a) (b)

Figure 8.10: Multiple states of oscillatory convection categorized as SY regimes (where all the units oscillate in a synchronous fashion, each unit being formed by a roll and its counter-rotating companion?refer to the single black line) and NSY regimes (non-synchronous states with three units in which two units share the same frequency, while the third displays a slightly different frequency-related frequencies being highlighted by the black and red interpolating lines, respectively). The additional blue and green line has been used to represent the long-period modulation produced for the NSY regimes by the non-linear interference between the other two oscillatory mechanisms.

Different branches of solutions can yet be identified in the space of parameters. These can be categorized as states with three units in which two units share the same frequency, while the third displays a slightly different frequency (reported in Figure 8.10 as NSY (non-synchronous) states) and other regimes ("ordered patterns") in which all the units oscillate in a synchronous fashion (SY states). Interestingly for the NSY branch, a long-period modulation is also present with frequency ω_3 equal to the difference of the two other frequencies (see, e.g., Figure 8.11). This phenomenon is produced by the obvious non-linear interference between the other two oscillatory mechanisms; "beats" are often observed in nature between oscillatory phenomena with similar frequencies.

Most notably, however, if Θ is further increased, the SY states featured by frequency locking are no longer a solution. For $\Theta \geq 0.084$ (Figure 8.10b), only the NSY states survive (see, e.g., Figure 8.12). For $0.084 \leq \Theta < 0.088$, these attractors display essentially the typical behaviour of a T^2 torus with two similar but incommensurate frequencies and related beats as shown in Figure 8.10b. For $\Theta \geq 0.088$, however, they clearly acquire a "fractal structure" This aspect is further illustrated in the following resorting to concepts and tools typical of the analysis of chaotic systems.

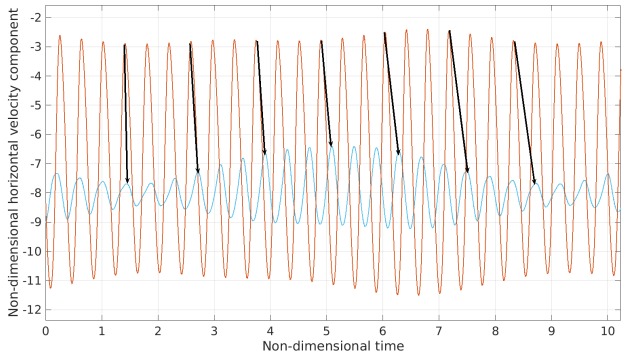

(a) Time series

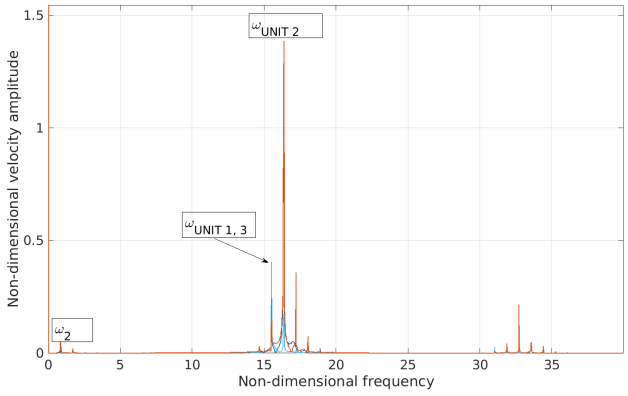

(b) Spectrum

Figure 8.11: Oscillatory convection for $\Theta = 0.083$. In blue units 1 and 3, in brown unit 2

As an example, the peculiar properties of the rate with which a typical orbit "visits" different parts of an attractor can naturally be incorporated into the definition of the natural measure. This scalar quantity can represent the percentage of the time that a long orbit on the attractor spends in any given region of the state space. A related concept is that of correlation dimension D_2 (Ref. [67]), already introduced in Chapter 6a and used in the Chapter 7 to understand how the system evolves towards chaos. This dimension is thought to be a measure of the number of "active modes" in a system, or of the "effective number of degrees of freedom" (Ref. [140]). Remarkably, this quantity can take non-integer values, which is generally regarded as a synonym of fractal behaviour or "fractalisation"; let us recall that a fractal was defined by Professor Benoit B. Mandelbrot in 1975 as *"a fragmented geometric shape that can be sub- divided into parts, each of which is, at least approximately, a reduced-size copy of the whole"*, which implies the concept of non-integer dimension.

Algorithms able to yield an estimate of the correlation dimension have been originally

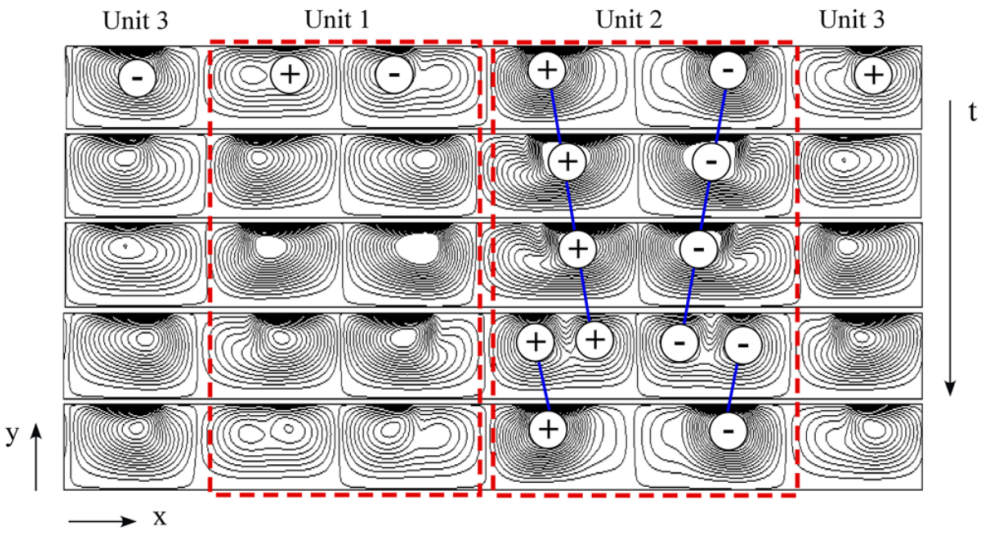

Figure 8.12: Snapshot of the ψ iso-lines evenly distributed along the period for the NSY instability at $\Theta = 0.085$. The "+" and "-" symbols represent counter-clockwise and clockwise rotating rolls respectively.

developed by Grassberger and Procaccia [68],[139]. The values taken by D_2 for the conditions considered in the present work (computed with the algorithm by Grassberger and Procaccia [68],[139] and described in detail in Chapter 6a) when Θ exceeds the value 0.084 have been collected in Figure 8.13. By embodying the concept of progressively increasing structure on finer and finer length scales, the increasing values taken by the correlation dimension when Θ becomes higher clearly reveal the emergence of features typical of chaos.

This can be clearly seen in the range$8.6 * 10^{-2} \leq \Theta \leq 9.4 * 10^{-2}$, where the correlation dimension takes non-integer values ranging between 2 and 3 (before it attains ≈ 4 for $\Theta \approx 9.6 * 10^{-2}$). Most remarkably, the behaviour of the system in this interval is even more interesting of what happens when (on further increasing Θ) D_2 becomes larger than 3.

The meaning of the above statement is not as straightforward as one would imagine as it has a hidden connection with another very important question in fluid-dynamics (a problem still of a very controversial nature), namely, the number of degrees of freedom required to produce transition to turbulence (i.e.,fractalisation). As already discussed in Chapter 6, according to the classical Ruelle-Takens scenario, a third independent frequency should appear, i.e., the attractor should become a hypertorus T^3 , before transitioning to a strange attractor.

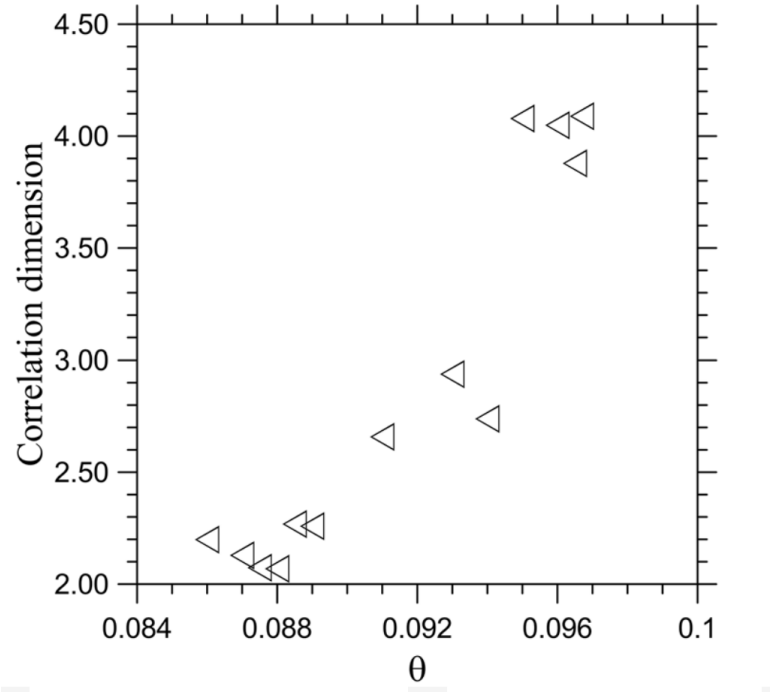

Figure 8.13: Correlation dimension as function of Θ

In other words, according to this route at least two Hopf bifurcations would be required to produce chaos, the first causing the transition from a periodic regime to a quasi-periodic regime with two incommensurate frequencies and the second leading to a new regime with three incommensurate frequencies. This is indeed formalised by the so-called Newhouse-Ruelle-Takens theorem (Ref. [72]), which asserts that a torus T^3 , under the actions of some perturbations, degenerates to a "strange attractor" ,and therefore the existence of three frequencies (i.e., three degrees of freedom) should be regarded as a necessary and sufficient condition for the emergence of a chaotic regime. On the one hand, this means that the present findings with fractalisation being produced starting from a T^2 torus do support the alternate route toward chaos proposed by Curry and Yorke [73] where transition to chaos is permitted from a torus T^2 ; on the other hand, they lead to another very important question, generally connected with the dynamics of non-linear systems and related theories, namely, the problem relating to the existence of "universality classes" in such dynamics. The reader is also referred to the companion arguments elaborated in Section 8.4.2.

Here, we wish to emphasize that the Curry-Yorke scenario has been already reported for other problems in which viscoelastic fluids are involved, relevant examples being the Taylor-Couette flow [49] and Rayleigh-Bénard convection [175]. The main difference

here is represented by the apparently crucial role played in the present problem by the coexistence of multiple solutions and the localised oscillatory structures (oscillons). As explained in the next section , the latter become a persistent characteristic of the dynamics at relatively high values of Θ.

While the former (multiple states of convection) are a well-known property of thermo-gravitational convection in laterally heated liquid metals [102],[125] as discussed in the introduction of this chapter, oscillons have been previously observed essentially in vibrated systems ([156], [157], [158], [159]).

Both features can be found in viscoelastic Marangoni-Bénard convection. This is confirmed by the three-dimensional (3D) simulations performed to probe the system response in a region of the space of parameters where according to 2D computations the initial torus T^2 is taken over by a strange attractor (featuring oscillons as a pervasive characteristic of the flow). To do justice of these interesting findings, next section is entirely devoted to these 3D results.

8.3.2 Three-dimensional dynamics

A further understanding of the problem is gained by considering the role of the third spatial direction. Prior to embarking into an exhaustive description of such results, for the sake of completeness and clarity, in the following, first we provide some initial and fundamental information about the modification displayed by the flow in terms of the three-dimensional spatial structure as the elasticity number is increased. This strategy will prove very useful later when we will discuss the general features of such states from a temporal point of view and focus on the emergence of chaos and related dynamics.

Along these lines, we start from the simple observation that increasing Θ has a remarkable impact on the typical topology of MB flow.

As illustrated in Figure 8.14a, for $\Theta = 0$ (Newtonian fluid with $Pr = 1$) the pattern is very regular and includes many triangular cells. Remarkably, the lines bounding these cells organize themselves to form a very well-defined network resembling the typical architecture of reticular trusses. Many of these lines originate from some special knots which behave as the centres of closed polygonal multi-cell structures having the shape of a "flower" with each triangular cell representing a distinct "petal" of the flower [4]. Many of such structures can be recognised in Figure 8.14a. Though partial overlap among these sub-patterns is possible, the above-mentioned special knots

can be uniquely identified through the topological order p of the radial spokes which originate from them. As evident in Figure 8.14a, this topological order ($p_{max} = maximumnumberofdepartingspokes$) is $p_{max} = 6$, whereas for standard patterns with the classical hexagonal and square cells typically found in Newtonian high-Pr liquids, p_{max} would take values $p_{max} = 3$ and $p_{max} = 4$ (see, e.g., Ref. [180]).

As anticipated, however, an increase in Θ causes significant adjustments. As evident in Figure 8.14b, for a relatively small value of the elasticity parameter such as $\Theta = 7{*}10^{-3}$, the just-discussed regular organisation is no longer a well-defined and recognizable characteristic of the pattern. Though the average extension of the different cells along the horizontal direction does not change significantly, the number p associated with the different knots becomes appreciably smaller, varying randomly through the physical domain between 3 and 5 (Figure 8.14b). The related network may be seen as an evolution

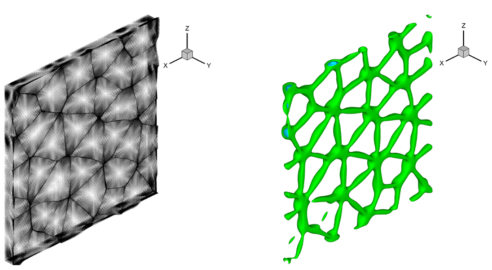

(a) $\Theta = 0$

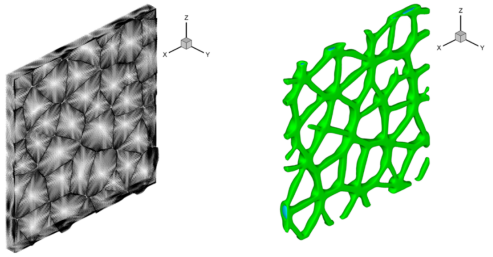

(b) $\Theta = 7 * 10^{-3}$

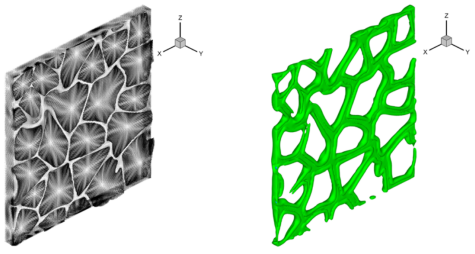

(c) $\Theta = 3 * 10^{-2}$

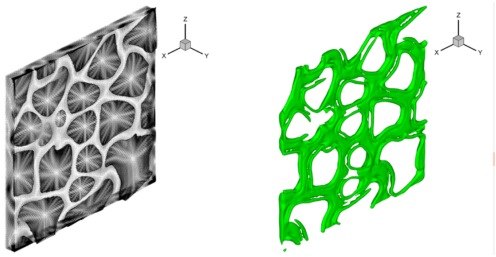

(d) $\Theta = 5 * 10^{-2}$

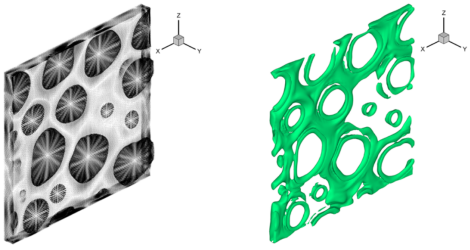

(e) $\Theta = 9 * 10^{-2}$

Figure 8.14: 3D convection for $Ma = 300$. Snapshots of the velocity vector field and isosurfaces of the velocity component perpendicular to the free surface in a 15x15x1 cavity at different values of Θ.

of the reticular trusses seen in Figure 8.14a due to the emergence of localised topological "defects" which prevent the formation of the regular polygonal multi-triangular-cell textures in some regions of the physical domain. However, a further increase in Θ can lead to much more significant modifications of the overall flow structure. This is witnessed by the results shown in Figure 8.14c for $\Theta = 3 * 10^{-2}$. Indeed, apart from the much more disordered appearance of the pattern, a remarkable alteration affects the extension of the cells, which following a trend similar to that revealed by the 2D simulations (see, e.g., Figures 8.5, 8.6, 8.7), grow in size (Figure 8.14c). Notably, such expansion in the horizontal plane occurs in conjunction with a decrease in the overall number of cells as made evident by the emergence of surface regions where the fluid is in almost quiescent conditions. These areas, where the (horizontal) surface velocity is close to zero (while the component of velocity perpendicular to the free surface takes a relatively small but non-negligible value in the bulk fluid located underneath), "separate" the different cells (see again Figure 8.14c). This trend is yet in agreement with our earlier observations about 2D flow (see Figure 8.7 and related discussion in the previous section).

The extension of these "buffer" regions of return flow keeps increasing as Θ becomes higher (see Figures 8.14d and 8.14e for $\Theta = 5 * 10^{-2}$ and $\Theta = 9 * 10^{-2}$, respectively). The initial configuration, crowded with a relatively large number of side-by-side cells, which transport heat from the bottom of the layer toward the surface in their centre and fluid in the opposite direction along their boundaries, is taken over by a progressively more sparse distribution in which cells look like (as seen in the temperature distribution) separated "islands" (the number of cells being depleted as Θ increases, Figure 8.15).

Having finished a description of the flow from a spatial perspective, we now turn to interpreting the related temporal dynamics. The progression from standard (Newtonian) Marangoni-Bénard convection to chaos as the elasticity number becomes higher can be appreciated by taking a look at Figures 8.17a-8.17e. These figures reveal how, on increasing the elasticity parameter (besides the aforementioned topological evolution), the pattern also undergoes substantial behavioural changes.

When Newtonian conditions are established, the flow dependence on time is relatively weak. As shown in Figure 8.17a, the pattern retains a large-scale nearly steady structure in which the location and spacing of the reticular trusses with triangular topology

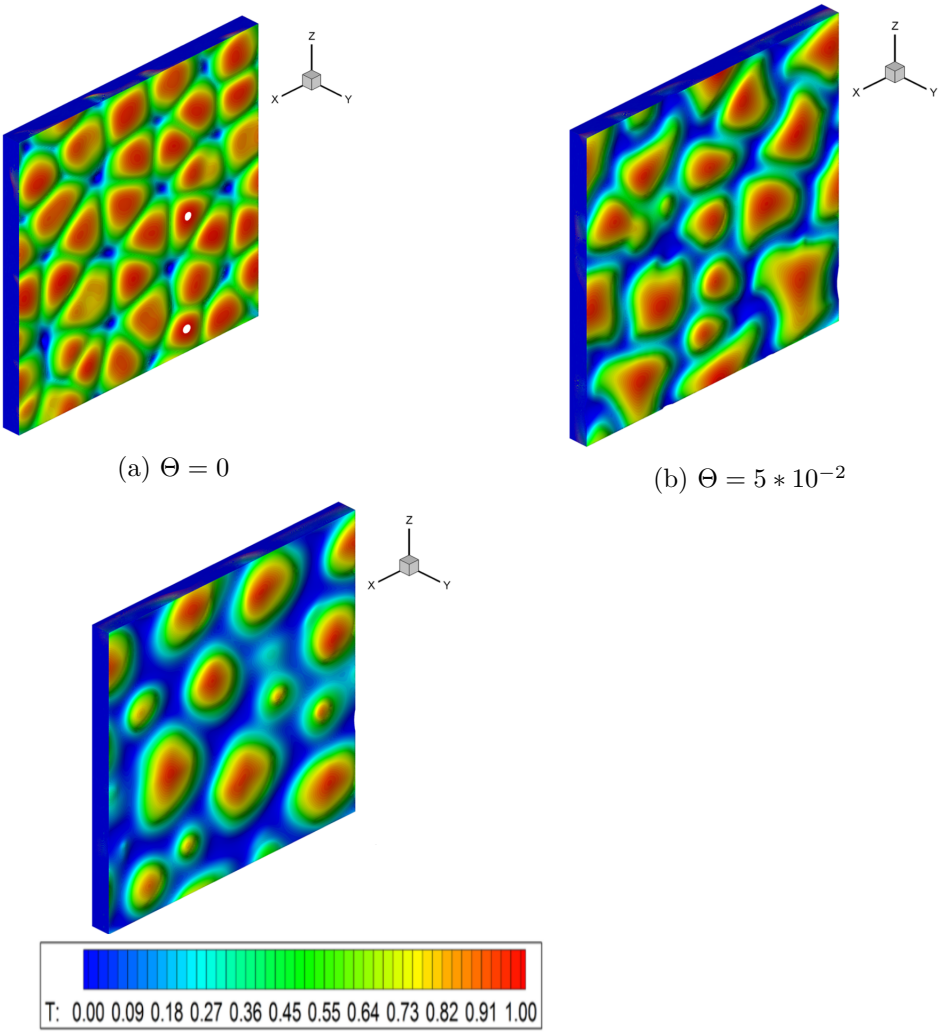

(a) $\Theta = 0$

(b) $\Theta = 5 * 10^{-2}$

(c) $\Theta = 9 * 10^{-2}$

Figure 8.15: Temperature contour plots for different values of the elasticity number.

is surprisingly regular [4]. For $\Theta = 3 * 10^{-2}$, however, the irregularity visible in the spatial distribution of cells seen in Figure 8.14c is also present in the temporal behaviour; this is confirmed by the temperature signals provided by a set of equally spaced thermocouples aligned along the x axis (Figure 8.16a).

Comparison of Figures 8.17b and 8.17c also leads to the very interesting realisation that the alterations are not limited to changes in the topology of the pattern and size of recognisable convective features. They also concern the morphology of the cells.

Indeed, as Θ is increased, such cells feature the development of cusps along initially straight sides, which are not possible at smaller Θ.

Moreover, Figure 8.17c reveals that since for $\Theta = 3 * 10^{-2}$, the cells are no longer arranged in a tight side-by-side configuration (as that seen in Figures 8.17a or 8.17b),

they can continuously change shape (by developing, as mentioned before, new cusp points, i.e., by replacing straight sides with edges and vice versa).

This behavior is retained and even reinforced for $\Theta = 5 * 10^{-2}$ (Figure 8.17d) due to the increased space (buffer) being available between neighbouring cells. In addition, a new phenomenon starts to take place, namely, the growth and decay of new (relatively small) cells nucleating in the buffer regions. Finally, as soon as Θ exceeds a value similar to that already identified in the 2D case (≈ 0.089), a chaotic state with apparently independent (well-separated in space) oscillons, which interact in time, is recovered (see Figure 8.17e) for $\Theta = 9 * 10^{-2}$). For this case, polygonal structures are no longer recognizable or evident. All the cells tend to acquire a more or less rounded boundary and change continuously their shape as time progresses, their interactions resulting in an endless wandering process (supported or promoted by the increased spacing among them). Apart from the aforementioned nucleation phenomena occurring randomly in the physical domain, interestingly, in this state new dynamics are allowed in the form of cells that split (with a process closely resembling that of the cellular mitosis) or merge with other cells.

In such a context, the additional information provided by equally spaced thermocouples aligned along a fixed direction (Figure 8.16b) is still instructive as it clearly shows the "localised" nature and temporally limited duration of the events mentioned above (which might be regarded as "bursts" causing at certain positions and over finite-extent time-frames an increase in the frequency of oscillations).

Unfortunately, we could not track precisely the evolution of the system in terms of correlation dimension as the algorithm by Grassberger and Procaccia [68], [139](and other similar approaches see Refs. [68] and [139]) works only for low dimensional chaos, i.e., when the correlation dimension does not exceed 4; notably, similar concepts also apply to the Lyapunov exponents and related quantities (see, e.g., Ref. [70]). In line with the considerations reported in all these studies, our attempts to measure D_2 for the above cases provided relatively high (not converging) values.

To conclude this section, we limit ourselves to mentioning that, most interestingly, this "ultimate" state of convection featuring convective cells that move, split, or collide, like continents drifting in the ocean, displays some analogies with another kind of thermally driven chaotic flow, namely, turbulent Rayleigh-Bénard (RB) convection in Newtonian fluids. Indeed, in turbulent RB, isolated thermal features in the form of plumes are

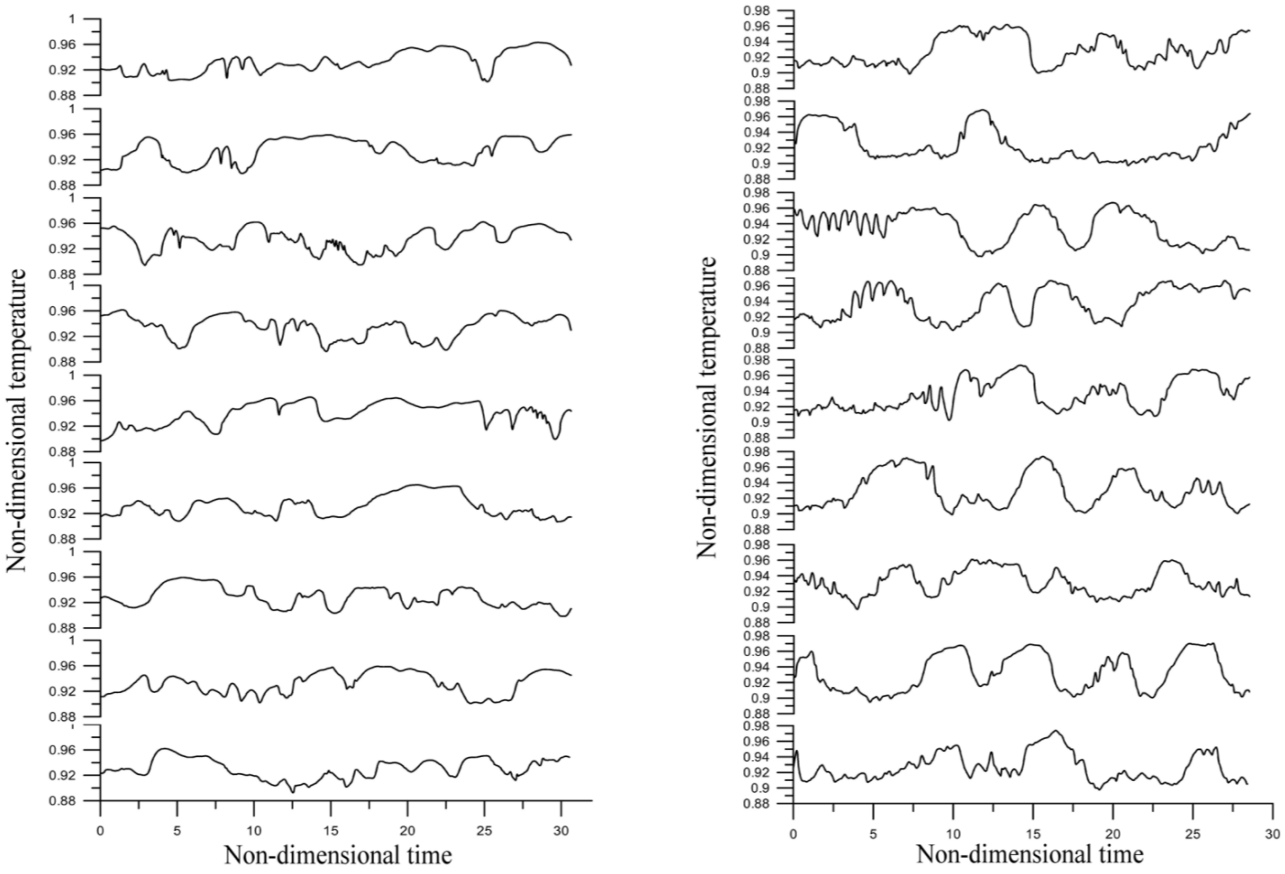

(a) $\Theta = 3 * 10^{-2}$

(b) $\Theta = 9 * 10^{-2}$

Figure 8.16: Temperature signals provided by 9 thermocouples evenly spaced along the x direction. $Ma = 300$ and 15x15x1 cavity.

known to emerge, grow, and move chaotically in the physical domain, being subjected at the same time to (1) instabilities promoted by the thermal buoyancy itself or by the shear, which can cause new plumes to develop from the original plume stem (i.e., branching phenomena; see, e.g., Ref. [181]) or (2) clustering phenomena, which produce large-scale features (see, e.g., Refs.[182], [183], [184]). As shown in Figure 8.17e, in our case the dynamics are formally similar: oscillons nucleating at different positions in the domain can split into different parts or coalesce forming larger cells while wandering in the horizontal direction. We will come back to this interesting concept in in the next section where this statement will be placed in a more general theoretical context in the light of existing theories on the subject.

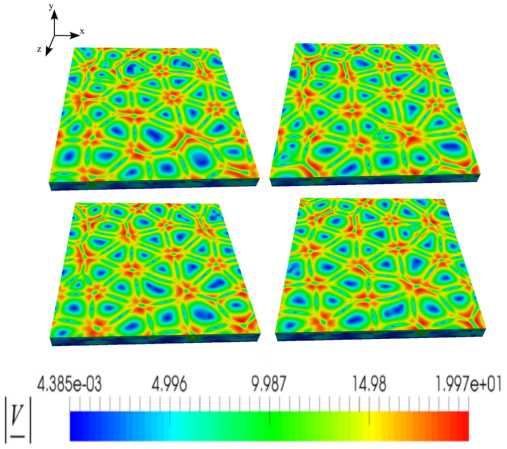

(a) $\Theta = 0$

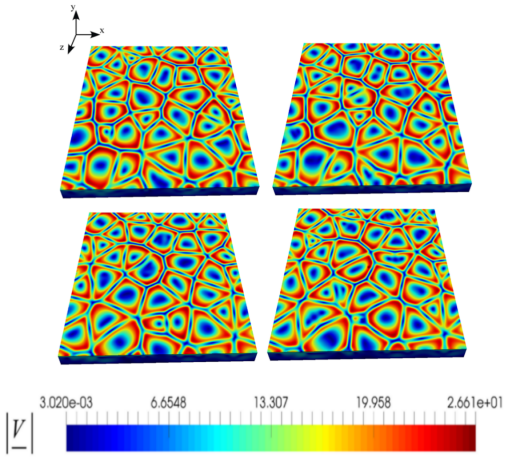

(b) $\Theta = 7 * 10^{-3}$

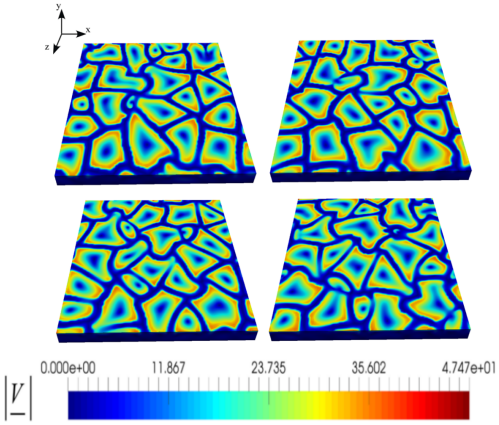

(c) $\Theta = 3 * 10^{-2}$

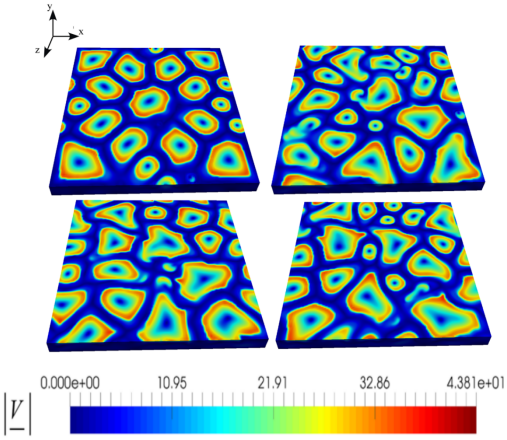

(d) $\Theta = 5 * 10^{-2}$

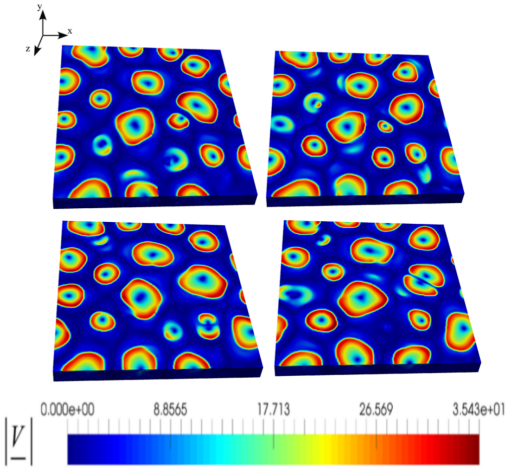

(e) $\Theta = 9 * 10^{-2}$

Figure 8.17: Snapshots of 3D convection: velocity magnitude on the free surface. 15x15x1 cavity,$Ma = 300$, periodic boundary conditions and for different values of Θ.

8.4 Further discussions

Toward the end to place the present findings in a more general context and get additional insights, there are some categories of flows and fluids that could be considered to establish interesting analogies (thereby enriching the discussion with some interdisciplinary flavour).
As already outlined in the introduction of this Chapter, oscillons are not an exclusive prerogative of the flow considered in the present work. Oscillons have been also observed in other contexts (e.g.,granular media).

8.4.1 Oscillons in granular media

Though granular media could be seen as a special kind of fluids, however, there are some special aspects that make their properties somehow unique, these being the dissipative nature of the interactions between grains (due to static friction) and the related collision phenomena, which contribute to the exchange of momentum at small scales (Refs. [158] and [185]).
Though the connection between granular materials and viscoelastic fluids in terms of mechanisms responsible for exchange of momentum within the medium and related "emerging" properties (in terms of macroscopic pattern) at this stage is still unclear, some similarities can be highlighted. Indeed, recent experiments with vibrated granular materials have provided evidence for an astonishing variety of collective behaviours formally similar to those seen in the present work. These include (but are not limited to) standing waves, oscillatory patterns with hexagonal or square symmetry (also referred to as "granular waves"), one-dimensional worms (Ref. [186]) and oscillons (which emerge with finite initial amplitude in a hysteretic region between patterns and featureless states under the same conditions required for granular waves [156],[157]).
Most interestingly, Umbanhowar et al. [157] described how these localised features can interact. Several dynamics were reported, such as oscillons with the same phase displaying a short-range repulsive interaction and oscillons of opposite phase attracting and "binding" to form stable dipole structures. Apart from dipoles, these authors also observed other stable configurations; among them, chains of oscillons (in which bound oscillons are able to influence each other even if they are not in direct contact) and triangular tetramers. Though structures of oscillons with square symmetry were not

found, patterns with square symmetry (granular waves) were observed to oscillate with an arrangement similar to that of an "ionic crystal".

Similar dynamics have been reported for vibrated colloidal suspensions. Along these lines, Lioubashevski et al. [159] clearly identified oscillons interacting and forming (depending on both the driving amplitude and initial conditions) localised patterns such as the triad structures of in-phase oscillons, short oscillon chains composed of either like or unlike-phase oscillons, and patterns of oscillons with an internal hexagonal symmetry.

Though it is not easy to identify common cause-and-effect relationships with respect to the viscoelastic problem treated in the present work, perhaps some commonality could be seen in the ability of interacting oscillons to produce stable crystalline-like structures such as those that we have identified in a given range of Θ (Figure 8.10a). As shown in Figure 8.10b, however, in the present case, these single-frequency crystalline-like structures, which initially coexist with bimodal T^2 states, are taken over as Θ exceeds a given threshold by entities that display a fractal behaviour.

This places our problem in a more general context, namely, the transition to turbulence and related theories.

8.4.2 Inertial and elastic turbulence and universality classes

Perhaps the best way to address this specific point would be to start from an analysis of the general (known) characteristics of elastic turbulence and its differences with respect to standard inertial turbulence (see, e.g., Refs. [187], [188], [189], [190]). A dichotomy is often drawn between these two forms of chaos.

Newtonian turbulence is, in general, ascribed to the role of inertial forces, which can destabilise the flow on increasing the Reynolds number. In turn, this implies that the velocity required for excitation of inertial turbulence must be somehow proportional to the viscosity of the considered Newtonian fluid. In other words, the more viscous the considered fluid is, the higher shall be its large-scale velocity. One may also state that this kind of turbulence is caused by excessive kinetic energy in parts of a fluid flow overcoming the opposite mitigating effect played by the fluid's viscosity. For this case, following Kolmogorov's hypothesis (Ref. [191]), the existence of an "inertial" wavenumber region can even be postulated, where the kinetic energy is transferred from large scales toward small scales (the energy being partitioned among eddies in proportion to $k^{-\frac{5}{3}}$, where k is the wavenumber, until it is dissipated at scales of the order of the

so-called Kolmogorov length).

Though the above concepts have been found to work well in many circumstances in the case of Newtonian fluids (even for typical problems of thermal convection; see, e.g., Ref. [134] and references therein), they are no longer applicable when elastic turbulence is considered.

Small-Reynolds number elastic turbulence arises when a certain value of the elasticity parameter is exceeded. Because (as illustrated for instance in Chapter 3a for the Oldroyd-B model), the polymer relaxation time, λ, usually grows proportionally to the polymer viscosity, this means, that, in principle, turbulence can be excited at lower velocities by using more viscous polymer solutions; this completely rules out the influence of inertia, which also explains why this kind of turbulence is often referred to as turbulence without inertia (Ref.[192]).

Even though an elaboration of a physical interpretation for the mechanism leading to elastic turbulence is not as straightforward as one would imagine, some general insights into its cause-and-effect relationships can be obtained on the basis of the mathematical arguments provided in Part I (more precisely in Chapters 3 and 4) by observing that the most notable property of a polymer solution is that the stresses are not immediately suppressed as the fluid velocity becomes zero (but rather decay with some characteristic time). This implies that the behaviour of a polymeric liquid has to depend on the history of the polymer molecules deformations, which provides these systems with a non-linear feedback mechanism potentially able to produce and amplify disturbances. The degree of non-linearity in these mechanical properties is typically expressed via the so-called Weissenberg number We, defined in 3.2, which could be rephrased for the purposes of this section as $Wi = V_r \frac{\lambda}{L}$, where V_r is a characteristic reference velocity. This number, which can be seen as a product of the characteristic rate of deformation and the relaxation time, for the problem considered in the present work would read $Wi = Ma\Theta$. By virtue of these feedback loops, effects relating to the stretching of polymer molecules can lead to new instability mechanisms; as an example, polymer molecules stretching caused by a primary flow, may cause irregular secondary flow able to exert their influence back on the polymer molecules, stretching them further and making the resulting flow increasingly turbulent, until a kind of saturated state is attained [189],[192]. It is in this way that non-linearity can be regarded as "loop" that feeds information back into the system where it is iterated, or used multiplicatively;

these arguments also apply the case of thermally driven viscoelastic flows; see, e.g., Khayat [50], [51].

To some extent all these concepts apparently simplify the problem by abstracting some essential and distinctive features. Nevertheless, at this stage, we should expressly point out that, despite these remarkable differences between inertial and elastic turbulence, some notable (and unexpected) similarities can be identified between the present phenomena and another seemingly innocuous problem, namely, the transition from laminar to turbulent (Newtonian) flow in an ordinary pipe.

This problem has been already considered in the past given its outstanding implications in the elaboration of a general theory for turbulence where the evolution toward chaos proceeds in form of localised patterns. Originating from the pioneering study of Reynolds in the late 19th century, it continues to burgeon and bring surprises to this day. That it is why it has been recently used as a workhorse to assess the role potentially played by the spatial coupling of transiently chaotic localised features in sustaining turbulence (Ref. [193]). As originally illustrated by Wygnanski and Champagne, [194] turbulence develops in ordinary pipes in the form of localised patches generally known as "puffs". These localised features emerge as isolated islands (subregions with relatively limited spatial extension) in a laminar flow and are known to grow or decay according to the value taken by the control parameter (the Reynolds number for this specific situation, Ref. [195]). From a temporal point of view, all these turbulent sites relax toward a laminar phase if the control parameter is below the critical point. However, as soon as such a threshold is exceeded, because of the spatial coupling among such sites which produces a statistical phase transition, there is always an appreciable fraction of chaotic sites that grows on increasing the Reynolds number. The alternating laminar and turbulent regions typical of pipe flow are intrinsic to this problem and "place pipe flow in the larger theoretical framework of spatio-temporal intermittency" [193] which somehow resembles the present dynamics (Figures 8.4 and 7.37) in which the interaction among coexisting branches of solutions or oscillons can give rise to inlets of chaotic behaviour for moderate values of the elasticity parameter or "fractal" dynamics (in the sense that has been given to this adjective in the preceding pages) as this parameter exceeds a given threshold.

Such a similarity becomes even more interesting and meaningful if one takes into account that, as explained before, the physical mechanisms responsible for the emergence

of high-Re turbulence in Newtonian fluids and low-Re chaos in viscoelastic fluids are, in general, thought to be very different.

Following up on the previous point, some additional information can be found in the aforementioned study by Avila et al., [193] who correctly observed that, qualitatively, the behaviour with the spatial coupling of transiently chaotic domains giving rise to the sustainment of turbulence (such as that shown in Fig. 8.17e), is reminiscent of the dynamics of a class of model systems called coupled map lattices (Ref. [196]). This may, therefore, indicate the existence of a class of universality which transcends the differences between inertial and the elastic turbulence. Put simply, the above considerations might imply that non-linearities related to the specific way by which the considered medium transports or exchanges momentum at microscopic level may not be necessarily required to justify the observed behaviours, these being the manifestation of a general class of phenomena which is exclusive neither of granular media nor of viscoelastic fluids. Remarkably, this commonality may inspire in the future other fresh directions of interdisciplinary inquiry.

8.4.3 Interacting localised convective features in other dissipative systems

In order to stake out some common ground by providing a synthesis of other known relevant phenomena in Newtonian fluids where the coupling of spatially separated sites can give rise to the sustainment of turbulence, in the following we discuss other similar categories of phenomena. In particular, we concentrate on known processes where the emergence of unsteady isolated features is somehow supported by the intrinsic or inherent tendency of the considered system to produce plumes, relevant examples being represented by binary fluid convection and moist turbulent convection.

As an example, Lappa [197] investigated the pattern formation process driven by N droplets out of thermodynamic equilibrium, uniformly distributed (evenly spaced) on the bottom of a container filled with a partially miscible organic liquid (cyclohexane-methanol system), as a model of the typical phenomena which occur during the thermal processing of liquid-liquid systems exhibiting a miscibility gap (the so- called "immiscible alloys"). These special alloys exist as two immiscible liquid phases within a certain interval of temperature. In particular, for a monotectic system a homogeneous solution exists only at temperatures above the so-called critical temperature T_c ; if the tem-

perature is decreased below T_c , the melt starts to decompose into two liquid phases of different composition and density which coexist, generally known as the "majority" and "minority" phases.

Initially these alloys behave as a homogeneous phase. However, as soon as the temperature is decreased by cooling the container from below, new droplets nucleate in the bulk of the liquid and move (due to sedimentation) to the colder bottom of the container where they start to dissolve because they are no longer in equilibrium with the surrounding phase. As a result, convention driven by solute gradients is produced by buoyancy effects around each droplet in the form of unsteady rising jets or plumes periodically released from the top of each droplet. Remarkably, spatial coupling among these convective structures can be produced by the return flow associated with the primary plume generated by each droplet. As a result, the rising currents originating from the different droplets interact in unexpected ways giving rise to "ensemble behaviours", which may be regarded as another occurrence of dynamics produced by the mutual interference of oscillons.

Interestingly, Lappa [197] observed the plumes (originating from different droplets) to produce in the initial stages of evolution "crystalline states" similar to those seen for the case of vibrated granular matter. More precisely, the frequency of plume emission was found to be the same for all droplets with couples of droplets that release plumes with opposite phase behaving as "dipoles" .However, progression from order to disorder was reported for later time, with the system undergoing transition to a condition in which the time-dependent release of solutal plumes becomes completely erratic from both spatial and temporal points of view [198].

The route to chaos described in Chapter 6a also closely resembles that reported by Paul et al., [141] for standard Rayleigh-Bénard convection in water. On increasing the control parameter, indeed, these authors obtained time-periodic rolls, quasi-periodicity, phase-locked states, and chaos. Periodic and quasi-periodic states were found to reappear after the first chaotic window and develop chaos again through an "attractor-merging crisis", i.e., the merging of "coexisting attractors".

Other examples can yet be found in the literature for binary fluids. For instance, for the case of convective structures that are spatially confined and surrounded by quiescent fluid, it is worth considering the study by Barten et al. [199] where non-linear, spatially localised structures of travelling convection rolls in horizontal layers of binary

fluids heated from below were investigated as a function of Rayleigh number for different conditions (two Soret coupling strengths, i.e., separation ratios, in ethanol-water mixtures).

Other relevant analogies could be drawn with regard to another very interesting phenomenon in nature (still involving plumes), i.e., moist turbulent convection, thereby offering another potential chance for cross-fertilisation of different literatures. As an example, recently Pauluis and Schumacher [200] have focused on one particularly important regime, that is, the conditionally unstable layer that occurs when the atmosphere is stable for unsaturated parcels, but unstable for saturated parcels. Though this problem is yet closely related to the classical Rayleigh-Bénard convection (see, e.g., Ref. [184] and the rich list of reference therein), it involves phase transitions between the gaseous and liquid phase and also depends on the effect of latent heat release on the buoyancy of air parcels. As a result, although unsaturated parcels are stable with respect to small vertical shifts, saturated moist air parcels produce saturated convective plumes. The case of moist turbulent convection may be regarded as another example in which the spatial coupling of isolated entities can produce transition to chaos, with the role of oscillons seen in our case being replaced by the onset of isolated thermal plumes and related multiplicity (which depends on the effective spatial extension of the considered system). These authors observed states in which convection is suppressed or only present as a recharge-discharge mechanism, with short intense bursts of convection separated by long quiescent intervals or statistically stationary convective regimes.

8.5 Conclusions

The present results may be summarised as follows. In assessing the changes produced by an increase in the control parameter (elasticity number) in a problem of viscoelastic flow, it has been found that a seemingly innocuous and general system such as Marangoni-Bénard convection can display very rich and fascinating bifurcation scenarios.

Due to the disorganized appearance of the three- dimensional solutions (initially resisting a deeper analysis), we have followed a deductive approach with systems of growing complexity being considered progressively. More specifically, we have initiated our investigation from the simplified conditions in which the number of involved spatial dimensions is reduced to two, which proved instrumental in unravelling processes that

are interwoven or overshadowed in 3D.

As revealed by these results, while for relatively small values of Θ multiple solutions occur in the form of ordered stationary multicellular states differing in wavelength and/or standing waves that coexist in the space of parameters, an increase in Θ makes regimes with "localised features" the preferred mode of convection.

Indeed, we could identify the following sequence of events taking place along the ideal path bringing the system from initial laminar conditions toward chaos: initially, localised phenomena manifest in the form of an isolated oscillator in an otherwise stationary background flow; as Θ is increased, however, the number of such features increases leading them to "interact" . Such interplay finally results into two coexisting possible lines of evolution, namely, it can produce completely synchronous behaviours (i.e., "crystalline" patterns) or T^2 tori and associated beats in the same interval of the elasticity parameter (i.e., yet in the form of multiple solutions).

Two-dimensional simulations also proved to be a good test bed to get a "quantitative" measure of the fractal nature of these attractors. Indeed, given the relatively low-dimensional nature of chaotic states emerging under the constraint of 2D flow, we could evaluate precisely the so-called correlation dimension. By embodying the concept of progressively increasing structure on finer and finer length scales, this quantity can be used to reveal the emergence of features typical of chaos.

In this way, we could clearly discern that the scenario with T_2 tori remains relatively stable until, by further increasing the elasticity parameter past a critical value ($\Theta \geq 0.088$), the torus corrugates leading ultimately to strange attractors.

As shown by the three-dimensional simulations, the ultimate scenario with localised convective features, each independently contributing to increase the degrees of freedom of the system is retained if the third spatial dimension is considered. Such simulations (relatively limited in number due to their extremely high computational cost) allowed us to pinpoint a variety of interesting spatio-temporal dynamics.

Indeed, starting from conditions corresponding to Newtonian flow for which the pattern can be sketched as a very regular texture consisting of triangular cells, which self-organise giving rise to structures resembling flowers with symmetrically located petals, on increasing Θ, a complex sequence of modifications is enabled. Initially ($\Theta \leq O(10^{-2})$), these alterations essentially manifest in the form of localised defects in the flow topology, which prevent the pattern from displaying a regular polygonal

multi-cellular structure in some sub-regions of the physical domain. For larger Θ, the topological alterations are coupled with significant modifications in the morphological structure of the cells. Indeed, following a trend similar to that revealed by the 2D simulations, the cells grow in size, such expansion in the horizontal direction running in parallel with a decrease in the overall number of convective features, as witnessed by the emergence of surface areas of apparently quiescent fluid "separating" the different cells.

The extension of these buffer regions keeps increasing as Θ becomes higher until, as soon as Θ exceeds a value similar to that already identified in the 2D case (≈ 0.088), a chaotic state is produced with apparently independent (separated in space) oscillons. For this case polygonal structures are no longer a characteristic of the flow. All the oscillons have rounded boundaries and change continuously shape as time passes. Their interactions result in an endless wandering process manifested by islands moving back and forth along different directions that are not fixed but change in time (the instantaneous direction of horizontal motion not being necessarily the same for contiguous cells). This ultimate state also displays remarkable phenomena of cell nucleation, splitting and coalescence, which, taken together, are somehow reminiscent of the so-called "plate tectonics theory" and related "continental drift" (a phenomenon well-known to geophysicists, driven by the interplay of thermal plumes in the mantle of our planet). This key observation led us to sift through existing studies with different foci in order to glean hints and draw inferences about what factors may facilitate the transition to chaos in spatially extended systems that are dissipative in nature.

The affinity with other categories of phenomena seems to indicate that for the present conditions the emergence of chaos is driven by a process formally similar to that seen in problems where turbulence is sustained by the spatial coupling of unsteady localised features (relevant examples being the transition from laminar to turbulent flow in an ordinary pipe or the buoyancy flow in the form of plumes being produced by spatially separated sources of buoyancy). These arguments may be considered as a clue or hint for the existence of a class of universality that transcends the differences in the micro-physical behaviour of different systems such as Newtonian fluids, viscoelastic liquids, and granular media.

This commonality, which over recent years has led to the initiation of specific work devoted to the investigation of these aspects, can be regarded as the spark at the root

of the present study.

On the basis of all these findings and related considerations, we conclude that the emergence of oscillons in the form of multiple solutions, which progressively increase the number of degrees of freedom of a dissipative system, may be regarded as another of the mechanisms potentially used by Nature to produce "fractalisation" that is the basic of creating turbulence through the development of strange attractors.

Chapter 9

On the influence of thermal boundary conditions in thermo-gravitational convection: numerical and experimental analysis

In Chapters 3 and 7, we have introduced several examples of thermo-gravitational convection, underlining many situations in which it plays a central role both in natural phenomena and in industrial processes. Moreover, due to its highly non-linear dynamics, it has attracted many researchers in the last and present centuries under a theoretical point of view. Indeed thermo-gravitational flows offer a great tool to study more general mathematical and physical phenomena such as the onset of chaos and turbulence. Due to this theoretical imprint, very simplified domains and boundary conditions have been considered in literature in order to keep the problem as simple as possible and to detect and analyse the underlying physics correctly. If this approach led to growing the knowledge about many complicated phenomena such as those related to chaotic systems, on the other hand, the problems involving more complicated domains and realistic boundary conditions have received much less attention. In Chapter 4 indeed we have reported a very detailed analysis of a layer with an infinite extension, where the thermal boundary conditions considered were or the adiabatic walls or

boundaries with a fixed temperature. In some cases, a heat flux has been taken into account through a Biot number. In chapter 7 we have considered a more complicated domain: a cavity with converging or diverging horizontal walls, the boundary conditions, however, have been kept very simple, considering the walls perfectly conducting (fixed temperature) or adiabatic.

Chapter 4 has served as an introduction to the thermal convection, being focused only on the underlying physics and leaving aside the "collateral" effects produced by the shape of the container or its conditions at the boundaries. Once we gained some knowledge about the fundamental dynamics occurring in thermo-gravitational convection in Chapter 7, we tried to increase the level of difficulty by introducing a more complicated shape of the enclosure and looking how this could affect the dynamics. A very reach scenario, consisting of travelling waves, coalescing and "kissing" rolls (see Chapter 7) has been found in case of 2D cavities, while for 3D domains a competition among thermal and hydrodynamical instabilities have been reported. Throughout this chapter, we try to shed some light about another aspect which can, in principle, profoundly influence the dynamics: the heat flux through the walls of the domain. To pursue this aim, we consider a relatively simple domain, namely a cubic cavity.

The present work examines the consequence of this long-held assumption/weakness of the popular way of thinking illustrated above, which appears to have scarcely been questioned in the literature.

The aim of the present chapter is, therefore, to get an insight into the impact of different thermal boundary conditions through a combined numerical/experimental approach. The heat flux through the walls is indeed taken into account by modelling the solid walls as well.

The inclination among the imposed temperature gradient and gravity vector is changed, making use of an experimental facility, ranging from the Rayleigh-Bénard configuration to the pure Hadley flow.

Moreover, we vary the heat exchanged by increasing or decreasing the average temperature of the liquid. The control parameter, namely the Rayleigh number, is based on the temperature difference between the hot and cold walls and it is kept fixed in order to have a precise picture about the consequences of having a different heat loss, which in principle could produce a departure from the initial steady or oscillatory states to chaos. After a two-dimensional study, three-dimensional numerical simulations are

carried out relying on the finite-volume method (FVM), considering the dependence of the fluid thermophysical properties on temperature.

The study conducted in the present chapter has a twofold intent: first to analyse the impact produced by dropping away from the assumption of the adiabatic walls, secondly to consider more complex hypothesis, which in future could help to build more realistic models.

9.1 Experimental apparatus and procedure

The facility, used to conduct the experiments, has been designed by Christopher Haughey.

The facility used to conduct the experiments is the TCFS (Thermal Convection Fluid Science) Test Rig. This rig is equipped with a set of Perspex parallelepiped enclosures with different dimensions, called in the following "Fluid Containers" (FCs). To investigate different configurations (i.e. the relative inclination among temperature gradient and gravity), the apparatus is capable to hold the FCs in an inclined configuration, ranging from the horizontal direction up to 180°.

It is possible to gain a more detailed insight about the rig from Figure 9.1, where two

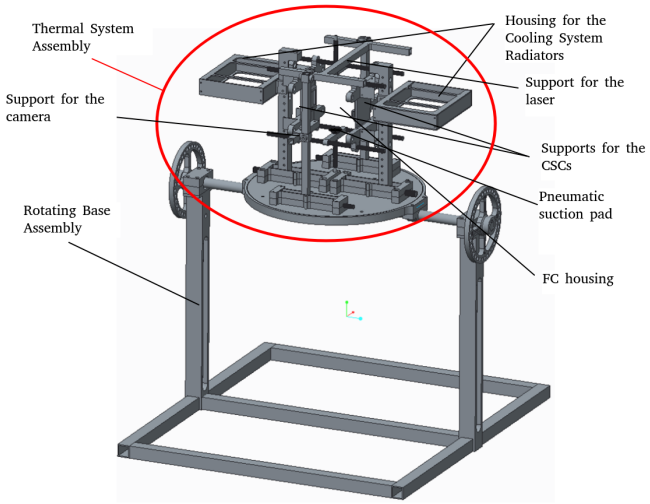

Figure 9.1: CAD model of the TCFS Test Rig used to conduct the experiments.

main sub-parts can are evident, namely the Rotating Base Assembly (aimed to hold the facility and control the angle of inclination) and the Thermal Systems Assembly (devoted to controlling the temperature on the walls of the FCs). The TCFS is also

provided by the Fan Support Assemblies (FSA), needed in order to remove the heat efficiently from the Cooling System Radiators. The FSA is separated from the rest of the rig in order to prevent the vibrations, originated by the fans, propagating towards the fluid containers.

The FC is locked into its position by two opposing Cooling System Containers (CSCs), consisting of a Peltier Module and liquid-based CPU cooler. The CSCs are placed on two sliding Support Frames, which can be moved according to the size of the FC. Thermal contact among the FC and the Peltier cells is improved by the application of silicone gel, which avoids the formation of a layer of air between these two components. Additionally to the constrain brought by the CSCs, when the rig is in the horizontal configuration, the FC is kept in its position also by two pneumatic suction pads which are suspended on rods between the CSCs, a 12V vacuum pump is employed to produce the vacuum of approximately 16" Hg. The suction pads, which can meet the size of the FC, can be placed onto two of the other remaining faces (other than those connected to the CSCs). This fact gives the possibility to have different perspectives by placing the Microscope in different positions. However, it is worth remarking here that it is not possible to have a bottom view of FC. So, when the FC is in the horizontal configuration, two sides of the FC are in contact with the CSCs, another two with the suction pads. The final two sides are in front of the Microscope and the Light Source. When the FC is in the horizontal configuration, the CSCs are connected by screws to their Support Frames. If there is the need to have a view of the FC from a different side, the rig can rotate respect the FC to allow the camera to be placed against another face, allowing the operator to observe the fluid from different angles.

Three kinds of cubic and parallelepipedic FCs, having different inner sizes: 60 x 60 x 60 mm,40 x 40 x 40 mm or 40 x 40 x 90 comes with the rig. The temperature difference is obtained using two Peltier Modules opposite to each other, with the following characteristic: 40 mm x 40 mm x 4 mm, 12V, 6A. Moreover, they are connected to two PID Temperature Controllers (Omega CN32PT-440-DC: accurate to +/- 0.2 °C), and a 5 $k\Omega$ thermistor (with an accuracy of +/- 0.1 °C) measures the temperature on the wall FC. With the above considerations the error in measuring the temperature on the outer side of the FC wall is +/-0.3 °C. The Temperature Controller comes with a self-tuning function, however in some circumstances, for temperatures smaller than 70 °C, the PID values assessed by such function suffered from low accuracy. This fact

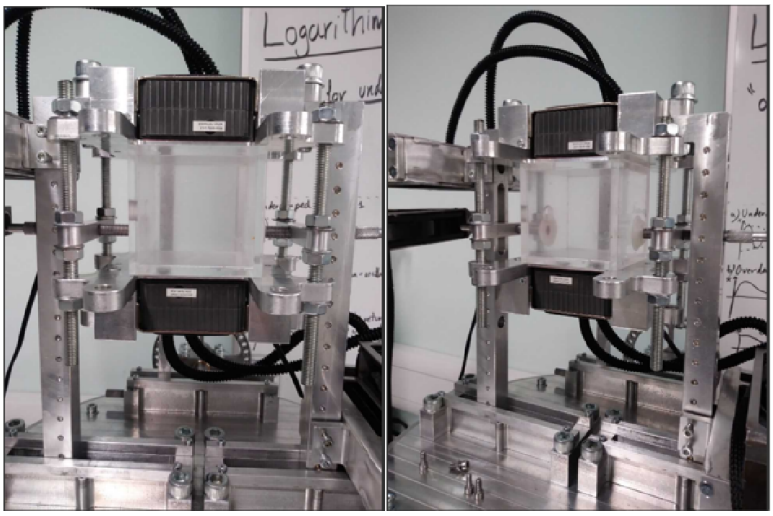

Figure 9.2: The rig with an original 60x60x60 mm Perspex FC.The Peltier Brackets, Peltier Devices and associated wiring have been removed for clarity.

is the reason why the PID parameters are, in some cases, manually tuned. Following this path, the error has been kept in the range of +/-0.1 °C(in many cases inside the interval of +/-0.02 °C).

The DC signals produced by the Temperature Controllers pass through two Solid State Relays (SSR), connected with the Peltier Module in order to form a circuit in series, as shown in Figure 9.3). The SSR aims to convert the continuous output of the Temperature Controllers into a discrete "on-off" signal. In this manner, the temperature is kept at the desired value by modulating the voltage supplied to the Peltier cells.

Each Peltier Module dissipates the heat tanks to a Cooler Master Seidon 120V Version 2.0. This CPU cooler relies on a thermally conductive fluid, pumped in a circuit comprising a copper plate and a radiator. Each cooler can dissipate up to around 300W. Several tests have been run, leading to the conclusion that a constant temperature up to 100 °C on the external wall of the FC can be maintained. On the other hand, it is possible to achieve colder temperatures up to 10 °C. A Digital Microscope with a zoom up to 50x records the moving glass tracers which are enlightened by a laser with the following properties: 532 nm ± 10 wavelength and power max output < 50 mW. Dedicated tools come with the rig in order to settle both the Microscope and laser light source. Finally, thanks to a central rotating shaft, upon which is located the structure described above, it is possible to incline the FCs. The shaft enables the inclination angle to be changed with variations of 10°, allowing to study several configurations.

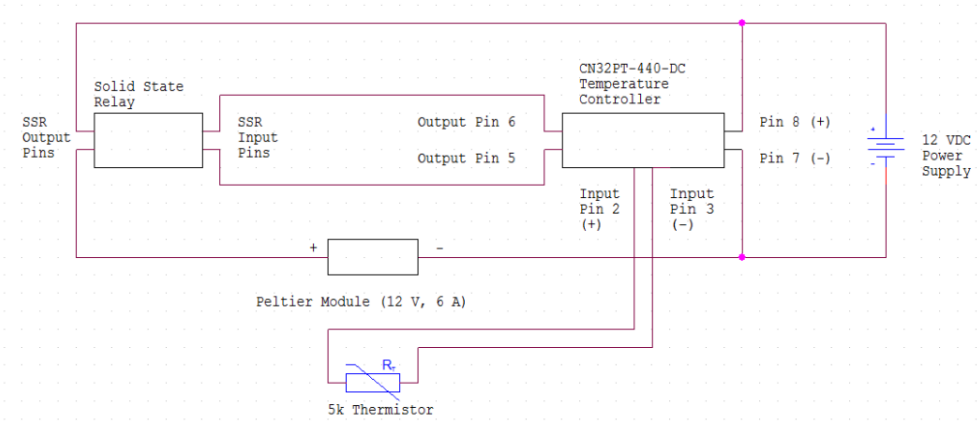

Figure 9.3: Circuit Diagram of the Temperature Control Circuit of the TCFS Test Rig. Overall, there are two such circuits i.e. one for each Peltier Device.

9.1.1 Methodology and post-processing techniques

The present section aims to describe the procedure followed in conducting the experiments and the methods used to post-process the outcomes.

A first task which has to be accomplished is the preparation of the fluid containers, which have to be filled with water and the glass tracers. After the operator has correctly prepared the containers, they are placed inside their housing (see 9.1). Once the fluid cells are in the correct position, the temperature needs to be set up to produce the desired thermal difference between the two sides. The following step consists of waiting for the system to reach thermal equilibrium (this could require more than 30 minutes). Once the fluid containers are heated up, it is possible to turn on the laser (placed above the FC) and start to record the video, which is the input for the subsequent PIV analysis. An important aspect to take into consideration is the duration of the video: it has to last for enough time to detect possible time-dependent feature of the flow. On the other hand, excessively long recordings are memory consuming (in terms of gigabytes of the video files) and are challenging to handle. Based on these observations, a duration of 10 minutes seems to be an acceptable compromise to conduct the PIV analysis.

The post-processing relies on the PIV technique. A detailed description of the theoretical foundations, behind the PIV analysis, are out of scopes of the present chapter. However, it is worth saying that the frames of the recording have to be extracted in PNG (or JPG) format with an adequate sampling (0.2 s seems to work fine for the present experiments). As a tool to perform the PIV analysis, OpenPIV [201] has been used. This software provides an API and a GUI (in Matlab, Python and C++), which

allows the user a correct set up and analysis. An important aspect to take into consideration is the subdivision of each frame into subwindows (each window corresponds to a velocity vector). Indeed, as input parameters, the user is asked to enter the width and height of the windows in pixels. Also, in this case, a compromise has to be reached: smaller windows allow more accurate decomposition and vector plots (in terms of the number of velocity vectors). On the other hand, small windows are computationally expensive and are more prone to noise, which manifests itself as the insurgence of outlier vectors. The software automatically removes these, but having an excessive number of them, brings to less accurate vector plots.

9.2 Mathematical model

9.2.1 Geometry

The following investigations rely upon the so-called modelling hierarchy according to which the models are progressively made more sophisticated from the fundamental ones by considering or disregarding various effects, allowing in this manner a deeper understanding about the phenomena related to thermal convection.

As discussed above, the thermal convection has been studied so far by researchers prevalently considering simplified boundary conditions: conducting and purely adiabatic boundaries have been taken in consideration in order to model the solid walls where the temperature is not actively controlled.

The first one is approximated in the real world by walls made of materials with very low thermal conductivity (such as wood or plastic materials), whereas the second can be achieved with materials with high thermal conductivity (metals).

Unfortunately, materials having infinite or zero thermal conductivity do not exist, making simplified boundary conditions purely mathematical concepts.

In the present study, these idealized conditions are replaced by a more realistic framework. The thickness and the nature of the material (perspex) of the FCs walls are taken into consideration. Moreover, the heat dissipated in the ambient through the walls where the temperature is not actively controlled. The model is shown in Figure 9.4 in case of Rayleigh-Bénard and Hadley flow configurations.

The present study intends to investigate a basic model according to which the properties of the wall are constant and isotropic in all directions, while heat transfer occurs

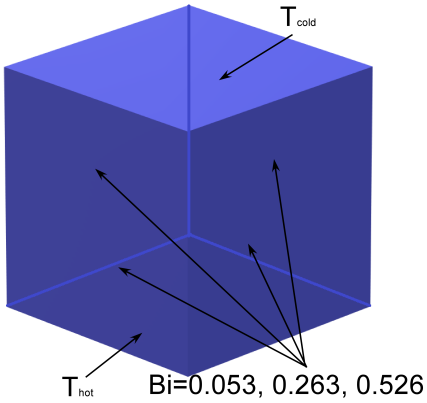

(a) 3D sketch of the geometry (Hadley flow configuration)

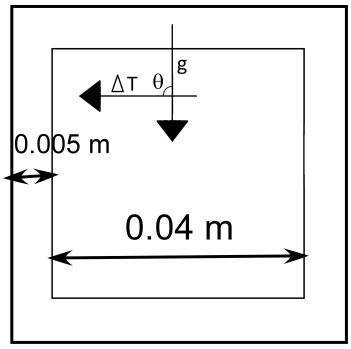

(b) Two-dimensional view (Hadley flow)

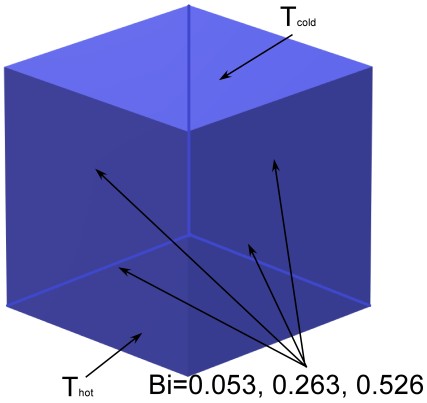

(c) 3D sketch of the geometry (Rayleigh-Bénard configuration)

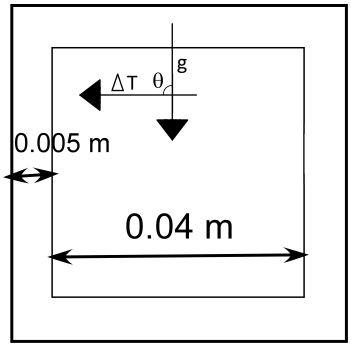

(d) Two-dimensional view (Rayleigh-Bénard)

Figure 9.4: Geometry

at their outer surface. Although much more sophisticated models could be considered, with such a configuration, we are capable of modelling the heat flux through the solid walls.

In Figure 9.4, only the two basic configurations have been represented. However, an entire matrix of cases is considered throughout the present Chapter, varying not only the inclination of the box but also the temperature on the cold and hot walls. More precisely, the set of cases shown in Figure 9.5 has been considered for the experiments and 2D simulations.

9.2.2 Equations and boundary conditions

Fluid region The equations which have been solved are the continuity, Navier-Stokes and energy, represented by 2.2,2.9 and 2.4 respectively (see Chapter 2). Moreover, the Boussinesq approximation has been dropped, considering the physical and ther-

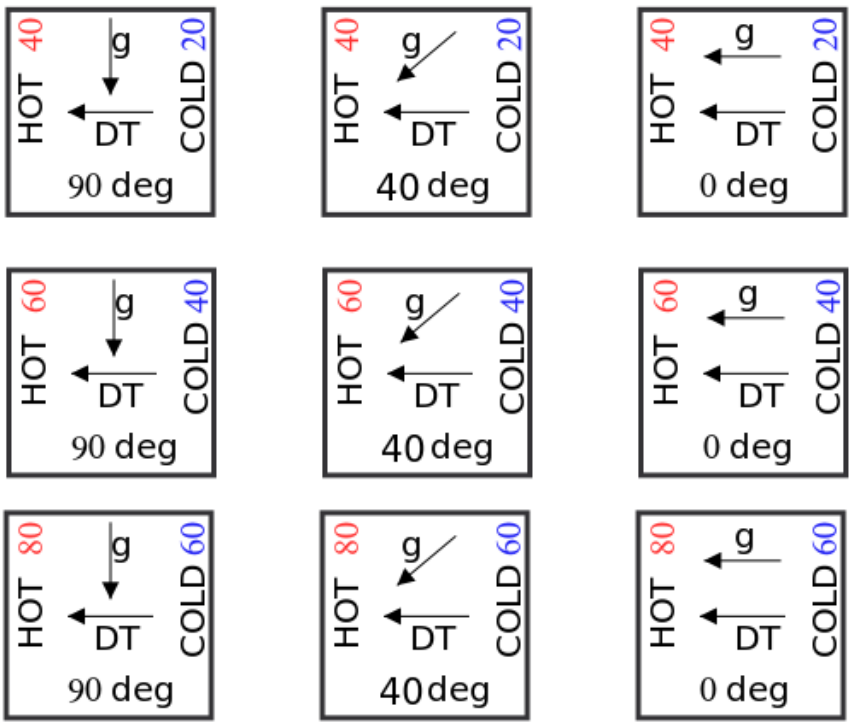

Figure 9.5: Matrix of the cases taken into consideration.

mal properties varying as a function of the temperature according to a fourth-degree polynomial law. In Table 9.1, it is possible to see the properties of water at different temperatures.

Temp	k	ρ	Cp	μ	ν	α	Pr
10	0.57864	999.77	4192	0.001308	1.3083e-6	1.3807e-7	9.4759
20	0.59803	998.29	4182	0.001003	1.0047e-6	1.4325e-7	7.0139
30	0.6145	995.71	4178	0.000798	8.0144e-7	1.4771e-7	5.4256
40	0.62856	992.25	4179	0.000653	6.5810e-7	1.5158e-7	4.3415
50	0.6406	988.02	4181	0.000547	5.5363e-7	1.5507e-7	3.5701
60	0.65091	983.13	4185	0.000467	4.7500e-7	1.5820e-7	3.0026
70	0.65969	977.63	4190	0.000404	4.1324e-7	1.6100e-7	2.5660
80	0.66702	971.6	4196	0.000355	3.6538e-7	1.6361e-7	2.2332
90	0.67288	965.06	4205	0.000315	3.2640e-7	1.6581e-7	1.9685
100	0.67703	958.05	4216	0.000282	2.9435e-7	1.6762e-7	1.7561

Table 9.1: Physical properties of water as function of the temperature

Solid region In the solid region made of perspex, the diffusion equation has been solved:

$$\rho c_p \frac{\partial T}{\partial t} = \nabla \cdot k \nabla T \tag{9.1}$$

Moreover, the properties of perspex are reported in Table 9.2:

$\rho \left[\frac{Kg}{m^3}\right]$	$c_p \left[\frac{J}{Kg*K}\right]$	$\lambda \left[\frac{W}{m*K}\right]$
1190	1459	0.19

Table 9.2: Properties of perspex.

Coupling and thermal boundary conditions The results presented throughout the present chapter rely on a multi-region approach. Indeed, also the heat flux through the walls has been quantified through the equation 9.1. Moreover, the finite thickness of the walls leads to having thermal boundary conditions both on the internal and on the outer side. On the inner side, the solid perspex comes in touch with water, whereas on the external one, the air is in contact with the solid. This fact leads to the following two boundary conditions:

External side of the walls

$$h_{air}(T_\infty - T_{wall}) = -k_{solid}\frac{\partial T}{\partial y}_{extwall} \tag{9.2}$$

Internal side of the walls

$$k_{fluid}\frac{\partial T}{\partial y}_{intwallfluid} = k_{solid}\frac{\partial T}{\partial y}_{intwallsolid} \tag{9.3}$$

In the equations 9.2 and 9.3 h is the convective coefficient while k is the thermal conductivity.

Solution procedure The computations showed throughout this chapter are carried out using OpenFoam, which relies on the Finite Volume Method (FVM). It is not the aim of this paragraph an accurate description of such a method, addressing the interested reader to Chapter 5 and references therein. The main purpose here is only to make the reader aware of the specific methods used. The non-transient equations described in Chapter 2 (see equations 2.2, 2.9 and 2.4) indeed have been solved relying upon the so-called family of the projection methods and more specifically the PISO (Pressure Implicit Split Operator) has been used. According to such a set of algo-

rithms, continuity is not directly solved but used to build a Poisson equation for the pressure. Moreover in order to avoid problems of weak coupling among the pressure and momentum a special interpolation for the pressure on a collocated grid has been used, namely the so-called Rhie and Chow interpolation (see [55]).
The momentum and temperature equations have been discretised employing a second-order central difference scheme for both convective diffusive terms. The resulting system of algebraic equations has been solved through a preconditioned Bi-Conjugate Gradient (PBiCG) with an Incomplete Lower Upper (DILU) preconditioner. The elliptic equation for the pressure has been treated with a Generalised Geometric-Algebraic Multi-Grid (GAMG).

9.2.3 2D vs 3D

The rationale leading to an introductory parametric two-dimensional study is pretty similar to that of the previous chapter: 3D simulations are computationally expensive, and a complete three-dimensional study is difficult to conduct.
On the other hand, as discussed in the following, the 2D-simulations fail to reproduce the experiments correctly, so a 3D analysis is needed. However, the 2D outcomes are still useful to highlight the relevant departures from the experimental outcomes. Moreover, an entire grid of 2D-cases is needed to identify the starting points of the 3D analysis.

9.3 Code validation

In this section the code has been validated for two different basic configurations: the cavity heated from below and cooled from above (Rayleigh-Bénard convection) and for the box subjected to a horizontal temperature gradient (Hadley flow). Due to the differences between RB and Hadley convection, two different subsections has been devoted to the validation.

9.3.1 Rayleigh-Bénard

In this subsection, the validation study related to the Rayleigh-Bénard convection is presented. The comparison is made with the results in Refs. [202] and [203] and the parameters checked are the maximum vertical and horizontal velocity components

(U_{max} and V_{max}) and the average Nusselt number on the cold and hot walls Nu_c and Nu_h respectively. The average Nusselt number can be defined in general as:

$$Nu_{wall} = -\frac{1}{L}\int_0^L \left.\frac{\partial T}{\partial y}\right|_{wall} dx \tag{9.4}$$

where *wall* could be the hot bottom wall or the cold upper one. L is the length of the boundary, and the derivative is taken in the normal direction of the boundary.

	Present results	Ref. [202]	error %
U_{max}	0.3443	0.3442	0.029
V_{max}	0.3754	0.3756	0.053
Nu_h	3.9204	3.9097	0.274

Table 9.3: $A = 1$, $Ra = 10^5$, $Pr = 0.71$. Comparison with Table 2 of Ref. [202], mesh $128x128$. $u_0 = \sqrt{g\beta H\Delta T}$, H being the characteristic length.

	Present results	Ref. [202]	Ref. [203]	error % with [202]	error % with [203]
Nu_h	2.53163	2.52523	2.52234	0.253	0.368
Nu_c	2.53164	2.52525	2.52525	0.253	0.365

Table 9.4: $A = 4$, $Ra = 10000$, $Pr = 0.71$. Comparison with Table 3 of Ref. [202] and Table 2 Ref. [203].

As it can be seen from Tables 9.3 and 9.4 the error is well below the 1% both for $Ra = 10^4$ and for $Ra = 10^5$.

9.3.2 Hadley flow

The validation for this configuration follows the benchmark studies of De Vahl Davis and Jones [204]. The comparison is made at $Ra = 10^6$ in a square cavity with air ($Pr = 0.71$) as fluid. The outcome of the validation is presented in Table 9.5, where it is evident that the error is smaller than 3% for all the parameters taken into account.

9.4 Mesh refinement study

As proceeded in the previous two chapters, after the validation of the code, the minimum grid size needs to be assessed. This section aims to provide the minimum number of nodes, used in the following sections. As already done previously also in this section, the discussion is split among the two main configurations, namely the Rayleigh-Bénard

	Description	present results	Ref. [204]	error %
$\|\psi\|_{max}$	Maximum absolute value of the stream function	16.919	16.750	1.009
v_{max}	Max vertical velocity component on a horizontal mid-plane	216.09	219.36	1.491
x_{max}	Position of v_{max}	0.0368	0.0379	2.902
u_{max}	Max horizontal velocity component on a vertical mid-plane	64.97	64.63	0.526
y_{max}	Position of u_{max}	0.848	0.850	0.235
Nu_{hot}	Average Nusselt number on the hot wall	8.913	8.817	1.089
$Nu_{max,hot}$	Max Nu on the hot boundary	18.193	17.925	1.495
$y_{Nu,max}$	Position of $Nu_{max,hot}$	0.0368	0.0379	2.902
$Nu_{min,hot}$	Min Nu on the hot wall	0.970	0.989	1.921
$y_{Nu,min}$	Position of $Nu_{min,hot}$	1	1	0

Table 9.5: $Ra = 10^6$, $Pr = 0.71$, $A = 1$. Comparison with the results of Ref [204].

and Hadley flow convection. For simplicity, the cavity is supposed to have perfectly adiabatic walls, and both cases rely upon the Boussinesq approximation.

9.4.1 Rayleigh-Bénard

The considered Prandtl number is $Pr = 6.9$ and the Rayleigh number is $Ra = 4.4 * 10^5$, corresponding to a $\Delta T = 0.5$, for which an oscillatory pattern has been found. As shown in Table 9.6, three (uniform) mesh resolutions have been considered: 60x60, 100x100, 150x150. As the Rayleigh number presented in the following results is generally higher than that characterising the Table 9.6, we also consider a mesh refinement study for $Ra = 10^6$. However, being the flow for this value of the Rayleigh number chaotic, the main peak of the frequency spectra is compared. From Tables 9.6 and 9.7 it can be noted that, when a mesh 100x100 is employed, the error is always less than 1 % for $Ra = 4.4 * 10^5$, whereas, when the Ra is increased up to 10^6, the error in the frequency

Mesh	ω	error %
60x60	332.366	0.566
100 x 100	334.225	0.125
150x150	334.644	/

Table 9.6: Non-dimensional frequency as a function of mesh size ($Pr = 6.9$, $Ra = 4.4x10^5$)

Mesh	ω_{peak}	error %	Ampl.	error %
100x100	439.6	1.011	46.44	2.334
150 x 150	435.2	/	47.55	/

Table 9.7: Comparison of the main peak of the frequency spectrum:ω_{peak} is the frequency of the main peak, Ampl. is the value of vertical velocity component of the peak.$Pr = 6.9$, $Ra = 1x10^6$

of the peak of the spectrum is $\approx 1\%$ (and 2.334 % in the peak amplitude).

9.4.2 Hadley flow

The parameters used for the Hadley flow are Prandtl number $Pr = 6.9$ and Rayleigh number $Ra = 1.77x10^7$,corresponding to $\Delta T = 20°C$, which is the value used in the experiments. Three (uniform) mesh resolutions have been considered: 60x60, 100x100, 150x150 (see Table 9.8). As made evident by Table 9.8, a uniform mesh with resolution

Mesh	ω	error %
60x60	42.345	3.18
100 x 100	41.041	1.41
150x150	40.469	/

Table 9.8: Non-dimensional stream function as function of mesh size ($Pr = 6.9$, $Ra = 1.77x10^7$)

100x100 makes the relative variation smaller than 2 %.

9.5 Results

As a common practice in the present chapter also in this section, the discussion is split into two main subsections: one devoted to describing the phenomena occurring in the Rayleigh-Bénard convection and the other focused on the Hadley flow and inclined configurations. Moreover, for both cases, the discussion is structured as follows: first,

a two-dimensional analysis is presented, followed by a paragraph explaining the experimental results. After a comparison aimed to highlight the differences between the 2D and experimental results, a three-dimensional analysis is undertaken with the purpose to obtain a better agreement with the experimental outcomes.

9.5.1 Rayleigh-Bénard convection

Following the procedure outlined above, we start in this subsection to discuss the results, however, before embarking in the analysis of the two-dimensional cases, it is worth introducing the difference among the "nominal" and "effective" Rayleigh number (Ra and Ra_{eff}). The latter is defined using the mean temperature on the inner side of the hot and cold walls (that in contact with the fluid). Being the temperature on these sides free to vary Ra_{eff} could also become negative when the temperature of the top side is on average greater than that on the bottom side. This fact could become particularly true when a pattern like sa (symmetric-anti-symmetric, as shown in Figure 9.6) is triggered. Indeed the fluid descending close to the lateral walls exchanges heat with them arriving colder on the bottom and causing a drop of the temperature on the inner side of the bottom wall. This fact is more evident when Bi on the lateral patches is high and when the T_{cold} and T_{hot} are much higher than the ambient temperature. To highlight this fact in Table 9.9 and 9.10 different ΔT, Ra and R_{aeff} are reported for $T_{cold} = 60$ °C and 40 °C. It is evident that R_{aeff} is much smaller than Ra (or even

ΔT °C	Ra	Ra_{eff}
5	$2.18 * 10^7$	$-6.068 * 10^6$
9	$3.93 * 10^7$	$-4.614 * 10^6$
12	$5.24 * 10^7$	$-2.336 * 10^6$

Table 9.9: Ra and Ra_{eff} at different ΔT. $T_{cold} = 60°C$, $Bi = 0.526$ ($h = 20$)

ΔT °C	Ra	Ra_{eff}
6.6	$1.61 * 10^7$	$7.092 * 10^5$
8	$1.95 * 10^7$	$1.021 * 10^6$
12	$2.92 * 10^7$	$1.914 * 10^6$

Table 9.10: Ra and Ra_{eff} at different ΔT. $T_{cold} = 40°C$, $Bi = 0.263$ ($h = 10$)

negative), when the T_{cold} and Bi are high. This fact is due to the mechanism outlined above. The R_{aeff} indeed increases when the heat exchange through the lateral walls is

reduced: from the negative values of the Table 9.9 we obtain the positive ones of Table 9.10 by decreasing both Bi and T_{cold}.

Two-dimensional simulations

As discussed above, a review of the outcomes of the two-dimensional simulations is given in the present section. The 2D constraint turns out to be very useful in the present case, as the two-dimensional simulations are computationally much cheaper than their 3D counterparts, allowing in this manner a wider investigation in the space of parameters (e.g. the imposed ΔT and Biot number).

As done several times in the previous chapters, a focused review of the related literature is conducted in order to identify the characterising features of the problem investigated in the present study (comparing and identifying the similarities and differences with the cases widely considered in the literature, namely the configurations involving conducting or adiabatic walls).

It is known from the literature that the cavities on which the classical boundary conditions (adiabatic or conducting) are imposed, display different modes of perturbations, which are able to replace each other when the aspect ratio is changed. Kurzweg [205] and Velte [206] are the authors of seminal studies about Rayleigh-Bénard convection in enclosures, having different aspect ratios in case of adiabatic (Kurzweg [205]) and conducting boundary conditions(Velte [206]). Moreover, the case adiabatic boundaries were further investigated by Luijkx and Platten [207]; furthermore, the studies of Mizushima [208] and Chana and Daniels [209] are worth of consideration in order to retrieve important information about the existing symmetries of the flow patterns, a significant feature characterising the present findings as well.

The RB convection in a square enclosure, indeed, can produce different combinations of the possible symmetric and antisymmetric patterns along with the horizontal and vertical directions. Different roll structures can, in principle be derived by reflecting them respect to the horizontal, vertical centreline or both of them, due to the symmetric/antisymmetric nature of the governing equations and the boundary conditions. Performing opportunely such operations four cases are possible, as shown in Figure 9.6.

As depicted in Figure 9.6, the patterns distinguish to each other, mainly for the number of rolls along with the vertical and horizontal directions. Depending on the

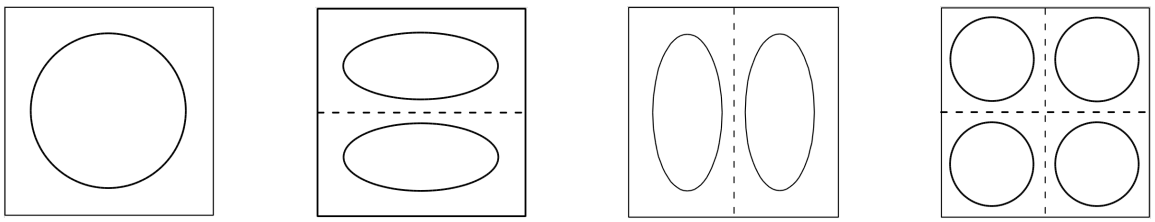

(a) aa (b) as (c) sa (d) ss

Figure 9.6: Possible emerging roll structures of RB convection in two-dimensional finite cavities explained in terms of the symmetries/anti-symmetries.

number of cells met both vertically and horizontally: if it is odd, the flow belongs to the group of antisymmetric-antisymmetric (aa) modes. On the other hand, if it is even in both directions, the pattern pertains to the symmetric-symmetric (ss) family of modes. Moreover, the hybrid combinations of symmetric-antisymmetric (sa) and antisymmetric-symmetric (as) modes are also possible (depending on the even/odd number of rolls in the horizontal and vertical directions respectively). The Rayleigh number and the thermal boundary conditions play a central role in the selection of the preferred mode. If the value of the Rayleigh number is highly supercritical respect to the onset of the convective state, originated from the initially quiescent state, it is a known fact that the (aa) or (sa) patterns can excite modes with other symmetries through non-linear interactions, as discussed by Mizushima and Adachi [210] for the conducting boundary conditions imposed on the sides. On the other hand, if the original roll structure has the (aa) symmetry, the (ss) mode could also be triggered; the pattern, emerging after bifurcation has occurred, is a linear combination of these two modes. When a (sa) symmetry characterises the initial structure of the pattern, all the four modes (aa, sa, as and ss) could raise as non-linear interaction; in this case, according to Mizushima and Adachi [210] no symmetries are present in the flow.

Having in mind the notions just explained, it can be argued that heat loss through the sides can, in principle, play a significant role in the selection process of the modes characterised by the symmetries/anti-symmetries discussed above.

The case with $T_{cold} = 60°C$, due to its the most exciting dynamics and implications, is presented before the other ones.

As represented in Figure 9.6, the 2D flow is subjected to a Hopf bifurcation, absent when conducted the lateral walls have been assumed to be adiabatic. When $Ra < Ra_{cr}$ the heat flowing towards the external environment through the side walls is responsible of the emergence of a single and central thermal plume, in which the hot fluid

is rising at the centre, while the colder one is sinking near to the lateral walls, as depicted in Figures 9.7a and 9.7b). This instability is triggered depending on the heat loss and becomes more critical as the Biot number is increased (Figure 9.7c). In case

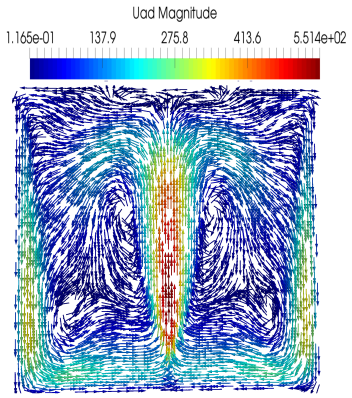

(a) Vector plot of the velocity field

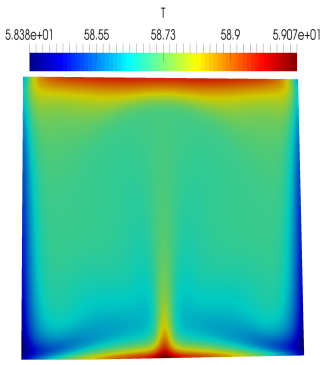

(b) Temprature contour

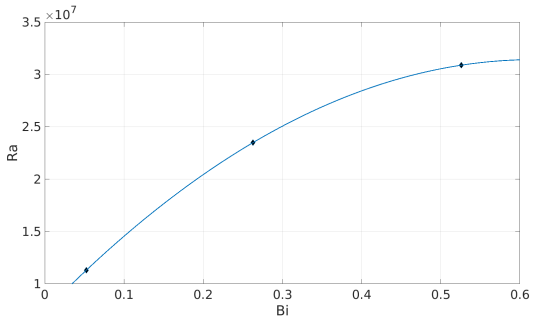

(c) First instability threshold as function of the Biot number

Figure 9.7: $Ra = 8.7 * 10^6 (\Delta T = 2)°C$, $Ra_{eff} = 4.165 * 10^5 Bi = 0.0526$ ($h = 2\ \frac{W}{m^2 K}$

of $h = 2\frac{W}{m^2 K}$ ($Bi = 0.0526$), the oscillations arise from the originally steady pattern between $\Delta T = 2.6$ and $2.7°C$ ($Ra = 1.131 * 10^7$-$1.175 * 10^7$) (a state with one frequency characterised by a plume showing pulsations in the vertical direction); another Hopf bifurcations occurs between $\Delta T = 2.7$ and $2.8°C$ ($Ra = 1.175 * 10^7$-$1.218 * 10^7$), bringing the system to a quasi-periodic regime, in which wobbling mechanism with a higher period is combined with the pulsating one. These two different mechanisms are shown in Figure 9.8, using four snapshots evenly distributed along the period of the oscillating signal: the high frequency pulsating component is depicted in the first row, while the low-frequency wobbling plume is represented in the second one (in order to have a picture of the second phenomenon the first mechanism with higher frequency has been filtered out).

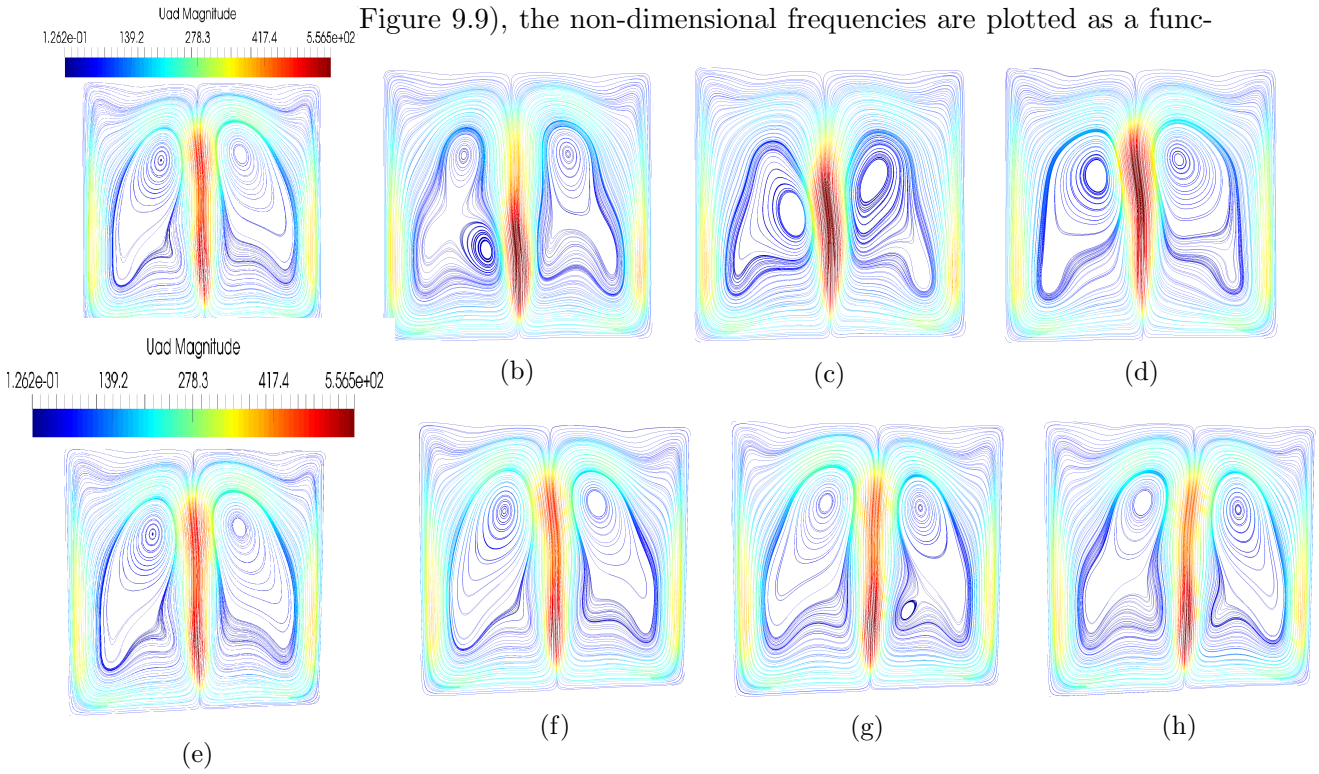

Figure 9.8: $\Delta T = 2.9$ ($Ra = 1.26 * 10^7$, $Ra_{eff} = 3.186 * 10^5$) and $h = 2\ \frac{W}{m^2 K}$ ($Bi = 0.0526$). First row plume pulsating phenomenon. Second row: wobbling instability with a lower frequency.

Figure 9.9), the non-dimensional frequencies are plotted as a function of Rayleigh number: there is a periodic regime where only one frequency, related to the pulsating mechanism, exists. Then, above a value of $\Delta T = 2.8$ °C a second Hopf bifurcation occurs and the wobbling mechanism is turned on. In the end, when a threshold of $\Delta T = 3$ °C is overtaken, the chaotic regime is triggered, but what to say about chaos? How is it triggered, and how does it develop? Before answering to all these questions it is better to have an overall picture of the dynamics, which is depicted in Figure 9.10, where the time series and spectra are plotted in order to highlight the different regimes which the system undergoes: periodic(9.10a and 9.10b), quasi-periodic(9.10c and 9.10d), T^3 bifurcation and onset of chaos (9.10e and 9.10f), developed chaos (9.10g and 9.10h). Moreover in figure 9.11 the phase portraits and the attractors in embedded space are represented for the same values of temperature of Figure 9.10.

Once we have gained a better insight of the overall dynamics of the system it is worth shedding some light on the third Hopf bifurcation, which leads the T^2 torus to become a T^3 tours, following the Ruelle-Takens-Newhouse scenario [72].To be able to see this we plotted the Poincaré sections in the embedded space at x constant (in the middle

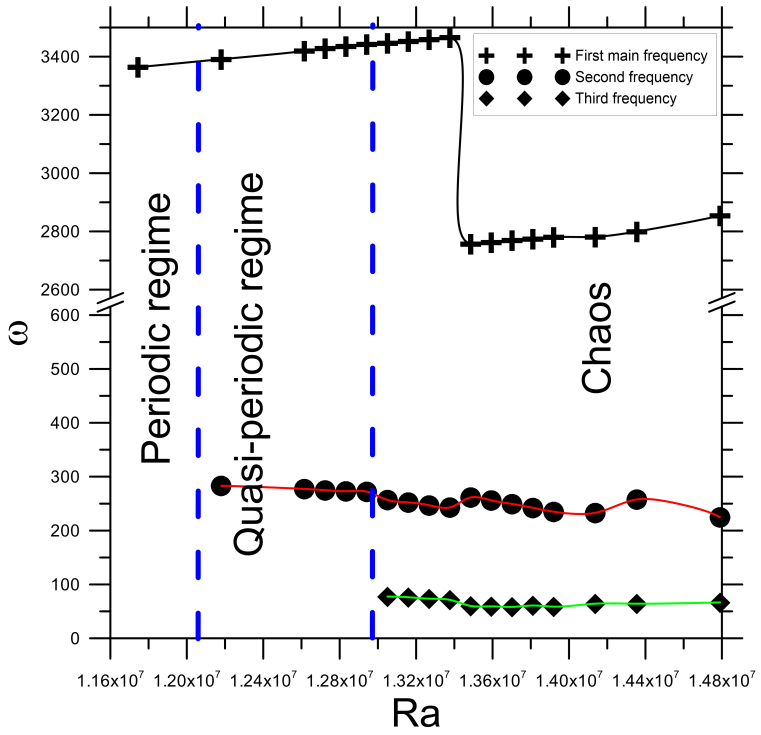

Figure 9.9: Non-dimensional frequency as a function of the Rayleigh number for the cases with $T_{cold} = 60°C$ and $Bi = 0.0526$ ($h = 2\frac{W}{m^2K}$).

of the attractor) in Figure 9.12. From this figure indeed the T^3 bifurcation is pretty evident: looking at the 9.12b and 9.12c we can clearly distinguish a sudden destruction of the T^2 torus. This fact suggests that the system follows the Ruelle-Takens-Newhouse scenario and not the Curry-Yorke one, according to which the system undergoes chaos gradually from a T^2 torus. Moreover, the correlation dimension has been plotted as function of the Rayleigh number in Figure 9.13, where is possible to see that the system jumps from a value very close to 2 from one very close to 3 and there are no points in the range between 2 and 3, as chaos and fractalisation occur at a dimension greater than 3. Moreover, this figure highlights another interesting aspect: the correlation dimension does not increase monotonically with the control parameter (Rayleigh number in this case), showing a transition region between $Ra = 1.218 * 10^7$ ($\Delta T = 3°C$) and $Ra = 1.392 * 10^7$ ($3.2°C$), where the system jumps from a correlation dimension close to 3 to a state with higher degree of chaos.

For $h = 10\frac{W}{m^2K}$ ($Bi = 0.263$), the evolutionary path is quite different. We have detected only wobbling instability. However, the transition to chaos follows the same route already discussed for $h = 2\frac{W}{m^2K}$. For these reasons, we no longer describe this configuration here. Rather we proceed further to the description about the case in

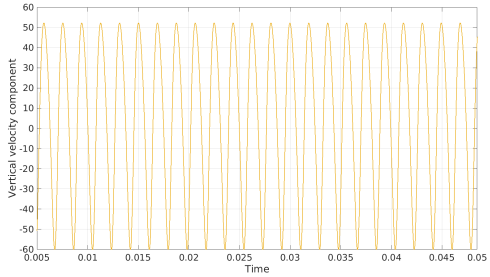

(a) $\Delta T = 2.7$(Ra=11745000)

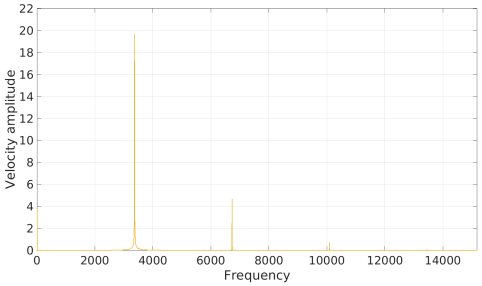

(b) $\Delta T = 2.7$(Ra=11745000)

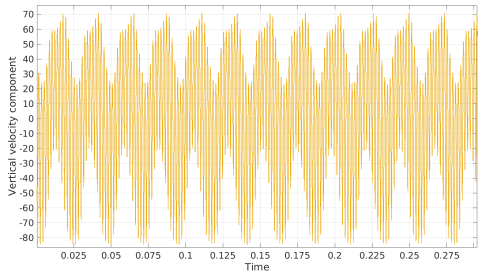

(c) $\Delta T = 2.975$(Ra=12941250)

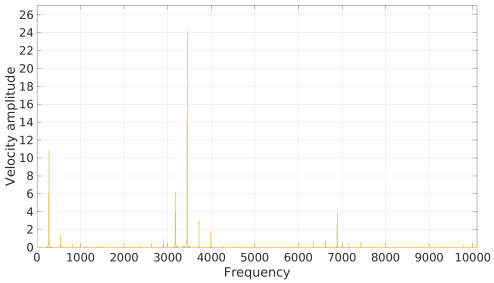

(d) $\Delta T = 2.975$(Ra=12941250)

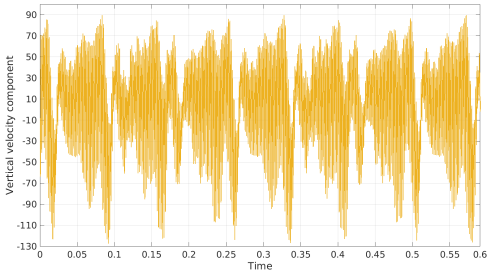

(e) $\Delta T = 3$(Ra=13050000)

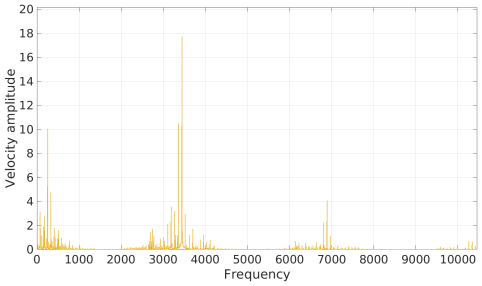

(f) $\Delta T = 3$(Ra=13050000)

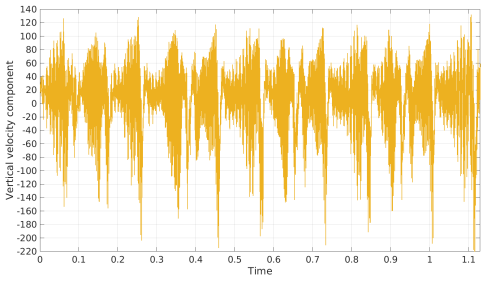

(g) $\Delta T = 3.4$(Ra=14790000)

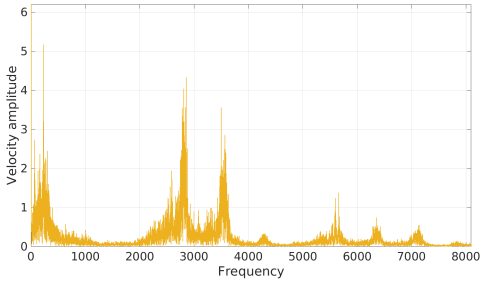

(h) $\Delta T = 3.4$(Ra=14790000)

Figure 9.10: Time series and frequency spectra at $\frac{X}{L} = \frac{1}{2}$ and $\frac{X}{L} = \frac{3}{4}$ with $T_{cold} = 60°C$ and $Bi = 0.0526$ ($h = 2\frac{W}{m^2K}$).

which $h = 20\frac{W}{m^2K}$ ($Bi = 0.526$).

At this value of the Biot number, two different branches of solutions have emerged, which share the same region of the phase space, namely a wobbling regime with some similarities with that just described above and an asymmetric pulsating pattern, char-

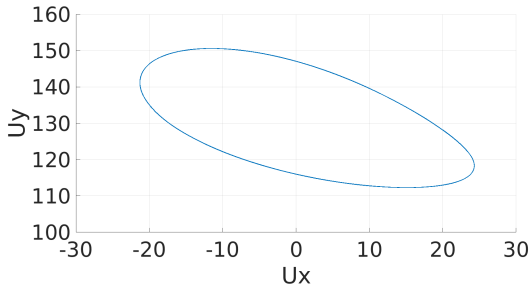

(a) $\Delta T = 2.7$(Ra=11745000)

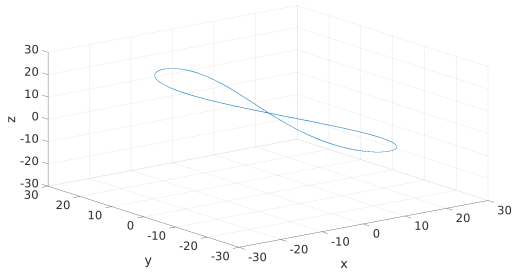

(b) $\Delta T = 2.7$(Ra=11745000)

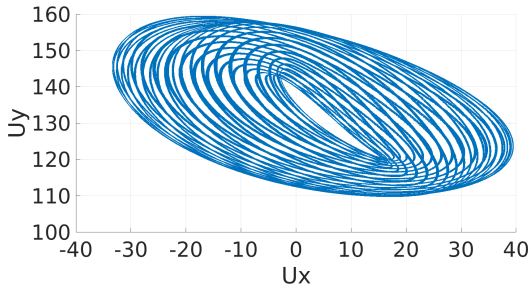

(c) $\Delta T = 2.975$(Ra=12941250)

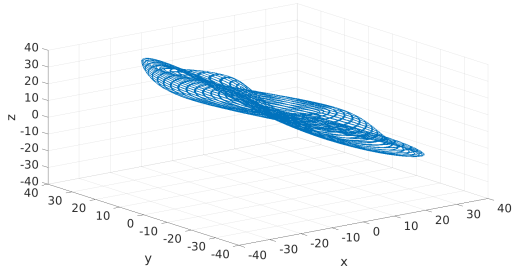

(d) $\Delta T = 2.975$(Ra=12941250)

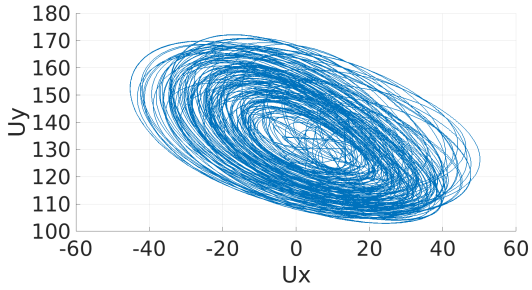

(e) $\Delta T = 3$(Ra=13050000)

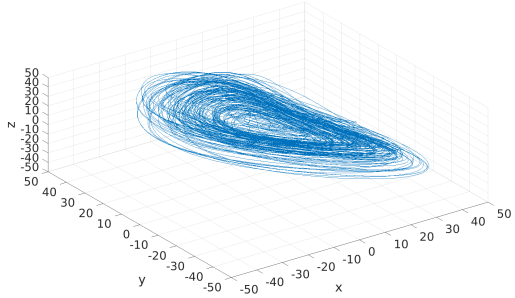

(f) $\Delta T = 3$(Ra=13050000)

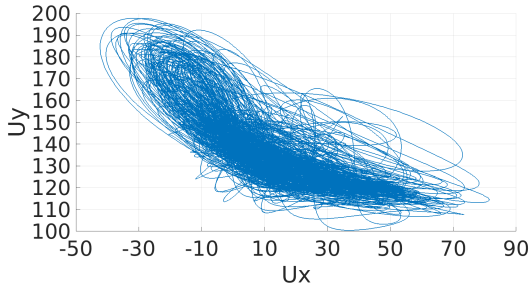

(g) $\Delta T = 3.4$(Ra=14790000)

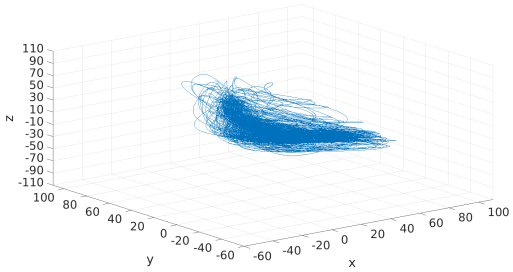

(h) $\Delta T = 3.4$(Ra=14790000)

Figure 9.11: Phase portraits in real and embedded phase space with $T_{cold} = 60°C$ and $Bi = 0.0526$ ($h = 2\frac{W}{m^2K}$).

acterised by a central plume having the central rising stem bent left or right (with these two possible variants being specular images of the other).

The non-dimensional frequencies are represented in Figure 9.14 as function of Ra. It is possible to notice that at Rayleigh numbers comprised between $Ra \approx 3.1 * 10^7$ and $Ra \approx 4.1x10^7$ (or equivalently $\Delta T = 7$ and $9.5°C$) these two possible flow structures

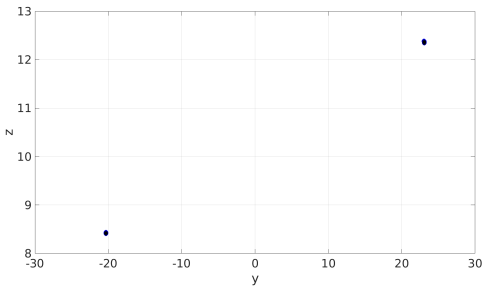

(a) $\Delta T = 2.7$(Ra=11745000)

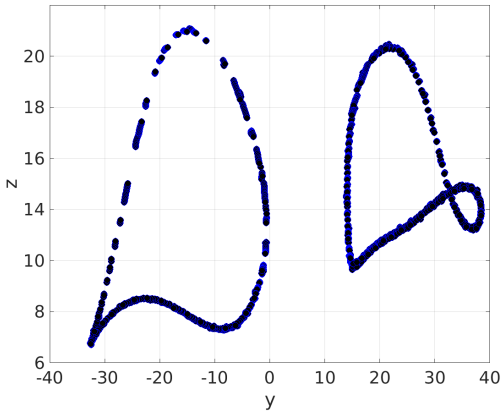

(b) $\Delta T = 2.975$(Ra=12941250)

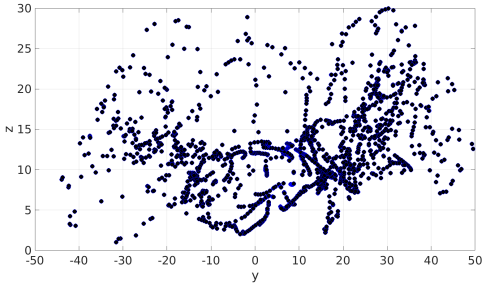

(c) $\Delta T = 3$(Ra=13050000)

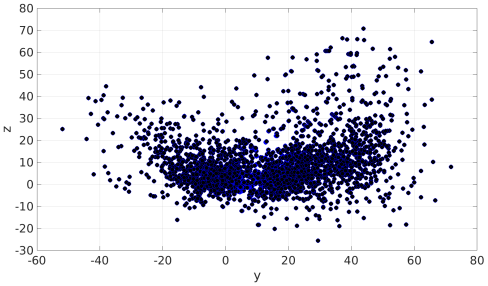

(d) $\Delta T = 3.4$(Ra=14790000)

Figure 9.12: Poincaré sections of the attractor in the embedded space at x constant in the middle of the attractor.

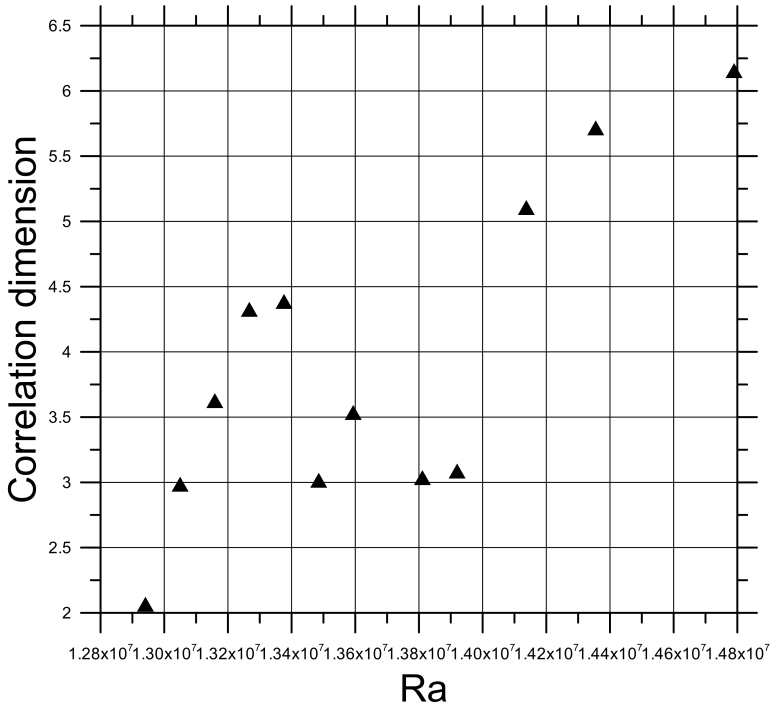

Figure 9.13: Correlation dimension at $h = 2\frac{W}{m^2K}$ and $T_{cold} = 60°C$

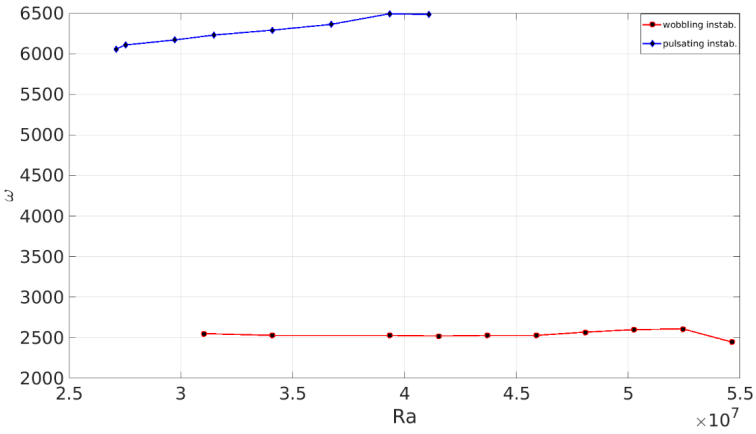

Figure 9.14: Main frequency as function of Ra. $T_{cold} = 60°C$ and $Bi = 0.053$.

take the form of multiple solutions, namely patterns which can be displayed by the system depending on the different initial conditions.

Remarkably, the scenario of the path towards chaos is different concerning that shown in Figure 9.13: the system, after being subjected to a first Hopf bifurcation from the initial steady state (at $\Delta T = 6.1°C$ in case of the pulsating mechanism and at $7.1°C$ for the wobbling mechanism), undergoes a quasi-periodic state (through a second Hopf bifurcation) when the temperature difference is further increased. This fact transforms the attractor into T^2 torus. Suddenly after this second bifurcation has occurred, the T^2 torus becomes unstable, leading the trajectories to wander in the phase space in a highly chaotic manner. This fact occurs without the intermediate stage of the T^3 torus.

As a common practice made in the present work, we try to make valuable connections of these new and surprising findings for $Bi = 0.526$ with similar outcomes present in the literature of the past years, expressly aimed to give a more general and theoretical perspective. In the case of low-Pr fluids (liquid metals and semiconductor melts), a recurrent scenario is the period-doubling (Feigenbaum) (see Gollub and Benson [19], Libchaber et al. [211]). On the other hand, if the Prandtl number increases, the landscape is different due to the competition of more than one mechanism, taking part in the transition from a starting steady pattern to an oscillatory one (e.g. the Busse balloon discussed in Chapter 4). In case of cavities nearly square-shaped, like that considered in the present simulations, two different possible scenarios have been reported by Bucchignani and Stella [212]: the Feigenbaum one and the Ruelle-Takens-Newhouse route to chaos. particularly, the second is often encountered in the Rayleigh-Béard problems when the fluids have a large Pr number as found by Curry et al., [213] and

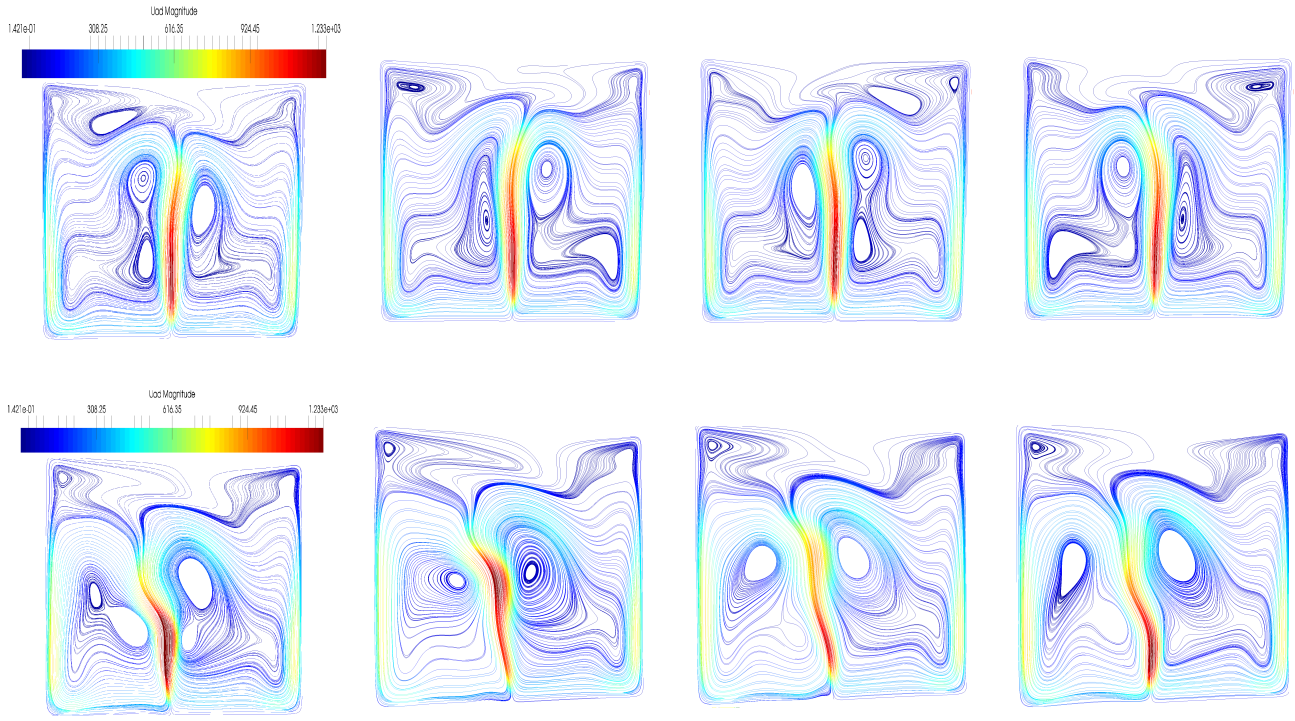

Figure 9.15: First row: the wobbling symmetric instability. Second row: non-symmetric pulsating mechanism. $Bi = 0.526$, $T_{cold} = 60°C$, $Ra = 3.93 * 10^7$.

Gollub and Benson, [19] .

Similarly to other thermal convective problems, where the systems are uniformly heated from below (e.g. as described by Lappa and Ferialdi, [214]), Rayleigh-Bénard convection, could also be characterised by a phenomenon called attractor crisis (Paul et al. [215]). Grebogi et al. [78] explained these phenomena. arguing that the could arise when a collision happens among an unstable periodic orbit and a coexisting strange attractor. Strictly linked with the crises are phenomena, occurring suddenly such as the destruction, creation or a growing/shrinking of a strange attractor. Three different kinds of crises exist the "boundary" (or "exterior") crisis, "interior" crisis and "attractor merging" (see Chapter 6 for more details). The outcomes related to $Bi = 0.526$ and $T_{cold} = 60°C$ can be interpreted as reported in the following (the patterns related to the values of those parameters are reported in Figure 9.15).

To resume at such value of the parameters (namely $Bi = 0.526$ and $T_{cold} = 60°C$), three stable attractors occupy the phase space, one related to the symmetric wobbling mechanism and the other two linked to the non-symmetric pulsating one (physically seen as a distorted plume bent right or left, being these two configurations reflections of each other respect to the vertical centreline). Aligned with similar outcomes about

different kind of problems (see, e.g. Kitano et al., [216], or Lappa and Ferialdi, [214]), it is possible to state that the interaction between these attractors is the cause of the crisis, which manifests itself with the sudden destruction of the T^2 torus, leading to high-dimensional chaos.

To get back to our case of study ($Bi = 0.526$, $T_{cold} = 60°C$) the two oscillatory instabilities are depicted in Figure 9.15: the first line shows the wobbling instability, and in the second the non-symmetric pulsating instability is reported. It is worth saying at this point that three stable attractors enrich the phase space. One related to the symmetric wobbling instability and two belonging to the non-symmetric pulsating one, plus the unstable fixed point related to the symmetric steady state, which loses its stability at $\Delta T \approx 6°C$ (see Figures 9.7 and 9.14: Figure 9.7 is related to $Bi = 0.0526$, but the pattern is the same at low Rayleigh number). The interplay among these four attractors could lead to very complex dynamics, which is hard to categorise entirely under a mechanism described above. The fact that high dimensional chaos (in terms of correlation dimension) appears suddenly from a T^2 torus suggests that a crisis phenomenon occurs. In order to try to explain, we may try to follow the line of enquiry of Kitano et al. [216], although here the situation is made more complex due to the presence of the wobbling mechanism. Even if the problem pertains to a different topic (optic polarisation), we have all the ingredients we need: two non-symmetric (equivalent) solutions asymmetric one both steady and oscillatory (after a certain threshold). Indeed following the non- symmetric pulsating branch at $\Delta T \approx 9.5°C$ the "symmetry recovery crisis" is triggered, when the interaction among the two non-symmetric pulsating branches occurs. Indeed the flow now oscillates chaotically but with the rising plume wobbling and pulsating around the centre of the cavity (it jumps continuously from a non-symmetric solution to the other) as depicted in Figure 9.16. Following the wobbling branch (red line in Figure 9.14) a boundary crisis may occur: at $\Delta T \approx 12.5°C$ the branch, previously undergone to a T^2 bifurcation, loses definitely its stability and the pattern of Figure 9.16 is recovered.

In order to further investigate the oscillatory RB convection, it is worth discussing other results appearing in the literature (in case of adiabatic or conducting side-walls). In particular, complex flows and textural transitions involving chaotic and non-chaotic states along with multistability (see also Lappa, [184]) were reported by Goldhirsch et al. [217]. They reported chaotic (aperiodic) patterns similar to those described

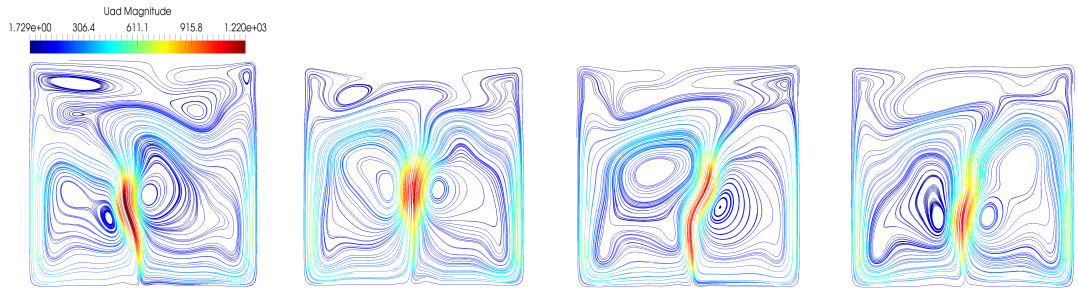

(a) (b) (c) (d)

Figure 9.16: Chaotic pattern made as interaction of the two non-symmetric solutions. $Bi = 0.526$, $T_{cold} = 60°C$, $Ra = 4.15 * 10^7$.

above. Differently from the present findings, however, separation and merging of the rolls were not an important feature of the dynamics. Those authors reported in some cases a migration and a growth of the corner rolls towards the inner enclosure part. Consequently, the largest ones formerly occupying the centre of the cavity shrinks and retreats into corners.

The "symmetry" of emerging patterns is probably one of the most remarkable differences in the present outcomes. Indeed as depicted in Figs. 9.7, 9.8, 9.15 and 9.16, the heat exchange, through the side-walls of the container is responsible to drive flow to take the (sa) mode, disregarding the values of the Rayleigh number considered (sa mode involves the a central plume). Moreover, no growing or shrinking rolls similar to those reported in the work of Goldhirsch et al. [217] or Lappa [184] have been observed here.

In order to have a better understanding about how the impact of the heat dissipated through the walls could affect the emerging pattern it is worth investigating other values of the T_{cold} and T_{hot}. In particular, in the following we consider $T_{cold} = 40°C$, $Bi = 0.0526$ ($h = 2\frac{W}{m^2K}$). At those values of the parameters, the pattern is steady and characterised by a bi-cellular and symmetric structure, where a central rising plume is present. This configuration is held up to a value $\Delta T = 2.9°C$ ($Ra = 7.01 * 10^6$). When this threshold is overtaken, the central plume (Figure 9.17 first row) undergoes a time-dependent wobbling behaviour. Moreover, on further growths of the temperature difference, the flow takes a non-symmetric structure with the plume mentioned above shifting towards the right or to the left (as shown Figure 9.17 second row); this fact is responsible of two different non-symmetric solutions, one the mirror of the other.

For $Bi = 0.263$ ($h = 10$)), the flow becomes time-periodic between $\Delta T = 6.4$ and $6.5°C (Ra = 1.56 * 10^7$ and $1.58 * 10^7$) characterised by a pulsating mechanism of the cen-

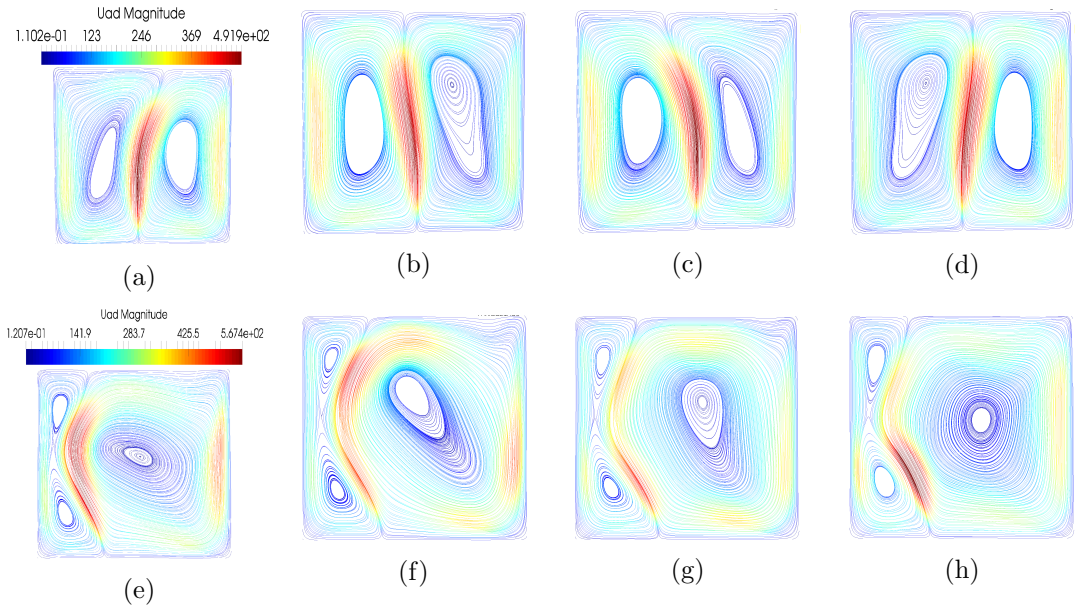

Figure 9.17: Four snapshots evenly distributed along the period. First row: $\Delta T = 3°C$ ($Ra = 7.06 * 10^6$,$R_{aeff} = 5.874 * 10^5$) and $h = 2(Bi = 0.0523)$, wobbling instability. Second row: Four snapshots evenly distributed along the period. $\Delta T = 4.5°C$ ($Ra = 1.06 * 10^7$, $Ra_{eff} = 9.754 * 10^5$) and $h = 2(Bi = 0.0523)$.

tral rising plume, which shares many similarities with the case at $T_{cold} = 60°C$. If ΔT is further increased, the flow undergoes a quasi-periodic state, when $\Delta T \approx 6.8°C (Ra = 1.65 * 10^7)$ is reached. Now a wobbling behaviour is added to to the previous one, bringing the system to an hybrid time-dependent state. Differently from the configuration, where $T_{cold} = 60°C$ and $Bi = 0.053$ ($h = 2\frac{W}{m^2K}$), here the transition to chaos occurs suddenly, without any region of transition such as that depicted in Figure 9.13. Indeed in this case the high dimensional chaos occurs just after the T^3 bifurcation of Figure 9.18, making the estimation of the correlation dimension impossible.

Experimental results

The experimental results for $T_{cold} = 20°C$ and $T_{cold} = 60°C$ with $T_{amb} \approx 22°C$ are shown in Figures 9.19 and 9.20, respectively. For the cases considered, measurements at fixed positions of the velocity (as a function of time) and some vector plots (obtained with the PIV) are shown. These results are particularly instructive as they show that an increase in the average temperature of the system leads to a significant simplification in the frequency spectrum and the flow patterning behaviour. Moreover, in comparison with the rich landscape emerging from the 2D numerical simulations, provides evidence that the 3D flow is much more stable. As reported in the previous

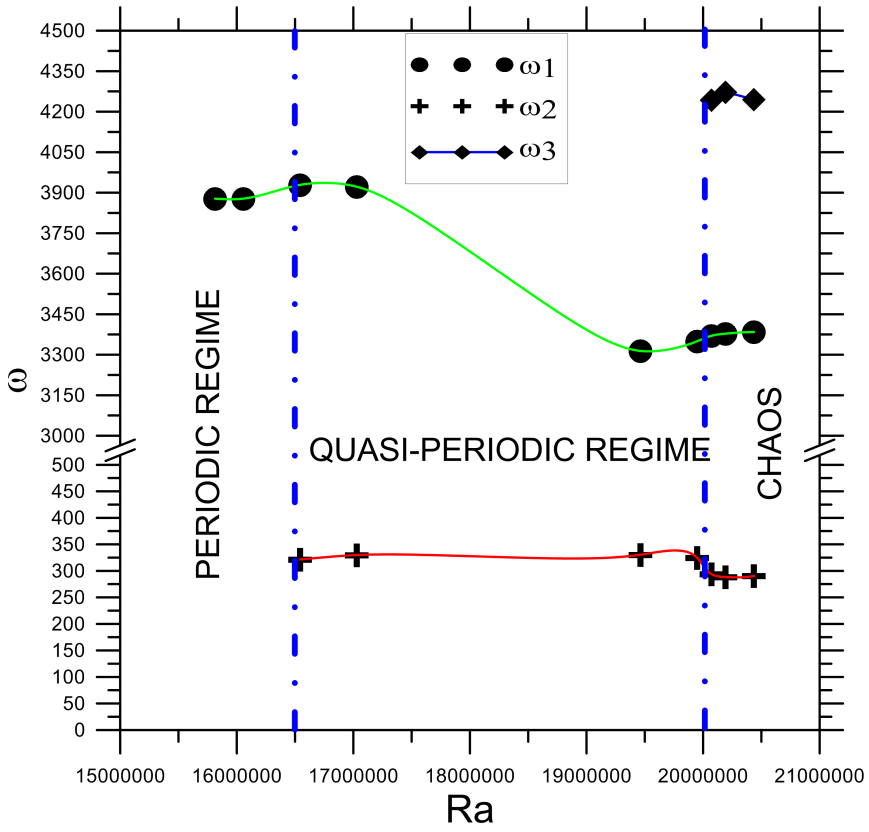

Figure 9.18: Non-dimensional frequencies as function of Rayleigh number: $T_{cold} = 40°C$, $h = 10$, $Bi = 0.265$

subsection related to the two-dimensional numerical simulations, for the same values of the control parameters, the equivalent 2D patterns would undergo a chaotic behaviour due to the transition to chaos originating from a T^3 torus (Ruelle-Takens route) or the sudden occurrence of crisis phenomena. Once again we ascribe this more stable pattern to the heat exchanged through the sides in the third direction (perpendicular to the z-axis), which are with the other two pairs of side-walls a source of heat dissipation.

Interestingly, as shown by a comparison of Figs 9.19 and 9.20, there are two different consequences, when the average temperature of the liquid inside the cavity increases and, at the same time, the imposed temperature gradient is kept fixed First, a transition occurs from the spectrum shown in Figure 9.19, characterised by a many frequencies to the time-periodic behaviour shown by the probes represented in Figure 9.20. Secondly, the enhanced heat loss through the walls is also responsible for relevant modifications of the flow pattern. In Figure 9.19, a single convective cell ((aa) symmetry), occupying most of the internal portion of the cavity, represents the main circulation of the system. It can be associated with the so-called "large-scale circulation" (LSC) which is a feature

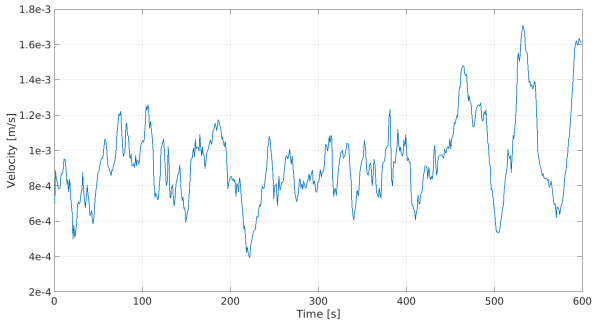

(a) Probe at $x = 0.02$ and y=0.01

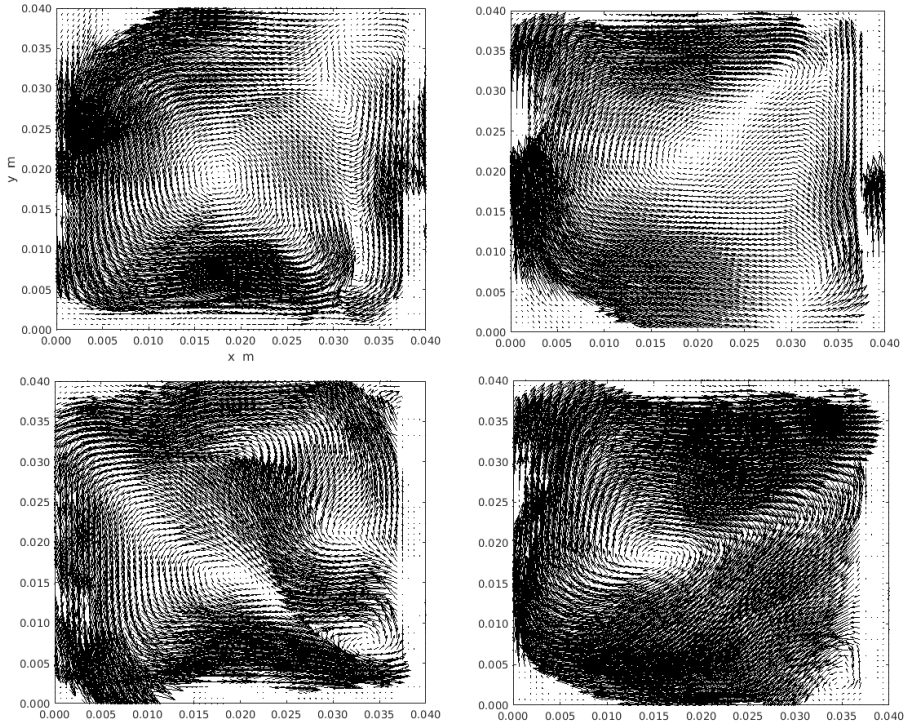

(b) 4 snapshot of the velocity vector plot.

Figure 9.19: $T_{cold} = 20°C$, $\Delta T = 20°C$.

of the turbulent RB convection (see Lappa,[184]). The thermal boundary layers on the hot and cold walls are subjected to eruptive behaviour, which is responsible for the production of smaller vortices. Consequently, these latter small scale structures undergo a merging, forming the LSC. Moreover, these boundary layers are characterised by waves travelling in parallel to the hot and cold boundaries. These disturbances generate localised distortions of the thickness of the layers, which becomes thermal plumes by growing in time. The cap of these thermal plumes carries some vorticity (manifested as a toroidal vortex) towards the internal part of the cavity, after detaching from the boundary layers. Once more of such structures reach the centre of the en-

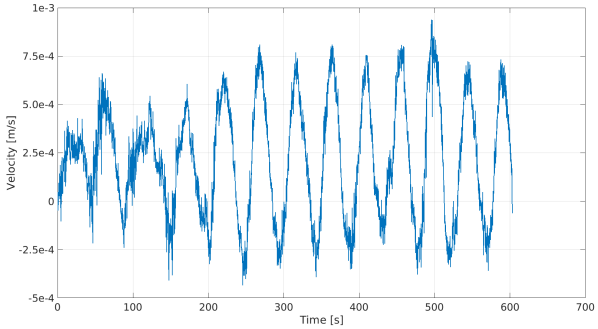

(a) Probe at the point indicated with the red square in the figure below.

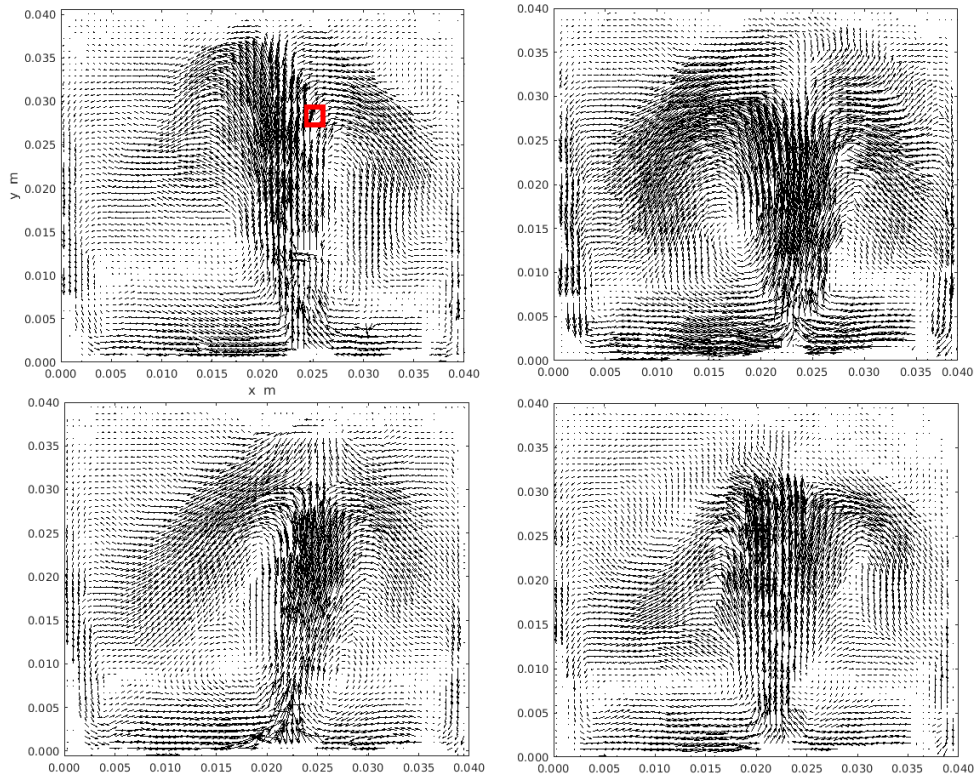

(b) 4 snapshot of the velocity vector plot.

Figure 9.20: $T_{cold} = 20°C$, $\Delta T = 20°C$.

closure, they merge, giving rise of an almost two-dimensional pattern shown in Figure 9.19. Moreover, the LSC is characterised by waves located in the boundary layer and propagating with the same direction of the fluid transported by the large circulation. However, as reported in Figure 9.20, this dynamics can be strongly changed by the increased heat loss happening through the side walls. Similarly to the two-dimensional cases, the colder fluid sinking near the lateral walls leads the pattern to assume a (sa) mode, characterised by a single central rising plume. According to the mechanism just

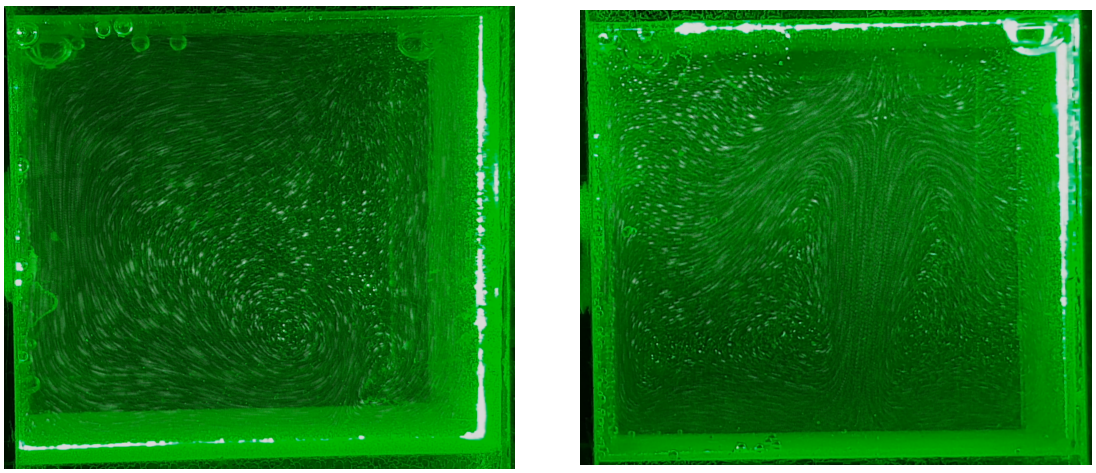

(a) $T_{cold} = 20°C$ (b) $T_{cold} = 60°C$

Figure 9.21: Stremlines taken from the experiments.

outlined, the boundary layers are no longer subjected to the presence of waves and the consequent creation of small-scale vortices. The two mechanisms described above are also evident in Figure 9.21a and 9.21b, where we have reported the experimentally determined streamlines for the case $T_{cold} = 20$ °C and $T_{cold} = 60$ °C, respectively.

Three-dimensional numerical simulations

In this section, we finally present the outcomes of the three-dimensional numerical simulations, which are of primary importance in unveiling other characteristic features of the configurations considered above.

The parameters taken into account have the following values $T_{cold} = 60°C$ and $Bi =$ 0.26315, 0.5263, 0.78945 and 1.3158. Primarily the latter corresponds to values of convective coefficient of $h = 10$, 20, 30, 50 $\frac{W}{m^2K}$, respectively. As already shown by the experiments, when the heat loss through the walls grows, the flow undergoes a stabilisation, evolving from a turbulent pattern for the lowest value of Biot number taken into account (0.26315) to a regular time-periodic flow at $Bi = 1.315$ (Figure 9.22).

At this stage it is worth highlighting that the values taken by "nominal" Rayleigh number and the "effective" are very different in the 3D simulations. Indeed all the four cases considered have been run at a fixed Ra of $8.74 * 10^7$ (which corresponds to a $\Delta T = 20°C$) but the change of Ra_{eff} here is very important: starting from a positive value at $Bi = 0.263$ but ending to a negative one at $Bi = 1.316$. In Table 9.11 the effective Rayleigh numbers are reported as function of Bi.

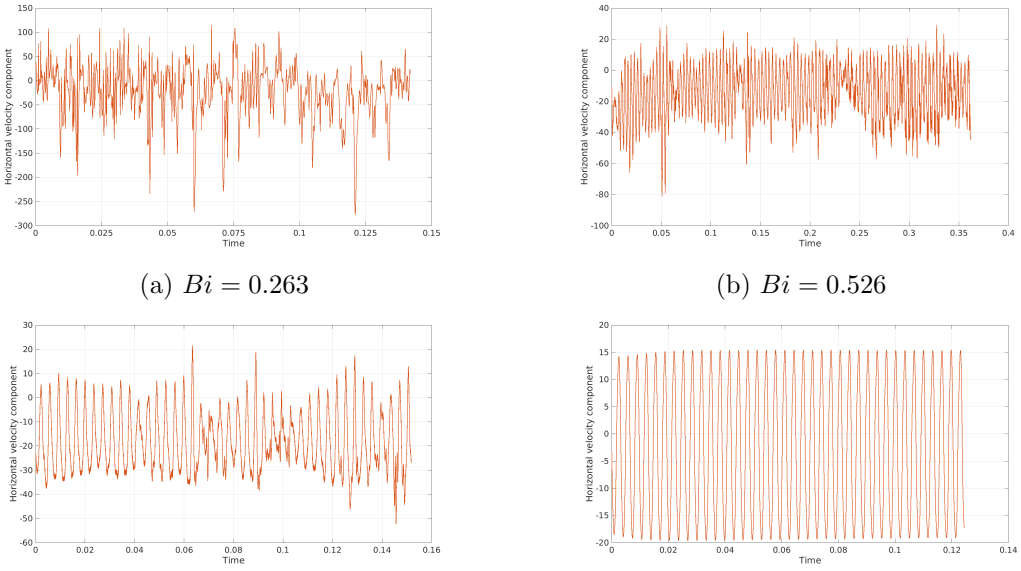

(a) $Bi = 0.263$ (b) $Bi = 0.526$

(c) $Bi = 0.789$ (d) $Bi = 1.32$

Figure 9.22: Horizontal velocity component at $\frac{x}{L} = \frac{1}{2}$, $\frac{y}{L} = \frac{1}{2}$, $\frac{z}{L} = \frac{1}{2} + \frac{1}{8}$ and $T_{cold} = 60°C$.

Along these lines, also a comparison with actual results for the adiabatic and con-

Bi	Ra_{eff}
0.263	$1.855 * 10^6$
0.526	$-2.02 * 10^6$
0.789	$-4.682 * 10^6$
1.315	$-7.794 * 10^6$

Table 9.11: Effective Rayleigh number as function of Bi.

ducting walls is instrumental in clarifying the role of solid walls and heat transfer in these dynamics. Mizushima and Nakamura [218] and Puigjaner et al. [219], indeed, studied a cubic cavity with adiabatic vertical walls, interestingly they found that the critical Rayleigh number ($Ra_{cr} = 3389$) is larger respect that assessed under the two-dimensional constraint ($Ra_{cr} \approx 2585$).According to them, the solid walls along the third dimension, which are a source of additional friction, are responsible for this behaviour. If a three-dimensional cubic cavity with vertical conducting boundaries is considered, according to Mizushima and Matsuda [220] the value of the critical Rayleigh number is even larger ($Ra_{cr} = 6796$). These authors explained this fact as an enhanced dissipation of the temperature perturbations brought by the conducting walls.

Here we recall the consideration made about the pattern symmetries in case of the 2D

outcomes and put them in a more general context. Indeed if the fully three-dimensional problem is taken under consideration, the complexity is increased due to a vast number of symmetries is made possible. Moreover, the flow could undergo different patterns (multiple solutions), depending on the initial conditions.

The impact of the adiabatic or conducting boundary conditions on the raise of multiple solutions and the bifurcation hierarchy, characterising these systems is described in the related literature. Along these lines several supercritical steady states (manifesting as distinct branches) were found by Pallarès et al. [221] for different values of the Prandtl number (namely $Pr = 0.71$, 10, 130 and $Pr = 0.01$). These states could take the form of straight rolls having the axis parallel to one of the vertical sides or being oriented along one of the diagonals or having a shape of a toroidal vortex. When the flow in the cubical cavity with adiabatic boundary conditions assumes an oscillatory behaviour ($Ra > 10^4$ for $Pr = 0.01$ and $Ra > 1.2 * 10^5$ for $Pr = 0.71$) a single convective cell is aligned with the direction of one of the sides (along x or along y). Similar outcomes for $Pr = 130$ and Rayleigh number up to 1.5×10^5 were yielded by Puigjaner et al. [222]. They discovered that six possible patterns exist.

Moreover, according to them a coexistence of two, three, or even four of these states could also occur in certain intervals of Ra (this can be regarded as a manifestation of multiple solutions).

The present results, shown in Figure 9.23, indicate once again that the heat transfer occurring through the sides can deeply influence the selection of the convective modes made by the system. As evident in Figure 9.23, similarly to the two-dimensional configuration, only the symmetry, characterised by the single rising plume departing from the bottom (toroidal vortex), survives..

A comparison among the case with $Bi = 1.3$ and a cavity with adiabatic walls ($Bi = 0$) is made in Figure 9.24. The temperature field is one of the main detectors of the great differences between these two cases. Indeed, as in the first ($Bi = 1.3$), the structure of the plumes is much more regular, the latter ($Bi = 0$) undergoes a more complex spatio-temporal behaviour.

The comparison between the computations for $Bi = 1.3$ ($T_{cold} = 60°C$) and the experiments for the same value of T_{cold} is shown for completeness in Figure 9.25, where the streamlines are reported on an x-y plane: both the 3D simulations and the experiments show a central thermal plume rising at the centre of the cavity.

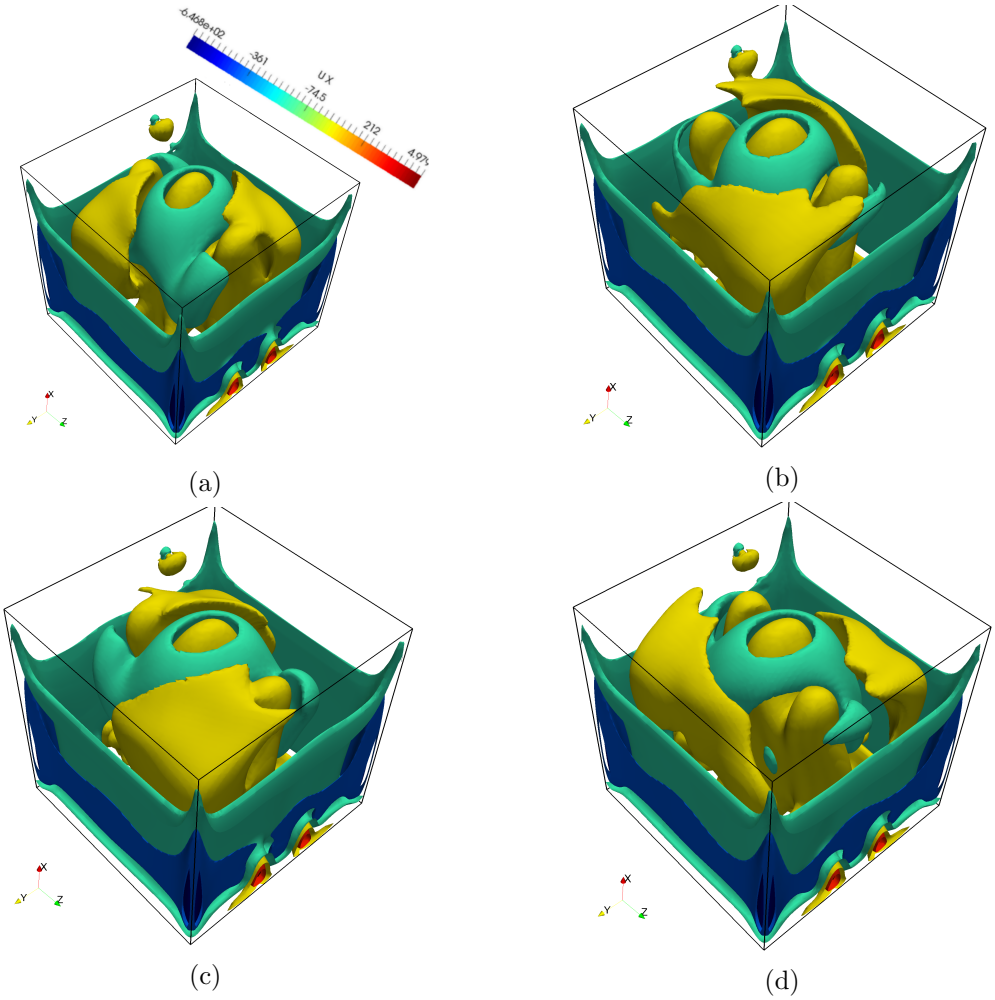

Figure 9.23: Four snapshots of axial velocity evenly distributed along the period at $Ra = 8.74 * 10^7$, $Bi = 1.3158$ and $T_{cold} = 60°C$.

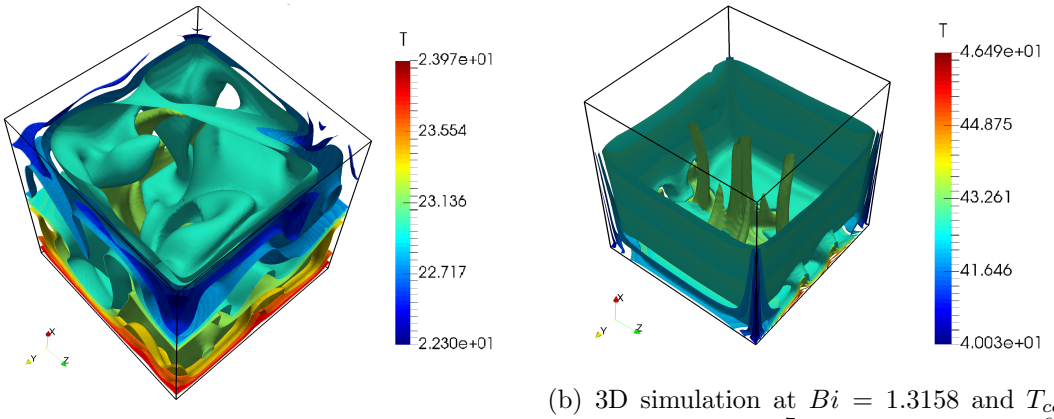

(a) Cavity with adiabatic walls at $Ra = 1779828$ $60°C$ $Ra = 8.74 * 10^7$,$Ra_{eff} = -7.794 * 10^6$

(b) 3D simulation at $Bi = 1.3158$ and $T_{cold} =$

Figure 9.24: Temperature iso-surfaces.

In Table 9.12 the non-dimensional main frequencies (in which the main peak of the spectrum) and dimensional main periods are reported together with that related to the

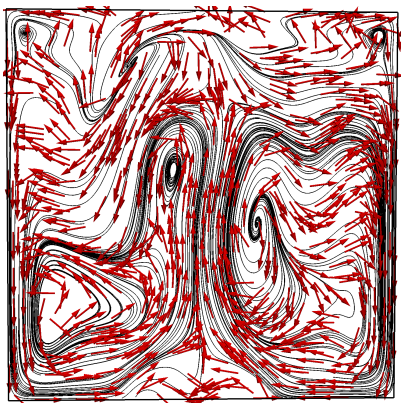

(a) 3D simulation at $Bi = 1.3158$ and $T_{cold} = 60°C$

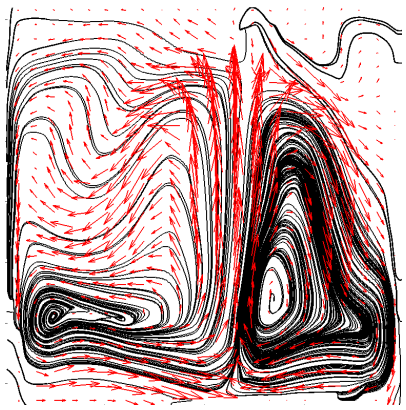

(b) Experiment at $T_{cold} = 60°C$

Figure 9.25: Streamlines in a x-y plane at $\frac{x}{L} = \frac{1}{2}$, $\frac{y}{L} = \frac{1}{2}$, $\frac{z}{L} = \frac{1}{2} + \frac{1}{8}$

experiment at $T_{cold} = 60°C$. With those values it is possible to make a comparison: the value of the experiment is lower in terms of non-dimensional frequency, however, decreasing the Biot number helps to achieve a closer frequency to that of the experiments. On the other hand, decreasing Bi too much leads to an irregular flow (at $Bi = 0.263$).

Bi	Non-dimensional freq.	Dimensional period [s]
Experimental	1488	42.7
0.526	1701	37.4
0.789	1763	36.0
1.316	1926	33

Table 9.12: Non-dimensional frequency as function of the Biot number.

9.5.2 Hadley flow and inclined configuration

In order to present the results about the Hadley flow and inclined configurations we follow the same path undertaken about the Rayleigh-Bénard convection: first, we present the 2D simulations, followed by the experimental results, and then we conclude with the 3D numerical outcomes. First, we examine the cases where the prevailing temperature gradient is essentially horizontal, for which the interpretation of the dynamics is relatively straightforward. Then we move to the much more complex situation in which the direction of this gradient becomes inclined concerning the horizontal direction. While for the former situation, the flow is relatively stable in the considered range of parameters, the emerging patterns being limited to stationary or single-frequency states, in

the latter progression towards fully developed chaos is possible.

Two-dimensional numerical simulations

As proceeded for the Rayleigh-Bénard problem in the previous section, we first present the outcomes obtained considering the 2D cases, as a comparison between these results and the experimental ones is expected to be instrumental in clarifying the role of 3D effects. The reader will also realize how complex the problem can be even neglecting the role of the third dimension. The temperature difference is fixed to $20°C$, while three values of T_{cold} are taken in consideration in order to explore the impact of the increasing average temperature respect to the ambient. Moreover three different values of the Biot number , namely 0.0526, 0.2632, 0.5263 have been considered (corresponding to values of convective coefficient h of 2, 10, 20 $\frac{W}{m^2K}$).
According to the considerations given above the total number of the simulations is 18 (three values of the T_{cold} multiplied by the three Biot numbers mentioned above).
Results are shown using maps as the reader can see in Figure 9.27 for the case of the horizontal temperature gradient. Such maps have the following structure: each row represents a value of the T_{cold} while the Biot number is kept fixed along the columns. Moreover, different labels describe steady (S) or oscillatory (O) states, the latter coming with the associated non-dimensional frequency. The oscillatory pattern is shown in Figure 9.26 (in case of Hadley flow), where it is evident the time-dependent behaviour of the roll positioned near the top right corner. Indeed it moves downwards, losing its strength (frames 1, 2, 3) until a new roll on the top right nucleates.

By taking a look at these figures, it is possible to notice how on increasing the Rayleigh

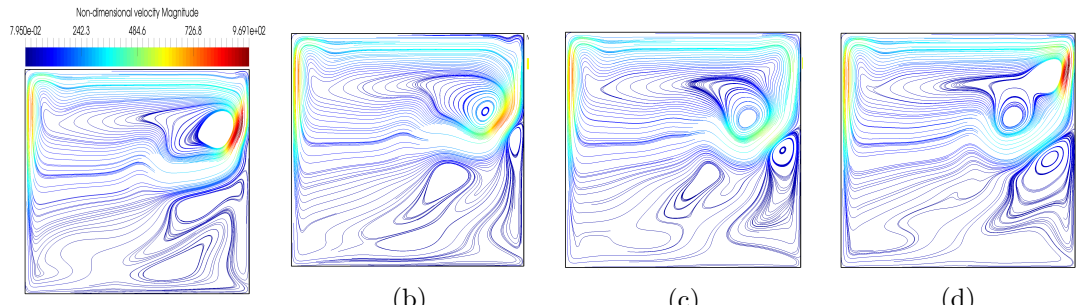

(a) (b) (c) (d)

Figure 9.26: Four snapshots evenly distributed along the period.Hadley flow with $T_{cold} = 60°C$ and $Bi = 0.5263$. $Ra_{eff} = 5.51 * 10^6$,$Ra_{nom} = 8.7 * 10^7$.

number the flow evolves from a diffusive regime to a boundary-layer regime in which

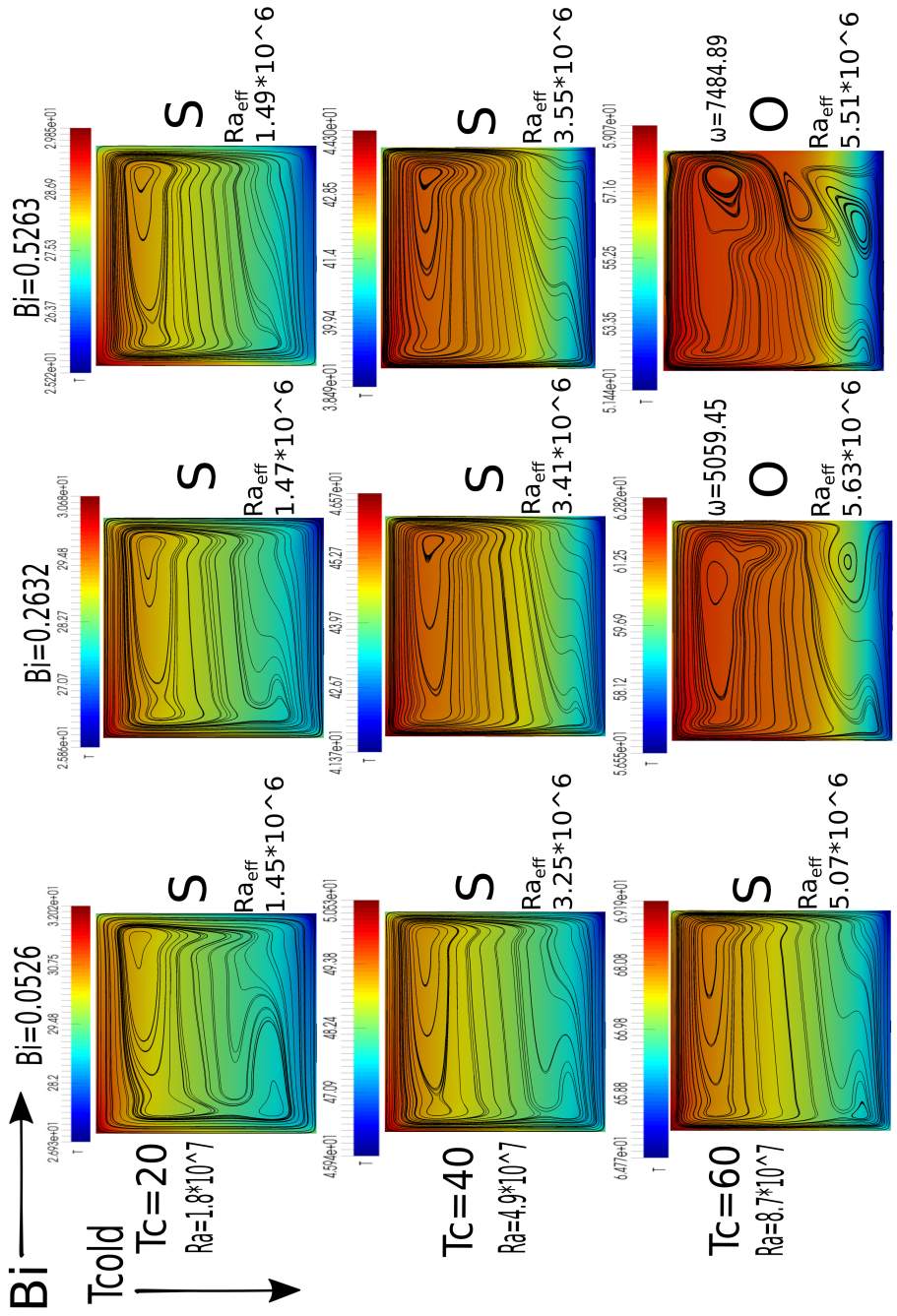

Figure 9.27: Map of possible spatio-temporal states as a function of T_{cold} and Bi (temperature gradient perpendicular to gravity). T_{hot} on the left side of the cavity while T_{cold} on the right of the cavity.

almost all the temperature drop and the vorticity production are localised in thin layers adjacent to the end lateral walls. This mechanism leads to the formation of a stagnant region in the central part of the enclosure with the flow therein produced essentially as a result of the entrainment of mass from the vertical boundary layers being confined in thin intruding streams near the horizontal walls.

When the boundary-layer regime is attained in the Hadley flows, the central region is stabilised by the emergence of cross-stream thermal stratification (characterised by a small temperature gradient).

At this stage, we expressly consider the existing literature relating to buoyancy flow in cavities with adiabatic or conducting boundary conditions as such meaningful cross-comparison might help to interpret the observed behaviours and the impact of heat exchange on the emerging dynamics properly. As such, rather than a systematic and comprehensive review, what follows provides a critical review of potentially key aspects responsible for the behaviours observed here.

In this regard, it is worth starting from the simple observation that many numerical studies have been devoted to the investigation of the capacity of buoyancy convection to give rise to permanent time-periodic states in enclosures subjected to a horizontal temperature gradient. According to the related literature, also the 2D configurations are characterised by a strong multi-scale nature even with canonical boundary conditions. Relevant information about this topic is due to Le Quéré and Penot [223], Henkes and Hoogendoorn [224], Bucchignani [225]. The turbulence could also rise in certain conditions (see e.g. Paolucci and Chenoweth [226]; Paolucci, [136]; Janssen and Henkes [227]; Xin and Le Quéré [228]; Farhangnia et al., [137]; Yahata [229]; Le Quéré and Behnia [230]; Mayne et al. [231]; Tian and Karayiannis [232]).

As the reader might have already realised based on the introductory arguments provided in Chapter 4, these mechanisms are different from the classical disturbances occurring in the Hadley flow at low Prandtl numbers ($Pr < O(1)$) as the related perturbations (hydrodynamic in nature) are not possible for $Pr > 1$.At the Prandtl numbers considered in the present study indeed, the only possible kind of perturbations are the disturbances growing in the boundary layers located in proximity to the side-walls or similar effects.

Along these lines, the work of Ravi et al. [233] for a square cavity filled with air is instrumental in order to explain the results presented in Figure 9.27. They, indeed, found a recirculating fluid pocket near to the corners downstream of the vertical walls, with a consequent separation and reattachment of the flow along the horizontal boundaries close to this recirculation pocket (together with a noticeable growth of the thickness of the horizontal layer). According to these authors, the origin of this corner has a thermal nature: the temperature undershoots in lateral boundary layer (originated by

the stable thermal stratification of the central portion of the cavity), allows the colder fluid to reach the corner located in the upper part and hence making the cold plume to detach from the ceiling,. A similar effect can be observed in Figure 9.27.

Paolucci and Chenoweth [226] were the first to show that time-periodic pattern rising in such conditions is caused by a perturbing mechanism occurring in the proximity of the departing corners located in the region where the flow is detached from the horizontal boundaries (happening for $Ra = O(10^8)$ in a square container for $Pr = 0.71$). Le Quéré and Behnia [230] highlighted that this mode is responsible for a departure of the usual centro-symmetry. They also elaborated original explanations about the related instabilities, which, according to them are due to the propagation of internal gravity waves excited by the peculiar structure of the detached flow region.

Leaving aside for a while the different interpretations relating to the relationship between the detached flow and the bifurcation to oscillatory flow, at this stage, we should recall that in our case the horizontal boundaries delimiting the fluid do not behave as adiabatic boundaries. Therefore, the above explanations should only be used to support the discussions from a qualitative point of view (providing only a partial perspective on the mechanisms leading to oscillatory flow). Again, critical comparison with the existing literature may be used to get some insights into the potential effect played by the heat exchange taking place on the horizontal walls.

As explained to a certain extent in the introduction, if conducting walls are considered, the zones of unstable stratification formed near these walls can locally produce convection of the RB type. This fact is the reason why the hierarchy of bifurcations relating to cavities with conducting boundaries exhibits notable differences concerning those with adiabatic walls. As an example, at $Pr = 0.71$ convection becomes time-periodic in a square enclosure at $Ra = O(10^8)$ and $Ra = O(10^6)$ for adiabatic and perfectly conducting walls, respectively (see Jones and Briggs [234]).

Some additional interesting numerical results for such a case ($A = 1$ with conducting horizontal walls) can be found in the study of Winters [235] and Gelfgat and Tanasawa [236], for $Pr = 0.71$ and $Pr = 0.015$, $Pr = 0.71$ and $Pr = 7$, respectively. Several possible modes were reported as waves travelling along the cavity walls breaking or preserving the symmetry of the basic flow (as an example, for $Pr = 7$ three possible modes were observed, the first and the third anti-centrosymmetric and the second centrosymmetric, i.e. possessing the same symmetry of the base solution, i.e.

$V(1-x,1-y) = -V(x,y)$ and $T(1-x,1-y) = -T(x,y)$). Xin and Le Quéré [237] re-examined the problem for $Pr = 0.1$, 1, 3, and 20. They observed that as the critical Rayleigh number grows with the Prandtl number, the boundary layers become thinner, and the wave structures in the critical mode shrink. Moreover, the symmetry of the unstable mode changes as a function of the thickness of the boundary layers. Most interestingly, yet for the case of conducting boundaries and $A = 1$, these authors also assessed the spatial nature of the most dangerous disturbances, which were found to be three-dimensional for $Pr = 1$ and almost 2D for $Pr = 3$, 7, and 20.

Coming back to the present results (Figures 9.27 and 9.26), we ascribe the time-dependent convective patterns located in the bottom side of the container to a mechanism of the Rayleigh-Bénard (the so-called Rayleigh modes), whereas those taking place in the upper portion of the cavity can be explained relying on the detachment flow widely described above.

The Rayleigh modes have an even bigger impact if the container is inclined (Figures 9.28 and 9.29). Figure 9.29 shows the pattern in the $\theta = 40°$ inclined cavity, the most remarkable feature, in this case, being the inclined sinking flow, characterised by a time-dependent intensity. The heat dissipated through the upper boundary can have such a big impact in some cases to produce a sinking plume, which splits the system into two main circulations. Moreover, by inspecting Figure 9.29 and comparing it with the map shown in Figure 9.27 the reader will also realise the more chaotic nature of the patterns appearing in the first concerning the steady one of the second.

Numerical studies to be used to interpret the present results for inclined cavities have also appeared in literature, among them Yang et al. [238] [239], Lock and Han ([240] and, in particular, Catton et al. [241], Kuyper et al. [242] and Adachi and Mizushima [243] for the square cavity. Moreover, a inclined square enclosure with adiabatic top and bottom boundaries filled with a $Pr = 7$ fluid has been taken in consideration by Williamson et al. [244], who conducted an analysis involving several numerical simulations, finding that the location of the first instability (produced by increasing the inclination, starting from the Hadley flow) is in the boundary layer. On increasing the tilt, boundary layers become thinner with plumes directed towards the internal of the cavity. Moreover, they demonstrated that the critical angle at which this occurs is a decreasing function of the Rayleigh number. In our case (40 °inclination) the minimum Rayleigh number of the onset of the bifurcation is $Ra \approx 5 * 10^6$.

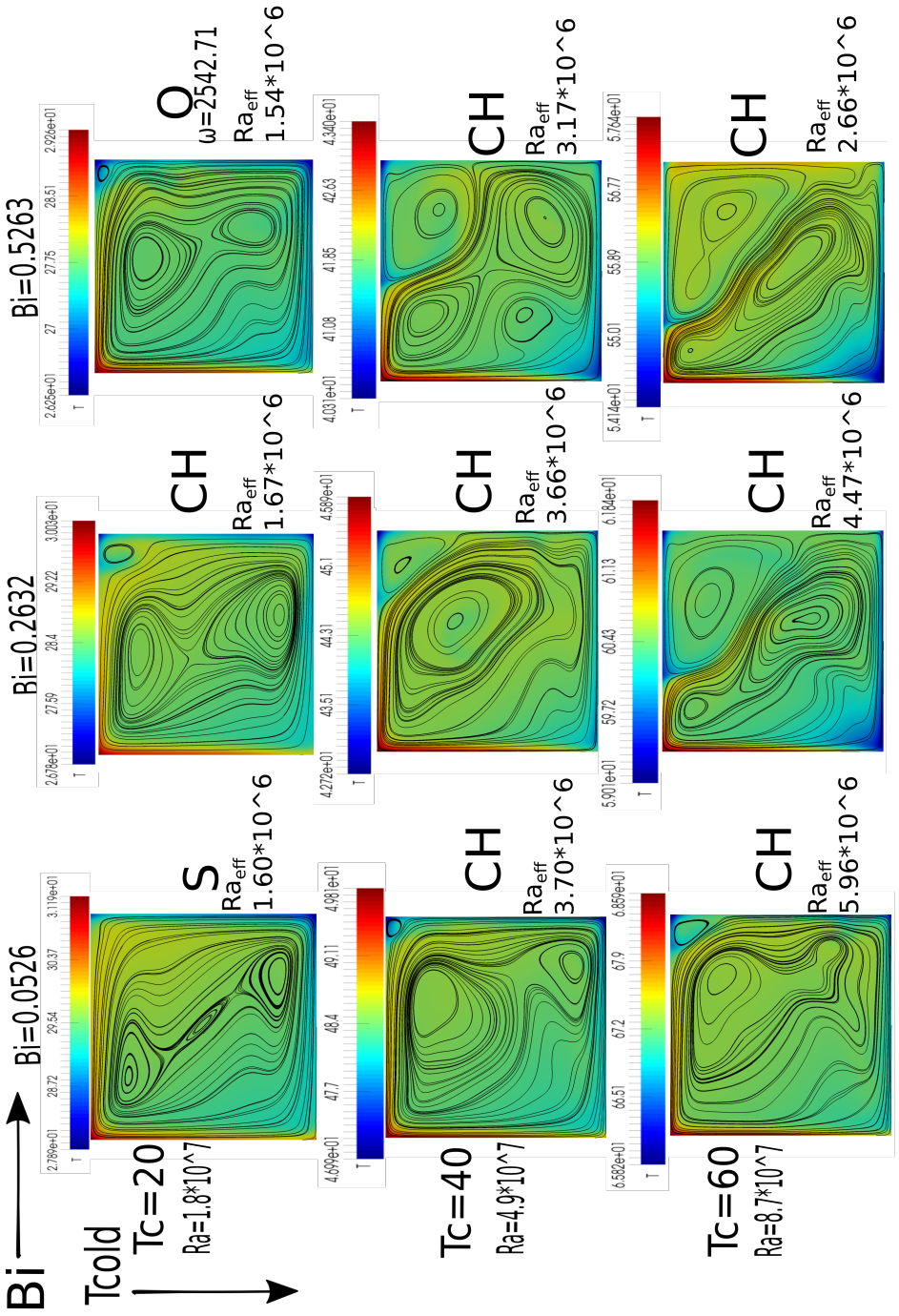

Figure 9.28: Map of possible spatio-temporal states as function of T_{cold} and Bi (temperature gradient inclined with respect to gravity, $\theta = 40°$). Legend: steady (S), oscillatory (OS), chaotic (CH).

Our outcomes, related to weak heat exchange, can be easily explained. In Figure 9.30, indeed, it is clear that the instability characterising the system takes the form of a disturbance travelling in the boundary layer. The situation is much different when the magnitude of the heat exchange increases. Comparing Figure 9.30 with Figure 9.31, it is

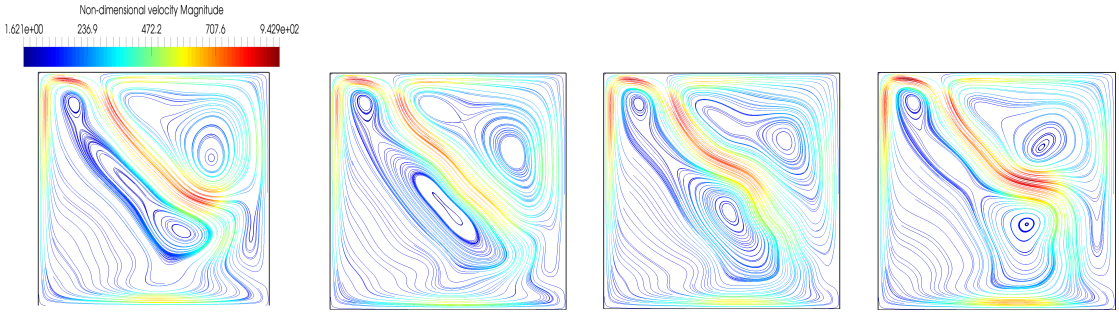

(a) (b) (c) (d)

Figure 9.29: Four snapshots evenly distributed along the main period. Inclined cavity flow with $T_{cold} = 60°C$ and $Bi = 0.5263$, $Ra_{eff} = 2.66 * 10^6$, $Ra_{nom} = 8.7 * 10^7$.

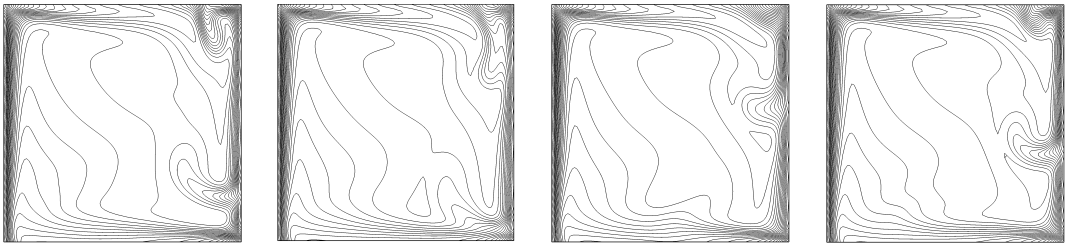

(a) (b) (c) (d)

Figure 9.30: Four snapshots of the temperature iso-lines evenly distributed along the period. $Bi = 0.5263$, $T_{cold} = 20°C$, $Ra_{eff} = 1.54 * 10^6$, $Ra_{nom} = 1.8 * 10^7$, $Ra_{nom} = 8.7 * 10^7$

possible to notice that the second case is characterised by a more extended the unsteady behaviour which also spreads in the central part of the cavity. The intruding oscillating plume located on the top wall could be regarded as a Rayleigh-Bénard type feature. The alternate chaotic and regularly oscillating behaviour at different combination of $T_{cold} - Bi$ (see map in Fig. 9.27) is typical of this latter configuration, which displays a significant multiplicity of solutions. Among other things, such finding is in qualitative agreement with Torres et al. [245]. The problem considered by them involved a cubic enclosure inclined with different angles (from the Rayleigh-Bénard configuration to the Hadley flow one), moreover, in the study, several Prandtl numbers have been investigated. The aim of the work was in the identification of the critical angles at which the multiplicity of solutions, characterising the Rayleigh-Bénard problems, is no longer possible and a transition to the typical single roll pattern occurs (being this latter one a feature of the Hadley flows). Additional insights can be gathered from the work of Wang et al. [246], who showed that the system, undergoing several collisions and singularities of the bifurcation points at given critical inclination angles, is shifted from a configuration, characterised by the multiplicity of solutions (Rayleigh-Bénard), to one in which this phenomenon is no longer a feature of the flow.

Before leaving this section, it is worth highlighting that also in the inclined cavity

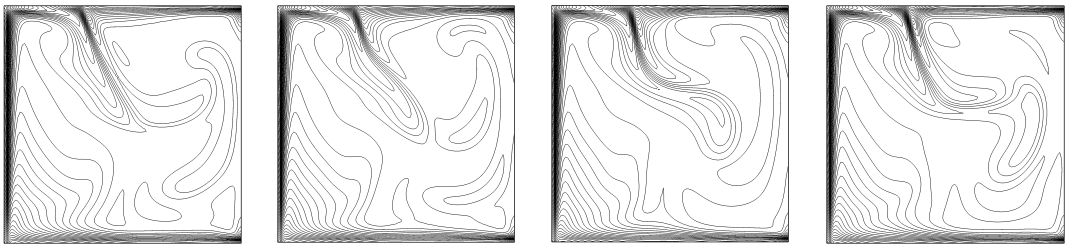

(a) (b) (c) (d)

Figure 9.31: Four snapshots of the temperature iso-lines evenly distributed along the period. $Bi = 0.2632$, $T_{cold} = 60°C$, $Ra_{eff} = 4.47 * 10^6$, $Ra_{nom} = 1.8 * 10^7$, $Ra_{nom} = 8.7 * 10^7$

configuration at specific values of the Biot number the system could undergo the phenomenon of the multiplicity of solutions. Indeed, as happened in case of the Rayleigh-Bénard convection, these occur at the highest values of the Biot number, as witnessed in Figure 9.32. This Figure should be compared with Figure 9.29, where it is possible to note the different location of the descending plume. The multiple solutions become

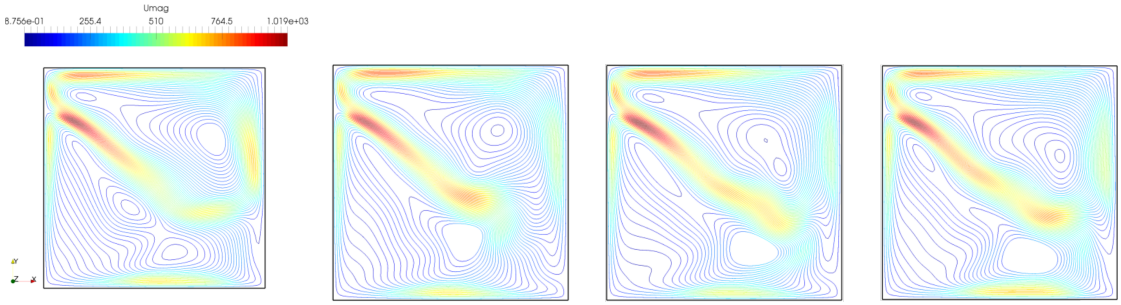

(a) (b) (c) (d)

Figure 9.32: Four snapshots evenly distributed along the main period. Inclined cavity with $T_{cold} = 60°C$ and $Bi = 0.5263$, $Ra_{nom} = 8.7 * 10^7$.

a characterising feature of the flow at the highest values of the Biot number. The two solutions, which differ for the position of the descending plume, are represented at a higher value of the Biot number, namely $Bi = 0.7895$, in Figure 9.33. The two rows indeed highlight the comparison among two different flow patterns, which may take place at the same values of the parameters but starting from different initial conditions. Similarly to the RB convection the most of the cases shown in Figure 9.28 are turbulent, and in order to highlight this aspect the different spectra referred to the simulations of 9.28 are plotted in Figure 9.34. However, it is still possible to notice two main peaks: on around 5000 (non-dimensional frequency), which could be related to

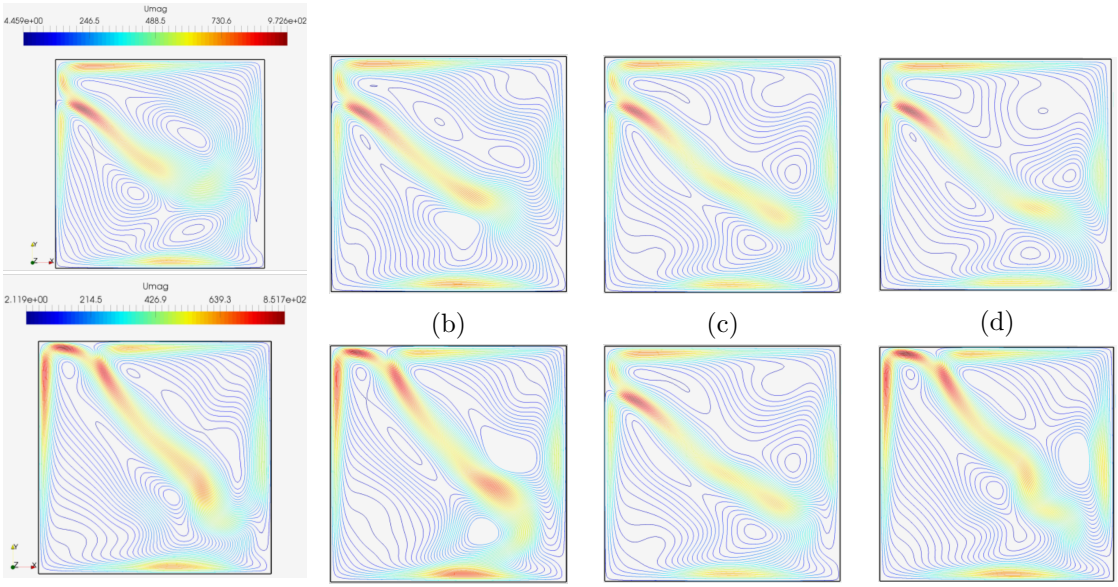

(b) (c) (d)

(e) (f) (g) (h)

Figure 9.33: Four snapshots evenly distributed along the main period. First row Hadley flow with $T_{cold} = 60°C$ and $Bi = 0.7895$, $Ra_{nom} = 8.7 * 10^7$. The first and second row represent the two different flow patterns, which may occur at the same parameters but starting the simulations from different initial conditions.

the motions of the pure Hadley flows as the frequency is very similar (see the map in Figure 9.27 to compare) and another one around 1000. At $T_{cold} = 40°C$ we can notice the phenomenon related to the lower frequency is predominant respect to the higher frequency mechanism (that at $Ra = 5000$), while at $T_{cold} = 60°C$ the spectra show the opposite behaviour, having the primary peak corresponding to the high-frequency phenomenon.

9.5.3 Experimental results

All the experiments have been run at an ambient temperature between $21°C$ and $22°C$. Figures 9.36 and 9.37 show the results for horizontal and inclined temperature gradient, respectively. The temperature difference between the two sides has been kept fixed: $\Delta T = 20°C$(as in previous section) and three different values have been considered, namely $T_{cold} = 20$, 40 and $60°C$ (in the first, second and third row, respectively). Moreover, in all the cases considered the emerging pattern is always steady. The vector plots are drawn relying on the PIV (Particle Image Velocimetry) technique applied to experimental videos providing the evolution in time of tracer particles (size $50\mu m$ made

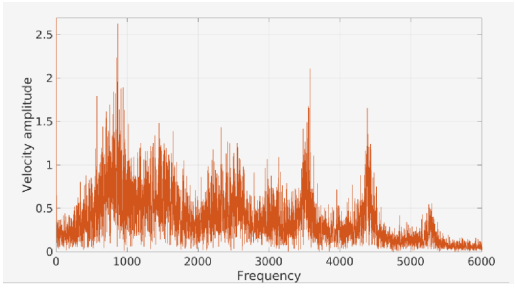

(a) $T_{cold} = 40°C$, $Bi = 0.0526$, $Ra_{nom} = 4.9{*}10^7$.

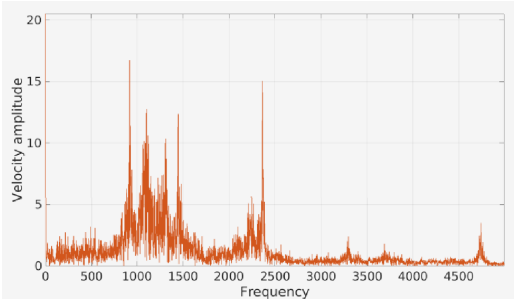

(b) $T_{cold} = 40°C$, $Bi = 0.5263$, $Ra_{nom} = 4.9{*}10^7$.

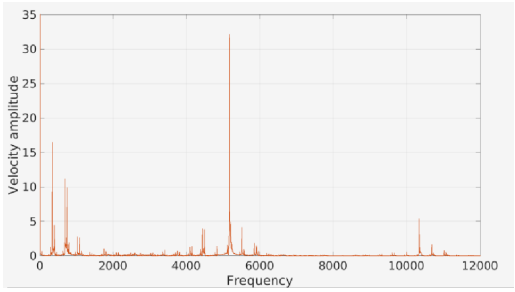

(c) $T_{cold} = 60°C$, $Bi = 0.2632$, $Ra_{nom} = 8.7{*}10^7$.

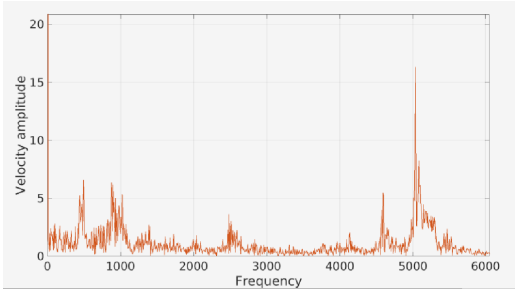

(d) $T_{cold} = 60°C$, $Bi = 0.5265$, $Ra_{nom} = 8.7{*}10^7$.

Figure 9.34: Frequency spectra at different values of the T_{cold} and Bi.

visible by a light cut).

For every case, the vector plot and the horizontal velocity profile drawn on al vertical line at the centre of the cavity ($x = 0.02$ m) are reported. It is worth highlighting that, especially for the Hadley flow, due to the very thin boundary layers, the reconstruction of the velocity near the walls is not very precise owing to the lack of points on which the PIV code perform its calculations. The classical recirculation characteristic of the Hadley flows can be seen: the fluid rises near the hot side and sinks near the colder one. A roll is located near the top left corner. Moreover, in the velocity profile, the velocity peaks relating to the direct and return flow can be appreciated.

We start our description with the case $T_{cold} = 40°C$ (Figure 9.36, second row), in which a localised roll is present near the top right corner (close to the colder wall). Comparing this case with Figure 9.36 (first row) leads to the conclusion that the peak in the velocity profile, characterising to the return flow is substituted in this case by a wider zone in which the velocity has a negative horizontal component. Interestingly, this fact can be seen as an indicator of the presence of 3D effects.

If the T_{cold} increases to a value of $60°C$, the anticlockwise rotating circulation observed in the previous case becomes bigger and stronger. The increasing trend of such a structure could mean that the mechanism responsible for its production is connected

to the relevant heat lost in the surrounding ambient through the upper boundary. This fact results in a sinking plume (made of colder fluid), which is not present in the patterns emerging from classical Hadley flow configurations with adiabatic sides. Also, in this case, the peak (located near the bottom) in the horizontal velocity profile is no longer present, indicating a possible three-dimensional structure of the flow.

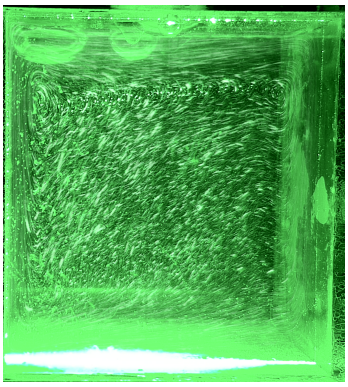

(a) $T_{cold} = 20°C$, Hadley flow.

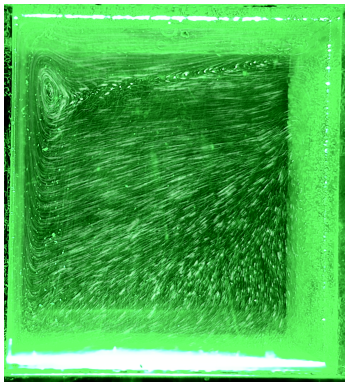

(b) $T_{cold} = 40°C$, Hadley flow.

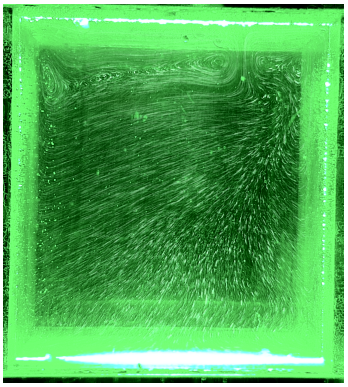

(c) $T_{cold} = 60°C$, Hadley flow.

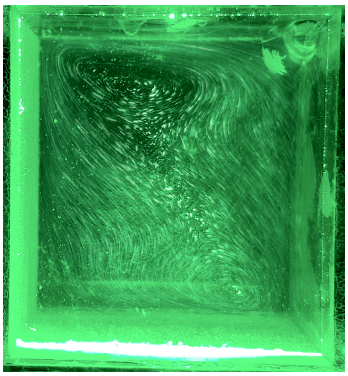

(d) $T_{cold} = 20°C$, 40° inclined cavity.

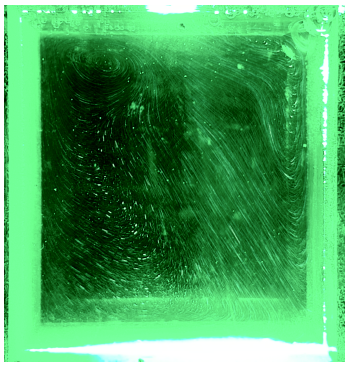

(e) $T_{cold} = 40°C$, 40° inclined cavity.

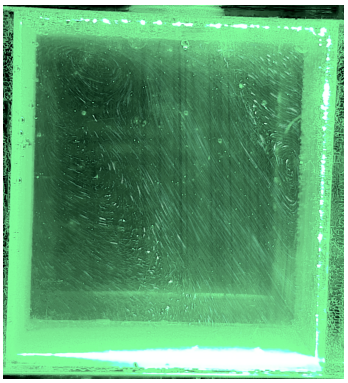

(f) $T_{cold} = 60°C$, 40° inclined cavity.

Figure 9.35: Stream-lines of the six experimental cases. First row: Hadley flow, second row: 40° inclined cavity.

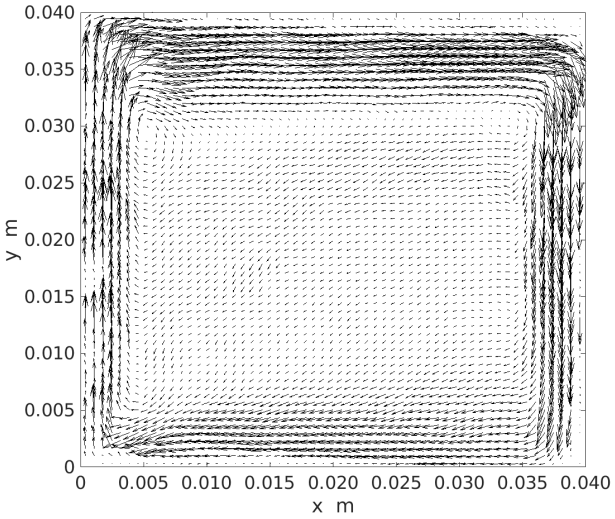

(a) $T_{cold} = 20°C$, vector plot

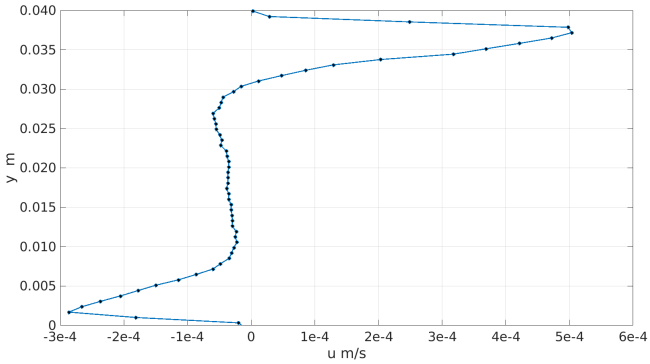

(b) $T_{cold} = 20°C$, velocity profile at $x = 0.02m$

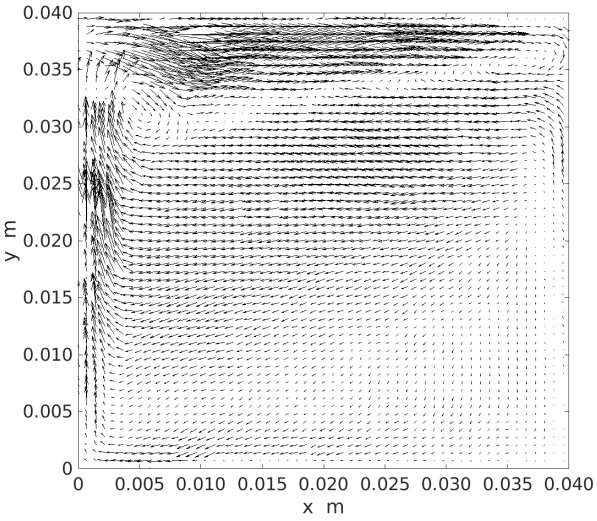

(c) $T_{cold} = 40°C$, vector plot

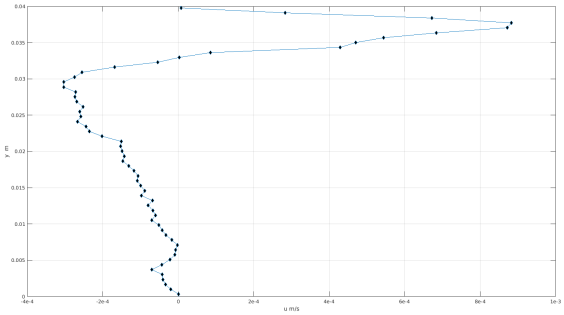

(d) $T_{cold} = 40°C$, velocity profile at $x = 0.02m$

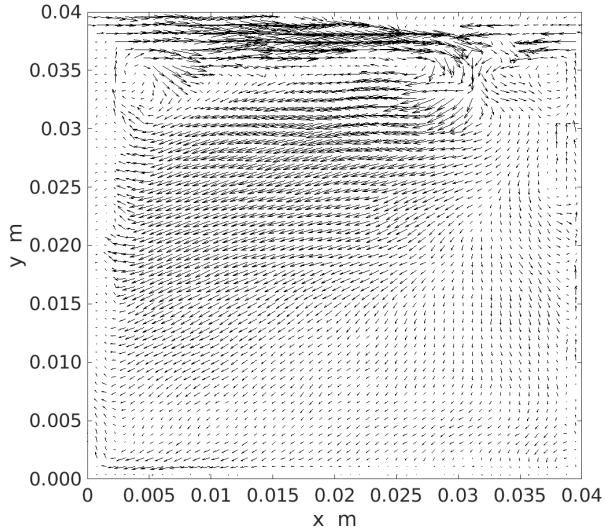

(e) $T_{cold} = 60°C$, vector plot

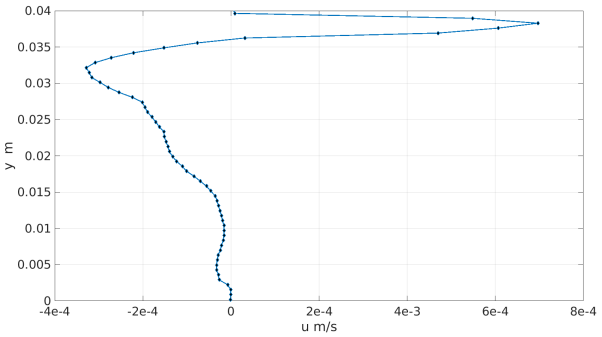

(f) $T_{cold} = 60°C$, velocity profile at $x = 0.02m$

Figure 9.36: Vector plot obtained with PIV technique for $\theta = 0°$ (hot side on the left, cold side on the right) and horizontal velocity component along a line at$x = 0.02m$ (half of the cavity length).

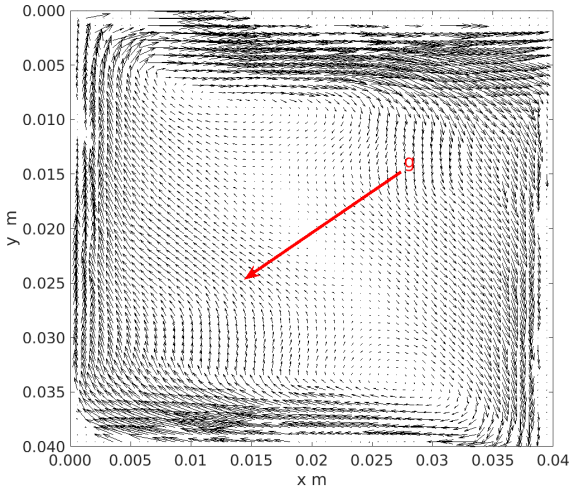

(a) $T_{cold} = 20°C$, vector plot

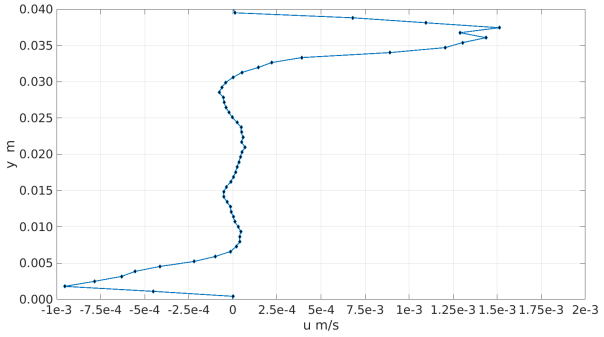

(b) $T_{cold} = 20°C$, velocity profile at $x = 0.02m$

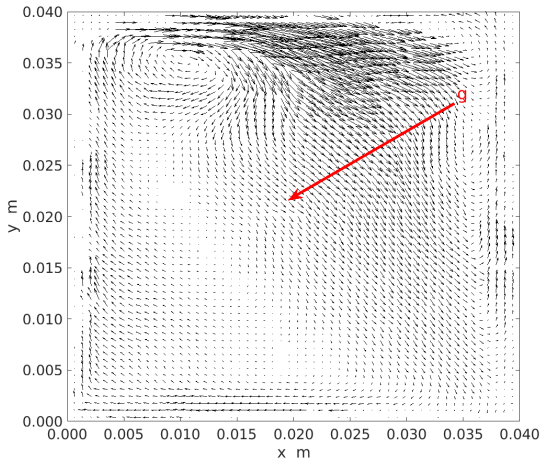

(c) $T_{cold} = 40°C$, vector plot

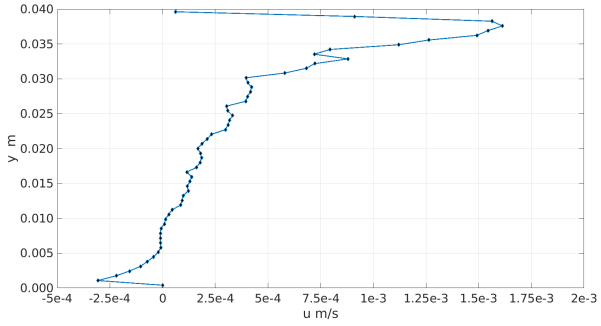

(d) $T_{cold} = 40°C$, velocity profile at $x = 0.02m$

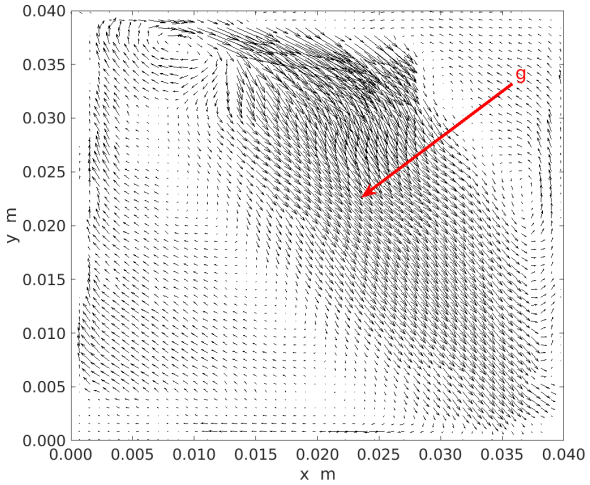

(e) $T_{cold} = 60°C$, vector plot

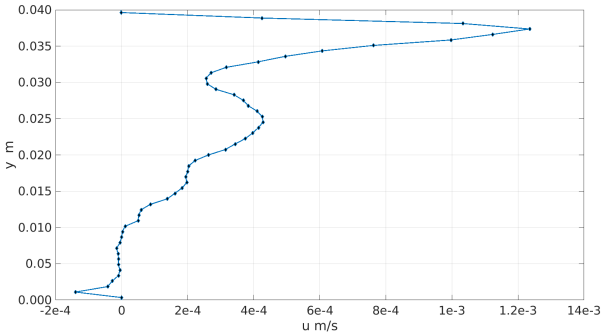

(f) $T_{cold} = 60°C$, velocity profile at $x = 0.02m$

Figure 9.37: Vector plot obtained with PIV technique for $\theta = 40°$ (hot side on the left, cold side on the right) and horizontal velocity component along a line at$x = 0.02m$ (half of the cavity length).

As shown in Figure 9.37, the pattern has a steady behaviour also when the cavity is inclined. On the other hand, the emerging flow has some features in common with those presented in Figure 9.28: at higher values of the T_{cold} a roll is created in the top right corner, growing as the average temperature of the system rises. The pattern is shown in Figure 9.37 can yet be (qualitatively) interpreted in the light of the existing literature. Many authors studied buoyancy convection in these geometries in the framework of analytical or numerical approaches towards the end to determine in the space of parameters the regions of existence of possible "basic" flow solutions (categorised according to the dominant mechanism of heat transfer as conductive, transition and boundary-layer regimes; see Delgado-Buscalioni and Crespo del Arco [80]. According to these studies, for increasing values of Ra no stagnant region is formed at the centre of the core. However, it is possible to notice a region with approximately constant shear (which can be regarded as a clear distinguishing mark of these inclined systems concerning the horizontal counterparts). Numerical results about three-dimensional steady states in a cubical cavity (filled with air) depending on the Rayleigh number and inclination angle can be found in the work by Lee and Lin [247] (the reader being referred to the next section for additional relevant information).

9.5.4 Three-dimensional numerical simulations

Before starting to deal with the 3D numerical results, it is worth highlighting that the present 2D outcomes and the experiments differ mainly about the Spatio-temporal dynamics of the emerging pattern. While the experimental results show a steady pattern for all the cases, the numerically simulated flows undergo an oscillatory or even chaotic instability when the heat loss becomes more relevant (when h, T_{cold} or both are increased). This behaviour has an even more important impact in the inclined enclosure (Figure 9.28) and leads to the remarkable conclusion that the heat lost through the boundaries delimiting the container in the span-wise direction may stabilise the flow. Moreover, the good agreement among the 2D simulations and the experimental outcomes at values of T_{cold} close to the ambient temperature and low Biot numbers, provides a further evidence about the stabilising effect these two additional walls. The resulting 2D flow at $T_{cold} = 20°C$ and $Bi = 0.0526$, indeed, shares many similarities with that found experimentally for both Hadley flow and inclined cavities. This agree-

ment get worse in the manner described above if the heat losses increase.

The main goal we try to reach by conducting the 3D simulations is acquire a more detailed knowledge about the phenomena observed in the experiments. According to this purpose, we start presenting the three different cases, shown in Figure 9.38: Hadley flow configuration for $Bi = 0.5263$, $T_{cold} = 20$ and $60°C$ and inclined enclosure at $T_{cold} = 60°C$, $Bi = 0.5263$. Moreover a direct comparison among 2D, experimental and 3D results in the XY plane, is reported in Figures 9.39, 9.40 and 9.41 for the three different cases reported in Figure 9.38.

For the lowest value of $Tcold = 20°C$ we can see from Figure 9.39 that the 2D and 3D numerical simulations are very similar: both being very close to the pattern observed in the experiments, except for the dimensions of the roll located in the top-right corner. Nevertheless, the other two cases do not show a good agreement among two-dimensional simulations and experiments. Probably the most relevant aspect responsible of the differences among the two cases, is the kind of the flow: it is time-periodic according to the two-dimensional simulations, whereas the emerging pattern is steady according to both the experiments and the 3D simulations. It can be seen that making the cavity three-dimensional allows us to get much closer to the experimental outcomes. Indeed the counter-rotating circulation located in the top right of the cavity (see Figure 9.40), which is not captured by 2D simulations,is correctly predicted by the 3D ones. On the other hand there are still some departures between 3D numerical simulations and experimental outcomes, due probably to the value of the Biot number employed in the numerical simulations, which could slightly differ in the two cases.

Given the almost 2D nature of the flow shown in Figure 9.38 (velocity variations along the span-wise direction being relatively small) we conclude that the departure of 3D outcomes from the 2D ones is essentially due to effects having a thermal nature, namely the heat exchanged through the boundaries in the z-direction. Again, additional insights into these behaviours can be gathered through comparison with other similar results in the literature. Steady 3D flows have indeed been reported in various circumstances.

There is a vast amount of literature dealing with the case of liquid metals that we do not review here as it is scarcely relevant. The role played by the failure to achieve strictly adiabatic conditions on the sidewalls for high-Pr liquids has been considered for (not inclined) water-filled cavities by Schladow et al. [248], Hiller et al. [249] and

Kowalewski [250]. For relatively small values of the Rayleigh number, the differences between the experimental flow and idealised two-dimensional convection (see, e.g., the discussion in Hiller et al. .[249]) are almost negligible.

As shown by existing numerical studies, if idealised adiabatic boundaries are considered (Schladow et al. [248], Kowalewski[250] and Melnikov and Shevtsova [251]), the 3D effects consist of weak spiralling motions. These correspond to the emergence of a cross-flow along z (from the sidewalls towards the mid-plane $z = \frac{L_z}{2}$). The main result is a double spiral configuration, with adjacent spirals, which develop between the non-heated sidewalls and the mid-plane.

These findings indirectly confirm that the flow stabilisation in 3D concerning 2D that we have observed is not a fluid-dynamic effect resulting from the increased friction to which the fluid is exposed (due to six walls in place of four); rather it is determined by the loss of energy due to the heat transferred to the ambient. We also argue that a further increase in the applied temperature difference (not possible with the present experimental apparatus) would lead to oscillatory flow following a transition path qualitatively similar to that obtained in the 2D case. Boundary-layer instabilities have indeed been detected in experimental studies on the subject. As an example, Belmonte et al. [252] observed a turbulent flow characterised by a large-scale circulation ($Ra > 3 \times 10^7$) extended across the entire extension of the cavity with side eddies along with each lateral plate. Similar findings are due to Fusegi et al. [253], who examined three-dimensional natural convection for $Pr = 0.71$ for $10^3 \leq Ra \leq 10^{10}$ giving emphasis to the differences with respect to two-dimensional computations. The reader specifically interested in the differences between the specific evolutionary paths taken by 2D and 3D flow in their progression towards turbulence may also consider the numerical studies conducted for air-filled enclosures by Labrosse et al. [254], Soria et al. [255] and Trias et al. [256].

In order to strengthen the above considerations made about the thermal nature of the stabilisation occurring in the 3D cavities, it is worth remarking that if the average temperature increases further also the three-dimensional cases undergo an oscillatory behaviour. This fact can be appreciated in Figure 9.42, where the temperature difference among the two sides has been set to 40 °C. It is possible to notice that, as a result of such increase the steady pattern is taken over by an oscillatory one.

We do not strive to review all these aspects. Rather, as a concluding remark, we

conclude that the significative heat loss can produce a significant stabilisation of the inclined 3D cavity as well.

[h!]

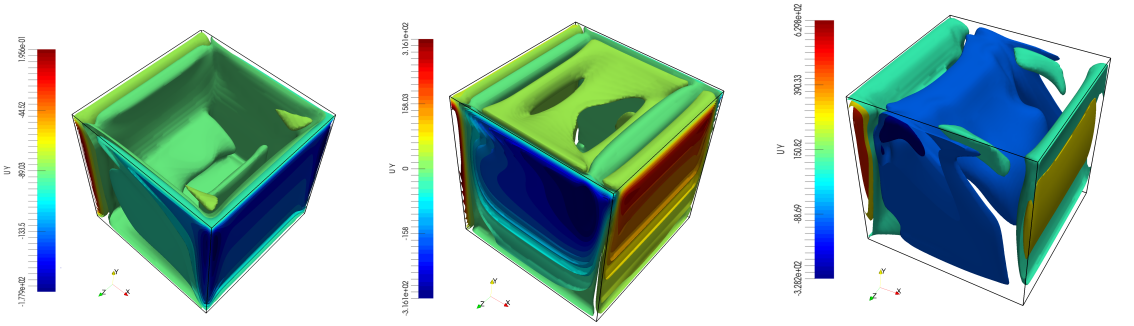

(a) Hadley flow: $T_{cold} = 20°C$, $Bi = 0.5263$,$Ra_{nom} = 1.8 * 10^7$, $Ra_{eff} = 9.00 * 10^5$.

(b) Hadley flow: $T_{cold} = 60°C$, $Bi = 0.5263$,$Ra_{nom} = 8.7 * 10^7$, $Ra_{eff} = 4.63 * 10^6$.

(c) $Hadley flow 40°$ inclined cavity: $T_{cold} = 60°C$, $Bi = 0.5263$,$Ra_{nom} = 8.7 * 10^7$, $Ra_{eff} = 1.490 * 10^5$.

Figure 9.38: Iso-surfaces of vertical velocity component.

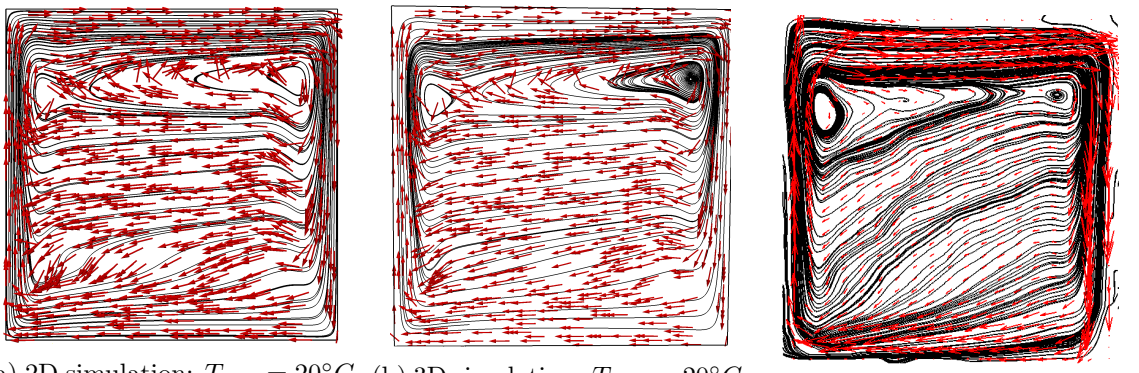

(a) 2D simulation: $T_{cold} = 20°C$, $Bi = 0.0526$,$Ra_{nom} = 1.8 * 10^7$, $Ra_{eff} = 1.45 * 10^6$.

(b) 3D simulation: $T_{cold} = 20°C$, $Bi = 0.0526$,$Ra_{nom} = 1.8 * 10^7$, $Ra_{eff} = 9.00 * 10^5$.

(c) Experiment $T_{cold} = 20°C$, $\Delta T = 20°C$.

Figure 9.39: Hadley flow:stream lines and vector plots ($T_{cold} = 20°C$).

9.6 Conclusions

The main purpose of the present study is to highlight the role played by thermal boundary conditions. Different configurations have been investigated, namely Rayleigh-Bénard convection, Hadley flow and an inclined configuration ($\theta = 40°$). The heat dissipated through the walls indeed is responsible for remarkable changes in the flow patterns respect to the ideal boundary conditions (adiabatic or perfectly conducting walls): oscillatory behaviours may arise. At the same time, the inclination angle is strictly linked with the onset of multiple solutions. The two aspects described above

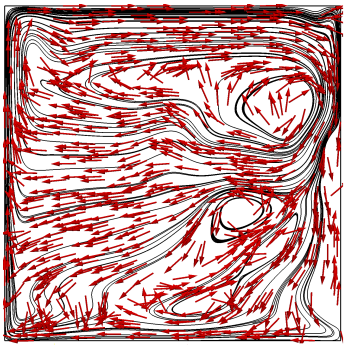

(a) 2D simulation: $T_{cold} = 60°C$, $Bi = 0.5263$,$Ra_{nom} = 8.7 * 10^7$, $Ra_{eff} = 5.51 * 10^6$.

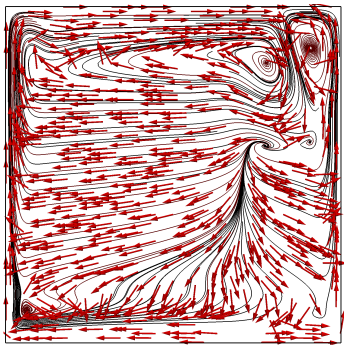

(b) 3D simulation: $T_{cold} = 60°C$, $Bi = 0.5263$,$Ra_{nom} = 8.7 * 10^7$, $Ra_{eff} = 4.63 * 10^6$.

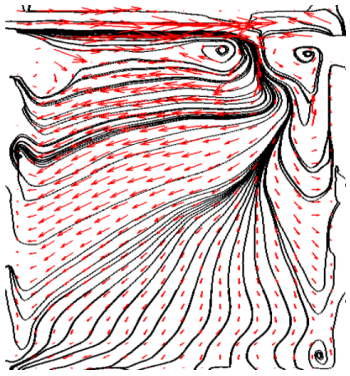

(c) Experiment $T_{cold} = 60°C$, $\Delta T = 20°C$.

Figure 9.40: Hadley flow:stream lines and vector plots ($T_{cold} = 60°C$).

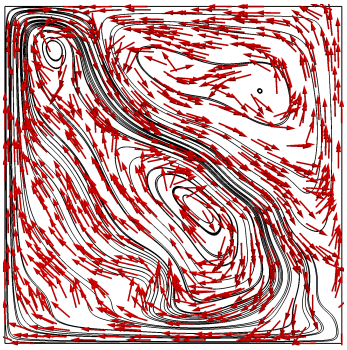

(a) 2D simulation: $T_{cold} = 60°C$, $Bi = 0.5263$,$Ra_{nom} = 8.7 * 10^7$, $Ra_{eff} = 2.66 * 10^6$.

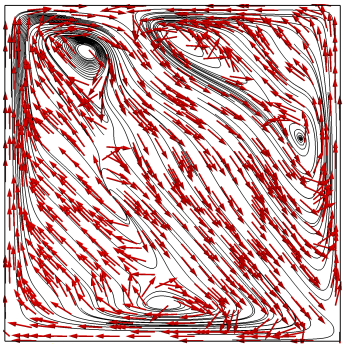

(b) 3D simulation: $T_{cold} = 60°C$, $Bi = 0.5263$,$Ra_{nom} = 8.7 * 10^7$, $Ra_{eff} = 1.490 * 10^5$.

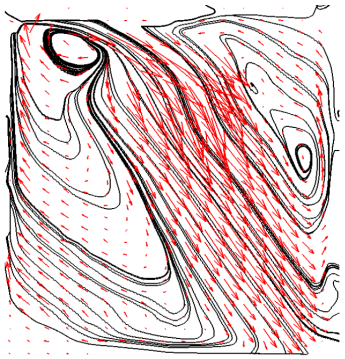

(c) Experiment $T_{cold} = 60°C$, $\Delta T = 20°C$.

Figure 9.41: Inclined cavity:stream lines and vector plots ($T_{cold} = 60°C$).

indeed are closely interwoven: the heat exchanged through the walls could in principle bend the system to different branches of the solution, which share the same portion of the phase space.

The sensitivity of the flow to the heat exchange and the complex structure of the phase space represents a bottleneck, limiting the validity of the experimental results. In order to overcome this shortcoming in the present study, the experiments have been supported with two and three-dimensional simulations to understand the impact brought by the more complex conditions at boundaries considered.

As a result, of a departure from idealised boundary conditions, significant modifications can occur in the typical route followed by these systems in their evolution towards chaos even if numerical simulations are carried out under the constraint of two-dimensionality. Accounting for the extra loss through the walls delimiting the fluid along the third dimension can even cause complete re-stabilisation of the flow with the emergence of

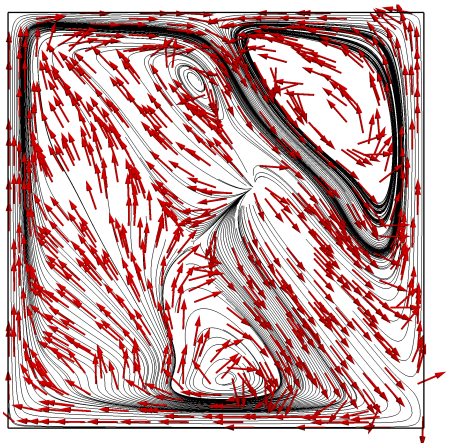

(a) Streamlines of the velocity fields

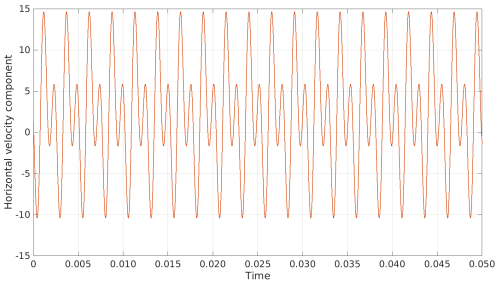

(b) Time signal of the horizontal velocity component.

Figure 9.42: Numerical simulations of three-dimensional inclined 40° cavity: $\Delta T = 40$ °C, $Bi = 0.526$, $T_{cold} = 60$°C and with a non-dimensional angular frequency $\omega = 2.47 * 10^3$.

steady states in broad regions of the space of parameters.

The landscape resulting from the present analysis displays a very complex scenario in terms of the emerging patterns, which in the most of the cases are characterised by substantial departures from the usual adiabatic or perfectly conducting cavities. So we hope with the present study to shed some light about the complexities which may arise when more realistic models are considered and give in this manner a more detailed picture about the mechanisms which could occur even in a simplified but realistic system such that considered.

Chapter 10

Conclusions

To investigate the existence of multiple solutions and their impact on the emergence of strange attractors and the progression of thermal convection towards chaos, we have considered different archetypal systems, namely, cavities heated from the side or from below supporting fluid motion generated by buoyancy or surface-tension effects and hosting different types of fluids (liquid metals, air, water, viscoelastic liquids). More specifically, in Chapter 7, we have investigated cavities filled with liquid metals subjected to a horizontal temperature gradient (Hadley flow). Also, we have added a further degree of freedom: the convergence or divergence of the horizontal walls (i.e. these walls were no longer horizontal). Remarkably we have found a wide landscape of possible instabilities mechanisms: the classical pulsating rolls (a typical outcome of two-dimensional hydrodynamic disturbances in liquid metals) indeed can be a possible mechanism only when the upper and lower walls were nearly horizontal. However, when the contraction (or the divergence) was increased unseen mechanism could arise: from the so-called kissing rolls to the travelling waves, occurring at the most severe slopes of the walls considered.Many of these modes exist as multiples solutions, i.e. as different types of flow coexisting in the space of parameters, which can effectively be selected by the fluid depending on its initial state. In this study, we also took into consideration the three-dimensional cavities (with an extrusion along z of the two-dimensional ones). In this case, the multi-roll patterns found are no longer possible when the third direction is present. On the other hand, an interesting competition among the hydrodynamic and OLR instability emerged. Yet multiple solutions are possible due to the intricate interplay of such disturbances with different natures.

Chapter 8 aims to investigate Marangoni-Bénard convection in an infinite layer (sim-

ulated through periodic boundary conditions on the vertical walls). Moreover, the problem has been enriched by considering the viscoelastic behaviour of the fluid. In this case, remarkable deviations from the Newtonian case appeared. The latter case indeed, is characterised by the emergence of geometrically shaped patterns on the free-surface. In particular hexagons, triangle or squares may arise, depending on the Prandtl and Marangoni numbers. More specifically, in the case considered in Chapter 8 ($Ma = 300$ and $Pr = 1$), the Newtonian case is characterised by triangles. Such pattern, however, undergoes a remarkable modification when the level of viscoelasticity of the fluid increases: the triangular cells are taken over by the so-called oscillons,i.e. spatially localised oscillatory structures having the shape of rounded convective cells. Remarkably, these oscillons exist in the form of multiple solutions, which progressively increase the number of degrees of freedom of the considered dissipative system and promote the transition to chaos. These structures have been observed in granular media as well, and they consist of insulated structures (convective in this case) surrounded by an almost quiescent background.

In Chapter 9, a combined experimental and numerical analysis about gravitational flows inside cavities has been conducted. Water has been used as the working fluid. Such study focused particularly on the impact of the heat exchange through the non-adiabatic walls, moreover different inclinations have been taken into account: from the pure Rayleigh-Bénard flows to the Hadley ones. Also in this case complex behaviours have been observed, depending on the heat exchanged through the walls: the steady patterns found when the walls are almost adiabatic could be replaced by oscillatory or even chaotic one when the heat exchanged through the walls grows. Heat exchange has also exerted a deep influence on the different branches of multiple solutions which are typical of Rayleigh-Bénard convention in Newtonian fluids. In some circumstances, heat exchange can even cause a transition from the Ruelle-Takens scenario to the Curry-Yorke one. Though the studies considered in the present thesis may look as unrelated, such disjoint subjects were intentionally considered towards the end to identify some "universal features" in the thermal convention.

The first unifying feature is the presence of the so-called multiple solutions, which are present in all the cases mentioned above. Multiple solutions were already known as a typical feature of the Hadley flow in liquid metals and Rayleigh-Bénard convention regardless of the considered type of fluid. The present thesis has investigated how the

richness of these solutions can increase by introducing variations in the geometry never considered before for the Hadley flow or new type of thermal boundary conditions for Rayleigh-Bénard convention. The ensuing expansion in the set of possible branches of multiple solutions has allowed an analysis of how these solutions can interfere with the evolution of these convective systems towards chaos. The present work has also demonstrated the existence of multiple solutions in Marangoni-Bénard convention for the first time. The multiplicity of such solutions (emerging as "oscillons") is made possible by the viscoelasticity of the fluid. Regardless of the specific type of convention (Hadley flow, Rayleigh-Bénard convention or Marangoni-Bénard convection) or fluid considered (liquid metal, water or viscoelastic liquid), multiple solutions can produce interesting phenomena known as "crisis".

In most of the cases treated above the chaos and the turbulence are not achieved gradually, as the control parameter is varied. The regular spatiotemporal patterns instead are taken suddenly over by highly chaotic and irregular ones, which is no longer possible to estimate the indicators of chaos, such as the correlation dimension. The emergence of the crises indeed can be interpreted as the interaction of different attractors in the phase space. An attractor reflects itself in physical space as a specific pattern, so the multiplicity of solutions can be viewed as the presence of more attractors in the phase space. With this perspective, the onset of crises occurs when two attractors (or their basin of attraction) shares the same portion of the phase space or when one of them loses its stability. As the stability and the basis of attraction strongly depends on the control parameter (e.g. Rayleigh number and Marangoni number) only a slight variation of this quantity could produce a great change in emerging patterns.

Based on these observations and arguments, the main conclusion of the present work of thesis is that by producing crisis phenomena and the formation of strange attractors, multiple solutions can have a significant effect on the evolution of thermal convention towards chaos. They can indeed cause frequent departures from canonical paths such as the Ruelle-Takens scenario and replacement of this route with the Curry-Yorke or other evolution mechanisms.

Appendices

Appendix A

Symbols

ρ density

RHS Right Hand Side

LHS Left Hand Side

$\underline{n}$ normal vector

$\underline{U}$ velocity vector

E internal energy

h enthalpy

T temperature

λ thermal conductivity

α thermal diffusivity

$\underline{\mathbf{g}}$ gravity vector

$\underline{\underline{\tau}}$ stress tensor

β thermal expansion coefficient

σ surface tension

$\underline{\underline{\mathbf{I}}}$ identity matrix

Pr Prandtl number

Ra Rayleigh number

Gr Grashof number

Re Reynolds number

Ma Marangoni number

Bi Biot number

Bo Bond number

$\underline{\underline{\dot{\gamma}}}$ Shear rate tensor

μ Newtonian viscosity

η General viscosity

Γ_{ijk} Christoffel symbol of the first kind

Γ^i_{jk} Christoffel symbol of the second kind

$\underline{\underline{g}}$ metric tensor

Ca capillary number

De Deborah number

Wi Weissenberg number

Θ Elasticity number

λ Relaxation time

CFD Computational Fluid Dynamics

FVM Finite Volume Method

Appendix B

Gauss theorem

In Chapter 2 and 5, we have based our discussion on the Gauss theorem, so in this Appendix, we shortly enunciate this theorem. This theorem, also known as **divergence theorem** states that the integral of the divergence of a differentiable vector field $\underline{\psi}$ over a compact subset V of R^n is equal to its flux across the boundaries S of V (S is supposed to be smooth). Mathematically the statement can be written:

$$\iiint_V (\nabla \cdot \underline{\psi})\, dV = \oiint_S (\underline{\psi} \cdot \underline{n})\, dS \tag{B.1}$$

The equation B.1 is graphically depicted in Figure B.1. Physically the equation B.1 has

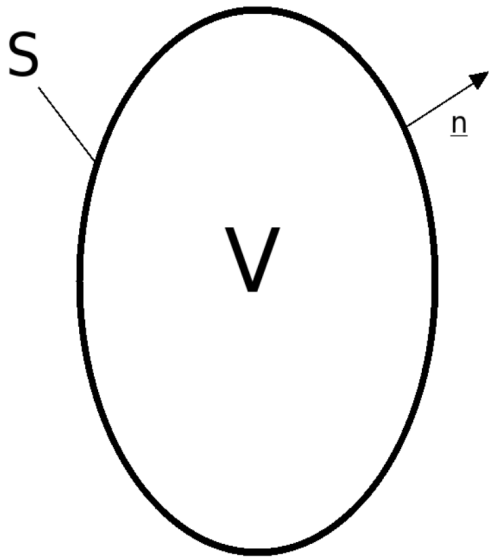

Figure B.1: Gauss theorem

the meaning that all the sources and sinks (mathematically they are represented by the

divergence operator $\nabla\cdot$) of the vector field located in the volume V $\underline{\psi}$ are responsible for the flux across the boundaries S.

Appendix C

Boundary conditions in OpenFoam

The present Appendix aims to explain how the boundary conditions are treated in OpenFoam and in particular hoe the Marangoni BC is implemented.
Despite the great variety of BCs present in OpenFoam, they are treated in the same manner (at least the classical ones): the value on the patch (ϕ_b) is obtained with a linear interpolation of the value at the centre of the nearest cell to the patch ϕ_C. Mathematically this concept is expressed by the following expression:

$$\phi_b = A\phi_C + B \tag{C.1}$$

In C.1 A and B are two parameters which depend upon the selected BC (for example in fixedValue BC A=0 and B is the value on the patch). The same concept can be applied to the gradient of the variable ($\nabla\phi_b$). Indeed:

$$\nabla\phi_b = C\phi_C + D \tag{C.2}$$

Again in C.2 C and D depending upon the selected BC. OpenFoam needs the two values described above in order to discretise the convective term with ϕ_b and the diffusive one with $\nabla\phi_b$. Applying the Gauss theorem, the two contributions can be written as:

$$\int_{\partial Cell} \rho * U_f \phi_f dA \tag{C.3}$$

$$\int_{\partial Cell} k\nabla\phi_f \cdot n dA \tag{C.4}$$

Where ∂C is the border of the generic cell and the subscript f denotes the variable taken on the cell faces. When a cell face coincides with a patch of the domain, we have: $\phi_f = \phi_b$ and $\nabla\phi_f = \nabla\phi_b$. Substituting the C.1 and C.2 in C.3 and C.4 respectively we obtain:

$$\int_{\partial Cell} \rho * U_f * A\phi_C dA + \int_{\partial Cell} \rho * U_f * B dA \tag{C.5}$$

$$\int_{\partial Cell} kC\phi_C dA + \int_{\partial Cell} kB dA \tag{C.6}$$

It is worth remarking that the first of the integrals in C.5 and C.6 are solved implicitly (the coefficients obtained from the discretisation of the integrals lie on the diagonal of the matrix) while the second ones are treated as explicit terms (are part of the vector of the source terms).

C.1 Two examples: the fixedValue and zeroGradient

In this subsection, the probably two most used BCs are brought as an example.

fixedValue In this BC we have simply that $\phi_B = \phi_{input}$, where ϕ_{input} is selected by the user. So the coefficients of the C.1 become:

- $A = 0$
- $B = \phi_{input}$

The gradient is slightly more complicated. In fact we can write it as:

$$\nabla\phi_B = \frac{\phi_{input} - \phi_C}{d} \tag{C.7}$$

Where d is the distance of the cell face from the cell centre. It is possible to notice from C.7 that the coefficients C and D take the following form:

- $C = -\frac{1}{d}$
- $D = \frac{\phi_{input}}{d}$

zeroGradient Setting the $\nabla\phi_b$ as zero simply yields to $C = 0$ and $D = 0$ for the two coefficients of the C.2. For those of the C.1 we can rewrite the equation as :

$$\nabla\phi_b = \phi_C + \nabla\phi_b * d \tag{C.8}$$

Being $\phi_b = 0$ we obtain: $\phi_B = \phi_C$. Hence $A = 1$ and $B = 0$.

C.2 A look at the Open Foam functions

As Open Foam code is written in an object-oriented manner, the BCs are thought as an object belonging to the class *fvPatchField*. This class is the base from which all the BCs should be constructed. It is not the aim of this guide describing all the methods and how they are rewritten in the child classes, but we will focus only on the methods which implement the concepts explained in the previous section. Before starting the description is worth remarking that all the methods already exist in the base class *fvPatchField*, but the keyword **virtual** precedes most of them. In this way, it is possible to rewrite the base class functions for each of child ones, according to the needs of the single derived classes (polymorphism). In this way, the same method will act in a different manner depending on the object created.
Having this clear in mind, we can state that in order to customize a BC we only need to derive our BC from $fvPatchField$ and rewrite those methods which are important for the calculations of the quantities described above. So the functions which have to be rewritten in order to build the BC are:

- *updateCoeffs* or (*evaluate*): this method calculate explicitly ϕ_b using the C.1 (*evaluate*) or using some expressions (see *updateCoeffs* in *oscillatingFixedValue* BC). When *evaluate*, defined according to C.1 is used,it usually executed just after the calculation of the field ϕ. On the other hand, when *updateCoeffs* is used in a Dirichlet based BC (as the *oscillatingFixedValue* in which the value is no longer fixed in time but change according to a sinusoidal law) it is necessary to call the method before the solution of the field *phi*;

- *valueInternalCoeffs*: this function computes and return the A coefficient of the C.1;

- *valueBoundaryCoeffs*:it calculates the B coefficient of the C.1.

- *gradientInternalCoeffs*:returns the C coefficient of the C.2;

- *gradientInternalCoeffs*: it is responsible of the assessment of the D coefficient.

- *snGrad*: explicitly calculates the normal to the surface gradient on the cell face on the patch.

C.3 Marangoni Boundary condition

This section is devoted to describing the Marangoni boundary condition. We will start with the description of the Newtonian case in order to introduce later the viscoelastic one. For the sake of clarity, we will suppose the free surface as a non-deformable boundary which is subjected to a temperature gradient, which yields to viscous stresses on the surface.

C.3.1 Newtonian case

Mathematically the above considerations are expressed by the following formula:

$$\underline{\underline{\tau}} \cdot \underline{n} = -\sigma_T(\underline{\underline{I}} - \underline{nn}) \cdot \underline{\nabla} T \tag{C.9}$$

Where:

- $\underline{\underline{\tau}}$ is the stress tensor;
- $\underline{n}$ is the vector normal to the free surface;
- σ_T is the derivative of the surface tension respect to the temperature (made at a temperature of reference);
- $\underline{\underline{I}}$ is the identity tensor;
- $\underline{\nabla} T$ is the temperature gradient.

The equation C.9 is a condition on the stresses, which can be transformed into one on the velocities thanks to the dynamic viscosity, which link the two quantities. Indeed:

$$\mu \frac{\partial \underline{V_T}}{\partial \underline{n}} = -\sigma_T \underline{\nabla_T} T \tag{C.10}$$

In the equation C.10, the subscript T denotes the tangential components respect to the free surface.
It is worth pointing out the fact that the condition expressed by C.9 applies only to the tangential components. As the free surface is supposed impermeable, the normal component has to be set at 0.

C.3.2 OpenFoam implementation

In the previous section, we have explained how OpenFoam treats the BCs in general. Here we will present the basic principles of the Marangoni BC. So the present paragraph aims to apply to concepts just described before to the Marangoni BC. In the following, we will give a detailed description of the functions defined above.

evaluate() This function explicitly calculates the value of the velocity on the boundary according to the equation C.1. It is executed just after the assessment of the velocity field (the cell value next to the free surface is needed). The value of the velocity on the boundary can be expressed as a function of that at the closest internal cell in the following way:

$$\underline{V_b} = \underline{V_{T,c}} + (\frac{\partial \underline{V_{T,b}}}{\partial \underline{n}}|d|)\frac{\underline{V_{T,c}}}{\|\underline{V_{T,c}}\|} \tag{C.11}$$

Where the subscripts b, c, T indicate the value at the boundary, at the closest cell centre from the patch and the tangential component respect to the boundary respectively. d is the distance vector of the face centre on the patch from the correspondent cell centre. Keeping in mind that:

$$\underline{V_{T,c}} = \underline{V_c} - (\underline{V_c} \cdot \underline{n})\underline{n} = (\underline{\underline{I}} - \underline{nn}) \cdot \underline{V_c} \tag{C.12}$$

and that (thanks to the relation C.10):

$$\frac{\partial \underline{V_{T,b}}}{\partial \underline{n}} = \frac{\sigma_T}{\mu} * \underline{\nabla_T} T \tag{C.13}$$

we have that the value on the boundary can be expressed as:

$$\underline{V_b} = (\underline{\underline{I}} - \underline{nn}) \cdot \underline{V_c} + \frac{\sigma_T}{\mu} * \underline{\nabla_T} T * |d| \tag{C.14}$$

snGrad() This function explicitly computes the gradient normal to the patch. The reasoning behind it is pretty similar to the previous case. Indeed from the equation C.14 we can clearly see that the normal gradient can be split in two contributes: the first which applies to the tangential components of the velocity at the cell centre $(-\frac{\sigma_T}{\mu} * \underline{\nabla_T} T)$ and the second, which is responsible of the cancellation of the normal velocity component at cell centre normal to the patch $(-\frac{\underline{nn} \cdot \underline{V_c}}{|d|})$.

valueInternalCoeffs() This function aims to compute the coefficient A of the equation C.1. It is possible to assess it by splitting the velocity vector into its three components and developing the first RHS term of the equation C.14:

$$(\underline{\underline{I}} - \underline{nn}) \cdot \underline{V_c} = \left\{ \begin{array}{l} (1-n_x^2)u_c - n_x n_y v_c - n_x n_z w_c \\ (1-n_y^2)v_c - n_x n_y u_c - n_y n_z w_c \\ (1-n_z^2)w_c - n_x n_z u_c - n_y n_z v_c \end{array} \right\} \tag{C.15}$$

A coefficient multiplies the cell centre value of the quantity which has to be calculated. It is worth remarking that A is solved implicitly and it is part of the matrix diagonal. Hence A is given by

$$A = \left\{ \begin{array}{l} (1-n_x^2) \\ (1-n_y^2) \\ (1-n_z^2) \end{array} \right\} \tag{C.16}$$

valueBoundaryCoeffs() While the valueInternalCoeffs() is responsible of the assessment of the A coefficient the valueBoundaryCoeffs() returns the B coefficient of the C.1. B is calculated explicitly, and it is part of the source terms vector. In it we find all the remaining terms of the C.15 (those which are not multiplied by the quantity which has to be solved) plus the second RHS term of the C.14. Hence:

$$B = \left\{ \begin{array}{l} -n_x n_y v_c - n_x n_z w_c - \frac{\sigma_T}{\mu} * ((1-n_x^2)\frac{\partial T}{\partial x} - n_x n_y \frac{\partial T}{\partial y} - n_x n_z \frac{\partial T}{\partial z}) * d \\ -n_x n_y u_c - n_y n_z w_c - \frac{\sigma_T}{\mu} * ((1-n_y^2)\frac{\partial T}{\partial y} - n_x n_y \frac{\partial T}{\partial x} - n_y n_z \frac{\partial T}{\partial z}) * d \\ -n_x n_z u_c - n_y n_z v_c - \frac{\sigma_T}{\mu} * ((1-n_z^2)\frac{\partial T}{\partial z} - n_x n_z \frac{\partial T}{\partial x} - n_y n_z \frac{\partial T}{\partial y}) * d \end{array} \right\} \tag{C.17}$$

gradientInternalCoeffs() This method aims to assess the C coefficient of the equation C.2. As outlined in the paragraph related to the *snGrad()* we can split the total normal gradient of the velocity into two contributes and write:

$$snGrad = (-\frac{\sigma_T}{\mu} * \underline{\nabla_T} T) + (-\frac{\underline{nn} \cdot \underline{V_c}}{|d|}) \tag{C.18}$$

$$(-\frac{\underline{nn} \cdot \underline{V_c}}{|d|}) = \left\{ \begin{array}{l} \frac{-n_x^2 u_c - n_x n_y vc - n_x n_z wc}{|d|} \\ \frac{-n_y^2 v_c - n_x n_y uc - n_y n_z wc}{|d|} \\ \frac{-n_z^2 w_c - n_x n_z uc - n_y n_z vc}{|d|} \end{array} \right\} \tag{C.19}$$

The only term of the C.19 which appears in the C coefficient is the first one (that multiplied by the component which has to be calculated). Hence:

$$C = \left\{ \begin{array}{c} -\frac{n_x^2}{|d|} \\ -\frac{n_y^2}{|d|} \\ -\frac{n_z^2}{|d|} \end{array} \right\} \tag{C.20}$$

gradientBoundaryCoeffs() This function is responsible for the assessment of the D coefficient in equation C.2. It is formed by the first RHS term of the C.18 and the remaining part of the C.19 (which does not appear in C.20). So as proceeded for the *valueBoundaryCoeffs()* case, we can write:

$$D = \left\{ \begin{array}{c} -\frac{n_x n_y v_c - n_x n_z w_c}{|d|} - \frac{\sigma_T}{\mu} * ((1-n_x^2)\frac{\partial T}{\partial x} - n_x n_y \frac{\partial T}{\partial y} - n_x n_z \frac{\partial T}{\partial z}) \\ -\frac{n_x n_y u_c - n_y n_z w_c}{|d|} - \frac{\sigma_T}{\mu} * ((1-n_y^2)\frac{\partial T}{\partial y} - n_x n_y \frac{\partial T}{\partial x} - n_y n_z \frac{\partial T}{\partial z}) \\ -\frac{n_x n_z u_c - n_y n_z v_c}{|d|} - \frac{\sigma_T}{\mu} * ((1-n_z^2)\frac{\partial T}{\partial z} - n_x n_z \frac{\partial T}{\partial x} - n_y n_z \frac{\partial T}{\partial y}) \end{array} \right\} \tag{C.21}$$

C.3.3 Viscoelastic case

In the previous subsection, the Marangoni BC has been described under the hypothesis of Newtonian fluid behaviour. However, some additions and modifications are needed when the viscoelasticity is taken into account. First of all, we shall recall the Marangoni BC for a Newtonian fluid (equation C.9):

$$\underline{\underline{\tau}} \cdot \underline{n} = -\sigma_T(\underline{\underline{I}} - \underline{nn}) \cdot \underline{\nabla} T$$

n order to adapt the equation to a viscoelastic fluid, we have to add a term containing the contributions of the viscoelastic stresses. So the new terms are the components of the viscoelastic stress tensor, introduced in Chapter 3. Hence the equation C.9 becomes:

$$\underline{\underline{\tau}} \cdot \underline{n} = -\sigma_T(\underline{\underline{I}} - \underline{nn}) \cdot \underline{\nabla} T - (\underline{\underline{\tau}}_{visco} \cdot \underline{n} - (\underline{n} \cdot (\underline{\underline{\tau}}_{visco} \cdot \underline{n}))\underline{n}) \tag{C.22}$$

In C.22 $\underline{\underline{\tau}}_{visco}$ is the viscoelastic part of the stress tensor, which is calculated according to the equation of the Chapter 3. Moreover, the equation C.10 is transformed in the following way:

$$\mu \frac{\partial \underline{V_T}}{\partial \underline{n}} = -\sigma_T \underline{\nabla_T} T - (\underline{\underline{\tau}}_{visco} \cdot \underline{n} - (\underline{n} \cdot (\underline{\underline{\tau}}_{visco} \cdot \underline{n}))\underline{n}) \tag{C.23}$$

Appendix D

Linear stability analysis

This Appendix is devoted to present the principles of the linear stability analysis, widely recalled throughout Chapter 4 and mentioned many times in Part II of this thesis.
The equations solved in the chapters above constitute a system of partial differential equations (PDE), which in general could be written as a vector of functions :

$$\underline{g}(t,x,y,z) = \{g_1(t,x,y,z), g_2(t,x,y,z), ..., g_n(t,x,y,z)\}$$

The $\underline{g}$ are explicit functions of the time a spatial coordinates. In most of the cases we are interested in their time evolution, ruled by a system of the PDEs, which for our purposes can be written in the following form:

$$\frac{\partial \underline{g}}{\partial t} = \underline{\mathcal{F}}(\underline{g}) \tag{D.1}$$

where $\underline{\mathcal{F}}$, generally may be a non-linear function g_i, time t and spatial coordinates x, y, z.
The main assumption behind the linear stability is that the system behaviour is investigated locally around an equilibrium solution $\underline{g}_0$ such that:

$$\frac{\partial \underline{g}_0}{\partial t} = 0 \tag{D.2}$$

The next step is to consider the Taylor expansion of $\underline{\mathcal{F}}$ truncated at the first order term:

$$\frac{\partial \underline{g}}{\partial t} = \dot{\underline{g}} = \underline{\mathcal{F}}(\underline{g}_0) + \left.\frac{\partial \underline{\mathcal{F}}}{\partial \underline{g}}\right|_{\underline{g}_0} \left(\underline{g} - \underline{g}_0\right) + O\left(\left(\underline{g} - \underline{g}_0\right)^2\right) \tag{D.3}$$

Being $\underline{\mathcal{F}}(\underline{g}_0) = 0$ the equation D.3 can be rewritten:

$$\dot{\underline{g}} = \left.\frac{\partial \underline{\mathcal{F}}}{\partial \underline{g}}\right|_{\underline{g}_0} \left(\underline{g} - \underline{g}_0\right) \tag{D.4}$$

The term $\left.\frac{\partial \underline{\mathcal{F}}}{\partial \underline{g}}\right|_{\underline{g}_0}$ is the Jacobian matrix of the linearised system and it plays a central role in discerning the kind of stability (we will return on that point). The Jacobian matrix is defined as:

$$\underline{\underline{J}} = \left.\frac{\partial \underline{\mathcal{F}}}{\partial \underline{g}}\right|_{\underline{g}_0} = \begin{bmatrix} \frac{\partial \mathcal{F}_1}{\partial g_1} & \frac{\partial \mathcal{F}_1}{\partial g_2} & \cdots & \frac{\partial \mathcal{F}_1}{\partial g_n} \\ \frac{\partial \mathcal{F}_2}{\partial g_1} & \frac{\partial \mathcal{F}_2}{\partial g_2} & \cdots & \frac{\partial \mathcal{F}_2}{\partial g_n} \\ \cdot & & & \\ & & \cdot & \\ & & & \cdot \\ \frac{\partial \mathcal{F}_m}{\partial g_1} & \frac{\partial \mathcal{F}_m}{\partial g_2} & \cdots & \frac{\partial \mathcal{F}_m}{\partial g_n} \end{bmatrix}_{\underline{g}_0} \tag{D.5}$$

The analysis proceeds as follows: once the equation D.4 has been derived it has to be subjected to infinitesimal disturbances $\delta\underline{g}$ of the **basic flow** $\underline{g}_0$. Being the perturbation arbitrarily small and recalling the equation D.2, the following relationship holds:

$$\delta\underline{g} = \left(\underline{g} - \underline{g}_0\right) \longrightarrow \delta\dot{\underline{g}} = \dot{\underline{g}} \tag{D.6}$$

Moreover considering the equation D.6 together with D.4 it is possible to write:

$$\delta\dot{\underline{g}} = \underline{\underline{J}} \cdot \delta\underline{g} \tag{D.7}$$

At this point it is worth recalling that the system in D.7 is linear and hence the disturbances have an exponential form :

$$\delta g_i = V_i e^{\lambda_i t} \tag{D.8}$$

Now as a common practice in the linear stability analysis we look at some particular solution $\underline{V}$ of the system D.7 such that:

$$\delta\dot{\underline{g}} = \underline{V}\lambda e^{\lambda t} = e^{\lambda t}\underline{\underline{J}} \cdot \underline{V} \tag{D.9}$$

and hence:

$$\underline{\underline{J}} \cdot \underline{V} = \lambda \underline{V} \tag{D.10}$$

In the language of linear algebra the vectors $\underline{V}$ are the **eigenvectors** while the λ_i are the **eigenvalues**.

It is not the aim of this Appendix, giving a review of all the theory behind the endomorphisms and the matrix diagonalisation. To our purposes, it is enough to say that in order to assess the λ_i we need to solve the **characteristic equation**:

$$det\left(\underline{\underline{J}} - \lambda \underline{\underline{I}}\right) \tag{D.11}$$

where $\underline{\underline{I}}$ is the identity matrix. Being $\underline{\underline{J}}$ an nxn matrix the D.11 is an algebraic equation of order n , having n complex roots of the form:

$$\lambda_j = u_j + i\omega_j \tag{D.12}$$

From the structure of the disturbances D.8 and from the form of the eigenvalues D.12 we can draw the following conclusions:

- the system is stable in the sense that all the disturbances tend to decay if and only if all the real parts of the eigenvalues $u_j = Re(\lambda_j)$ **are strictly negative**;
- the system becomes unstable if one of the eigenvalues has a **positive real part**;
- if the eigenvalues have positive real part and an imaginary part $Im(\lambda_j) = \omega_j \neq 0$ the system undergoes to a **Hopf bifurcation** and hence to a periodic behavior.

The linear stability analyses we report in Chapter 4 and Part II usually are interested in the determination of the λ_j as a function of a control parameter R (it could be the Rayleigh number, Marangoni number or some other parameter, depending on the specific problem.). Usually, we are interested in the critical value R_{crit} at which the real part of eigenvalues first become positive as R is increased.

Appendix E

Contravariant, covariant vectors and metric tensor

In this Appendix, we will define more precisely concepts which are extremely important when we deal with reference frames which in general are not Cartesian. The relations developed here are of central importance to understanding correctly the convected derivatives described in chapter 4. As already remarked in the previous chapters scalar fields are frame invariant under a change of coordinates but in general tensors with a rank greater than 0 are not, so it is useful to introduce at this point the **contravariant** and **covariant** components of a tensor. However before doing that it is worth defining two set of coordinates x_i and y_i with i=1,2,3. Moreover, the two sets are connected with a continuous and smooth function such that

$$x_i = x(y_1, y_2, y_3) \tag{E.1}$$

$$y_i = y(x_1, x_2, x_3) \tag{E.2}$$

The relations among the two sets of coordinates could be non-trivial but no matter on how complicated they could be, knowing the position of a particle (or fluid element) in one set allows us to locate the particle in the other set. Before generalising the concepts of the contravariant and covariant tensors, we introduce this notion in case of vectors with one index. Being vectors (and more in general tensors) objects which transform under a change of coordinates, these notions (covariance and contravariance) are related to the manner how these objects transform.

Contravariant vectors These vectors have the property that the components in one frame can be obtained from the components in the other frame with the following relation:

$$(V^m)' = \frac{\partial y^m}{\partial x^n} V^n \tag{E.3}$$

In equation E.3 the primed set of coordinates refers to the y reference while the unprimed to the x.

Moreover, the Einstein notation convention [1] has been used.

A typical example of the contravariant vector is the infinitesimal displacements dx and dy which are related by :

$$dy^m = \frac{\partial y^m}{\partial x^n} dx^n \tag{E.4}$$

The equation E.4 relates the infinitesimal changes in x with those in y.

The contravariant term means that such vectors transform in the opposite sense as the basis transforms: e.g. if we shrink the basis vectors by a factor k the vector components will be k time greater in the shrunk basis.

Covariant vectors Differently from the previous family the follows this relation:

$$(V_m)' = \frac{\partial x^n}{\partial y^m} V_n \tag{E.5}$$

An example of such a vector is the gradient of a scalar field ϕ. Using the E.1 and the chain rule we can write:

$$\frac{\partial \phi}{\partial y^m} = \frac{\partial \phi}{\partial x^n} \frac{\partial x^n}{\partial y^m} \tag{E.6}$$

The therm covariant derives from the fact that such vectors change in the same sense of the basis: e.g. if the basis undergoes a shrinkage or dilatation these vectors undergo the same transformation.

The two notions reported above can be generalised to tensors of any rank. Here we

[1] The repeated indices are summed over. However, to be consistent one index must be in the upper position and the other in the lower one.

only report the case of rank equals two:

$$(T^{mn})' = \frac{\partial y^m}{x^p}\frac{\partial y^n}{x^q}T^{pq} \tag{E.7}$$

$$(T_{mn})' = \frac{\partial x^p}{y^m}\frac{\partial x^q}{y^n}T_{pq} \tag{E.8}$$

$$(T^m_n)' = \frac{\partial y^m}{\partial x^p}\frac{\partial x^q}{\partial y^n}T^p_q \tag{E.9}$$

As it can be noted from equations above a tensor could have both contravariant or covariant indices or one contra and one covariant: the higher is the rank, the more possibilities are allowed.
Another way to consider the contra and covariant vectors are to think about the vector space formed by contravariant elements and the covariant vector space as its **dual space**.

E.1 Metric tensor

The metric tensor is a fundamental quantity related to a space described by a set of coordinates, describing the notion of distance in that space. Distance is an invariant of the considered space and must remain the same regardless of the particular set of coordinates considered and, denoting with dr the infinitesimal distance between two elements we can write:

$$\underline{dr} = \underline{g}_m dx^m \tag{E.10}$$

being $\underline{g}_m$ the m-th basis vector (m spans from 1 to 3 in a three-dimensional space). The basis vectors associated to a generic reference frame are in general function of the position, hence $\underline{g}_m = \underline{g}_m(x_1, x_2, 2_3)$. To define the metric tensor, we will square the equation E.10:

$$\underline{dr} \cdot \underline{dr} = \underline{dr}^2 = \left(\underline{g}_m \cdot \underline{g}_n\right) dx^m dx^n = g_{mn} dx^m dx^n \tag{E.11}$$

From the definition given in E.11 the mn-th component of the metric tensor is given by: $g_{mn} = \underline{g}_m \cdot \underline{g}_n$. It could be noticed that we put the two indices downstairs, this is because the metric tensor is covariant. It can be easily seen recalling that dr is invariant

and $dx^m = \frac{\partial x^m}{\partial y^p} dy^p$:

$$
\begin{aligned}
(g_{mn})' dy^m dy^n &= g_{pq} dx^p dx^q \\
(g_{mn})' dy^m dy^n &= g_{pq} \frac{\partial x^p}{\partial y^m} \frac{\partial x^q}{\partial y^n} dy^m dy^n \\
(g_{mn})' &= g_{pq} \frac{\partial x^p}{\partial y^m} \frac{\partial x^q}{\partial y^n}
\end{aligned} \tag{E.12}
$$

We discovered that the metric tensor is effectively a tensor; in a sense, it transforms as a covariant quantity. Moreover, it has some remarkable properties: it is symmetric, due to the symmetry of the scalar product in E.11 and it has no 0 eigenvalues since the distance is defined to be always positive ($dr \geq 0$). Having these two properties ensures that it always has an inverse such that:

$$g_{mp} g^{pn} = \delta^n_m \tag{E.13}$$

and

$$g^{mn} = \underline{g}^m \cdot \underline{g}^n \tag{E.14}$$

$$\tag{E.15}$$

he symbol δ^n_m is the Kronecker delta and it is 1 when m=n and 0 else. The matrix g^{mn} is the inverse of the metric tensor, and it is formed by the dual vectors (constituting a basis of the dual space) of the basis $\underline{g}^m$. It is an easier way to visualise these two sets of basis vectors:being m, n, p three indices the $\underline{g}_m$ are tangent to the m-th constant coordinate lines and their dual vectors e.g $\underline{g}^m$ is orthogonal to the plane containing $\underline{g}^n$and $\underline{g}^p$.

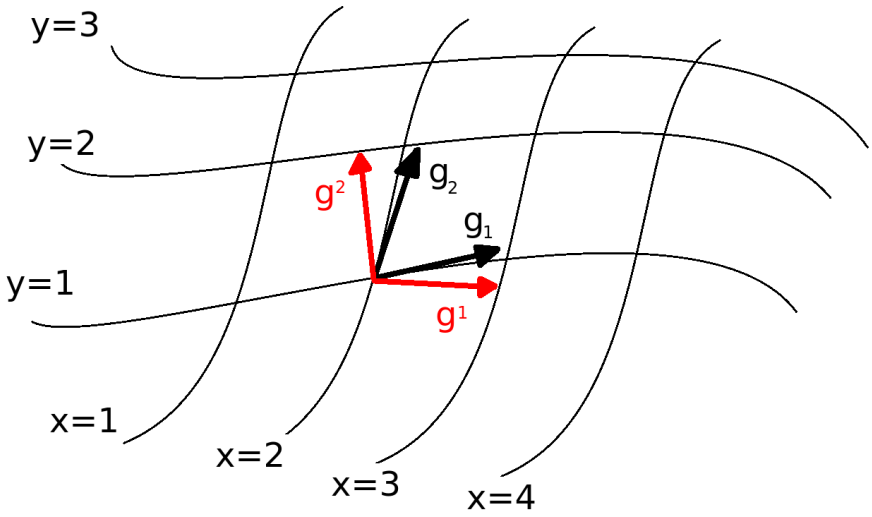

Figure E.1: Curvilinear frame basis vectors

In Figure E.1 a two-dimensional sketch of basis vectors and their duals is represented, moreover it could be noted that:

$$\underline{g}_i \cdot \underline{g}^j = \delta_i^j \tag{E.16}$$

and more in general the following relation holds

$$\underline{g}^i = \frac{\underline{g}^j \times \underline{g}^k}{\underline{g}_i \cdot \left[\underline{g}^j \times \underline{g}^k\right]} \tag{E.17}$$

The notions just defined above allow us the illustrate the concept of **raising and lowering indices** which relates the contravariant and covariant components of a vector $\underline{V}$:

$$\underline{V} = \underline{g}_i V^i = \underline{g}^j V_j$$

Performing the scalar product on both sides by $\underline{g}^j$:

$$\underline{g}^j \cdot \underline{g}_i V^i = \underline{g}^j \cdot \underline{g}^i V_j =$$

$$V^j = g^{ij} V_i \tag{E.18}$$

E.2 Covariant derivative

All the notions defined above are necessary to introduce a more general concept of the derivative. Such generalisation indeed is mandatory because a simple differentiation of the components of a tensor leads to objects which are not in general tensors in the

sense they do not transform as discussed in the previous section. In general curvilinear coordinate systems as that of figure E.1 the component of a tensor could change along a coordinate due to two different effects: one related to the effective change of such component along a coordinate and the other depending on the variation of the orientation of the basis vectors. As an example, we may think about a constant vector field, which in Cartesian coordinates would have all its ordinary derivatives respect to the coordinates equal to 0 (indeed in Cartesian frames the ordinary differentiation leads to tensors) but that it is not true in general coordinate systems. On the other hand, we know that a constant vector in Cartesian coordinates has a null gradient and, owing to its tensorial nature, it must be null in every coordinate frame. So this section aims to come to a formulation which preserves such frame independence, and it is called **covariant derivative**.

In order to introduce these concepts, let us start thinking about a vector expressed in the general coordinate system with basis vectors $\underline{g}^j$:

$$\underline{V} = V_j \underline{g}^j \tag{E.19}$$

Now differentiating the E.19 respect to the coordinate x^i we obtain:

$$\frac{\partial \underline{V}}{\partial x^i} = \frac{\partial V_j}{\partial x^i}\underline{g}^j + V_j \frac{\partial \underline{g}^j}{\partial x^i} \tag{E.20}$$

From the equation E.20 becomes clear that the differentiation has two different terms: one related to the derivative of the components (ordinary derivatives) and one which takes into account the derivative of the basis vectors and it is proportional to the vector component V^j. In the Cartesian coordinates, the second terms vanishes because the basis vector does not change respect to the coordinates, leaving the ordinary derivative as the only term. The equation E.20 may be rewritten in terms of components:

$$\frac{\partial V_m}{\partial x^i} = \frac{\partial V_m}{\partial x^i} - \Gamma^t_{im} V_t \tag{E.21}$$

The above notion can be generalised to tensors of any rank, here for simplicity only the formula for the second rank tensor is reported:

$$\frac{\partial T_{mn}}{\partial x^i} = \frac{\partial T_{mn}}{\partial x^i} - \Gamma^t_{im} T_{tn} - \Gamma^t_{in} T_{mt} \tag{E.22}$$

The symbols Γ are known as **Christoffel symbols** and depends on the particular metric of the reference system. As we said in the previous section knowing the metric tensor is important because it allows us to access all the quantities related to any coordinate system, included the Christoffel symbols. In order to define them, it is worth noticing that the metric tensor can be differentiated using the equation E.22, moreover this equation should be 0 because if we performed it in a Cartesian reference, it would be 0, and it must be frame invariant as well:

$$\frac{\partial g_{mn}}{\partial x^i} - \Gamma^t_{im} g_{tn} - \Gamma^t_{in} g_{mt} = 0 \tag{E.23}$$

In the present thesis moreover, it is supposed that the Christoffel symbols have symmetry: $\Gamma^t_{im} = \Gamma^t_{mi}$, however, this is not always true, but for the present purposes we can rely on this fact. Another fact to observe is the symmetry of $\underline{\underline{g}}$. With the two hypotheses just explained these relations holds:

$$\frac{\partial g_{mn}}{\partial x^i} - \Gamma^t_{im} g_{tn} - \Gamma^t_{in} g_{mt} = 0 \tag{E.24}$$

$$\frac{\partial g_{in}}{\partial x^m} - \Gamma^t_{im} g_{tn} - \Gamma^t_{mn} g_{it} = 0 \tag{E.25}$$

$$\frac{\partial g_{im}}{\partial x^n} - \Gamma^t_{in} g_{tm} - \Gamma^t_{mn} g_{it} = 0 \tag{E.26}$$

With the equations written above, it is possible to write an expression for each of the Christoffel symbols, summing and subtracting them. As an example, it is possible to sum E.25 and E.26 and subtract E.24 obtaining:

$$2\Gamma^t_{mn} g_{it} = \frac{\partial g_{im}}{\partial x^n} + \frac{\partial g_{in}}{\partial x^m} - \frac{\partial g_{mn}}{\partial x^i} \tag{E.27}$$

Using the metric tensor with upper indices:

$$\Gamma^t_{mn} = \frac{1}{2} g^{it} \left[\frac{\partial g_{im}}{\partial x^n} + \frac{\partial g_{in}}{\partial x^m} - \frac{\partial g_{mn}}{\partial x^i} \right] \tag{E.28}$$

The symbols just defined above are the so-called **second kind Christoffel symbols**, however, there are a bunch of them: there are the **first kind** ones which are related to those described above just by lowering the upper index:

$$\Gamma_{imn} = g_{it} \Gamma^t_{mn} = \frac{1}{2} \left[\frac{\partial g_{im}}{\partial x^n} + \frac{\partial g_{in}}{\partial x^m} - \frac{\partial g_{mn}}{\partial x^i} \right] \tag{E.29}$$

Appendix F

Bifurcations: a brief review

This Appendix expands the description given in Chapter 6 about different kinds of bifurcations to which dynamical systems may undergo. As already stated, they consist in a change of the underlining dynamics after a certain threshold has been overtaken. In Chapter 6, we have briefly described the difference among a stationary and a Hopf instability. The landscape, however, is much more variegated, and this Appendix aims to get some more in-depth insight into this topic. In the next paragraphs, the main bifurcations are briefly described[1].

F.1 Saddle-node Bifurcation

The saddle-node is a local bifurcation[2] in which two fixed points or equilibria one stable and the other unstable collides and annihilate each other. In order to have a visual clue of such bifurcation it is worth considering a simple non-linear ODE (probably one of the simplest in which this phenomenon is observable):

$$\dot{x} = x^2 + p \tag{F.1}$$

The equation F.1 is a first-order ordinary differential equation, which has a line as phase space. Having only one degree of freedom it is worth plotting $\dot{x}$ as function of x, according to F.1.

[1] The examples in the following sections are taken from[257]

[2] local bifurcations occur when there is a change in the stability of an equilibrium point. There are also global bifurcations in which the fixed points collide with sets of higher dimensionality such as limit cycles.

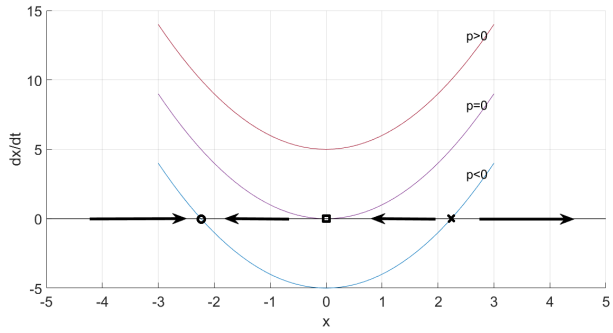

(a) Saddle node bifurcation. Circle: stable equilibrium, X: unstable equilibrium, Square: bifurcation point

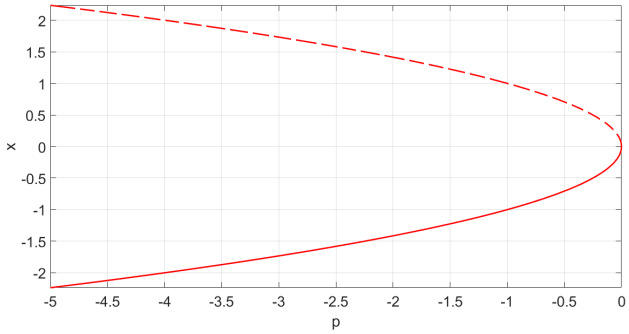

(b) Bifurcation diagram: solid line: stable equilibrium, dashed line: unstable equilibrium

Figure F.1

In Figure F.1a it is possible to see that for $p < 0$ the F.1 shows two distinct equilibria: one stable (circle) an one unstable (cross). At p=0, the two fixed points collide, disappearing at $p > 0$. The arrows in Figure F.1a indicate the direction in which x flows, depending on the sign of the derivative $\dot{x}$. The bifurcation diagram in Figure F.1b illustrates the two fixed points at$p < 0$, which no longer exist when p becomes positive.

F.2 Transcritical Bifurcation

Differently from the saddle-node bifurcation, this one is not characterised by a disappearance of some fixed point but by an exchange of stability among two equilibria. As done in the previous case, it is better to show a simple example. In this case, a basic dynamical system undergoing a transcritical bifurcation is given by:

$$\dot{x} = px - x^2 \tag{F.2}$$

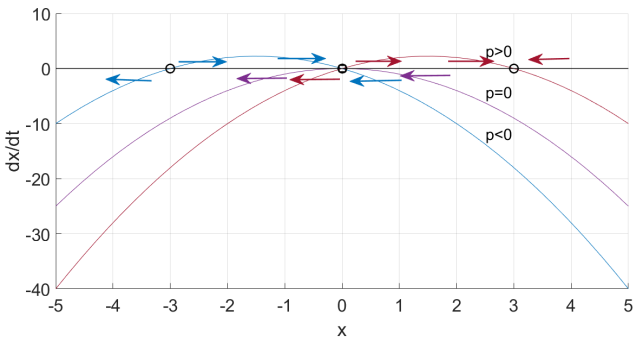

(a) Transcritical bifurcation.

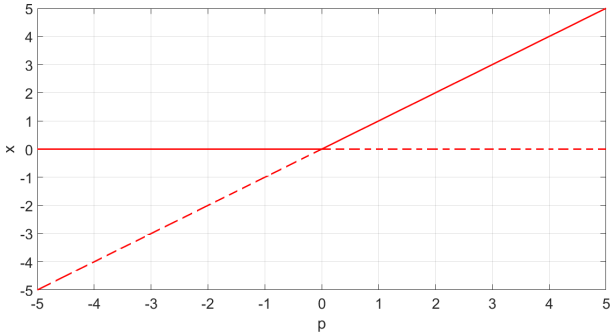

(b) Bifurcation diagram: solid line: stable equilibrium, dashed line: unstable equilibrium

Figure F.2

In Figure F.2a it is possible to follow what happens at the fixed point located at $x = 0$ while p is increased: when $p < 0$ it is a stable equilibrium while it switches to an unstable one when p becomes positive.

F.3 Supercritical Pitchfork Bifurcation

This kind of bifurcation involves three fixed points: below the critical value, only one stable equilibrium exists, but after the threshold is overtaken this point loses its stability, and two other stable equilibria appear. The pitchfork bifurcations often occur in systems with spatial symmetry where the solutions appear in symmetric couples. As an example of particular interest of this thesis is the first bifurcation of the Rayleigh-Bénard convection in infinite layers and rectangular enclosures, where the flow is at rest below a certain Rayleigh number, but when the critical threshold is overtaken clock-wise, or anti-clockwise rolls could emerge. Also, in this case, this bifurcation can be shown through a straightforward example:

$$\dot{x} = px - x^3 \tag{F.3}$$

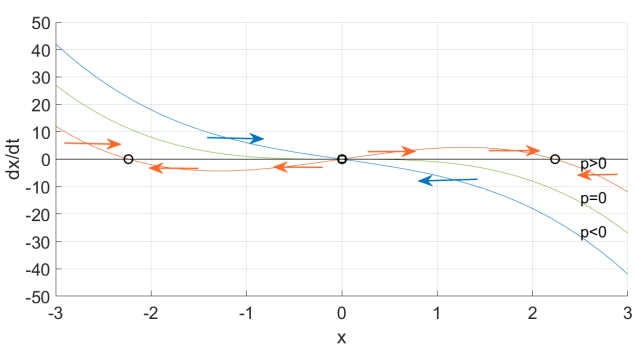

(a) Supercritical Pitchfork Bifurcation

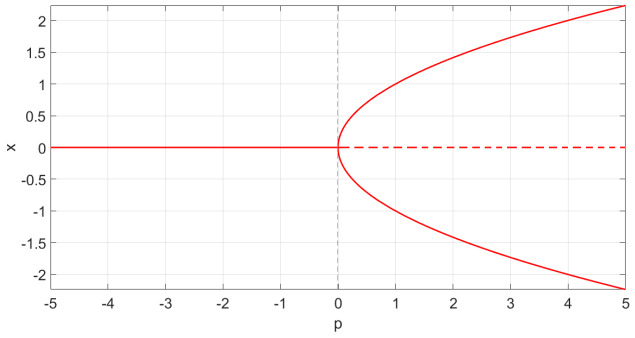

(b) Bifurcation diagram: solid line: stable equilibrium, dashed line: unstable equilibrium

Figure F.3

In Figures F.3a and F.3b it becomes clear how the fixed point at $x = 0$ is stable when $p < 0$ and becomes unstable if $p > 0$, at the same time two symmetric stable equilibria arise.

F.4 Subcritical Pitchfork bifurcation

Differently from the saddle-node and transcritical bifurcations the pitchfork one comes in two versions: supercritical, discussed above and subcritical. To introduce the latter, we may think about F.3, noticing that the cubic term has the opposite sign respect to the linear one and acts as a restoring. So if we consider the following equation:

$$\dot{x} = px + x^3 \tag{F.4}$$

In the equation F.4 there is no longer the restoring term, having both the terms in the RHS the same sign. Due to this fact, when p becomes positive, there are no longer stable fixed points, and hence the trajectories tend to go to infinity. This fact is depicted in Figure F.4.

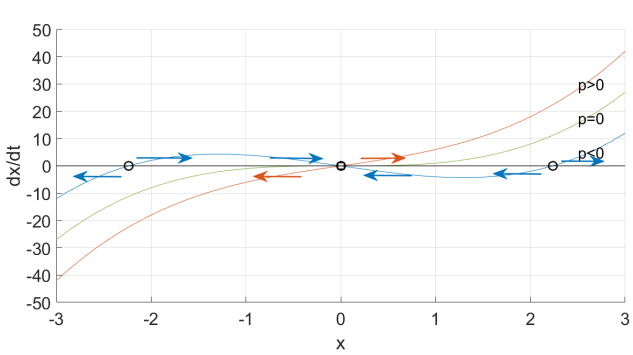

(a) Subcritical Pitchfork Bifurcation

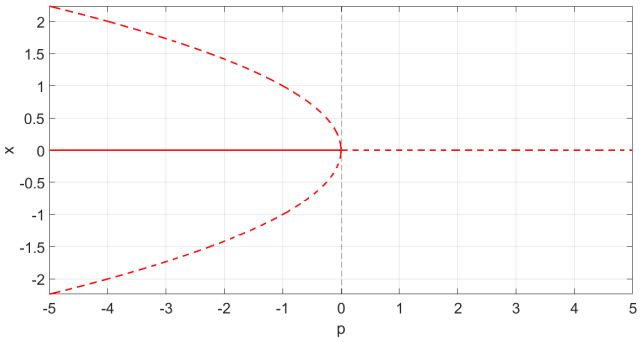

(b) Bifurcation diagram: solid line: stable equilibrium, dashed line: unstable equilibrium

Figure F.4

F.5 Supercritical Hopf Bifurcation

Up to now we have considered only fixed points or in other words, systems having as a final solution a steady state. To distinguish this bifurcation from the previous one it is worth relying on the linear stability analysis of Appendix D. Indeed, linearising the examples above around their equilibrium points, brings to real eigenvalues, positive for unstable fixed points and negative for the stable ones. Moreover, having the example discussed above only one degree of freedom, the Jacobian associated is a 1x1 matrix with strictly real eigenvalues. However linearising a system which has two or more degrees of freedom does not guarantee that all the eigenvalues are pure real numbers, one or more of them could also have an imaginary part. This fact is the leading property of Hopf bifurcations. Indeed a system displaying them is subjected to the appearance of an imaginary part in the eigenvalues of an equilibrium point which at the same time becomes unstable. In other words, this produces a periodic motion once the fixed points become unstable. In the phase space this could be viewed as the creation of a limit cycle as shown in Figure F.5

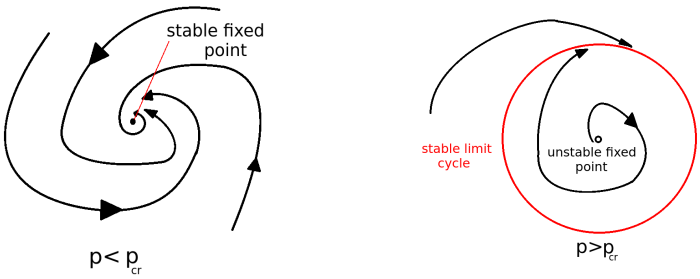

(a) $p > p_{cr}$ (b) $p > p_{cr}$

Figure F.5: Supercritical Hopf Bifurcation

F.6 Subcritical Hopf Bifurcation

As occurred for the pitchfork bifurcation also in this case a subcritical counterpart exists. It differentiates from its supercritical companion for the presence of an unstable limit cycle when the control parameter is smaller than the critical value, as shown in Figure F.6.

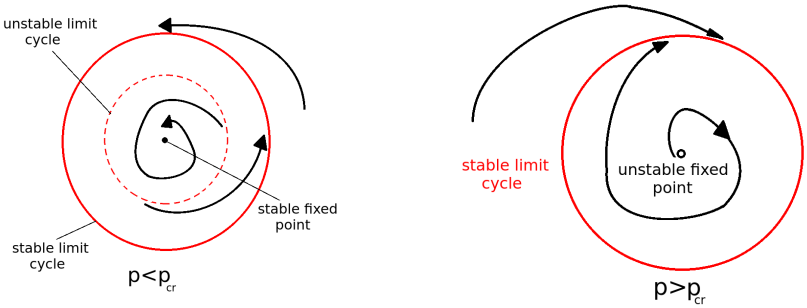

(a) $p > p_{cr}$ (b) $p > p_{cr}$

Figure F.6: Subcritical Hopf Bifurcation

F.7 Other bifurcations

The bifurcations discussed above are the main ones which occur in dynamical systems. However, there are a bunch of other phenomena which may occur when two or more attractors interact. The cases considered up to now are local bifurcations, in the sense that they involve a portion of the phase space in the nearby of an equilibrium point. On the other hand, there are other mechanisms, which are **global** because they affect a larger portion of the phase space.

In this section, we discuss more in detail these global bifurcations. The first we consider

is the **Saddle-node Bifurcation of Cycles** and, as the name suggests, it is similar to that occurring among two fixed points, which are substituted by limit cycles. Indeed, in this case, there are two limit cycles, one stable and one unstable which collide and annihilate each other.

There also could be cases where there is an interaction between fixed points and closed orbits such as the **Infinite-period Bifurcation**. In this kind of mechanism initially, there is only a limit cycle, but when a threshold is overtaken, creation of a fixed point on it occurs. The fixed point tends to attract all the trajectories which fall on the closed orbit, resulting in an infinite period. If the control parameter increases further the point on the cycle splits itself in one stable node and one saddle [3].

Another bifurcation which deserves a brief explanation is the **Homoclinic Bifurcation**, according to which a limit cycle moves closer and closer to a saddle point until they touch each other. As shown in figure F.7 a peculiar feature of this bifurcation is that a trajectory starting from one side of the unstable manifold of the saddle could end up to the other side of the same manifold.

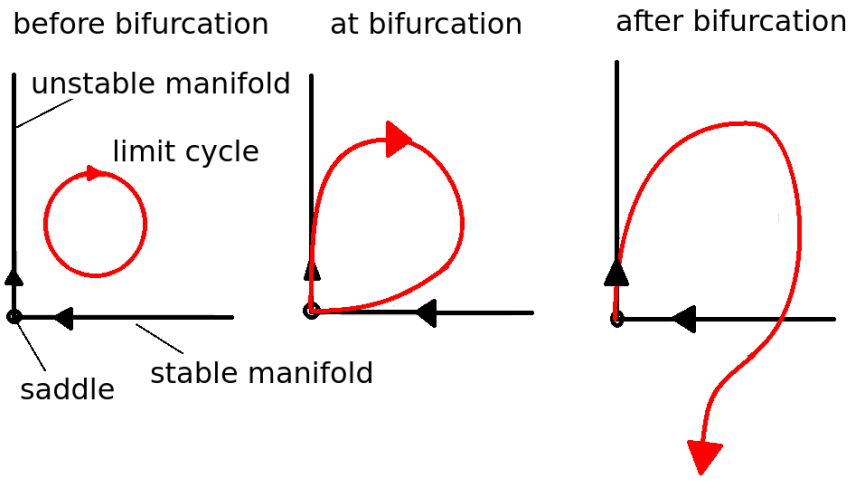

Figure F.7: Homoclinic bifurcation

[3] If the phase space has more than one dimension there are points which are attractive respect to all the directions: they are called nodes. However, there could also be points which are attractive in same directions and repulsive in others: they are the so-called saddle points.

Bibliography

[1] G. Amberg and J. Shiomi, "Thermocapillary flow and phase change in some widespread materials processes," *FDMP: Fluid Dynamics & Materials Processing*, vol. 1, no. 1, pp. 81–95, 2005.

[2] R. Prud'homme and M. El Ganaoui, "Solid/liquid phase change: recent studies and models," *Fluid Dynamics &Materials Processing*, vol. 3, no. 2, pp. 161–172, 2007.

[3] A. Hirata, "A unified theory for interphase transport phenomena with interfacial velocity and surface tension gradients: applications to single crystal growth and microgravity sciences," *Fluid Dyn. Mater. Process*, vol. 3, no. 3, pp. 203–230, 2007.

[4] M. Lappa, "Thermal convection: Patterns, evolution and stability." John Wiley e Sons, 2009.

[5] R. Delves, "Theory of the stability of a solid-liquid interface during growth from stirred melts. ii," *Journal of Crystal Growth*, vol. 8, no. 1, pp. 13–25, 1971.

[6] T. Schulze and S. H. Davis, "The influence of oscillatory and steady shears on interfacial stability during directional solidification," *Journal of crystal growth*, vol. 143, no. 3-4, pp. 317–333, 1994.

[7] S. H. Davis and T. Schulze, "Effects of flow on morphological stability during directional solidification," *Metallurgical and Materials Transactions A*, vol. 27, no. 3, p. 583, 1996.

[8] R. S. Dietz, "Continent and ocean basin evolution by spreading of the sea floor," *Nature*, vol. 190, no. 4779, pp. 854–857, 1961.

[9] W. J. Morgan, "Convection plumes in the lower mantle," *Nature*, vol. 230, no. 5288, p. 42, 1971.

[10] W. J. Morgan, "Deep mantle convection plumes and plate motions," *AAPG bulletin*, vol. 56, no. 2, pp. 203–213, 1972.

[11] G. Hadley, "Concerning the cause of the general trade-winds." Transactions of the Royal Society of London, 1735.

[12] D. D. Gray and A. Giorgini, "The validity of the boussinesq approximation for liquids and gases." International Journal of Heat and Mass Transfer, 1976.

[13] L. G. Napolitano, "Thermodynamics and dynamics of surfaces phases." Acta Astronautica, 1979.

[14] A. Morozov and S. E. Spagnolie, *Introduction to Complex Fluids*, pp. 3–52. New York, NY: Springer New York, 2015.

[15] R. Bird, R. Armstrong, and O. Hassager, "Dynamics of polymeric liquids. vol. 1, 2nd ed. : Fluid mechanics," 1 1987.

[16] P. Grassberger, "Generalized dimensions of strange attractors," *Physics Letters A*, vol. 97, no. 6, pp. 227–230, 1983.

[17] M. Chilcott and J. M. Rallison, "Creeping flow of dilute polymer solutions past cylinders and spheres," *Journal of Non-Newtonian Fluid Mechanics*, vol. 29, pp. 381–432, 1988.

[18] A. Peterlin, "Hydrodynamics of macromolecules in a velocity field with longitudinal gradient," *Journal of Polymer Science Part B: Polymer Letters*, vol. 4, no. 4, pp. 287–291, 1966.

[19] Gollub and Benson, "Many routes to turbulent convection." Journal of Fluid Mechanics, 1980.

[20] F. H. Busse, "Non-linear properties of thermal convection." Reports on Progress in Physics, 1978.

[21] R. M. Clever and F. H. Busse, "Transition to time-dependent convection." Journal of Fluid Mechanics, 1974.

[22] J. R. Carruthers, "Crystal growth in a low gravity environment." Journal of Crystal Growth, 1977.

[23] D. Thevenard, A. Rouzand, J. Comera, and J. J. Favier, "Crystal growth in a low gravity environment." Journal of Crystal Growth, 1991.

[24] D. T. J. Hurle, "Hydrodynamics, convection and crystal growth." Journal of Crystal Growth, 1972.

[25] Rayleigh, "On the convective currents in a horizontal layer of fluid when the higher temperature is on the under side." Phil. Mag, 1916.

[26] A. Pellew and R. Southwell, "On mantained convective motion in a fluid heated from below." Proc. R. Soc. London, 1940.

[27] W. V. R. Malkus and G. Veronis, "Finite ampltude cellular convection." J. Fluid Mech., 1958.

[28] R. M. Clever and F. H. Busse, "Hexagonal convection cells under conditions of vertical symmetry." Phys. Rev. E, 1996.

[29] F. H. Busse and R. M. Clever, "Asymeetric squares as an attracting set in rayleigh-bénard." Phys. Rev. Letters, 1998.

[30] F. H. Busse and R. M. Clever, "Instabilities of convection rolls in a fluid of moderate prandtl number." J. Fluid Mech., 1979.

[31] S. H. Davis, "Convection in a box: linear theory." J. Fluid Mech., 1967.

[32] M. Cross, P. G. Daniels, P. C. Hohenberg, and E. D. Siggia, "Effects of distant sidewalls on wave-number selection in rayleigh-bénard convection." Phys. Rev. Letters, 1980.

[33] J. E. Hart, "Stability of thin non-rotating hadley circulations," *Journal of the Atmospheric Sciences*, vol. 29, no. 4, pp. 687–697, 1972.

[34] J. Hart, "Low prandtl number convection between differentially heated end walls," *International Journal of Heat and Mass Transfer*, vol. 26, no. 7, pp. 1069 – 1074, 1983.

[35] A. E. Gill, "A theory of thermal oscillations in liquid metals," *Journal of Fluid Mechanics*, vol. 64, no. 3, pp. 577 – 588, 1974.

[36] H. P. Kuo and S. A. Korpela, "Stability and finite amplitude natural convection in a shallow cavity with insulated top and bottom and heated from a side," *The Physics of Fluids*, vol. 31, no. 1, pp. 33 – 42, 1988.

[37] B. Roux, H. Ben Hadid, and P. Laure, "Hydrodynamical regimes in metallic melts subject to a horizontal temperature gradient," *Eur. J. Mech., B/Fluids*, vol. 8, no. 5, pp. 375 – 396, 1989.

[38] G. Z. Gershuni, P. Laure, M. Myznikov, B. Roux, and E. M. Zhukhovitsky, "On the stability of plane-parallel advective flows in long horizontal layers," *Microgravity Q.*, vol. 2, no. 3, pp. 141 – 151, 1992.

[39] M. J. Block, "Surface tension as the cause of bénard cells and surface deformation in a liquid film," *Nature*, vol. 178, no. 4534, pp. 650 – 651, 1956.

[40] J. R. A. Pearson, "On convection cells induced by surface tension," *Journal of Fluid Mechanics*, vol. 4, no. 5, pp. 489 – 500, 1958.

[41] S. Nakamura, T. Hibiya, N. Imaishi, and S. ichi Yoda, "Observation of marangoni convection in half-zone silicon melt," *Advances in Space Research*, vol. 24, no. 10, pp. 1417 – 1421, 1999.

[42] D. Schwabe and A. Scharmann, "Some evidence for the existence and magnitude of a critical marangoni number for the onset of oscillatory flow in crystal growth melts," *Journal of Crystal Growth*, vol. 46, no. 1, pp. 125 – 131, 1979.

[43] M. Bestehorn, "Square patterns in bénard-marangoni convection," *Phys. Rev. Lett.*, vol. 76, no. 1, pp. 46 – 49, 1996.

[44] K. Eckert, M. Bestehorn, and A. Thess, "Square cells in surface-tension-driven bénard convection: experiment and theory," *Journal of Fluid Mechanics*, vol. 356, pp. 155 – 197, 1998.

[45] A. Thess and M. Bestehorn, "Planform selection in bénard-marangoni convection: l hexagons versus g hexagons," *Phys. Rev. E*, vol. 52, pp. 6358–6367, 1995.

[46] M. K. Smith and S. H. Davis, "Instabilities of dynamic thermocapillary liquid layers. part 1. convective instabilities," *Journal of Fluid Mechanics*, vol. 132, pp. 119 – 144, 1983.

[47] M. K. Smith, "Instability mechanisms in dynamic thermocapillary liquid layers," *The Physics of Fluids*, vol. 29, no. 10, pp. 3182 – 3186, 1986.

[48] J.-F. Mercier and C. Normand, "Influence of the prandtl number on the location of recirculation eddies in thermocapillary flows," *International Journal of Heat and Mass Transfer*, vol. 45, no. 4, pp. 793 – 801, 2002.

[49] R. Khayat, "Low-dimensional approach to nonlinear overstability of purely elastic taylor-vortex flow," *Phys. Rev. Lett*, vol. 78, no. 26, pp. 4918–4921, 1997.

[50] R. E. Khayat, "Chaos and overstability in the thermal convection of viscoelastic fluids," *Journal of non-newtonian fluid mechanics*, vol. 53, pp. 227–255, 1994.

[51] R. E. Khayat, "Non-linear overstability in the thermal convection of viscoelastic fluids," *Journal of non-newtonian fluid mechanics*, vol. 58, no. 2-3, pp. 331–356, 1995.

[52] P. Parmentier, G. Lebon, and V. Regnier, "Weakly nonlinear analysis of bénard–marangoni instability in viscoelastic fluids," *Journal of non-newtonian fluid mechanics*, vol. 89, no. 1-2, pp. 63–95, 2000.

[53] F. Moukalled, L. Mangani, M. Darwish, *et al.*, "The finite volume method in computational fluid dynamics," *An advanced introduction with OpenFoam® and Matlab®. Nueva*

York: Springer. Recuperado de http://www. gidropraktikum. narod. ru/Moukalled-et-al-FVM-OpenFOAM-Matlab. pdf, 2016.

[54] M. Ciofalo, G. Comini, G. Croce, E. Nobile, and C. Nonino, "Fondamenti di termofluidodinamica computazionale," *SGE editoriali, Padova*, 2004.

[55] C. Rhie and W. L. Chow, "Numerical study of the turbulent flow past an airfoil with trailing edge separation," *AIAA journal*, vol. 21, no. 11, pp. 1525–1532, 1983.

[56] S. V. Patankar, "Numerical heat transfer and fluid flow, hemisphere publ," *Corp., New York*, vol. 58, 1980.

[57] S. V. Patankar and D. B. Spalding, "A calculation procedure for heat, mass and momentum transfer in three-dimensional parabolic flows," in *Numerical Prediction of Flow, Heat Transfer, Turbulence and Combustion*, pp. 54–73, Elsevier, 1983.

[58] R. I. Issa, "Solution of the implicitly discretised fluid flow equations by operator-splitting," *Journal of computational physics*, vol. 62, no. 1, pp. 40–65, 1986.

[59] J. Van Doormaal and G. Raithby, "Enhancements of the simple method for predicting incompressible fluid flows," *Numerical heat transfer*, vol. 7, no. 2, pp. 147–163, 1984.

[60] J. Van Doormaal and G. Raithby, "An evaluation of the segregated approach for predicting incompressible fluid flows," *ASME paper*, no. 85-HT, p. 9, 1985.

[61] S. Acharya and F. Moukalled, "Improvements to incompressible flow calculation on a nonstaggered curvilinear grid," *Numerical Heat Transfer, Part B Fundamentals*, vol. 15, no. 2, pp. 131–152, 1989.

[62] D. Spalding, "Mathematical modelling of fluid-mechanics, heat-transfer and chemical-reaction processes," *A Lecture Course, Imperial College CFDU Report*, 1980.

[63] E. N. Lorenz, "Deterministic nonperiodic flow," *Journal of the atmospheric sciences*, vol. 20, no. 2, pp. 130–141, 1963.

[64] A. Wolf, J. B. Swift, H. L. Swinney, and J. A. Vastano, "Determining lyapunov exponents from a time series," *Physica D: Nonlinear Phenomena*, vol. 16, no. 3, pp. 285–317, 1985.

[65] F. Takens, "Detecting strange attractors in turbulence," in *Dynamical systems and turbulence, Warwick 1980*, pp. 366–381, Springer, 1981.

[66] J. L. Kaplan and J. A. Yorke, "Chaotic behavior of multidimensional difference equations," in *Functional differential equations and approximation of fixed points*, pp. 204–227, Springer, 1979.

[67] J. Balatoni and A. Renyi, "Remarks on entropy," *Publ. Math. Inst. Hung. Acad. Sci*, vol. 1, pp. 9–40, 1956.

[68] P. Grassberger and I. Procaccia, "Characterization of strange attractors," *Physical review letters*, vol. 50, no. 5, p. 346, 1983.

[69] E. J. Kostelich and H. L. Swinney, "Practical considerations in estimating dimension from time series data," *Physica Scripta*, vol. 40, no. 3, p. 436, 1989.

[70] J.-P. Eckmann and D. Ruelle, "Fundamental limitations for estimating dimensions and lyapunov exponents in dynamical systems," *Physica D: Nonlinear Phenomena*, vol. 56, no. 2-3, pp. 185–187, 1992.

[71] L. D. Landau, "On the problem of turbulence," in *Dokl. Akad. Nauk USSR*, vol. 44, p. 311, 1944.

[72] S. Newhouse, D. Ruelle, and F. Takens, "Occurrence of strange axioma attractors near quasi periodic flows on t^m ,$m \geq 3$," *Communications in Mathematical Physics*, vol. 64, no. 1, pp. 35–40, 1978.

[73] J. H. Curry and J. A. Yorke, "A transition from hopf bifurcation to chaos: Computer experiments with maps on r 2," in *The structure of attractors in dynamical systems*, pp. 48–66, Springer, 1978.

[74] S. Fauve and A. Libchaber, "Rayleigh-bénard experiment in a low prandtl number fluid, mercury," in *Chaos and Order in Nature*, pp. 25–35, Springer, 1981.

[75] M. J. Feigenbaum, "The onset spectrum of turbulence," *Physics Letters A*, vol. 74, no. 6, pp. 375–378, 1979.

[76] M. J. Feigenbaum, "The universal metric properties of nonlinear transformations," *Journal of Statistical Physics*, vol. 21, no. 6, pp. 669–706, 1979.

[77] Y. Pomeau and P. Manneville, "Intermittent transition to turbulence in dissipative dynamical systems," *Communications in Mathematical Physics*, vol. 74, no. 2, pp. 189–197, 1980.

[78] C. Grebogi, E. Ott, and J. A. Yorke, "Crises, sudden changes in chaotic attractors, and transient chaos," *Physica D: Nonlinear Phenomena*, vol. 7, no. 1-3, pp. 181–200, 1983.

[79] Y. Okano, M. Itoh, and A. Hirata, "Natural and marangoni convections in a two-dimensional rectangular open boat," *Journal of chemical engineering of Japan*, vol. 22, no. 3, pp. 275–281, 1989.

[80] R. Delgado-Buscalioni and E. C. Del Arco, "Flow and heat transfer regimes in inclined differentially heated cavities," *International Journal of heat and mass transfer*, vol. 44, no. 10, pp. 1947–1962, 2001.

[81] S. Kaddeche, D. Henry, and H. BenHadid, "Magnetic stabilization of the buoyant convection between infinite horizontal walls with a horizontal temperature gradient," *Journal of Fluid Mechanics*, vol. 480, pp. 185–216, 2003.

[82] Y. Li, L. Peng, S. Wu, N. Imaishi, and D. Zeng, "Thermocapillary-buoyancy flow of silicon melt in a shallow annular pool," *Crystal Research and Technology: Journal of Experimental and Industrial Crystallography*, vol. 39, no. 12, pp. 1055–1062, 2004.

[83] T. Jaber, M. Saghir, and F. Source, "The effect of rotating magnetic fields on the growth of sige using the traveling solvent method," *Fluid Dyn. Mater. Process*, vol. 2, no. 3, pp. 175–190, 2006.

[84] A. Ludwig, M. Gruber-Pretzler, M. Wu, A. Kuhn, and J. Riedle, "About the formation of macrosegregations during continuous casting of sn-bronze," *Fluid Dyn. Mater. Process*, vol. 1, no. 4, pp. 285–300, 2005.

[85] E. Abhilash, M. Joseph, and P. Krishna, "Prediction of dendritic parameters and macro hardness variation in permanent mould casting of al-12% si alloys using artificial neural networks," *Fluid Dynamics & Materials Processing*, vol. 2, pp. 211–220, 2006.

[86] M. Lappa, "Thermal convection and related instabilities in models of crystal growth from the melt on earth and in microgravity: Past history and current status," *Crystal Research and Technology: Journal of Experimental and Industrial Crystallography*, vol. 40, no. 6, pp. 531–549, 2005.

[87] F. Dupret and N. Van den Bogaert, "Modelling bridgman and czochralski growth," *Handbook of Crystal Growth*, vol. 2, no. Chap. 15, pp. 875–1010, 1994.

[88] E. Monberg, "Bridgman and related growth techniques," *Handbook of Crystal Growth*, vol. 2, no. Part A, pp. 51–97, 1994.

[89] A. Zrodnikov, A. Efanov, Y. I. Orlov, P. Martynov, V. Troyanov, and A. Rusanov, "Heavy liquid metal coolant–lead–bismuth and lead–technology," *Atomic Energy*, vol. 97, no. 2, pp. 534–537, 2004.

[90] D. Gorse-Pomonti and V. Russier, "Liquid metals for nuclear applications," *Journal of Non-Crystalline Solids*, vol. 353, no. 32-40, pp. 3600–3614, 2007.

[91] M. Luo and J. Liu, "Experimental investigation of liquid metal alloy based mini-channel heat exchanger for high power electronic devices," *Frontiers in Energy*, vol. 7, no. 4, pp. 479–486, 2013.

[92] G. Ostroumov, "Free convection under the conditions of an internal problem (moscow, gostekhizdat)," 1952.

[93] R. Birikh, "Thermocapillary convection in a horizontal layer of liquid," *Journal of Applied Mechanics and Technical Physics*, vol. 7, no. 3, pp. 43–44, 1966.

[94] M. Lappa, "Exact solutions for thermal problems-buoyancy, marangoni, vibrational and magnetic-field-controlled flows," *Review of Applied Physics*, vol. 1, no. 1, pp. 1–14, 2012.

[95] G. Adomian, "A review of the decomposition method and some recent results for nonlinear equations," *Mathematical and Computer Modelling*, vol. 13, no. 7, pp. 17–43, 1990.

[96] Y. Cherruault and G. Adomian, "Decomposition methods: a new proof of convergence," *Mathematical and Computer Modelling*, vol. 18, no. 12, pp. 103–106, 1993.

[97] E. Babolian, A. Vahidi, and G. A. Cordshooli, "Solving differential equations by decomposition method," *Applied mathematics and computation*, vol. 167, no. 2, pp. 1150–1155, 2005.

[98] O. Makinde, "Steady flow in a linearly diverging asymmetrical channel," *Computer Assisted Mechanics and Engineering Sciences*, vol. 4, pp. 157–166, 1997.

[99] P. Mhone and O. Makinde, "Unsteady mhd flow with heat transfer in a diverging channel," *Romanian Journal of Physics*, vol. 51, no. 9/10, p. 967, 2006.

[100] M. Asadullah, U. Khan, R. Manzoor, N. Ahmed, and S. T. Mohyud-Din, "Mhd flow of a jeffery fluid in converging and diverging channels," *Int. J. Mod. Math. Sci*, vol. 6, no. 2, pp. 92–106, 2013.

[101] M. Lappa and H. Ferialdi, "On the general properties of steady gravitational thermal flows of liquid metals in variable cross-section containers," *Review of Applied Physics*, vol. 5, no. 1, pp. 1–10, 2017.

[102] A. Y. Gelfgat, P. Bar-Yoseph, and A. Yarin, "Stability of multiple steady states of convection in laterally heated cavities," *Journal of Fluid Mechanics*, vol. 388, pp. 315–334, 1999.

[103] W. Tollmien, "General instability criterion of laminar velocity distributions," 1936.

[104] C. Lin, "On the stability of two-dimensional parallel flows," *Proc. Nat. Acad. Sci. USA*, vol. 30, no. 10, pp. 316–324, 1944.

[105] M. N. Rosenbluth and A. Simon, "Necessary and sufficient condition for the stability of plane parallel inviscid flow," *The Physics of Fluids*, vol. 7, no. 4, pp. 557–558, 1964.

[106] P. Drazin and L. Howard, "Hydrodynamic stability of parallel flow of inviscid fluid," in *Advances in applied mechanics*, vol. 9, pp. 1–89, Elsevier, 1966.

[107] E. Crespo del Arco, J.-P. Pulicani, and A. Randriamampianina, "Complex multiple solutions and hysteresis cycles near the onset of oscillatory convection in a pr=0 liquid submitted to a horizontal temperature gradient," *Comptes rendus de l'Académie des sciences. Série 2, Mécanique, Physique, Chimie, Sciences de l'univers, Sciences de la Terre*, vol. 309, no. 19, pp. 1869–1876, 1989.

[108] J. Pulicani, E. C. Del Arco, A. Randriamampianina, P. Bontoux, and R. Peyret, "Spectral simulations of oscillatory convection at low prandtl number," *International Journal for Numerical Methods in Fluids*, vol. 10, no. 5, pp. 481–517, 1990.

[109] K. Okada and H. Ozoe, "Various computational conditions of oscillatory natural convection of zero prandtl number fluid in an open boat heated and cooled from opposing vertical walls," *Numerical Heat Transfer, Part A: Applications*, vol. 23, no. 2, pp. 171–187, 1993.

[110] F. Moukalled, L. Mangani, M. Darwish, *et al.*, "The finite volume method in computational fluid dynamics," *An advanced introduction with OpenFoam® and Matlab®. Nueva York: Springer. Recuperado de http://www. gidropraktikum. narod. ru/Moukalled-et-al-FVM-OpenFOAM-Matlab. pdf*, 2016.

[111] J. Hart, "A note on the stability of low-prandtl-number hadley circulations," *Journal of Fluid Mechanics*, vol. 132, pp. 271–281, 1983.

[112] P. Laure and B. Roux, "Linear and non linear study of the hadley circulation in the case of infinite cavity," *J. Cryst. Growth*, vol. 97, no. 1, pp. 226 – 234, 1989.

[113] V. Shevtsova, A. Nepomnyashchy, and J. C. Legros, "Thermocapillary-buoyancy convection in a shallow cavity heated from the side," *Physical Review E*, vol. 67, no. 6, p. 066308, 2003.

[114] M. Lappa, "Patterning behavior of gravitationally modulated supercritical marangoni flow in liquid layers," *Physical Review E*, vol. 93, no. 5, p. 053107, 2016.

[115] M. Lappa, "Hydrothermal waves in two-dimensional liquid layers with sudden changes in the available cross-section," *International Journal of Numerical Methods for Heat & Fluid Flow*, vol. 27, no. 11, pp. 2629–2649, 2017.

[116] M. Lappa, "On the onset of multi-wave patterns in laterally heated floating zones for slightly supercritical conditions," *Physics of Fluids*, vol. 28, no. 12, p. 124105, 2016.

[117] M. Afrid and A. Zebib, "Oscillatory three-dimensional convection in rectangular cavities and enclosures," *Physics of Fluids A: Fluid Dynamics*, vol. 2, no. 8, pp. 1318–1327, 1990.

[118] M. C. Hung and C. D. Andereck, "Transitions in convection driven by a horizontal temperature gradient," *Physics letters A*, vol. 132, no. 5, pp. 253–258, 1988.

[119] J. M. Pratte and J. E. Hart, "Endwall driven, low prandtl number convection in a shallow rectangular cavity," *Journal of Crystal Growth*, vol. 102, no. 1-2, pp. 54–68, 1990.

[120] M. Lappa, "Secondary and oscillatory gravitational instabilities in canonical three-dimensional models of crystal growth from the melt. part 2: Lateral heating and the hadley circulation," *Comptes Rendus Mécanique*, vol. 335, no. 5-6, pp. 261–268, 2007.

[121] M. G. Braunsfurth and T. Mullin, "An experimental study of oscillatory convection in liquid gallium," *Journal of Fluid Mechanics*, vol. 327, pp. 199–219, 1996.

[122] S. Wakitani, "Numerical study of three-dimensional oscillatory natural convection at low prandtl number in rectangular enclosures," *Journal of heat transfer*, vol. 123, no. 1, pp. 77–83, 2001.

[123] R. Delgado-Buscalioni, "Convection patterns in end-heated inclined enclosures," *Physical Review E*, vol. 64, no. 1, p. 016303, 2001.

[124] R. Delgado-Buscalioni, "Effects of thermal boundary conditions and cavity tilt on hydrothermal waves: Suppression of oscillations," *Physical Review E*, vol. 66, no. 1, p. 016301, 2002.

[125] M. Lappa and H. Ferialdi, "On the oscillatory hydrodynamic instability of gravitational thermal flows of liquid metals in variable cross-section containers," *Physics of Fluids*, vol. 29, no. 6, p. 064106, 2017.

[126] H. B. Squire, "On the stability for three-dimensional disturbances of viscous fluid flow between parallel walls," *Proceedings of the Royal Society of London. Series A, Containing Papers of a Mathematical and Physical Character*, vol. 142, no. 847, pp. 621–628, 1933.

[127] T.-M. Wang and S. A. Korpela, "Convection rolls in a shallow cavity heated from a side," *Physics of Fluids A: Fluid Dynamics*, vol. 1, no. 6, pp. 947–953, 1989.

[128] K. Okada and H. Ozoe, "The effect of aspect ratio on the critical grashof number for oscillatory natural convection of zero prandtl number fluid; numerical approach," *Journal of crystal growth*, vol. 126, no. 2-3, pp. 330–334, 1993.

[129] A. N. Kolmogorov, "The local structure of turbulence in incompressible viscous fluid for very large reynolds numbers," *Proceedings of the Royal Society of London. Series A: Mathematical and Physical Sciences*, vol. 434, no. 1890, pp. 9–13, 1991.

[130] A. N. Kolmogorov, "On degeneration (decay) of isotropic turbulence in an incompressible viscous liquid," in *Dokl. Akad. Nauk SSSR*, vol. 31, pp. 538–540, 1941.

[131] A. N. Kolmogorov, "Dissipation of energy in locally isotropic turbulence," in *Akademiia Nauk SSSR Doklady*, vol. 32, p. 16, 1941.

[132] A. Kolmogorov, "Equations of motion of an incompressible turbulent fluid," *Izv Akad Nauk SSSR Ser Phys*, vol. 6, no. 6, pp. 56–58, 1942.

[133] A. K. De, V. Eswaran, and P. K. Mishra, "Scalings of heat transport and energy spectra of turbulent rayleigh-bénard convection in a large-aspect-ratio box," *International Journal of Heat and Fluid Flow*, vol. 67, pp. 111–124, 2017.

[134] M. Lappa and T. Gradinscak, "On the oscillatory modes of compressible thermal convection in inclined differentially heated cavities," *International Journal of Heat and Mass Transfer*, vol. 121, pp. 412–436, 2018.

[135] R. Delgado-Buscalioni, E. C. del Arco, and P. Bontoux, "Flow transitions of a low-prandtl-number fluid in an inclined 3d cavity," *European Journal of Mechanics-B/Fluids*, vol. 20, no. 5, pp. 657–672, 2001.

[136] S. Paolucci, "Direct numerical simulation of two-dimensional turbulent natural convection in an enclosed cavity," *Journal of Fluid Mechanics*, vol. 215, pp. 229–262, 1990.

[137] M. Farhangnia, S. Biringen, and L. Peltier, "Numerical simulation of two–dimensional buoyancy–driven turbulence in a tall rectangular cavity," *International journal for numerical methods in fluids*, vol. 23, no. 12, pp. 1311–1326, 1996.

[138] O. Shishkina, R. J. Stevens, S. Grossmann, and D. Lohse, "Boundary layer structure in turbulent thermal convection and its consequences for the required numerical resolution," *New journal of Physics*, vol. 12, no. 7, p. 075022, 2010.

[139] P. Grassberger and I. Procaccia, "Measuring the strangeness of strange attractors," *Physica D: Nonlinear Phenomena*, vol. 9, no. 1-2, pp. 189–208, 1983.

[140] J. Theiler, "Spurious dimension from correlation algorithms applied to limited time-series data," *Physical review A*, vol. 34, no. 3, p. 2427, 1986.

[141] S. Paul, P. Wahi, and M. K. Verma, "Bifurcations and chaos in large-prandtl number rayleigh–bénard convection," *International Journal of Non-Linear Mechanics*, vol. 46, no. 5, pp. 772–781, 2011.

[142] P. Bergè, Y. Pomeau, and C. Vidal, "Order within chaos: towards a deterministic approach to turbulence," 1984.

[143] P. Bontoux, B. Roux, G. Schiroky, B. Markham, and F. Rosenberger, "Convection in the vertical midplane of a horizontal cylinder. comparison of two-dimensional approximations with three-dimensional results," *International journal of heat and mass transfer*, vol. 29, no. 2, pp. 227–240, 1986.

[144] N. Imaishi, S. Yasuhiro, Y. Akiyama, and S. Yoda, "Numerical simulation of oscillatory marangoni flow in half-zone liquid bridge of low prandtl number fluid," *Journal of crystal growth*, vol. 230, no. 1-2, pp. 164–171, 2001.

[145] V. Shevtsova, D. Melnikov, and J. C. Legros, "Multistability of oscillatory thermocapillary convection in a liquid bridge," *Physical Review E*, vol. 68, no. 6, p. 066311, 2003.

[146] V. M. Shevtsova, A. Mialdun, and M. Mojahed, "A study of heat transfer in liquid bridges near onset of instability," *Journal of Non-equilibrium Thermodynamics*, vol. 30, no. 3, pp. 261–281, 2005.

[147] M. Lappa, *Fluids, Materials and Microgravity: numerical techniques and insights into Physics*. Elsevier, 2004.

[148] M. Lappa, "On the variety of particle accumulation structures under the effect of g-jitters," *Journal of Fluid Mechanics*, vol. 726, pp. 160–195, 2013.

[149] Y. Gaponenko and V. Shevtsova, "Heat transfer through the interface and flow regimes in liquid bridge subjected to co-axial gas flow," *Microgravity Science and Technology*, vol. 24, no. 4, pp. 297–306, 2012.

[150] A. Mialdun, I. Ryzhkov, D. Melnikov, and V. Shevtsova, "Experimental evidence of thermal vibrational convection in a nonuniformly heated fluid in a reduced gravity environment," *Physical review letters*, vol. 101, no. 8, p. 084501, 2008.

[151] J. Liu and G. Ahlers, "Spiral-defect chaos in rayleigh-bénard convection with small prandtl numbers," *Physical review letters*, vol. 77, no. 15, p. 3126, 1996.

[152] G. Ahlers, S. Grossmann, and D. Lohse, "Heat transfer and large scale dynamics in turbulent rayleigh-bénard convection," *Reviews of modern physics*, vol. 81, no. 2, p. 503, 2009.

[153] F. Chillà and J. Schumacher, "New perspectives in turbulent rayleigh-bénard convection," *The European Physical Journal E*, vol. 35, no. 7, p. 58, 2012.

[154] M. Z. Saghir, A. Ahadi, A. Mohamad, and S. Srinivasan, "Water aluminum oxide nanofluid benchmark model," *International Journal of Thermal Sciences*, vol. 109, pp. 148–158, 2016.

[155] M. Lappa, *Rotating thermal flows in natural and industrial processes*. John Wiley & Sons, 2012.

[156] E. Clément, L. Vanel, J. Rajchenbach, and J. Duran, "Pattern formation in a vibrated two-dimensional granular layer," *Physical Review E*, vol. 53, no. 3, p. 2972, 1996.

[157] P. B. Umbanhowar, F. Melo, and H. L. Swinney, "Localized excitations in a vertically vibrated granular layer," *Nature*, vol. 382, no. 6594, p. 793, 1996.

[158] L. S. Tsimring and I. S. Aranson, "Localized and cellular patterns in a vibrated granular layer," *Physical review letters*, vol. 79, no. 2, p. 213, 1997.

[159] O. Lioubashevski, Y. Hamiel, A. Agnon, Z. Reches, and J. Fineberg, "Oscillons and propagating solitary waves in a vertically vibrated colloidal suspension," *Physical review letters*, vol. 83, no. 16, p. 3190, 1999.

[160] F. H. Busse and J. Whitehead, "Instabilities of convection rolls in a high prandtl number fluid," *Journal of Fluid Mechanics*, vol. 47, no. 2, pp. 305–320, 1971.

[161] M. Dennin, G. Ahlers, and D. S. Cannell, "Spatiotemporal chaos in electroconvection," *Science*, vol. 272, no. 5260, pp. 388–390, 1996.

[162] H. Riecke and G. D. Granzow, "Localization of waves without bistability: worms in nematic electroconvection," *Physical review letters*, vol. 81, no. 2, p. 333, 1998.

[163] J. L. Rogers, W. Pesch, and M. F. Schatz, "Pattern formation in vertically oscillated convection," *Nonlinearity*, vol. 16, no. 1, p. C1, 2002.

[164] D. Schwabe, "Marangoni instabilities in small circular containers under microgravity," *Experiments in fluids*, vol. 40, no. 6, pp. 942–950, 2006.

[165] P. Colinet, J. C. Legros, and M. G. Velarde, *Nonlinear dynamics of surface-tension-driven instabilities*. Wiley-vch, 2001.

[166] P. Parmentier, V. Regnier, G. Lebon, and J. C. Legros, "Nonlinear analysis of coupled gravitational and capillary thermoconvention in thin fluid layers," *Physical Review E*, vol. 54, no. 1, p. 411, 1996.

[167] D. Getachew and S. Rosenblat, "Thermocapillary instability of a viscoelastic liquid layer," *Acta mechanica*, vol. 55, no. 1-2, pp. 137–149, 1985.

[168] G. Lebon and A. Cloot, "An extended thermodynamic approach to non-newtonian fluids and related results in marangoni instability problem," *Journal of non-newtonian fluid mechanics*, vol. 28, no. 1, pp. 61–76, 1988.

[169] G. Lebon, P. Parmentier, O. Teller, and P. Dauby, "Bénard-marangoni instability in a viscoelastic jeffreys' fluid layer," *Rheologica acta*, vol. 33, no. 4, pp. 257–266, 1994.

[170] P. Dauby, P. Parmentier, G. Lebon, and M. Grmela, "Coupled buoyancy and thermocapillary convection in a viscoelastic maxwell fluid," *Journal of Physics: Condensed Matter*, vol. 5, no. 26, p. 4343, 1993.

[171] P. Siddheshwar, G. Sekhar, and G. Jayalatha, "Surface tension driven convection in viscoelastic liquids with thermorheological effect," *International Communications in Heat and Mass Transfer*, vol. 38, no. 4, pp. 468–473, 2011.

[172] H. Ramkissoon, G. Ramdath, D. Comissiong, and K. Rahaman, "On thermal instabilities in a viscoelastic fluid," *International Journal of Non-Linear Mechanics*, vol. 41, no. 1, pp. 18–25, 2006.

[173] I. H. Hernández and L. Dávalos-Orozco, "Competition between stationary and oscillatory viscoelastic thermocapillary convection of a film coating a thick wall," *International Journal of Thermal Sciences*, vol. 89, pp. 164–173, 2015.

[174] S. Wilson, "Growth rates of the marangoni instability in a layer of elastic liquid," *Rheologica acta*, vol. 34, no. 6, pp. 601–605, 1995.

[175] Z. Li and R. E. Khayat, "Finite-amplitude rayleigh–benard convection and pattern selection for viscoelastic fluids," *Journal of Fluid Mechanics*, vol. 529, pp. 221–251, 2005.

[176] J. Favero, A. R. Secchi, N. Cardozo, and H. Jasak, "Viscoelastic fluid analysis in internal and in free surface flows using the software openfoam," *Computers & chemical engineering*, vol. 34, no. 12, pp. 1984–1993, 2010.

[177] M. A. Alves, P. J. Oliveira, and F. T. Pinho, "Benchmark solutions for the flow of oldroyd-b and ptt fluids in planar contractions," *Journal of Non-Newtonian Fluid Mechanics*, vol. 110, no. 1, pp. 45–75, 2003.

[178] J. Kengne, A. N. Negou, D. Tchiotsop, V. K. Tamba, and G. Kom, "On the dynamics of chaotic systems with multiple attractors: a case study," in *Recent Advances in Nonlinear Dynamics and Synchronization*, pp. 17–32, Springer, 2018.

[179] V. I. Arnold, V. Afrajmovich, Y. S. Il'yashenko, and L. Shil'nikov, *Dynamical systems V: bifurcation theory and catastrophe theory*, vol. 5. Springer Science & Business Media, 2013.

[180] M. Lappa, "An alternative theoretical approach for the derivation of analytic and numerical solutions to thermal marangoni flows," *International Journal of Heat and Mass Transfer*, vol. 114, pp. 407–418, 2017.

[181] T. Cortese and S. Balachandar, "Vortical nature of thermal plumes in turbulent convection," *Physics of Fluids A: Fluid Dynamics*, vol. 5, no. 12, pp. 3226–3232, 1993.

[182] T. Solomon and J. P. Gollub, "Sheared boundary layers in turbulent rayleigh-bénard convection," *Physical review letters*, vol. 64, no. 20, p. 2382, 1990.

[183] E. D. Siggia, "High rayleigh number convection," *Annual review of fluid mechanics*, vol. 26, no. 1, pp. 137–168, 1994.

[184] M. Lappa, "Some considerations about the symmetry and evolution of chaotic rayleigh–bénard convection: The flywheel mechanism and the "wind" of turbulence," *Comptes Rendus Mécanique*, vol. 339, no. 9, pp. 563–572, 2011.

[185] F. Nicot, N. Hadda, M. Guessasma, J. Fortin, and O. Millet, "On the definition of the stress tensor in granular media," *International Journal of Solids and Structures*, vol. 50, no. 14-15, pp. 2508–2517, 2013.

[186] H. M. Jaeger, S. R. Nagel, and R. P. Behringer, "Granular solids, liquids, and gases," *Reviews of modern physics*, vol. 68, no. 4, p. 1259, 1996.

[187] R. G. Larson, E. S. Shaqfeh, and S. J. Muller, "A purely elastic instability in taylor–couette flow," *Journal of Fluid Mechanics*, vol. 218, pp. 573–600, 1990.

[188] R. G. Larson, "Instabilities in viscoelastic flows," *Rheologica Acta*, vol. 31, no. 3, pp. 213–263, 1992.

[189] A. Groisman and V. Steinberg, "Mechanism of elastic instability in couette flow of polymer solutions: experiment," *Physics of Fluids*, vol. 10, no. 10, pp. 2451–2463, 1998.

[190] A. N. Morozov and W. van Saarloos, "Subcritical finite-amplitude solutions for plane couette flow of viscoelastic fluids," *Physical review letters*, vol. 95, no. 2, p. 024501, 2005.

[191] R. H. Kraichnan, "On kolmogorov's inertial-range theories," *Journal of Fluid Mechanics*, vol. 62, no. 2, pp. 305–330, 1974.

[192] A. Groisman and V. Steinberg, "Elastic turbulence in a polymer solution flow," *Nature*, vol. 405, no. 6782, p. 53, 2000.

[193] K. Avila, D. Moxey, A. de Lozar, M. Avila, D. Barkley, and B. Hof, "The onset of turbulence in pipe flow," *Science*, vol. 333, no. 6039, pp. 192–196, 2011.

[194] I. J. Wygnanski and F. Champagne, "On transition in a pipe. part 1. the origin of puffs and slugs and the flow in a turbulent slug," *Journal of Fluid Mechanics*, vol. 59, no. 2, pp. 281–335, 1973.

[195] B. Eckhardt, T. M. Schneider, B. Hof, and J. Westerweel, "Turbulence transition in pipe flow," *Annu. Rev. Fluid Mech.*, vol. 39, pp. 447–468, 2007.

[196] K. Kaneko, "Spatiotemporal intermittency in coupled map lattices," *Progress of Theoretical Physics*, vol. 74, no. 5, pp. 1033–1044, 1985.

[197] M. Lappa, "Oscillatory convective structures and solutal jets originated from discrete distributions of droplets in organic alloys with a miscibility gap," *Physics of Fluids*, vol. 18, no. 4, p. 042105, 2006.

[198] M. Lappa, "Single-and multi-droplet configurations out of thermodynamic equilibrium: Pulsating, traveling, and erratic fluiddynamic instabilities," *New Colloid and Surface Science Research*, pp. 1–58, 2007.

[199] W. Barten, M. Lücke, M. Kamps, and R. Schmitz, "Convection in binary fluid mixtures. i. extended traveling-wave and stationary states," *Physical Review E*, vol. 51, no. 6, p. 5636, 1995.

[200] O. Pauluis and J. Schumacher, "Self-aggregation of clouds in conditionally unstable moist convection," *Proceedings of the National Academy of Sciences*, vol. 108, no. 31, pp. 12623–12628, 2011.

[201] Z. J. Taylor, R. Gurka, G. A. Kopp, and A. Liberzon, "Long-duration time-resolved piv to study unsteady aerodynamics," *IEEE Transactions on Instrumentation and Measurement*, vol. 59, no. 12, pp. 3262–3269, 2010.

[202] N. Ouertatani, N. B. Cheikh, B. B. Beya, and T. Lili, "Numerical simulation of two-dimensional rayleigh–bénard convection in an enclosure," *Comptes Rendus Mécanique*, vol. 336, no. 5, pp. 464–470, 2008.

[203] C. Soong, P. Tzeng, D. Chiang, and T. Sheu, "Numerical study on mode-transition of natural convection in differentially heated inclined enclosures," *International Journal of Heat and Mass Transfer*, vol. 39, no. 14, pp. 2869–2882, 1996.

[204] G. D. V. Davis and I. Jones, "Natural convection in a square cavity: a comparison exercise," *International Journal for numerical methods in fluids*, vol. 3, no. 3, pp. 227–248, 1983.

[205] U. H. Kurzweg, "Convective instability of a hydromagnetic fluid within a rectangular cavity," *International Journal of Heat and Mass Transfer*, vol. 8, no. 1, pp. 35–41, 1965.

[206] W. Velte, "Stabilitätsverhalten und verzweigung stationärer lösungen der navier-stokesschen gleichungen," *Archive for Rational Mechanics and Analysis*, vol. 16, no. 2, pp. 97–125, 1964.

[207] J. Luijkx and J. Platten, "On the onset of free convection in a rectangular channel," *Journal of Non-Equilibrium Thermodynamics*, vol. 6, no. 3, pp. 141–158, 1981.

[208] J. Mizushima, "Onset of the thermal convection in a finite two-dimensional box," *Journal of the Physical Society of Japan*, vol. 64, no. 7, pp. 2420–2432, 1995.

[209] M. Chana and P. Daniels, "Onset of rayleigh–bénard convection in a rigid channel," *Journal of Fluid Mechanics*, vol. 199, pp. 257–279, 1989.

[210] J. Mizushima and T. Adachi, "Sequential transitions of the thermal convection in a square cavity," *Journal of the Physical Society of Japan*, vol. 66, no. 1, pp. 79–90, 1997.

[211] A. Libchaber, C. Laroche, and S. Fauve, "Period doubling cascade in mercury, a quantitative measurement," in *Universality in Chaos, 2nd edition*, pp. 137–142, Routledge, 2017.

[212] F. Stella, Edoardo Bucchignani, "Rayleigh-bénard convection in limited domains: Part 2-transition to chaos," *Numerical Heat Transfer: Part A: Applications*, vol. 36, no. 1, pp. 17–34, 1999.

[213] F. Stella and E. Bucchignani, "Rayleigh-bénard convection in limited domains: Part 1-oscillatory flow," *Numerical Heat Transfer Part A: Applications*, vol. 36, no. 1, pp. 1–16, 1999.

[214] M. Lappa and H. Ferialdi, "Multiple solutions, oscillons, and strange attractors in thermoviscoelastic marangoni convection," *Physics of Fluids*, vol. 30, no. 10, p. 104104, 2018.

[215] S. Paul, M. K. Verma, P. Wahi, S. K. Reddy, and K. Kumar, "Bifurcation analysis of the flow patterns in two-dimensional rayleigh–bénard convection," *International Journal of Bifurcation and Chaos*, vol. 22, no. 05, p. 1230018, 2012.

[216] M. Kitano, T. Yabuzaki, and T. Ogawa, "Symmetry-recovering crises of chaos in polarization-related optical bistability," *Physical Review A*, vol. 29, no. 3, p. 1288, 1984.

[217] I. Goldhirsch, R. B. Pelz, and S. A. Orszag, "Numerical simulation of thermal convection in a two-dimensional finite box," *Journal of Fluid Mechanics*, vol. 199, pp. 1–28, 1989.

[218] J. Mizushima and T. Nakamura, "Onset of three-dimensional thermal convection in a rectangular parallelepiped cavity," *Journal of the Physical Society of Japan*, vol. 72, no. 2, pp. 197–200, 2003.

[219] D. Puigjaner, J. Herrero, F. Giralt, and C. Simó, "Stability analysis of the flow in a cubical cavity heated from below," *Physics of fluids*, vol. 16, no. 10, pp. 3639–3655, 2004.

[220] J. Mizushima and O. Matsuda, "Onset of 3d thermal convection in a cubic cavity," *Journal of the Physical Society of Japan*, vol. 66, no. 8, pp. 2337–2341, 1997.

[221] J. Pallares, F. Grau, and F. Giralt, "Flow transitions in laminar rayleigh–bénard convection in a cubical cavity at moderate rayleigh numbers," *International journal of heat and mass transfer*, vol. 42, no. 4, pp. 753–769, 1999.

[222] D. Puigjaner, J. Herrero, F. Giralt, and C. Simó, "Bifurcation analysis of multiple steady flow patterns for rayleigh-bénard convection in a cubical cavity at pr= 130," *Physical Review E*, vol. 73, no. 4, p. 046304, 2006.

[223] P. Le Quéré and F. Penot, "Numerical and experimental investigation of the transition to unsteady natural convection of air in a vertical differentially heated cavity," *ASME HTD*, vol. 94, pp. 75–82, 1987.

[224] R. Henkes and C. Hoogendoorn, "On the stability of the natural convection flow in a square cavity heated from the side," *Applied Scientific Research*, vol. 47, no. 3, pp. 195–220, 1990.

[225] E. Bucchignani, "An implicit unsteady finite volume formulation for natural convection in a square cavity," *Fluid Dyn. Mater. Process*, vol. 5, no. 1, pp. 37–60, 2009.

[226] S. Paolucci and D. R. Chenoweth, "Transition to chaos in a differentially heated vertical cavity," *Journal of Fluid Mechanics*, vol. 201, pp. 379–410, 1989.

[227] R. Janssen and R. Henkes, "Influence of prandtl number on instability mechanisms and transition in a differentially heated square cavity," *Journal of Fluid Mechanics*, vol. 290, pp. 319–344, 1995.

[228] S. Xin and P. Le Quéré, "Direct numerical simulations of two-dimensional chaotic natural convection in a differentially heated cavity of aspect ratio 4," *Journal of Fluid Mechanics*, vol. 304, pp. 87–118, 1995.

[229] H. Yahata, "Thermal convection in a vertical slot with lateral heating," *Journal of the Physical Society of Japan*, vol. 66, no. 11, pp. 3434–3443, 1997.

[230] P. Le Quéré and M. Behnia, "From onset of unsteadiness to chaos in a differentially heated square cavity," *Journal of fluid mechanics*, vol. 359, pp. 81–107, 1998.

[231] D. A. Mayne, A. S. Usmani, and M. Crapper, "h-adaptive finite element solution of high rayleigh number thermally driven cavity problem," *International Journal of Numerical Methods for Heat & Fluid Flow*, vol. 10, no. 6, pp. 598–615, 2000.

[232] Y. Tian and T. Karayiannis, "Low turbulence natural convection in an air filled square cavity: part i: the thermal and fluid flow fields," *International Journal of Heat and Mass Transfer*, vol. 43, no. 6, pp. 849–866, 2000.

[233] M. Ravi, R. Henkes, and C. Hoogendoorn, "On the high-rayleigh-number structure of steady laminar natural-convection flow in a square enclosure," *Journal of Fluid Mechanics*, vol. 262, pp. 325–351, 1994.

[234] D. Jones and D. Briggs, "Periodic two-dimensional cavity flow: effect of linear horizontal thermal boundary condition," *Journal of heat transfer*, vol. 111, no. 1, pp. 86–91, 1989.

[235] K. Winters, "Hopf bifurcation in the double-glazing problem with conducting boundaries," *Journal of heat transfer*, vol. 109, no. 4, pp. 894–898, 1987.

[236] A. Y. Gelfgat and I. Tanasawa, "Numerical analysis of oscillatory instability of buoyancy convection with the galerkin spectral method," *Numerical Heat Transfer*, vol. 25, no. 6, pp. 627–648, 1994.

[237] S. Xin and P. Le Quéré, "Linear stability analyses of natural convection flows in a differentially heated square cavity with conducting horizontal walls," *Physics of Fluids*, vol. 13, no. 9, pp. 2529–2542, 2001.

[238] H. Yang, K. Yang, and J. Lloyd, "Laminar natural-convection flow transitions in tilted three-dimensional longitudinal rectangular enclosures," *International journal of heat and mass transfer*, vol. 30, no. 8, pp. 1637–1644, 1987.

[239] H. Yang, K. Yang, and J. Lloyd, "Three-dimensional bimodal buoyant flow transitions in tilted enclosures," *International journal of heat and fluid flow*, vol. 9, no. 2, pp. 90–97, 1988.

[240] G. Lock and J.-C. Han, "The effects of tilt, skew and roll on natural convection in a slender, laterally-heated cavity," *Mathematical and Computer Modelling*, vol. 13, no. 2, pp. 23–32, 1990.

[241] I. Catton, P. Ayyaswamy, and R. Clever, "Natural convection flow in a finite, rectangular slot arbitrarily oriented with respect to the gravity vector," *International Journal of Heat and Mass Transfer*, vol. 17, no. 2, pp. 173–184, 1974.

[242] R. Kuyper, T. H. Van Der Meer, C. Hoogendoorn, and R. Henkes, "Numerical study of laminar and turbulent natural convection in an inclined square cavity," *International Journal of Heat and Mass Transfer*, vol. 36, no. 11, pp. 2899–2911, 1993.

[243] T. Adachi and J. Mizushima, "Stability of the thermal convection in a tilted square cavity," *Journal of the Physical Society of Japan*, vol. 65, no. 6, pp. 1686–1698, 1996.

[244] N. Williamson, S. Armfield, W. Lin, and M. Kirkpatrick, "Stability and nusselt number scaling for inclined differentially heated cavity flow," *International Journal of Heat and Mass Transfer*, vol. 97, pp. 787–793, 2016.

[245] J. F. Torres, D. Henry, A. Komiya, and S. Maruyama, "Transition from multiplicity to singularity of steady natural convection in a tilted cubical enclosure," *Physical Review E*, vol. 92, no. 2, p. 023031, 2015.

[246] Q. Wang, Z.-H. Wan, R. Yan, and D.-J. Sun, "Multiple states and heat transfer in two-dimensional tilted convection with large aspect ratios," *Physical Review Fluids*, vol. 3, no. 11, p. 113503, 2018.

[247] T. Lee and T. Lin, "Three-dimensional natural convection of air in an inclined cubic cavity," *Numerical Heat Transfer, Part A: Applications*, vol. 27, no. 6, pp. 681–703, 1995.

[248] S. Schladow, J. Patterson, and R. Street, "Transient flow in a side-heated cavity at high rayleigh number: a numerical study," *Journal of Fluid Mechanics*, vol. 200, pp. 121–148, 1989.

[249] W. Hiller, S. Koch, and T. Kowalewski, "Three-dimensional structures in laminar natural convection in a cubic enclosure," *Experimental Thermal and Fluid Science*, vol. 2, no. 1, pp. 34–44, 1989.

[250] T. A. Kowalewski, "Experimental validation of numerical codes in thermally driven flows," in *ICHMT DIGITAL LIBRARY ONLINE*, Begel House Inc., 1997.

[251] D. Melnikov and V. Shevtsova, "Liquid particles tracing in three-dimensional buoyancy-driven flows," *Fluid Dyn Mater Process*, vol. 1, pp. 189–199, 2005.

[252] A. Belmonte, A. Tilgner, and A. Libchaber, "Turbulence and internal waves in side-heated convection," *Physical Review E*, vol. 51, no. 6, p. 5681, 1995.

[253] T. Fusegi, J. M. Hyun, and K. Kuwahara, "Three-dimensional simulations of natural convection in a sidewall-heated cube," *International journal for numerical methods in fluids*, vol. 13, no. 7, pp. 857–867, 1991.

[254] G. Labrosse, E. Tric, H. Khallouf, and M. Betrouni, "A direct (pseudo-spectral) solver of the 2d/3d stokes problem: transition to unsteadiness of natural-convection flow in a differentially heated cubical cavity," *Numerical Heat Transfer*, vol. 31, no. 3, pp. 261–276, 1997.

[255] M. Soria, F. Trias, C. Pérez-Segarra, and A. Oliva, "Direct numerical simulation of a three-dimensional natural-convection flow in a differentially heated cavity of aspect ratio 4," *Numerical Heat Transfer, Part A: Applications*, vol. 45, no. 7, pp. 649–673, 2004.

[256] F. Trias, M. Soria, A. Oliva, and C. Pérez-Segarra, "Direct numerical simulations of two-and three-dimensional turbulent natural convection flows in a differentially heated cavity of aspect ratio 4," *Journal of Fluid Mechanics*, vol. 586, pp. 259–293, 2007.

[257] S. H. Strogatz, *Nonlinear dynamics and chaos: with applications to physics, biology, chemistry, and engineering*. CRC Press, 2018.

[258] A. Schüter, D. Lortz, and F. H. Busse, "On stability of finite amplitude convection." J. Fluid Mech., 1965.

[259] W. Ostwald, "Ueber die geschwindigkeitsfunktion der viskosität disperser systeme. i," *Colloid & Polymer Science*, vol. 36, no. 2, pp. 99–117, 1925.

[260] A. De Waele, "Viscometry and plastometry," *Oil Color Chem Assoc J*, vol. 6, pp. 33–88, 1923.

[261] J. Oldroyd, "On the formulation of rheological equations of state," *Proceedings of the Royal Society of London. Series A. Mathematical and Physical Sciences*, vol. 200, no. 1063, pp. 523–541, 1950.

[262] J. White and A. Metzner, "Development of constitutive equations for polymeric melts and solutions," *Journal of Applied Polymer Science*, vol. 7, no. 5, pp. 1867–1889, 1963.

[263] J. Oldroyd, "The hydrodynamics of materials whose rheological properties are complicated," *Rheologica Acta*, vol. 1, no. 4-6, pp. 337–344, 1961.

[264] H. Giesekus, "A simple constitutive equation for polymer fluids based on the concept of deformation-dependent tensorial mobility," *Journal of Non-Newtonian Fluid Mechanics*, vol. 11, no. 1-2, pp. 69–109, 1982.

[265] A. M. Fraser and H. L. Swinney, "Independent coordinates for strange attractors from mutual information," *Physical review A*, vol. 33, no. 2, p. 1134, 1986.

[266] J. H. Curry, J. R. Herring, J. Loncaric, and S. A. Orszag, "Order and disorder in two-and three-dimensional bénard convection," *Journal of Fluid Mechanics*, vol. 147, pp. 1–38, 1984.

[267] J. Boussinesq, *Thōrie analytique de la chaleur mise en harmonie avec la thermodynamique et avec la thōrie mecanique de la lumi_re: Refroidissement et chauffement par rayonnement, conductibilit des tiges, lames et masses cristallines, courants de convection, thōrie mecanique de la lumi_re. 1903. xxxii, 625,[1] p*, vol. 2. Gauthier-Villars, 1903.